

# Solid state reactions in electroceramic systems

## Dissertation

zur Erlangung des akademischen Grades

doctor rerum naturalium (Dr. rer. nat.)

vorgelegt der

Naturwissenschaftlichen Fakultät II  
der Martin-Luther-Universität Halle-Wittenberg

von Herrn Andriy Lotnyk  
geb. am 16.03.1980 in Kupjansk (Ukraine)

Gutachter:

1. Prof. Dr. Dietrich Hesse, MPI für Mikrostrukturphysik, Halle, Germany
2. Prof. Dr. Hans-Peter Abicht, Martin-Luther-Universität Halle-Wittenberg, Halle, Germany
3. Dr. Vincenzo Scaglia (Head of Group), National Research Council, Genoa, Italy

Halle (Saale), 26 April 2007

verteidigt am 6 November 2007

**urn:nbn:de:gbv:3-000012648**

[<http://nbn-resolving.de/urn/resolver.pl?urn=nbn%3Ade%3Agbv%3A3-000012648>]

*Dedicated to my lovely wife Svitlana and my son Volodymyr*

# Contents

<b>1</b>	<b>Introduction</b>	<b>1</b>
<b>2</b>	<b>Literature review</b>	<b>4</b>
2.1	Thin film solid state reactions . . . . .	4
2.1.1	Thermodynamic model . . . . .	5
2.1.2	Nucleation-controlled model . . . . .	5
2.1.3	Kinetic model . . . . .	7
2.2	Synthesis of BaTiO <sub>3</sub> ceramics . . . . .	8
2.2.1	Crystal structure and some properties of TiO <sub>2</sub> . . . . .	8
2.2.2	Crystal structure of BaCO <sub>3</sub> , BaTiO <sub>3</sub> and Ba <sub>2</sub> TiO <sub>4</sub> . . . . .	10
	A. BaCO <sub>3</sub> . . . . .	10
	B. BaTiO <sub>3</sub> . . . . .	11
	C. Ba <sub>2</sub> TiO <sub>4</sub> . . . . .	12
2.2.3	Formation of BaTiO <sub>3</sub> from BaCO <sub>3</sub> and TiO <sub>2</sub> by solid state reactions . . . . .	13
2.2.4	Ti-rich barium titanates . . . . .	17
	A. Phase diagram . . . . .	17
	B. Crystal structure . . . . .	18
2.3	The system SrO-TiO <sub>2</sub> . . . . .	19
2.4	The system CaO-TiO <sub>2</sub> . . . . .	20
2.5	The system MgO-TiO <sub>2</sub> . . . . .	21
2.6	Modeling of powder reactions . . . . .	23
<b>3</b>	<b>Experimental and investigation procedures</b>	<b>24</b>
3.1	Sample preparations . . . . .	24
3.2	X-ray diffraction . . . . .	27
3.2.1	Basic principles . . . . .	27
3.2.2	XRD analysis performed in this work . . . . .	27
3.3	Transmission electron microscopy . . . . .	30
3.3.1	Basic concepts . . . . .	30
3.3.2	TEM sample preparation . . . . .	31
3.4	Atomic force microscopy . . . . .	32
<b>4</b>	<b>Results</b>	<b>34</b>
4.1	Solid state reactions of BaCO <sub>3</sub> and BaO with TiO <sub>2</sub> (rutile) . . . . .	34
4.1.1	Solid-solid reaction of BaCO <sub>3</sub> with TiO <sub>2</sub> (rutile) . . . . .	34
	A. Some properties of BaCO <sub>3</sub> thin films . . . . .	34

---

	B. Phase formation . . . . .	36
4.1.2	Vapour-solid reaction of BaO with TiO <sub>2</sub> (rutile) . . . . .	41
	A. Phase formation . . . . .	41
	B. Initial stage of vapour-solid reaction at 900 °C . . . . .	44
4.1.3	Orientation relationships . . . . .	46
	A. Orientation of Ba <sub>2</sub> TiO <sub>4</sub> . . . . .	46
	B. Orientation of BaTiO <sub>3</sub> . . . . .	48
	C. Orientations of Ti-rich phases . . . . .	57
4.2	Solid state reactions of BaCO <sub>3</sub> and BaO with TiO <sub>2</sub> (anatase) . . . . .	58
4.2.1	Epitaxial growth of TiO <sub>2</sub> anatase thin films . . . . .	58
	A. TiO <sub>2</sub> film growth on (100) SrTiO <sub>3</sub> and (100) LaAlO <sub>3</sub> . . . . .	58
	B. TiO <sub>2</sub> film growth on (110) SrTiO <sub>3</sub> and (110) LaAlO <sub>3</sub> . . . . .	61
	C. Origin of the epitaxy between TiO <sub>2</sub> (anatase) and SrTiO <sub>3</sub> /LaAlO <sub>3</sub> . . . . .	64
4.2.2	Phase formation and orientation relationships . . . . .	66
	A. Phase formation . . . . .	66
	B. Orientation relationships . . . . .	67
4.3	Solid state reactions of other alkaline-earth oxides with TiO <sub>2</sub> (rutile) . . . . .	71
4.3.1	Vapour-solid reaction of SrO with TiO <sub>2</sub> (rutile) . . . . .	71
4.3.2	Vapour-solid reaction of CaO with TiO <sub>2</sub> (rutile) . . . . .	73
	A. Phase formation . . . . .	73
	B. Orientation relationships . . . . .	75
4.3.3	Vapour-solid reaction of MgO with TiO <sub>2</sub> (rutile) . . . . .	77
<b>5</b>	<b>Discussion</b>	<b>79</b>
5.1	The reaction systems BaCO <sub>3</sub> -TiO <sub>2</sub> and BaO-TiO <sub>2</sub> . . . . .	79
5.1.1	Phase formation . . . . .	79
	A. Solid-solid reaction of BaCO <sub>3</sub> with TiO <sub>2</sub> . . . . .	79
	B. Vapour-solid reaction of BaO vapour with TiO <sub>2</sub> . . . . .	82
5.1.2	Orientation relationships . . . . .	84
	A. Orientation of Ba <sub>2</sub> TiO <sub>4</sub> on TiO <sub>2</sub> (rutile) . . . . .	84
	B. Orientations of BaTiO <sub>3</sub> on TiO <sub>2</sub> (rutile) . . . . .	84
	C. Orientations of BaTiO <sub>3</sub> on TiO <sub>2</sub> (anatase) . . . . .	89
	D. Orientations of Ti-rich phases on TiO <sub>2</sub> (rutile) . . . . .	90
5.1.3	Reaction of BaO vapour with TiO <sub>2</sub> surfaces at 900 °C . . . . .	91
	A. Reaction mechanism . . . . .	91
	B. Void formation . . . . .	92
5.2	The reaction systems SrO-TiO <sub>2</sub> , CaO-TiO <sub>2</sub> and MgO-TiO <sub>2</sub> . . . . .	93
5.2.1	Orientation of SrTiO <sub>3</sub> on TiO <sub>2</sub> (rutile) . . . . .	93
5.2.2	Orientation of CaTiO <sub>3</sub> on TiO <sub>2</sub> (rutile) . . . . .	93
5.2.3	Orientation of MgTiO <sub>3</sub> on TiO <sub>2</sub> (rutile) . . . . .	94

---

5.3 Factors influencing the first-phase selection in complex oxide thin film systems . . .	95
<b>6 Conclusions</b>	<b>98</b>
<b>Bibliography</b>	<b>Bib 1</b>
<b>Appendix</b>	<b>A 1</b>
<b>Eidesstattliche Erklärung</b>	
<b>Acknowledgments</b>	
<b>Curriculum Vitae</b>	
<b>List of publications</b>	
<b>Conference contributions</b>	

# 1 Introduction

Solid state reactions in ceramic materials are investigated since many years under both fundamental and technological points of view.<sup>1-4</sup> Under working conditions, many devices consisting of multi-phase or multilayered ceramics are often subjected to high temperatures. As a result, interfacial solid state reactions may occur between the components. Such reactions occurring on the nanometer scale may affect the desired properties of the devices, because chemical and physical properties of interfaces are changed. Thus, in order to optimise the properties of the existing materials as well as to produce new materials with desired properties, advanced knowledge of thin film solid state reactions is required.

Model experiments are well suited to study various aspects of complex solid state reactions. In this approach, instead of using polycrystalline materials, one reactant is a bulk single crystal. In such model experiments, the formation and orientation of the reaction products can well be characterised by several structural techniques such as X-ray diffractometry (XRD) and transmission electron microscopy (TEM). This approach has successfully been used by several research groups to study interfacial reaction mechanisms and reaction kinetics in oxides.<sup>5-11</sup> In the present work, solid state reactions in different oxide systems, viz.  $\text{BaCO}_3\text{-TiO}_2$ ,  $\text{BaO}\text{-TiO}_2$ ,  $\text{SrO}\text{-TiO}_2$ ,  $\text{CaO}\text{-TiO}_2$  and  $\text{MgO}\text{-TiO}_2$ , are investigated.

In the first two systems,  $\text{BaCO}_3\text{-TiO}_2$  and  $\text{BaO}\text{-TiO}_2$ , the solid state reaction of solid  $\text{BaCO}_3$  and  $\text{BaO}$  vapour with  $\text{TiO}_2$  substrates of different crystallographic structure (anatase and rutile) are studied in a thin film geometry. In particular, phase formation, phase sequence and orientation of the reaction phases are analysed. The main goal of this part of the Ph.D. work was to study the mechanism of  $\text{BaTiO}_3$  formation in vacuum and in air. The solid state reaction between  $\text{BaCO}_3$  and  $\text{TiO}_2$  raw materials is still one of the main industrial ways for  $\text{BaTiO}_3$  production. The  $\text{BaTiO}_3$  forming process usually occurs via an intermediate  $\text{Ba}_2\text{TiO}_4$  compound. There are many experimental works which describe the formation of  $\text{BaTiO}_3$ . At the beginning of the 1990s, Niepce and Thomas<sup>12</sup> have proposed a model based on spherical  $\text{TiO}_2$  particles surrounded by  $\text{BaCO}_3$ . For this arrangement, they have predicted that it is possible to prevent the formation of the  $\text{Ba}_2\text{TiO}_4$  phase by controlling the grain sizes of the initial powders. Such core-shell structured  $\text{BaCO}_3\text{-TiO}_2$  substances were prepared by Gablenz *et al.*<sup>13</sup> ( $\text{BaCO}_3$  (shell)- $\text{TiO}_2$  (core), with diameters of the core-shell grains up to several  $\mu\text{m}$ ) in the year 2001 and by Buscaglia *et al.*<sup>14</sup> ( $\text{BaCO}_3$  (core)- $\text{TiO}_2$  (shell), with sizes of the core-shell grains  $\approx 100\text{ nm}$ - $500\text{ nm}$  in length and  $\approx 50\text{ nm}$  in diameter) in the year 2007. Heating of the powders prepared by Gablenz *et al.*<sup>13</sup> showed a modified sequence of phases.<sup>13,15,16</sup> In addition to the intermediate  $\text{Ba}_2\text{TiO}_4$  phase, different Ti-rich barium titanates were observed depending on the annealing temperature. On the other hand, heating of the powders prepared by Buscaglia *et al.*<sup>14</sup> showed a formation of only the  $\text{BaTiO}_3$  compound. The effect of the particle size of the initial reactants and of the gas pressure on the solid state synthesis of barium titanate was given by Hennings *et al.*<sup>17</sup> and by Buscaglia *et al.*,<sup>18</sup> respectively. Hennings *et al.* found

---

that the formation of the  $\text{Ba}_2\text{TiO}_4$  compound in air can be suppressed in a reaction between submicrometer  $\text{BaCO}_3$  ( $0.17\ \mu\text{m}$ ) and fine  $\text{TiO}_2$  ( $0.2\ \mu\text{m}$ ). Buscaglia *et al.* reported that the calcination of nanocrystalline  $\text{BaCO}_3$  and  $\text{TiO}_2$  powders performed in flowing air at 1 bar (100 kPa) completely suppresses the formation of the  $\text{Ba}_2\text{TiO}_4$  secondary phase. However, the decrease of pressure to 40 mbar induced the formation of  $\text{Ba}_2\text{TiO}_4$  at a reaction temperature of  $740\ ^\circ\text{C}$ . Hence, the selection of this rather complex system for a phase formation study in model experiments should be a way to gain a better understanding of the processes. The commercial  $\text{TiO}_2$  powder usually contains a mixture of  $\text{TiO}_2$  rutile and  $\text{TiO}_2$  anatase. Thus, in the present work  $\text{TiO}_2$  rutile single crystals as well as epitaxial  $\text{TiO}_2$  anatase single crystalline thin films are used as substrates to provide a model system. In this Ph.D. work, the phase formation sequences and orientation relationships during  $\text{BaTiO}_3$  growth from  $\text{BaCO}_3$  (solid film with a thickness of  $\approx 50\ \text{nm}$ ) or  $\text{BaO}$  (vapour equivalent to a nominal  $\text{BaO}$  thickness up to  $\approx 50\ \text{nm}$ ) and  $\text{TiO}_2$  (substrate) are investigated using a combined application of XRD, TEM and high-resolution TEM (HRTEM).

In the next three systems,  $\text{SrO-TiO}_2$ ,  $\text{CaO-TiO}_2$  and  $\text{MgO-TiO}_2$ , the solid state reaction between  $\text{TiO}_2$  (rutile) single crystals and  $\text{SrO}$ ,  $\text{CaO}$  or  $\text{MgO}$  vapour was studied. The primary aims of this part of the Ph.D. thesis are: (1) To compare the orientation relationships found for the  $\text{BaTiO}_3$  perovskite grown on  $\text{TiO}_2$  (rutile) substrates with those for  $\text{SrTiO}_3$  and  $\text{CaTiO}_3$  perovskites as well as for the rhombohedral  $\text{MgTiO}_3$ ; (2) To determine possible topotaxial orientation relationships between tetragonal  $\text{TiO}_2$  (rutile) and the rhombohedral  $\text{MgTiO}_3$  phase. As has been shown recently on the example of the non-cubic, corundum-type phases  $\text{Mg}_4\text{Ta}_2\text{O}_9$  and  $\text{Mg}_4\text{Nb}_2\text{O}_9$  growing topotaxially on cubic  $\text{MgO}$  single-crystal substrates, surprising topotaxial orientation relationships and corresponding reaction mechanisms can be found in case of non-cubic reactants and/or reaction products.<sup>19,20</sup> (3) To study the role of crystallography in topotaxial first phase formation in the  $\text{MgO-TiO}_2$  system, taking into account previous results of investigations of vapour-solid reactions obtained using  $\text{MgO}$  substrates.<sup>11</sup> The question which phase forms first in a thin-film solid state reaction, if the corresponding phase diagram permits the formation of several phases, is of considerable scientific and technological significance. However, the role of crystallography in topotaxial first-phase selection has not been sufficiently considered so far.

In thin film diffusion couples not all of the equilibrium phases may be observed which are stable in bulk. Various reasons have been given in the literature. The selective formation of phases has been attributed to thermodynamic factors,<sup>21,22</sup> nucleation barriers<sup>23</sup> and kinetic factors.<sup>24-27</sup> The main statements of these models are presented in **Chapter 2**. This chapter also gives an introduction to the crystal structure and some properties of the investigated compounds such as  $\text{TiO}_2$ ,  $\text{BaTiO}_3$ ,  $\text{BaCO}_3$ ,  $\text{Ba}_2\text{TiO}_4$  and Ti-rich barium titanates. Experimental results on solid state reactions in the systems  $\text{BaCO}_3\text{-TiO}_2$ ,  $\text{BaO-TiO}_2$ ,  $\text{SrO-TiO}_2$ ,  $\text{CaO-TiO}_2$  and  $\text{MgO-TiO}_2$  are also presented in **Chapter 2**. The experimental set-up and investigation techniques used in the present study are given in details in **Chapter 3**. The results of the experiments are presented in **Chapter 4**. The findings on the solid state reactions in the systems  $\text{BaCO}_3\text{-TiO}_2$  (rutile) and  $\text{BaO-TiO}_2$  (rutile) are given in **Section 4.1**. A study of solid state reactions in the systems  $\text{BaCO}_3\text{-TiO}_2$  (anatase) and  $\text{BaO-TiO}_2$  (anatase) is presented in **Section 4.2**. In the last two systems, epitaxial  $\text{TiO}_2$  (anatase)

films were used as substrates. The growth of epitaxial  $\text{TiO}_2$  anatase films on  $\text{SrTiO}_3$  and  $\text{LaAlO}_3$  substrates is described in **Subsection 4.2.1**. **Section 4.3** describes vapour-solid reactions of  $\text{SrO}$  vapour,  $\text{CaO}$  vapour and  $\text{MgO}$  vapour with the  $\text{TiO}_2$  (rutile) substrates. **Chapter 5** is dedicated to the discussion of the experimental results obtained in this work. A summary is given in **Chapter 6**.

## 2 Literature review

### 2.1 Thin film solid state reactions

A solid state chemical reaction in the classical sense occurs when local transport of matter is observed in crystalline phases and new phases are formed.<sup>1</sup> This definition does not mean that gaseous or liquid phases may not take part in the solid state reactions. However, it does mean that the reaction product occurs as a solid phase. Thus, the tarnishing of metals during dry or wet oxidation is also considered to be a solid state reaction. Commonly, the solid state reactions are heterogeneous reactions. If after reaction of two substances one or more solid product phases are formed, then a heterogeneous solid state reaction is said to have occurred. Spinel- and pyrochlore-forming reactions are well-known examples of solid-state reactions where a ternary oxide forms.<sup>5-11</sup> In this Ph.D. thesis, heterogeneous solid state reactions are considered.

Extended crystal defects as high mobility paths for atoms are essential in the reactivity of solids. Furthermore, interfaces play an important role in the solid state reactions because during heterogeneous reactions interfaces move and mass transport occurs across them. The interfaces can be coherent, semicoherent or incoherent.<sup>28</sup> At the interface, chemical reactions take place between species and defects; they are often associated with structural transformations and volume changes.

The characteristics of thin film solid state reactions running on the nanometer scale are considerably different from solid state reactions proceeding in the bulk. During bulk reactions, the diffusion process is rate limiting and controls the growth. In this case, the thickness of the reaction layer ( $x$ ) usually increases as a function of the square root of time ( $t$ ), which is the well-known parabolic law of reaction kinetics and is characteristic of a diffusion controlled reaction:

$$x \sim \sqrt{t}. \quad (2.1)$$

During thin film solid state reactions, the diffusion paths of the reacting species are short and consequently the kinetics are determined by interfacial reactions. In this case, the thickness of the reaction layer typically increases linearly with time, which is known as linear reaction kinetics and is characteristic of an interface controlled reaction:

$$x \sim t. \quad (2.2)$$

Moreover, in thin film diffusion couples compared to bulk diffusion couples not all of the compound phases predicted by the equilibrium phase diagram have been observed to be present.<sup>29</sup> For example, nickel films deposited on silicon form an intermediate  $\text{Ni}_2\text{Si}$  compound at temperatures between 200 °C and 350 °C with no indication of the presence of other equilibrium phases as long as both unreacted nickel and silicon are still available.<sup>23</sup> Various reasons have been given in the lit-

erature as to why not all of the equilibrium phases may be observed in thin film diffusion couples. The selective formation of phases has been attributed to thermodynamic factors,<sup>21,22</sup> nucleation barriers<sup>23</sup> and kinetic factors.<sup>24-27</sup> The main ideas of the major models presented in the literature are given below.

### 2.1.1 Thermodynamic model

In several silicide systems it was well established that a layer of the most thermodynamically stable compound is the first phase to nucleate and grow. Pretorius *et al.*<sup>21,22</sup> have proposed the so-called effective heat of formation (EHF) model and have shown that thermodynamic data could be directly used to predict first phase formation and phase formation sequence in thin film reaction couples. According to this model an effective heat of formation  $\Delta H'$  is proposed, which is dependent on the concentrations of the reacting elements and is given by:

$$\Delta H' = \Delta H^\circ \times \frac{\text{effective concentration limiting element}}{\text{compound concentration limiting element}} = \Delta H^\circ \times \frac{ec'}{ec}, \quad (2.3)$$

where  $\Delta H^\circ$  is the standard heat of formation expressed in kJ/mole of atoms. If a compound  $A_{1-ec}B_{ec}$  is to be formed for an effective concentration  $ec'$  of element B, then element B will be the limiting element if  $ec' < ec$ , the effective heat of formation being linearly dependent on the effective concentration of the limiting element  $ec'$ . By choosing the effective concentration of the interacting species at the growth interface during the solid phase reaction to be that of the liquidus minimum, the model correctly predicts first phase formation during formation of silicides, germanides, aluminides, and other metal-metal binary systems. The EHF model has also been used to describe amorphous and metastable phase formation as well as the effect of impurities and diffusion barriers on phase formation.

### 2.1.2 Nucleation-controlled model

The basic statements of a nucleation-controlled model for silicide formation have been given by d'Heurle *et al.*<sup>23</sup> Although in most cases there is a lack of knowledge of the material parameters which does not allow a quantitative description, it was shown that the classical theory of nucleation allows for a good qualitative description of the processes involved. In this theory, a phase AB that is formed at the interface between two phases A and B is considered. The driving force for the reaction between A and B is the difference in free energy  $\Delta G_r$  between A+B and AB. However, because of the formation of AB, the system evolves from a situation with one interface A/B into a system with two interfaces A/AB and AB/B. This will usually result in an increase of the interfacial energy  $\Delta\sigma$ . For such a system, there is a competition between two mechanisms: on the one hand, the transformation of a volume of A+B into a nucleus AB with radius  $r$  results in an energy gain  $\Delta G_v \sim r^3 \Delta G_r$ . On the other hand the additional interfaces result in a surface energy

cost  $\Delta\sigma \sim r^2\sigma$ . The free energy change of the nucleus is thus given by:

$$\Delta G_N(r) = a_1 r^2 \sigma - a_2 r^3 \Delta G_r, \quad (2.4)$$

where  $a_1$  and  $a_2$  are geometrical terms that take into account the fact that if the nucleus is a crystal, it will generally not be spherical because of its anisotropic character;  $a_1$  will then represent some averaged coefficient for different values of the surface and interface energies.

The scheme of the relation between the free energy change of a nucleus and its radius  $r$  is shown in Fig. 2.1. As can be seen from this figure,  $\Delta G_N(r)$  passes through a maximum that corresponds

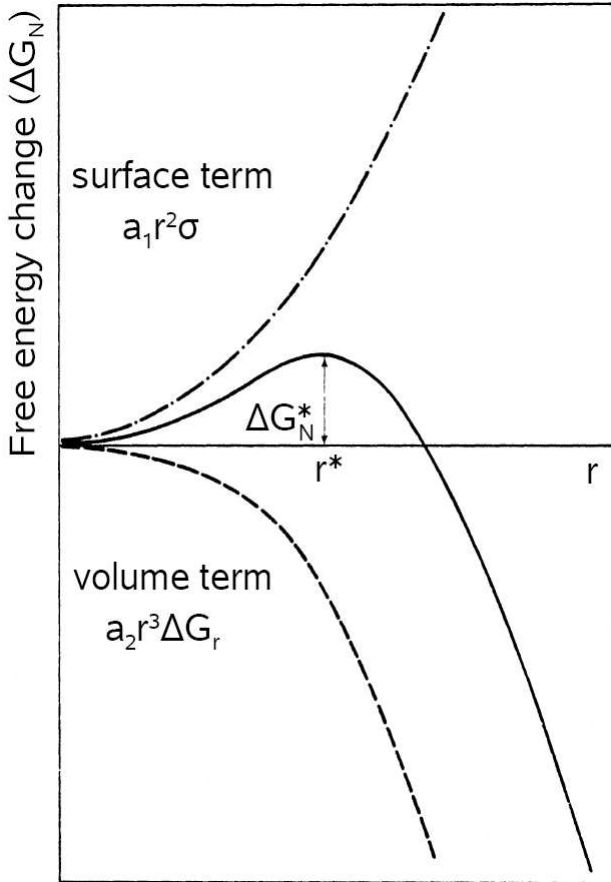


**Fig. 2.1.** The free energy change of a nucleus as a function of its radius ( $r$ ), showing the surface and the volume contributions, and their sum.<sup>23</sup>

to the critical size  $r^*$  of the nucleus. Only the population of nuclei bigger than  $r^*$  will tend to grow. Thus,  $\Delta G_N(r)$  has a maximum value  $\Delta G_N^*$  for a critical radius  $r^*$ :

$$r^* = \frac{2a_1\sigma}{3a_2\Delta G_r}, \quad (2.5)$$

$$\Delta G_N^* = \frac{4a_1^3\sigma^3}{27a_2^2\Delta G_r^2}. \quad (2.6)$$

$\Delta G_N^*$  can be regarded as the activation energy necessary for the nucleation of AB. From the formula, it is clear that nucleation phenomena will only be important if  $\Delta G_r$ , the free energy of formation of AB, is small.

The rate of nucleation  $\rho^*$  is given by the product of the concentration of nuclei with a critical

size and some kinetic term  $Q$ , taking into account the local atomic rearrangement needed to form the nucleus:

$$\rho^* \sim e^{\frac{-\Delta G_N^*}{kT}} e^{\frac{-Q}{kT}}, \quad (2.7)$$

where  $k$  is the Boltzmann constant and  $T$  is the temperature. One should retain the great significance of the relative magnitudes of either the surface energy or the Gibbs energy change, since  $\Delta G_N^* \sim \sigma^3 / \Delta G_r^2$ . Because the surface energy term is usually small, the activation energy for nucleation becomes significant only when the free energy change is also small.

### 2.1.3 Kinetic model

The concept based on a kinetic model is particularly attractive because it allows to discuss the general nature of thin film solid state reactions, viz. kinetics and phase formation sequence. The mostly adopted kinetic model was proposed by Gösele and Tu.<sup>27</sup> In this model, reaction barriers are generally introduced as purely phenomenological quantities, which limit the flux of atomic species through the interface or which otherwise restrict the rate of the interfacial reaction. The influence of such interfacial reaction barriers on the growth kinetics of single compound layers is shown in Fig. 2.2. A compound layer  $A_\beta B$  of thickness  $x_\beta$  grows between two saturated phases

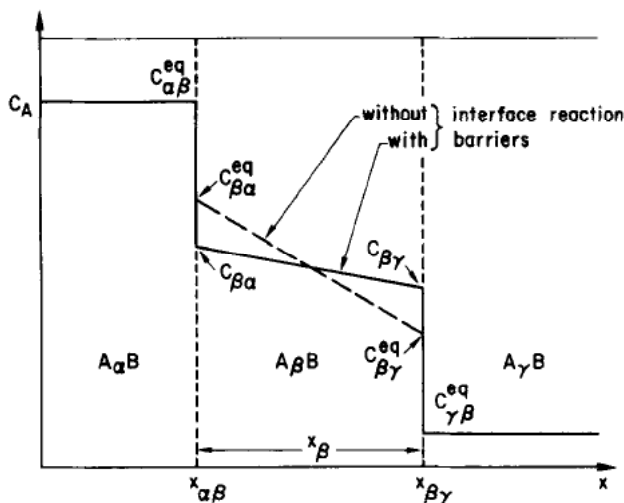


**Fig. 2.2.** Schematic of concentration profile of atoms A across an  $A_\alpha B/A_\beta B/A_\gamma B$  diffusion couple with and without interface reaction barriers.<sup>27</sup>

$A_\alpha B$  and  $A_\gamma B$  where the subscripts  $\alpha > \beta > \gamma$  characterise the composition of the compounds. The diffusion flux  $j_\beta^A$  of A atoms in the  $A_\beta B$  phase is given by:

$$j_\beta^A = \Delta C_\beta^{eq} k_\beta^{eff} / (1 + x_\beta k_\beta^{eff} / \tilde{D}_\beta), \quad (2.8)$$

where  $\Delta C_\beta^{eq}$  is the concentration difference of component A between the left and right sides of the reaction front of phase  $A_\beta B$  in equilibrium state,  $\tilde{D}_\beta$  is the chemical interdiffusion coefficient for the  $A_\beta B$  layer and  $k_\beta^{eff}$  is an effective interfacial reaction barrier for the  $A_\beta B$  layer composed of the two interfacial reaction barriers  $k_{\beta\alpha}$  and  $k_{\beta\gamma}$  according to:

$$1/k_\beta^{eff} = 1/k_{\beta\alpha} + 1/k_{\beta\gamma}. \quad (2.9)$$

The change of the layer thickness  $x_\beta$  is given by:

$$dx_\beta/dt = [1/(C_{\alpha\beta}^{\text{eq}} - C_{\beta\alpha}) + 1/(C_{\beta\gamma} - C_{\gamma\beta}^{\text{eq}})]j_\beta^A. \quad (2.10)$$

By combining Eq. (2.9) with Eq. (2.10), the following equation can be written:

$$dx_\beta/dt = G_\beta \Delta C_\beta^{\text{eq}} k_\beta^{\text{eff}} / (1 + x_\beta k_\beta^{\text{eff}} / \tilde{D}_\beta), \quad (2.11)$$

where  $G_\beta$  is a constant determined by the composition of the three phases  $\text{A}\alpha\text{B}$ ,  $\text{A}_\beta\text{B}$  and  $\text{A}\gamma\text{B}$ . The growth kinetics described by the last equation are different below and above a change-over thickness  $x_\beta^*$ , defined by:

$$x_\beta^* = \tilde{D}_\beta / k_\beta^{\text{eff}}. \quad (2.12)$$

From Eq. (2.12) it follows that

$$x_\beta \sim \sqrt{t} \quad \text{for } x_\beta \gg x_\beta^*, \quad (2.13)$$

and

$$x_\beta \sim t \quad \text{for } x_\beta \ll x_\beta^*. \quad (2.14)$$

Eqs. (2.13) and (2.14) are identical to Eqs. (2.1) and (2.2) and show again the well-known result that interface controlled growth kinetics will change over to diffusion controlled growth kinetics if the layer has grown to a sufficiently thick thickness  $x_\beta \gg x_\beta^*$ .

If  $\text{A}_\beta\text{B}$  grows in competition to other phases, certain of these phases will formally have negative growth rates, so that they are kinetically not stable.

## 2.2 Synthesis of $\text{BaTiO}_3$ ceramics

### 2.2.1 Crystal structure and some properties of $\text{TiO}_2$

There are at least five  $\text{TiO}_2$  structures.<sup>30</sup> The naturally occurring  $\text{TiO}_2$  polymorphs are rutile (tetragonal), anatase (tetragonal), brookite (orthorhombic) and  $\text{TiO}_2$  (B) (monoclinic). Among these structural modifications, rutile and anatase are the most often encountered and technically utilised forms. Anatase  $\text{TiO}_2$  has the same stoichiometry as rutile  $\text{TiO}_2$  but a different crystal structure (see Figs. 2.3-2.4). The relevant crystallographic parameters of rutile and anatase are listed in Table 2.1.

In the rutile and anatase structures, the titanium cation is surrounded by six oxygen anions in more or less distorted octahedral configuration (Figs. 2.3(b)-2.4(b)). These octahedra are the basic building blocks of the various polymorphic structures of  $\text{TiO}_2$  (rutile, anatase, brookite,  $\text{TiO}_2$  (B)) that differ from each other by the distortion within the octahedra and by their coordination as well as by their linkage. The bond lengths for rutile and anatase are similar, but the anatase octahedra exhibit a greater distortion in bond angles (see Table 2.1). Consequently, the anatase structure has a somehow more open structure (higher molar volume, lower density). There are open channels in the two lattices. The channels in the rutile lie parallel to the c axis (perpendicular to the (001) plane) as shown in Fig. 2.3(b). In contrast, the channels in the anatase run perpendicular

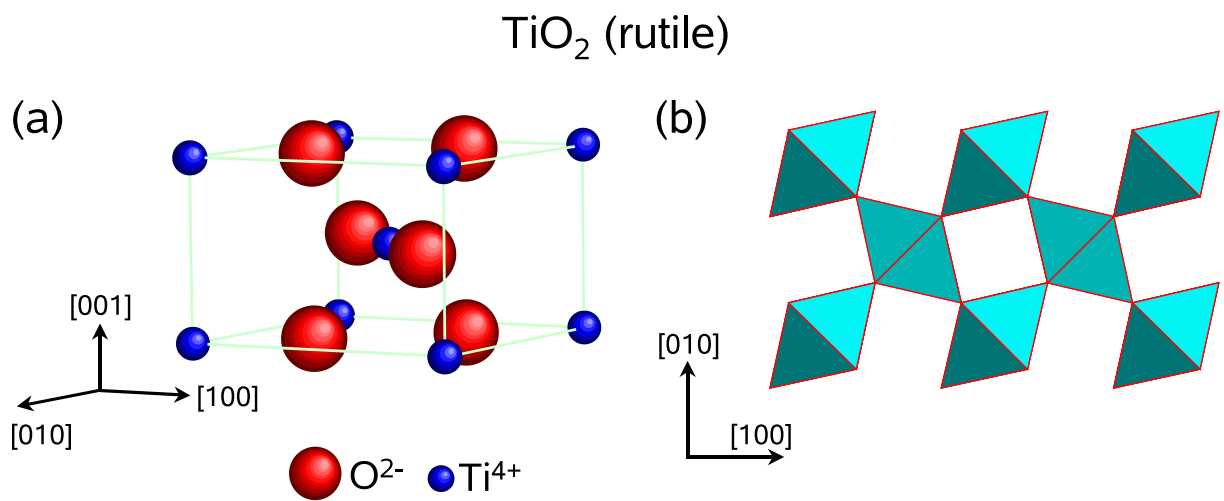


**Fig. 2.3.** (a) Unit cell of rutile  $\text{TiO}_2$  ( $a=b= 0.459$  nm,  $c= 0.295$  nm; space group  $\text{P}4_2/\text{mnm}$ ). (b) Representation of  $\text{TiO}_6$  octahedra of rutile.

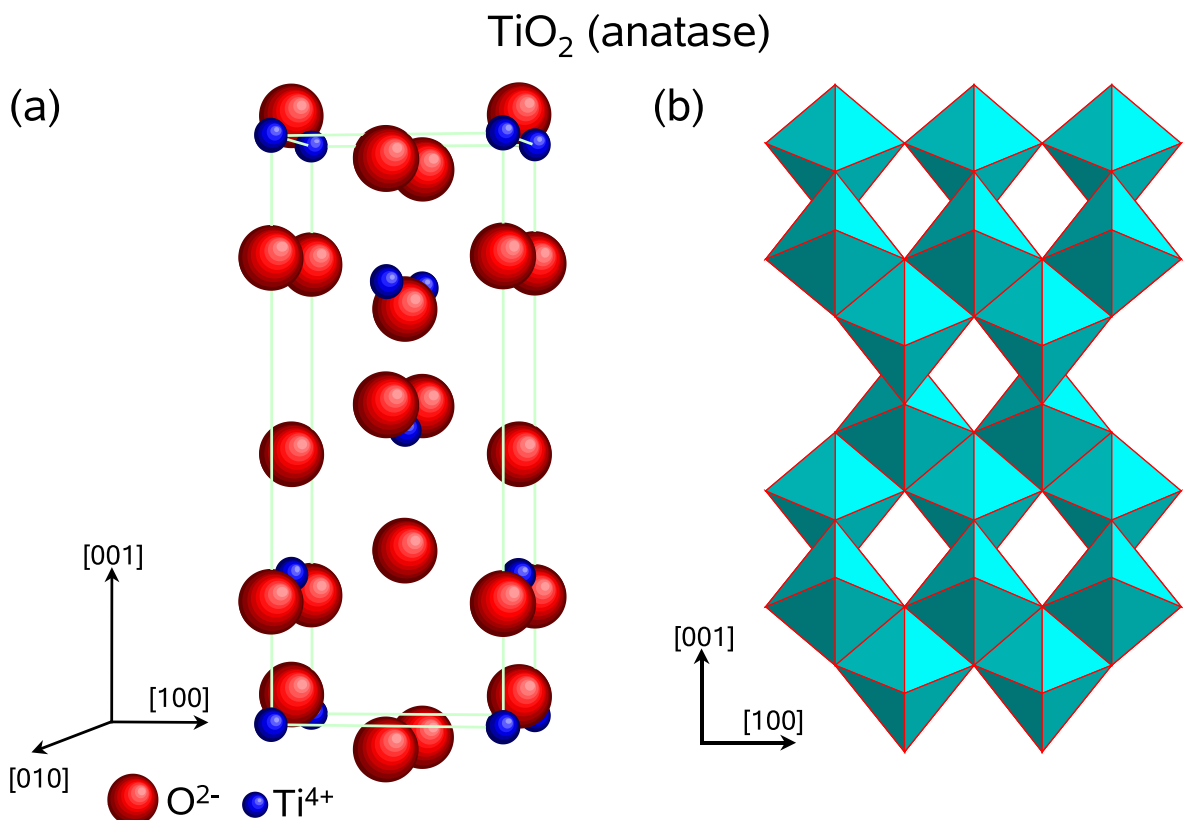


**Fig. 2.4.** a) Unit cell of anatase  $\text{TiO}_2$  ( $a=b= 0.378$  nm,  $c= 0.951$  nm; space group  $\text{I}4_1/\text{amd}$ ). b) Representation of  $\text{TiO}_6$  octahedra of anatase.

**Table 2.1.** Crystallographic parameters for rutile and anatase.<sup>31</sup>

Rutile	Unique Ti coordinates (0,0,0) and (1/2,1/2,1/2) Unique O coordinates ( $\pm u, \pm u, 0$ ) and ( $\pm(1/2+u), \pm(1/2-u), 1/2c$ ) where $u=0.3048$ Ti-O bond lengths: 0.195 nm (4 per octahedra) and 0.198 nm (2 per octahedra) O-Ti-O bond angles: 90°, 81.21° and 98.79° Molar volume: 18.80 cm <sup>3</sup> Density: 4.25 g/cm <sup>3</sup> a=b= 0.459 nm, c= 0.295 nm
Anatase	Unique Ti coordinates (0,0,0), (1/2,1/2,1/2), (1/2,0,1/4) and (0,1/2,3/4) Unique O coordinates (0,0, $\pm u$ ), (1/2,1/2,(1/2 $\pm u$ )), (1/2,0,(1/4 $\pm u$ )) and (0,1/2,(3/4 $\pm u$ ) where $u=0.2081$ Ti-O bond lengths: 0.1934 nm (4 per octahedra) and 0.198 nm (2 per octahedra) O-Ti-O bond angles: 90°, 78.1° and 101.9° Molar volume: 20.52 cm <sup>3</sup> Density: 3.894 g/cm <sup>3</sup> a=b= 0.378 nm, c= 0.951 nm

to the c axis (Fig. 2.4(b)).

Rutile is the most stable form of  $\text{TiO}_2$  whereas anatase and brookite are metastable and transform to the rutile phase on heating. There is no well-defined temperature for these transformations. However, the anatase-rutile transition was observed at temperatures between 400 °C and 1000 °C, depending on many factors such as presence of dopants and size of corresponding precipitates, deviations from stoichiometry, surface area, particle size and surrounding atmosphere.<sup>32-38</sup>

The two polymorphs rutile and anatase have also quite distinct crystal morphologies. Whereas rutile forms slender prismatic crystals,<sup>39</sup> anatase usually occurs in a bipyramidal shape.<sup>39,40</sup> The surface energy of periodic  $\text{TiO}_2$  rutile slabs was calculated by Ramamoorthy *et al.*<sup>41</sup> using a self-consistent ab-initio method. The (110) surface has the lowest surface energy while the (001) surface has the highest. The thermodynamic stability of the (100) surface was also considered, and it was found to be stable with respect to forming (110) facets. The surface energies of  $\text{TiO}_2$  anatase were estimated by Lazzeri *et al.*<sup>42</sup> using an ab-initio density functional method. The (001) and (101) faces of anatase were found as the most stable faces. The calculations indicated that the average surface energy of an anatase crystal is lower than that of a crystal in the rutile phase.

## 2.2.2 Crystal structure of $\text{BaCO}_3$ , $\text{BaTiO}_3$ and $\text{Ba}_2\text{TiO}_4$

### A. $\text{BaCO}_3$

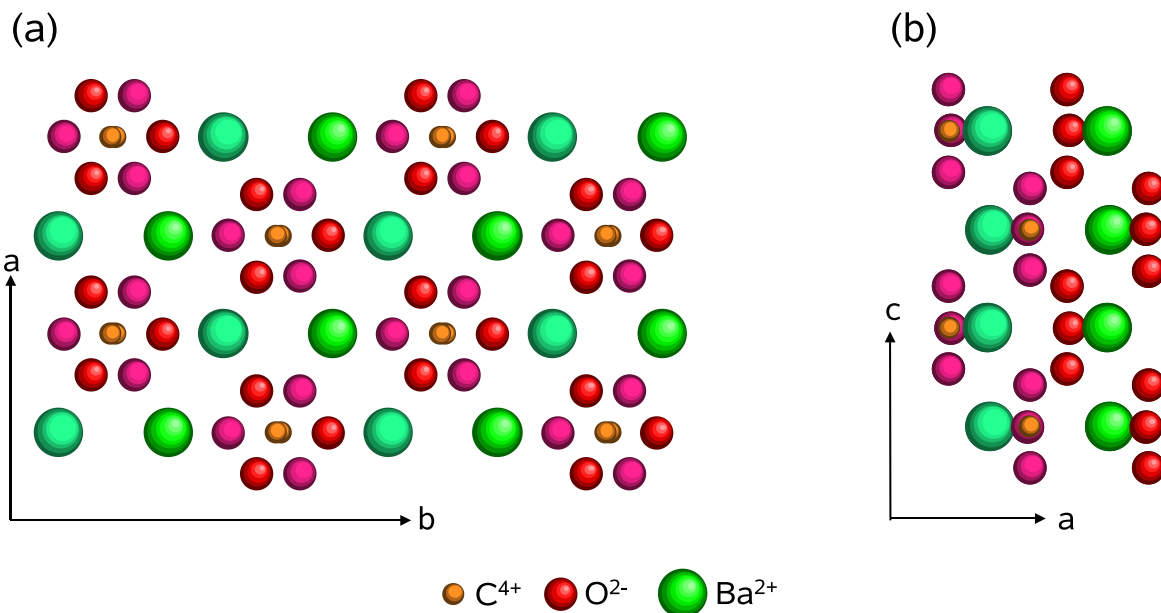
There are three modifications of  $\text{BaCO}_3$ . Crystallographic data for the room and high temperature forms of barium carbonate are listed in Table 2.2.

The aragonite-type modification is the only stable form under normal conditions at room temperature. Two other modifications of  $\text{BaCO}_3$ , of the calcite-type and of the NaCl-type, are reversibly formed above 830 °C and 960 °C, respectively.

The structure of aragonite-type  $\text{BaCO}_3$  (mineral name is witherite) is illustrated in Fig. 2.5.

**Table 2.2.** Crystallographic data for different modifications of  $\text{BaCO}_3$ .<sup>43</sup>

T, °C	Space group	Symmetry	a, nm	b, nm	c, nm	$\alpha$ , °	$\beta$ , °	$\gamma$ , °	Type
20	Pmcn	orthorhombic	0.53	0.888	0.642	90	90	90	aragonite
830	R3m	rhombohedral	0.52	0.52	1.055	90	90	120	calcite
960	Fm3m	cubic	0.696	0.696	0.696	90	90	90	NaCl

**Fig. 2.5.** Illustration of aragonite-type  $\text{BaCO}_3$ . (a) Top and (b) side view. Different colours for oxygen and barium ions used in (a) and (b) show different height levels of the ions in the projections.

In aragonite, each  $\text{CO}_3^{2-}$  ion is surrounded by six  $\text{Ba}$  ions and each  $\text{Ba}$  ion has nine nearest oxygen neighbours. The  $\text{Ba}$  ions in  $\text{BaCO}_3$  are approximately hexagonally close-packed, alternating with layers of  $\text{CO}_3^{2-}$  ions perpendicular to the  $c$ -axis. The  $\text{CO}_3^{2-}$  ion deviates very slightly from planarity, but the O-Ba-O angles do not differ from 120°.

## B. $\text{BaTiO}_3$

Several ferroelectrics crystallise in a perovskite structure with a general chemical formula  $\text{ABO}_3$ , where A and B are cations and O is an anion. Perovskite (calcium titanium oxide,  $\text{CaTiO}_3$ ) is a relatively rare mineral occurring in orthorhombic crystals. Perovskite was discovered in the Ural mountains of Russia by Gustav Rose in the year 1839 and named after the Russian mineralogist, L. A. Perovski.<sup>44</sup>

Barium titanate ( $\text{BaTiO}_3$ ) is well-known to have several phase transitions, depending on temperature. Above the Curie temperature ( $\approx 120$  °C), it has the cubic perovskite structure (with  $\text{Ba}^{2+}$  as A and  $\text{Ti}^{4+}$  as B,  $a \approx 0.4$  nm, space group Pm3m). This is a centrosymmetric cubic structure with  $\text{Ba}$  at the corners,  $\text{Ti}$  at the center and the oxygens at the face centers (Fig.2.6). The ions are

in the following positions: Ba at (0,0,0), Ti at (1/2,1/2,1/2) and three oxygen ions at (1/2,1/2,0), (1/2,0,1/2), (0,1/2,1/2). The titanium ion is surrounded by six oxygen ions in octahedral configuration (Fig. 2.6) and lies in octahedral holes of the Ba-O packing. Each barium ion has twelve oxygen neighbours.

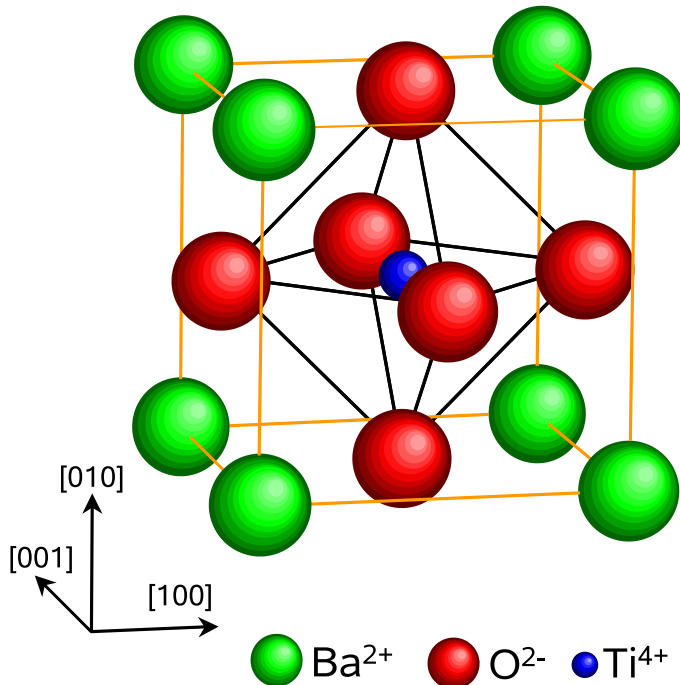


**Fig. 2.6.** Cubic unit cell of  $\text{BaTiO}_3$ .

However, there are two high temperature forms of  $\text{BaTiO}_3$ : cubic and hexagonal ( $a = 0.57$  nm and  $c = 1.405$  nm, space group C6/mmc). At temperatures above 1432 °C, the cubic form of  $\text{BaTiO}_3$  transforms into the hexagonal form.<sup>45,46</sup> These two modifications are built from close-packed (111) layers of composition  $\text{BaO}_3$ . In cubic  $\text{BaTiO}_3$  there is repetition after every third layer as  $ABC\ldots$ ; in the hexagonal form repetition occurs along the c axis after every sixth layer as  $ABCACB\ldots$ .<sup>47</sup>

As the temperature is lowered, cubic  $\text{BaTiO}_3$  goes through phase transitions to three different ferroelectric phases: cubic to tetragonal at 393 K, tetragonal to orthorhombic at 278 K, and orthorhombic to rhombohedral at 183 K. These three phases involve small distortions from the cubic symmetry.<sup>48</sup> At room temperature,  $\text{BaTiO}_3$  is usually considered as tetragonal with  $a = 0.3994$  nm and  $c = 0.4038$  nm (space group P4mm). It should be noted that this Ph.D. thesis is mainly focused on phase formation sequences during  $\text{BaTiO}_3$  synthesis. As shown below, the reaction experiments were performed at temperatures between 575 °C and 1000 °C, where  $\text{BaTiO}_3$  is cubic and the question of phase transitions of  $\text{BaTiO}_3$  will be not considered in detail. Consequently, the pseudocubic indexing for  $\text{BaTiO}_3$  will be used ( $a = 0.4$  nm).

### C. $\text{Ba}_2\text{TiO}_4$

$\text{Ba}_2\text{TiO}_4$  (barium orthotitanate) is the most Ba-rich compound in the system  $\text{BaO}-\text{TiO}_2$ . It is formed as an intermediate phase during the synthesis of  $\text{BaTiO}_3$  by solid state reaction between  $\text{BaCO}_3$  and  $\text{TiO}_2$ .  $\text{Ba}_2\text{TiO}_4$  exists in monoclinic<sup>49,50</sup> and orthorhombic<sup>51-54</sup> modifications. The orthorhombic form is stable at high temperatures while the monoclinic phase is stable at room

temperature.<sup>53,54</sup> The orthorhombic  $\text{Ba}_2\text{TiO}_4$  was observed to be a chemically unstable compound and it decomposed when exposed to air.<sup>55,56</sup>

Monoclinic  $\text{Ba}_2\text{TiO}_4$  has a  $\beta\text{-Ca}_2\text{SiO}_4$  type structure. Its unit cell has the dimensions:  $a = 0.612$  nm,  $b = 0.77$  nm,  $c = 1.05$  nm and  $\beta = 92.99^\circ$ . The orthorhombic modification of  $\text{Ba}_2\text{TiO}_4$  has a distorted  $\beta\text{-K}_2\text{SO}_4$  structure. Its unit cell has the dimensions:  $a = 0.765$  nm,  $b = 1.055$  nm,  $c = 0.61$  nm (space group Pnam).<sup>52</sup> The orthorhombic structure consists of tetravalent titanium cations in an unusual tetrahedral coordination (Fig. 2.7).

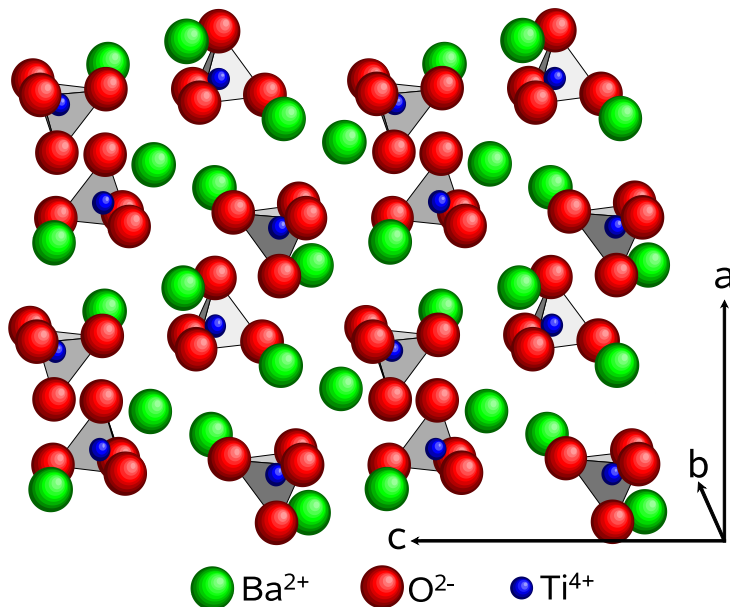


**Fig. 2.7.** Orthorhombic unit cell of  $\text{Ba}_2\text{TiO}_4$ .  $\text{TiO}_4$  tetrahedra are shown with lines.

### 2.2.3 Formation of $\text{BaTiO}_3$ from $\text{BaCO}_3$ and $\text{TiO}_2$ by solid state reactions

During the past decades, compounds in the  $\text{BaO-TiO}_2$  system are of interest because many ternary barium titanates are used as electronic materials for capacitive and microwave devices. One of the most important compounds is  $\text{BaTiO}_3$ . Due to their ferroelectric and dielectric properties, the perovskite-type  $\text{BaTiO}_3$ -based materials have many applications in electronics devices such as high-performance multilayer ceramics capacitors (MLCCs), sensors and thermoresistors. The industrial way to produce  $\text{BaTiO}_3$  is the solid state reaction between  $\text{BaCO}_3$  and  $\text{TiO}_2$  at temperatures as high as  $1200^\circ\text{C}$ . This reaction can be described as follows:



A lot of work has been devoted in order to understand details of reaction (2.15). The above reaction frequently occurs via an intermediate  $\text{Ba}_2\text{TiO}_4$  compound. Even a few percent of this phase unfavourably affect the electrical properties of  $\text{BaTiO}_3$  based ceramics.<sup>57</sup> In recent years a great

deal of attention has been given to the problem how to explain the formation of the two titanates ( $\text{BaTiO}_3$  and  $\text{Ba}_2\text{TiO}_4$ ). The main results and assumptions are summarised below.

In the 1950s, the formation of  $\text{BaTiO}_3$  has been extensively studied by several groups.<sup>57-64</sup> Tzebiatowski *et al.*<sup>58,59</sup> and Kubo *et al.*<sup>60-62</sup> studied the formation of  $\text{BaTiO}_3$  from  $\text{BaCO}_3$  and  $\text{TiO}_2$  (mainly rutile) by heating the raw materials at certain temperatures and analysing the reaction mixtures by using selectively acting acids. They agree that some  $\text{BaTiO}_3$  forms first according to reaction (2.15) and then  $\text{Ba}_2\text{TiO}_4$ , and finally  $\text{Ba}_2\text{TiO}_4$  combines with the remaining  $\text{TiO}_2$  to form  $\text{BaTiO}_3$ ; but they do not agree on the way of  $\text{Ba}_2\text{TiO}_4$  formation. Tzebiatowski *et al.* indicated that  $\text{Ba}_2\text{TiO}_4$  is formed directly from  $\text{BaCO}_3$  and  $\text{TiO}_2$  according to the following reaction:



whereas Kubo *et al.* concluded that  $\text{Ba}_2\text{TiO}_4$  can not be formed according to reaction (2.16) and is produced by reaction between  $\text{BaTiO}_3$  and  $\text{BaCO}_3$  according to the following reaction:



Templeton *et al.*<sup>65</sup> studied the formation of  $\text{BaTiO}_3$  in air and  $\text{CO}_2$  by differential thermal analysis. They found that a small amount of  $\text{BaTiO}_3$  is formed first directly from  $\text{BaCO}_3$  and  $\text{TiO}_2$  (rutile). Then,  $\text{Ba}_2\text{TiO}_4$  forms according to the reaction (2.17) and occurs in largest amounts until all the  $\text{BaCO}_3$  is gone; now experiments confirmed the formation of an intermediate compound according to the reaction proposed by Kubo *et al.*.  $\text{Ba}_2\text{TiO}_4$  was not at any time observed to form directly by the reaction (2.16). The authors found also that in 1 atmosphere (1 bar) of  $\text{CO}_2$  gas, the intermediate  $\text{Ba}_2\text{TiO}_4$  step was suppressed up to a temperature of about 1100 °C. But it was mentioned that  $\text{Ba}_2\text{TiO}_4$  reacts fast within an atmosphere of 1 atmosphere of  $\text{CO}_2$  below 1100 °C to produce  $\text{BaTiO}_3$  and  $\text{BaCO}_3$ . In addition, the authors reported that a high pressure of oxygen (heating was performed in air) is not necessary for  $\text{Ba}_2\text{TiO}_4$  formation. The results of Templeton *et al.*<sup>65</sup> performed with rutile  $\text{TiO}_2$  powder are in agreement with findings of Syama *et al.*<sup>66</sup> who studied the formation of  $\text{BaTiO}_3$  using  $\text{TiO}_2$  anatase powder.

Later, the dependence of the reaction kinetics on  $P_{\text{CO}_2}$ ,  $P_{\text{N}_2}$  and  $P_{\text{O}_2}$  for the reaction (2.15) with rutile  $\text{TiO}_2$  have been investigated by Cournil *et al.*<sup>67,68</sup> It was found that the formation rate of  $\text{BaTiO}_3$  continuously decreases with increasing  $P_{\text{CO}_2}$  or  $P_{\text{N}_2}$  whereas  $P_{\text{O}_2}$  leads to a minimum rate under a certain condition ( $P_{\text{O}_2} = 112.5$  mbar,  $T = 720$  °C for a given partial pressure of carbon dioxide between 75 mbar and 112.5 mbar).

The quantitative aspects of the experiments performed at the beginning of the 1980s by Beauger *et al.*<sup>69</sup> have supplemented the data already obtained on the synthesis of  $\text{BaTiO}_3$  in air and in the presence of  $\text{CO}_2$  (1 bar). In air,  $\text{BaTiO}_3$  is formed first according to reaction (2.15).  $\text{Ba}_2\text{TiO}_4$  then forms at the expense of  $\text{BaTiO}_3$  according to reaction (2.17). When all the  $\text{BaCO}_3$  has been consumed, the reaction (2.17) stops and the final reaction occurs according to the following equation:



The authors described also the sequence of forming phases for the reaction (2.15) that may occur during heating in vacuum of about  $10^{-3}$  mbar. Beauger *et al.* proposed two schemes.

First scheme:

a) Decomposition of  $\text{BaCO}_3$  according to:



b) Formation of  $\text{Ba}_2\text{TiO}_4$  by reaction between the two oxides:



c) Finally, synthesis of  $\text{BaTiO}_3$  according to the reaction (2.18).

Second scheme:

a) Decomposition of  $\text{BaCO}_3$  according to reaction (2.19);

b) Formation of  $\text{BaTiO}_3$  by direct reaction between the oxides:



c) Formation of  $\text{Ba}_2\text{TiO}_4$  at the expense of  $\text{BaTiO}_3$  according to:



d) Finally,  $\text{Ba}_2\text{TiO}_4$  reacts with the  $\text{TiO}_2$  nucleus to form  $\text{BaTiO}_3$  according to the reaction (2.18).

However, the experimental observations of Beauger *et al.*<sup>69</sup> did not allow to make a choice between these two schemes.

Beauger *et al.*<sup>70</sup> have also carried out investigations on planar polycrystalline solid-solid reaction couples in air such as  $\text{BaCO}_3/\text{TiO}_2$ ,  $\text{BaCO}_3/\text{BaTiO}_3/\text{TiO}_2$  and  $\text{Ba}_2\text{TiO}_4/\text{BaTiO}_3/\text{TiO}_2$ . In the first reaction couples, a layer of  $\text{BaTiO}_3$  was found after heat treatment at  $750$  °C for less than one hour inside the  $\text{TiO}_2$  layer. With longer treatment times (24 h) at the same temperature, two layers were observed within  $\text{TiO}_2$ : the inner layer (in contact with  $\text{TiO}_2$ ) consists of  $\text{BaTiO}_3$  and the outer layer consists of  $\text{Ba}_2\text{TiO}_4$ . In the second reaction couples, a layer of  $\text{Ba}_2\text{TiO}_4$  was formed after heat treatment at  $850$  °C for 3 days within the  $\text{BaTiO}_3$  pellet. The formation of  $\text{BaTiO}_3$  as well as  $\text{Ba}_2\text{TiO}_4$  were explained by diffusion of barium through  $\text{TiO}_2$  and  $\text{BaTiO}_3$ , respectively. In the third reaction couples, transformations were observed on both sides of the interface and near it. It was proposed that the conversion of  $\text{Ba}_2\text{TiO}_4$  into  $\text{BaTiO}_3$  occurred through an unidentified species of  $\text{BaO}$  stoichiometry which diffuses towards  $\text{TiO}_2$  through the  $\text{BaTiO}_3$  layer. Based on these experimental results, Mutin *et al.*<sup>71</sup> proposed a model consisting of  $\text{TiO}_2$  grains covered by  $\text{BaCO}_3$ .

At the beginning of the 1990s, Niepce *et al.*<sup>12</sup> summarised the main experimental results and suggested a model based on spherical  $\text{TiO}_2$  particles surrounded by  $\text{BaCO}_3$ . From this arrangement, they deduced that it is possible to prevent the formation of the  $\text{Ba}_2\text{TiO}_4$  phase by controlling

the grain sizes of the initial powders. They discussed also all the interfacial reactions at the various stages. It has been supposed that  $\text{BaTiO}_3$  can be formed according to different processes: directly by barium and oxygen diffusion into  $\text{TiO}_2$  and by degradation of  $\text{Ba}_2\text{TiO}_4$ . Such core-shell structured  $\text{BaCO}_3$ - $\text{TiO}_2$  substances were prepared by Gablenz *et al.*<sup>13</sup> ( $\text{BaCO}_3$  (shell)- $\text{TiO}_2$  (core), with diameters of core-shell grains up to several  $\mu\text{m}$ ) in the year 2001 and by Buscaglia *et al.*<sup>14</sup> ( $\text{BaCO}_3$  (core)- $\text{TiO}_2$  (shell), with sizes of core-shell grains  $\approx 100$  nm-500 nm in length and  $\approx 50$  nm in width) in the year 2007. Heating of the core-shell powders prepared by Gablenz *et al.*<sup>13</sup> showed a modified sequence of phases.<sup>13,15,16</sup> The formation of  $\text{BaTiO}_3$  besides remaining  $\text{BaCO}_3$  and  $\text{TiO}_2$  was observed after reaction at 800 °C (holding time 0 min). Further heating leads to the formation of the  $\text{Ba}_2\text{TiO}_4$  phase (900 °C-1100 °C, holding time 0 min) and different Ti-rich phases with the general formula  $\text{BaTi}_x\text{O}_{1+2x}$  ( $x = 2, 4, 5$ ) (850 °C-1050 °C, holding time 0 min). The formation of a single  $\text{BaTiO}_3$  phase occurred during heating at 1200 °C for 2 h. On the other hand, heating of the core-shell powders prepared by Buscaglia *et al.*<sup>14</sup> showed a complete formation of a single  $\text{BaTiO}_3$  compound after heating at 600 °C for 1 h without formation of any intermediate phases.

The effect of particle size of the initial reactants and pressure on the solid state synthesis of barium titanate was given by Hennings *et al.*<sup>17</sup> and by Buscaglia *et al.*,<sup>18</sup> respectively. Hennings *et al.* found that the formation of the  $\text{Ba}_2\text{TiO}_4$  compound in air can be suppressed in a reaction between submicrometer  $\text{BaCO}_3$  (0.17  $\mu\text{m}$ ) and fine  $\text{TiO}_2$  (0.2  $\mu\text{m}$ ). Thus, the predictions made by Niepce *et al.*<sup>12</sup> were confirmed. Buscaglia *et al.* reported that the calcination of nanocrystalline  $\text{BaCO}_3$  and  $\text{TiO}_2$  powders performed in flowing air at 1 bar (100 kPa) completely suppresses the formation of the  $\text{Ba}_2\text{TiO}_4$  secondary phase. However, the decrease of pressure to 40 mbar induced the formation of  $\text{Ba}_2\text{TiO}_4$  at a reaction temperature of 740 °C.

There was also one attempt to investigate the  $\text{BaTiO}_3$  formation in a thin-film system. Tochitsky *et al.*<sup>72</sup> have investigated solid state reactions in the multicomponent thin film systems  $\text{TiO}_2/\text{BaO}$ ,  $\text{TiO}_2/\text{BaCO}_3$ ,  $\text{TiO}_2/\text{PbO}$ , and  $\text{TiO}_2/\text{Bi}_2\text{O}_3$ . The systems were prepared by a layer-by-layer thermal evaporation of metals onto alkali halide single crystal substrates in a vacuum of about  $10^{-5}$  mbar followed by annealing at constant temperature in a vacuum furnace under a pressure of about  $10^{-4}$  mbar and in air. The authors found that in the  $\text{TiO}_2/\text{BaCO}_3$  system after annealing between 500 °C and 800 °C only the  $\text{BaTiO}_3$  compound formed whereas the synthesis of  $\text{BaTiO}_3$  during annealing of the  $\text{TiO}_2/\text{BaO}$  system occurred through an intermediate  $\text{Ba}_2\text{TiO}_4$  compound.

From the above, it is clearly seen that numerous factors influence the reaction (2.15), i.e. composition and pressure of the reaction atmosphere, and size and geometrical arrangement of the initial reactants. However, the mechanism of  $\text{BaTiO}_3$  formation from  $\text{BaCO}_3$  and  $\text{TiO}_2$  in vacuum is still open. The results performed with rutile powders are consistent with those conducted with anatase powders.

## 2.2.4 Ti-rich barium titanates

### A. Phase diagram

There are many compounds which form by a reaction between  $\text{BaTiO}_3$  and  $\text{TiO}_2$  as well as between  $\text{BaO}$  and  $\text{TiO}_2$ . Some of these compounds are of great interest and technological importance. Statton<sup>73</sup> has tried first to establish phase relations in the  $\text{BaO}-\text{TiO}_2$  system. Later, this phase diagram was restudied and improved by many other works.<sup>74-81</sup>

A high-temperature phase diagram constructed for the system  $\text{BaTiO}_3-\text{TiO}_2$  is shown in Fig. 2.8.<sup>45</sup> The determination of the phase relations was based on X-ray diffraction and micro-

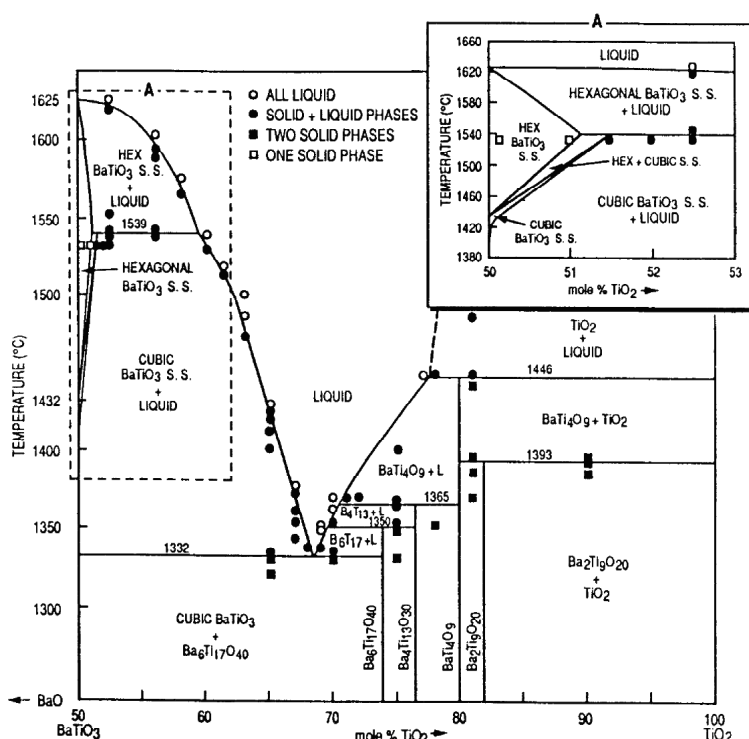


**Fig. 2.8.**  $\text{BaTiO}_3-\text{TiO}_2$  equilibrium phase diagram,<sup>45</sup> see also Fig. A.1 in the appendix (magnified version of the diagram).

scopic visual analyses of the samples quenched from high temperature. In the Ti-rich region, the results of Kirby *et al.*<sup>45</sup> are in general agreement with those of Negas *et al.*<sup>77</sup> and O'Bryan *et al.*<sup>76</sup> As can be seen from the phase diagram, the formation of Ti-rich barium titanates is depending on the ratio of Ba to Ti and temperature.

The stable Ti-rich barium titanates which exist at high temperatures are  $\text{Ba}_6\text{Ti}_{17}\text{O}_{40}$ ,  $\text{Ba}_4\text{Ti}_{13}\text{O}_{30}$ ,  $\text{BaTi}_4\text{O}_9$  and  $\text{Ba}_2\text{Ti}_9\text{O}_{20}$ .<sup>45</sup> The last two Ti-rich phases are used in microwave industry.<sup>81</sup> Other supposedly possible Ti-rich barium titanates such as  $\text{BaTi}_5\text{O}_{11}$  and  $\text{BaTi}_6\text{O}_{13}$ <sup>82</sup> have not been observed in these studies. The compound  $\text{BaTi}_2\text{O}_5$  was found in a sample with 65 mol%  $\text{TiO}_2$  quenched from the liquid state. However, heating of this sample at 1320 °C for 64 h resulted in a mixture of  $\text{BaTiO}_3$  and  $\text{Ba}_6\text{Ti}_{17}\text{O}_{40}$  with no evidence of any remaining  $\text{BaTi}_2\text{O}_5$ . It was noted that these three Ti-rich barium titanates form only through a liquid intermediate.

However, Ritter *et al.*<sup>78</sup> obtained  $\text{BaTi}_2\text{O}_5$  and  $\text{BaTi}_5\text{O}_{11}$  phases using low-temperature alkoxide synthesis techniques. Fig. 2.9 shows their phase diagram constructed from the data obtained by X-ray diffraction analyses. In this diagram, both  $\text{BaTi}_2\text{O}_5$  and  $\text{BaTi}_5\text{O}_{11}$  phases crystallise

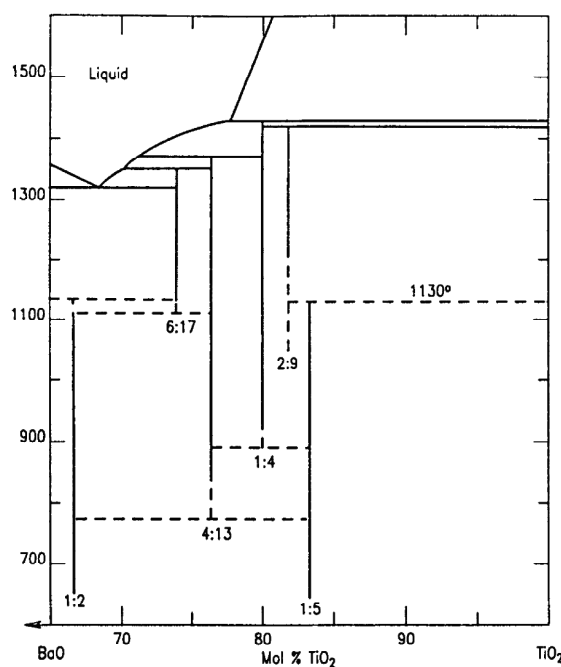


**Fig. 2.9.** Low temperature  $\text{BaTiO}_3$ - $\text{TiO}_2$  phase diagram,<sup>78</sup> see also Fig. A.2 in the appendix (magnified version of the diagram).

at  $\sim 700$  °C.  $\text{BaTi}_2\text{O}_5$  decomposes into  $\text{Ba}_6\text{Ti}_{17}\text{O}_{40}$  and  $\text{BaTiO}_3$  at  $\sim 1150$  °C while  $\text{BaTi}_5\text{O}_{11}$  decomposes to  $\text{TiO}_2$ ,  $\text{Ba}_2\text{Ti}_9\text{O}_{20}$  and/or  $\text{BaTi}_4\text{O}_9$  at  $\sim 1200$  °C. Thus, we can conclude that both these phases ( $\text{BaTi}_2\text{O}_5$  and  $\text{BaTi}_5\text{O}_{11}$ ) are either low-temperature stable phases or metastable phases obtained by crystallisation of an amorphous precursor.

## B. Crystal structure

The crystal structures of Ti-rich barium titanates have been extensively studied.  $\text{BaTi}_4\text{O}_9$  and  $\text{BaTi}_2\text{O}_5$  have structures which can be described as cubic close-packed arrangements of Ba and O atoms. Both these compounds have one short cell constant of about 0.4 nm. These structures have often been referred to as Wadsley-Andersson type phases (also called tunnel structures).<sup>83</sup> The structures of other Ti-rich barium titanates, i.e.  $\text{BaTi}_6\text{O}_{13}$ ,  $\text{BaTi}_5\text{O}_{11}$ ,  $\text{Ba}_4\text{Ti}_{13}\text{O}_{30}$ ,  $\text{Ba}_2\text{Ti}_9\text{O}_{20}$ ,  $\text{Ba}_2\text{Ti}_{13}\text{O}_{22}$  and  $\text{Ba}_6\text{Ti}_{17}\text{O}_{40}$ , are more complex but can be described as close packing of Ba and O atoms in which some of the octahedral O<sub>6</sub> interstices are occupied by Ti atoms.<sup>84,85</sup> These structures can be illustrated as being made up of Ba-O close-packed layers with 4, 6, 8 or 10 layers per unit cell. The unit cell dimensions of Ti-rich barium titanates as well the number of layers per unit cell are given in Table 2.3.

The mean thickness of each close-packed layer of the Ti-rich barium titanates is  $\approx 0.234$  nm which is similar to the (111) interplanar spacing of  $\text{BaTiO}_3$ . The orientation of the close-packed layer is usually derived from the morphology of the crystals or from the diffraction pattern and gives substantial structural information. For example, in the case of  $\text{Ba}_6\text{Ti}_{17}\text{O}_{40}$ , the lattice constant  $c = 1.892$  nm ( $\approx 8 \times 0.234$  nm) leads to the conclusion that the unit cell contains eight close-packed layers perpendicular to the c axis. Despite one unit cell repeating itself after 8 layers, the real crystallographic identity period of the packing of the complete structure is 24 layers.<sup>93</sup> This is because the direction of packing is [103]. The angle between the [103] direction and the (001)

**Table 2.3.** Unit cell parameters of Ti-rich barium titanates.

Phase	Space group	Symmetry	a, nm	b, nm	c, nm	$\alpha, {}^\circ$	$\beta, {}^\circ$	$\gamma, {}^\circ$	Number of layers	Ref.
<i>Wadsley-Andersson type</i>										
$\text{BaTi}_2\text{O}_5$	A2/m	monoclinic	0.9409	0.393	1.69	90	103.5	90		86
$\text{BaTi}_4\text{O}_9$	Pmmn	orthorhombic	1.452	0.379	0.629	90	90	90		87
<i>Close-packed type</i>										
$\text{BaTi}_6\text{O}_{13}$	P $\bar{1}$	triclinic	0.751	0.985	0.746	105.38	118.9	72.58	4	82
$\text{Ba}_2\text{Ti}_9\text{O}_{20}$	P $\bar{1}$	triclinic	0.747	1.408	1.434	89.94	79.43	84.45	6	88,89
$\text{BaTi}_5\text{O}_{11}$	P2 <sub>1</sub> /n	monoclinic	0.767	1.402	0.752	90	98.33	90	6	90
$\text{Ba}_2\text{Ti}_{13}\text{O}_{22}$	Bmab	orthorhombic	1.165	1.410	1.005	90	90	90	6	91
$\text{Ba}_4\text{Ti}_{13}\text{O}_{30}$	Cmca	orthorhombic	1.706	0.986	1.405	90	90	90	6	92
$\text{Ba}_6\text{Ti}_{17}\text{O}_{40}$	C2/c	monoclinic	0.988	1.708	1.892	90	98.42	90	8	93
$\text{Ba}_2\text{Ti}_5\text{O}_{12}$	Ammm	orthorhombic	0.99	1.14	2.35	90	90	90	10	94,95

plane in  $\text{Ba}_6\text{Ti}_{17}\text{O}_{40}$  is  $\approx 1.3^\circ$ . The compositions of other Ti-rich barium titanates can be derived by analogy to the layers in  $\text{Ba}_6\text{Ti}_{17}\text{O}_{40}$  and  $\text{Ba}_4\text{Ti}_{13}\text{O}_{30}$  as was shown by Roth *et al.*<sup>96</sup> for the phases  $\text{Ba}_6\text{Ti}_{14}\text{Nb}_2\text{O}_{39}$ ,  $\text{Ba}_{14}\text{Ti}_{40}\text{Nb}_2\text{O}_{99}$  and  $\text{Ba}_{18}\text{Ti}_{54}\text{Nb}_2\text{O}_{132}$ .

Recently, a topotaxial orientation relationship between  $\text{BaTiO}_3$  and  $\text{Ba}_6\text{Ti}_{17}\text{O}_{40}$ <sup>97–100</sup> as well as between  $\text{BaTiO}_3$  and  $\text{Ba}_4\text{Ti}_{13}\text{O}_{30}$ <sup>6,97</sup> has been established. Despite the different procedure of sample preparation (solid state reaction of  $\text{BaCO}_3$  and  $\text{TiO}_2$  at high temperatures in air<sup>98,100</sup> or chemical reaction of  $\text{SiO}_2$  film with  $\text{BaTiO}_3$  single crystals<sup>6,97,99</sup>), the Ti-rich phases (TRP) grow in all cases according to the following orientation relationship:

$$(001) \text{ TRP} \parallel (111) \text{ BaTiO}_3; [010] \text{ TRP} \parallel [1\bar{1}0] \text{ BaTiO}_3. \quad (2.23)$$

Thus, the close-packed planes of  $\text{Ba}_6\text{Ti}_{17}\text{O}_{40}$  and  $\text{Ba}_4\text{Ti}_{13}\text{O}_{30}$  lie parallel to the close-packed planes of  $\text{BaTiO}_3$ . Crystallographically, Kraševc *et al.*<sup>98</sup> explained the orientation relationship between  $\text{Ba}_6\text{Ti}_{17}\text{O}_{40}$  and  $\text{BaTiO}_3$  phases by the similarity of the stacking sequence of (111) planes of  $\text{BaTiO}_3$  and (001) planes of  $\text{Ba}_6\text{Ti}_{17}\text{O}_{40}$ , if the larger unit cell of the monoclinic  $\text{Ba}_6\text{Ti}_{17}\text{O}_{40}$  phase was appropriately cut.<sup>98</sup> On the base of the above relationship a model of a topotactic boundary between  $\text{Ba}_6\text{Ti}_{17}\text{O}_{40}$  and  $\text{BaTiO}_3$  phases was constructed.

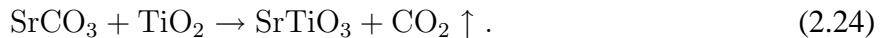
## 2.3 The system $\text{SrO-TiO}_2$

In the bulk phase diagram of the system  $\text{SrO-TiO}_2$  (Fig. 2.10<sup>101</sup>), several compounds are known such as  $\text{Sr}_2\text{TiO}_4$ ,  $\text{Sr}_3\text{Ti}_2\text{O}_7$  and  $\text{SrTiO}_3$ . There is an eutectic at 1440 °C between  $\text{SrTiO}_3$  and  $\text{TiO}_2$ .

$\text{Sr}_2\text{TiO}_4$  has a tetragonal structure with  $a=b= 0.388$  nm and  $c= 1.26$  nm (space group I4/mmm) while  $\text{Sr}_3\text{Ti}_2\text{O}_7$  has also a tetragonal structure with  $a=b= 0.39$  nm and  $c= 2.038$  nm (space group

$14/\text{mmm}$ ).  $\text{SrTiO}_3$  has a cubic perovskite structure with  $a = 0.39$  nm (space group  $\text{Pm}3\text{m}$ ) at room temperature and higher.

Strontium titanate is commonly produced by a solid state reaction of  $\text{SrCO}_3$  with  $\text{TiO}_2$  at high temperatures (above  $1000$  °C):



No intermediate products were observed during  $\text{SrTiO}_3$  synthesis by Tagawa and Igarashi<sup>102</sup> as well as by Chang and Liu.<sup>103</sup> However, recent results suggested that the above reaction occurred via an intermediate  $\text{Sr}_2\text{TiO}_4$  compound.<sup>104</sup>

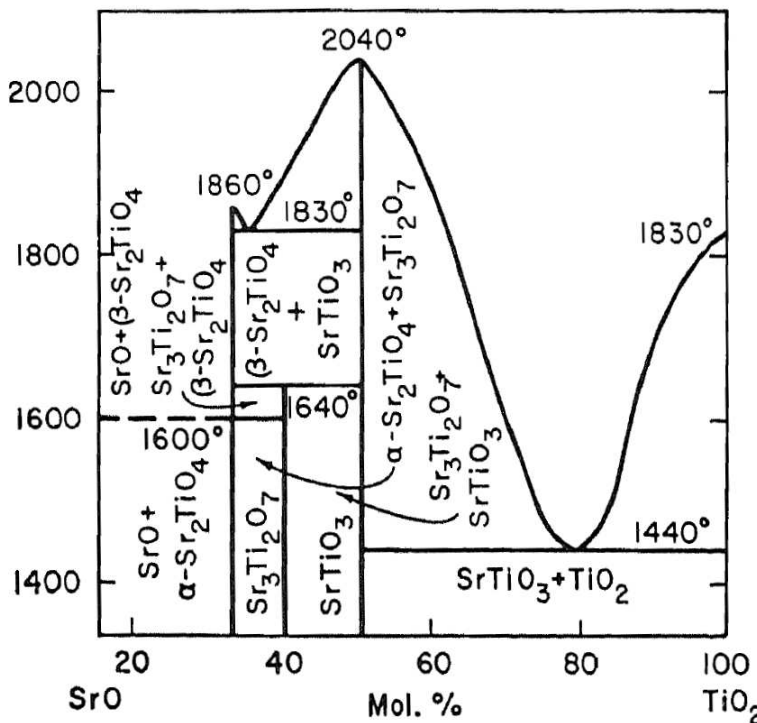


**Fig. 2.10.** Phase diagram of the system  $\text{SrO}-\text{TiO}_2$  (Fig. 297 in Ref.<sup>101</sup>), see also Fig. A.3 in the appendix (magnified version of the diagram).

$\text{SrTiO}_3$  is of technical significance. Owing to its high dielectric constant and large dielectric breakdown field,  $\text{SrTiO}_3$  is a potential candidate for storage capacitor cells in dynamic random access memories.<sup>105</sup>  $\text{SrTiO}_3$  single crystals and thin films are extensively used as substrates for high- $T_c$  superconducting,<sup>106</sup> ferroelectric<sup>107</sup> and multiferroic<sup>108</sup> thin films. Suitably doped  $\text{SrTiO}_3$  single crystals have been considered for non-volatile memories based on resistive switching.<sup>109,110</sup>

## 2.4 The system $\text{CaO}-\text{TiO}_2$

Several investigations of the bulk phase diagram of the system  $\text{CaO}-\text{TiO}_2$  (Fig. 2.11) predict the existence of three stable compounds such as  $\text{Ca}_3\text{Ti}_2\text{O}_7$ ,  $\text{Ca}_4\text{Ti}_3\text{O}_{10}$  and  $\text{CaTiO}_3$ . The first two phases peritectically decompose at  $1750$  °C and  $1840$  °C, respectively, whereas the  $\text{CaTiO}_3$  melts congruently at  $1960$  °C. There is also a eutectic at  $1450$  °C between  $\text{CaTiO}_3$  and  $\text{TiO}_2$ .

$\text{Ca}_3\text{Ti}_2\text{O}_7$  has an orthorhombic structure with  $a = 0.541$  nm,  $b = 1.94$  nm and  $c = 0.542$  nm (space

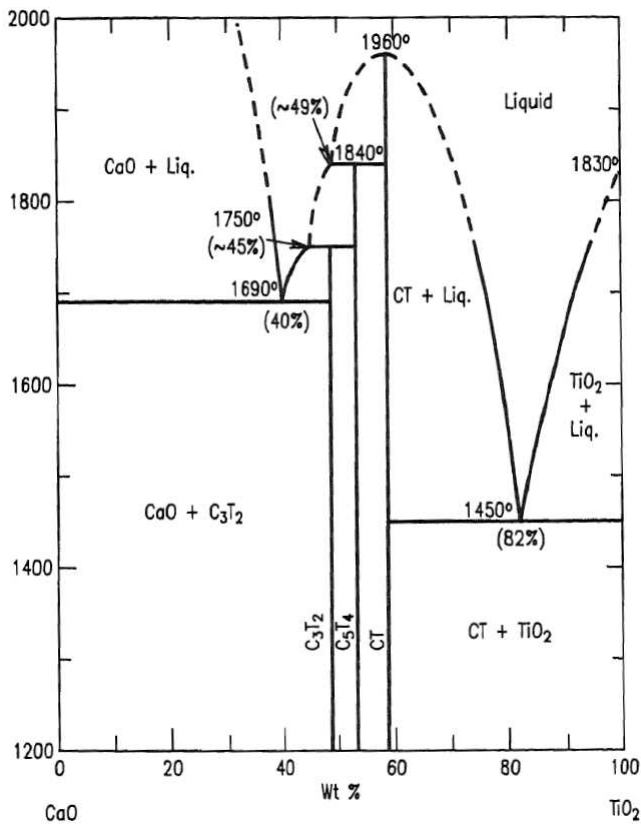


**Fig. 2.11.** Phase diagram of the system  $CaO$ - $TiO_2$  (Fig. 6385 in Ref.<sup>101</sup>), see also Fig. A.4 in the appendix (magnified version of the diagram). C=  $CaO$ , T=  $TiO_2$ .

group Ccm21) while  $Ca_4Ti_3O_{10}$  has also an orthorhombic structure with  $a= 0.54$  nm,  $b= 2.714$  nm and  $c= 0.543$  nm (space group Pcab). The mineral perovskite,  $CaTiO_3$ , has an orthorhombic structure at room temperature with  $a= 0.538$  nm,  $b= 0.544$  nm and  $c= 0.7654$  nm (space group Pbnm). The orthorhombic distortion of  $CaTiO_3$  decreases with increasing temperature. The phase transitions from the room temperature orthorhombic structure to a tetragonal ( $a=b= 0.549$  nm and  $c= 0.778$  nm, space group I4/mcm) polymorph occur at temperatures between 1373 K and 1423 K, followed by transformation to the cubic phase ( $a= 0.38$  nm, space group  $Pm\bar{3}m$ ) at  $1523\pm 10$  K.<sup>111</sup> In this Ph.D. work, the pseudocubic indexing for  $CaTiO_3$  will be used ( $a= 0.38$  nm).

$CaTiO_3$  is mostly prepared by a solid state reaction of  $CaO$  or  $CaCO_3$  with  $TiO_2$  at high temperatures. The undoped  $CaTiO_3$  is an incipient ferroelectric<sup>112</sup> with potential application in microwave-tunable devices,<sup>113</sup> but on doping with Pb it becomes a true ferroelectric.<sup>114</sup> The versatility of calcium titanate extends to its suitability as a material for the immobilization of radioactive waste<sup>115</sup> and a biocompatible coating for medical Ti implants.<sup>116</sup>

## 2.5 The system $MgO$ - $TiO_2$

In the system  $MgO$ - $TiO_2$ , several compounds are known such as  $MgTi_2O_5$ ,  $Mg_2TiO_4$  and  $MgTiO_3$  (Fig. 2.12).  $MgTi_2O_5$  (armalcolite) has a pseudobrookite structure with  $a= 0.97$  nm,  $b= 1$  nm and  $c= 0.37$  nm (space group Bbmm), while  $Mg_2TiO_4$  (quandilite) has either a cubic structure with  $a= 0.84$  nm at 700 °C (space group Fd3m, spinel) or a tetragonal structure with  $a= 0.59$  nm and  $c= 0.84$  nm (space group P4<sub>1</sub>22, spinel) at 500 °C.<sup>117</sup>  $MgTiO_3$  (geikielite) has a rhombohedral

ilmenite structure with  $a = 0.505$  nm and  $c = 1.389$  nm (space group  $R\bar{3}$ ).<sup>117</sup>

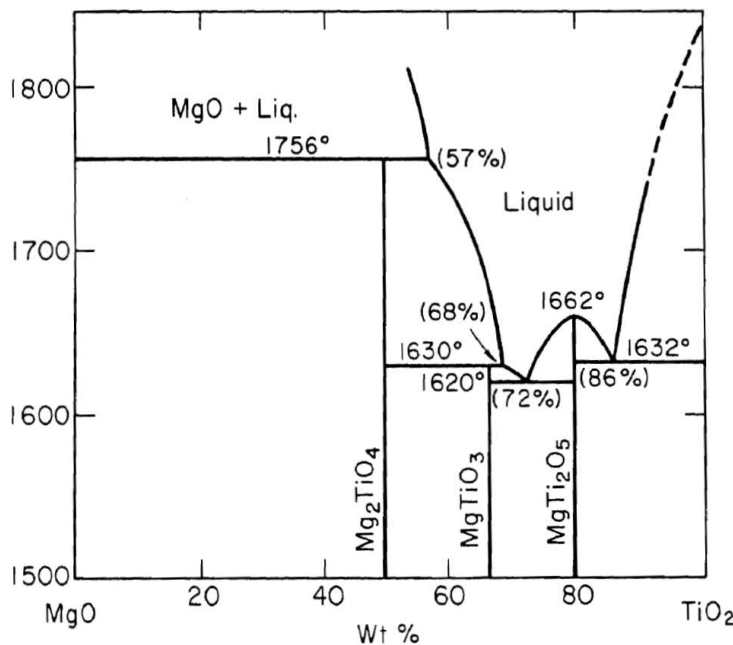
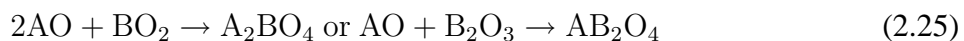


**Fig. 2.12.** Phase diagram of the system  $MgO-TiO_2$  (Fig. 4336 in Ref.<sup>101</sup>), see also Fig. A.5 in the appendix (magnified version of the diagram).

$Mg_2TiO_4$  has attracted attention because of its optical properties to be used in integrated optics and as a dielectric material. Epitaxial layers of  $Mg_2TiO_4$  grown by solid-state reaction between (001)  $MgO$  single crystals and  $TiO_2$  have been used as buffer layers for growing high temperature superconducting thin films.<sup>118–120</sup> On the other hand,  $MgTiO_3$  is known as a dielectric material which has good dielectric properties at high frequencies as well as a high thermal stability. Bulk  $MgTiO_3$  is used for microwave ceramic capacitors and resonators.<sup>121–124</sup>  $MgTiO_3$  has a refractive index of 1.95 which lies between that of  $LiNbO_3$  (2.2) and  $Al_2O_3$  (1.7).<sup>125</sup> Thus,  $MgTiO_3$  thin films can be used as a cladding layer. Mostly,  $MgTiO_3$  has been produced and studied in bulk ceramic form. However, there have been some reports on fabrication and properties of  $MgTiO_3$  thin films.<sup>126,127</sup>

Spinel-forming topotaxial solid state reactions like:



are prototypes of chemical reactions in complex oxides. Previously, a series of topotaxial reactions with (100)  $MgO$  single crystals were studied. Different spinels, such as  $Mg_2TiO_4$ ,  $Mg_2SnO_4$ ,  $MgIn_2O_4$ ,  $MgAl_2O_4$ ,  $MgCr_2O_4$  and  $MgFe_2O_4$ , with different values of spinel/ $MgO$  lattice misfit were considered.<sup>6,11</sup> In such cases of cube-on-cube orientation, the structure of the reaction fronts and the mechanism of the interfacial reaction were determined by the sign and amount of the lattice misfit. At positive misfit, the Burgers vector of the misfit dislocations present at the reaction front points out of the interface, enabling the dislocations to glide, when coping with the movement of the advancing reaction front. At negative misfit, the Burgers vector lies in the interface plane, so that a climb process is required for the movement of the dislocations. At very low misfit ( $< \pm 0.2\%$ ), no misfit (interfacial) dislocations form and the misfit is accommodated by point defects and antiphase boundaries.

## 2.6 Modeling of powder reactions

In order to enhance the speed of reaction, solid state reactions are usually performed by mixing powders of the reactants followed by heating. A reaction between two phases A and B can be regarded as a reaction between two grains A and B.

Fig. 2.13 shows a schematic drawing of two particles which are in contact with each other. The solid state reaction of these two particles occurs by different mass transport mechanisms such as surface diffusion, grain boundary diffusion and volume diffusion. Coupled grain-boundary and surface diffusion is often the dominant mechanism for the reaction of a fine particle compact. The different mass transport mechanisms occurring during the reaction can be studied in model experiments. In this approach, instead of using polycrystalline materials, one reactant is a bulk single crystal. Surface diffusion is a mass flow along the particle surface or along pore walls. Thus, the surface diffusion can be modeled in the reaction between vapour and single crystals as shown in Fig. 2.13. The interface between two (crystalline) particles is a grain boundary. Grain boundary diffusion results in mass flow along the grain boundary while volume diffusion results in mass flow across the newly formed layer. Thus, to model such a situation, the solid-solid reaction between thin films and single crystals can be studied as given in Fig. 2.13. Although solid state reactions involve usually three-dimensional aggregates of particles, the pseudo-two-dimensional problem used in model experiments can give significant insights into the reaction mechanism.

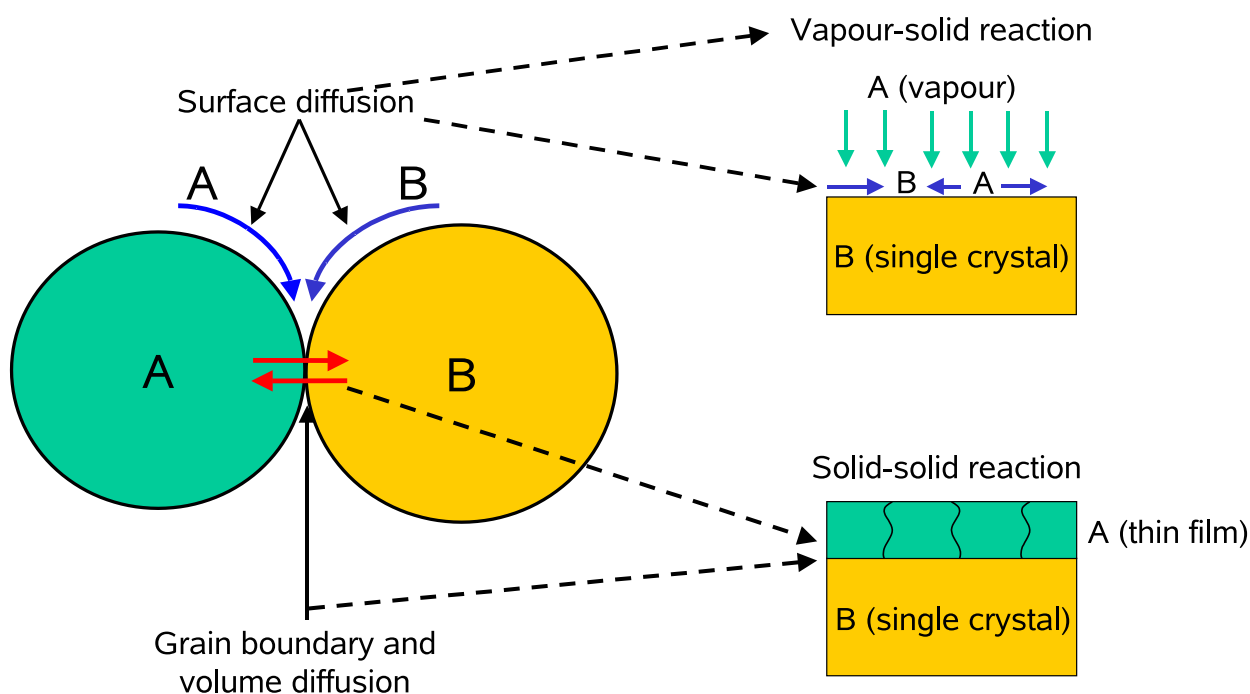


**Fig. 2.13.** Two different solid state reaction geometries which can be used to study the reaction of two particles in a powder.

### 3 Experimental and investigation procedures

#### 3.1 Sample preparations

Titanium dioxide ( $\text{TiO}_2$ ) with rutile and anatase structures was used. To provide a model system, single crystalline materials are usually used as one reactant.  $\text{TiO}_2$  rutile single crystals are commercially available with different surface orientations. But anatase single crystals are more difficult to obtain with appropriate size and purity. This problem has been addressed by growing epitaxial anatase thin films.

Thus in the case of  $\text{TiO}_2$  with rutile structure, polished (110) and (100) surfaces of commercial rutile  $\text{TiO}_2$  single crystals (CrysTec GmbH, Berlin, Germany) were used as substrates. Before the experiments the rutile crystals were annealed in air at 1100 °C for 1 h. After this heat treatment the (110) rutile surfaces involved terraces of about 450 nm in width with ordered steps of about 0.26 nm in height as shown by AFM in Fig. 3.1(a). An annealing at 1100 °C for 1 h was found to be optimal for the (110) rutile substrates. The surface morphology of thermally treated (100) rutile surfaces was significantly different from (110) ones. The surface of (100) rutile substrates consisted of terraces of 450 nm to 800 nm in width. The height of the steps ranged from 0.6 nm to 0.96 nm (Fig. 3.1(b)). Extensive step bunching was also observed on (100) surfaces.

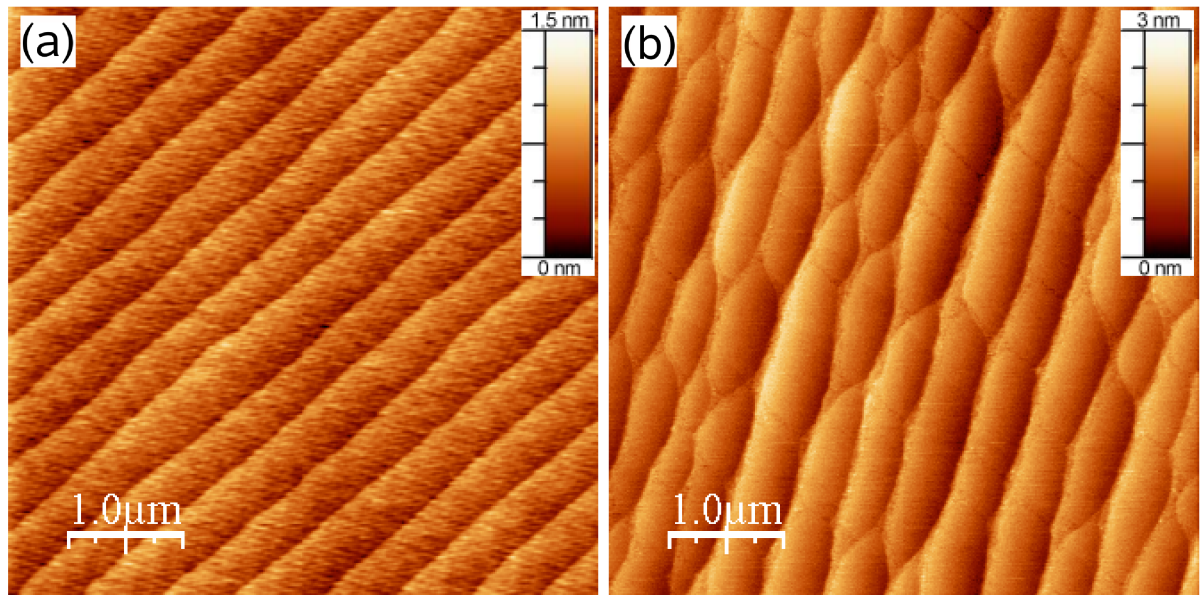


**Fig. 3.1.** AFM topography images after thermal treatment in air at 1100 °C for 1 h: (a) (110) rutile surface (root-mean-square roughness is 0.15 nm) and (b) (100) rutile surface (root-mean-square roughness is 0.25 nm).

In the case of  $\text{TiO}_2$  with anatase structure, (001) and (012) surfaces of epitaxial  $\text{TiO}_2$  anatase thin films were used for the reaction experiments. Epitaxial  $\text{TiO}_2$  thin films with a good crystalline quality and microstructure were prepared on (100)-oriented  $\text{SrTiO}_3$  and  $\text{LaAlO}_3$  substrates as well

as on (110)-oriented  $\text{SrTiO}_3$  and  $\text{LaAlO}_3$  substrates. Details on epitaxial thin film growth are given in **Chapter 4 (Section 4.2)**.

Two reaction geometries were used to study the solid state reactions (Fig. 3.2). Fig. 3.2(a) shows the so-called solid-solid regime of the solid state reactions. The solid-solid reaction between  $\text{BaCO}_3$  and  $\text{TiO}_2$  was initiated by heating in a high-vacuum environment and in air. The second regime of the solid state reactions, the so-called vapour-solid reaction, was performed between  $\text{TiO}_2$  and  $\text{BaO}$  vapour in a high-vacuum environment (Fig. 3.2(b)). For experiments with other vapours  $\text{BaO}$  was replaced by  $\text{SrO}$ ,  $\text{CaO}$  and  $\text{MgO}$ .

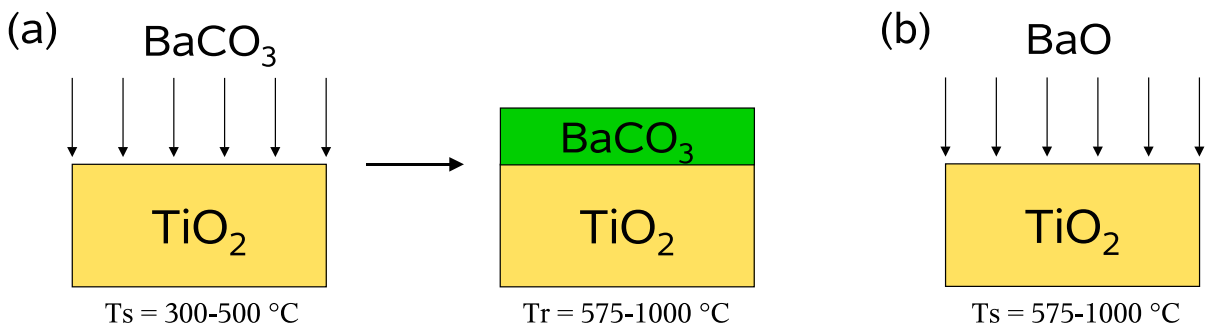


**Fig. 3.2.** Two solid state reaction geometries: (a) solid-solid reaction and (b) vapour-solid reaction.  $T_s$  is the substrate temperature during deposition while  $T_r$  is the annealing temperature.

A  $\text{BaCO}_3$  thin film or  $\text{BaO}$  vapour was obtained in a high-vacuum chamber by evaporating a  $\text{BaCO}_3$  powder target while  $\text{SrO}$ ,  $\text{CaO}$  or  $\text{MgO}$  vapour was produced by electron-beam evaporation of either a  $\text{SrCO}_3$ , a  $\text{CaCO}_3$  or a  $\text{MgO}$  powder target. Fig. 3.3 gives a schematic drawing of the evaporation system used in this study. The distance between evaporator and the sample is approximately 20 cm, which is quite large. This minimises the heat load on the sample and thus prevents a rise in sample temperature during deposition. The base pressure of the vacuum system was less than  $2 \times 10^{-5}$  mbar. During deposition pure oxygen was introduced to establish a pressure of  $1 \times 10^{-4}$  mbar. The deposition rate and film thickness were in-situ monitored during deposition by a quartz crystal microbalance (INFICON, gold coated crystals, 6 MHz), positioned just a few centimeters away from the sample. The thickness of the  $\text{BaCO}_3$  thin film was determined by cross-sectional transmission electron microscopy and it was found to be  $\approx 50$  nm thick. The substrates were heated in a tube furnace directly by thermal irradiation during deposition. They were put into a holder placed in the middle of the furnace and were hanging down with the polished surface pointing towards the electron-beam evaporator. The temperatures were measured by a Pt/PtRh10 thermocouple installed behind the substrate. After the solid state reactions the samples were kept in the vacuum chamber or in a laboratory furnace and allowed to cool to room temperature.

For the growth of  $\text{BaCO}_3$  thin films, the substrate temperature was kept at 300 °C, 400 °C or 500 °C. The solid-solid reactions in vacuum were performed directly after deposition (without cooling down to room temperature) by heating up to temperatures between 575 °C and 1000 °C for different length of time (0 min to 180 min holding time). For the solid-solid reaction experiments

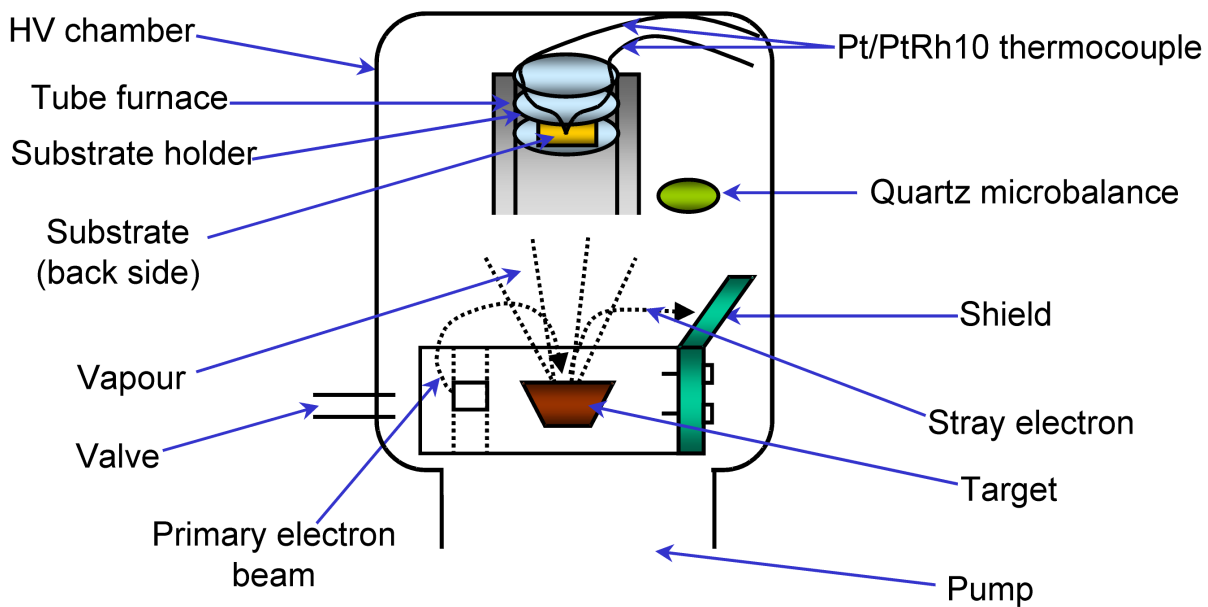


**Fig. 3.3.** Scheme of the electron beam evaporation system.

in air, the substrate with deposited  $\text{BaCO}_3$  thin film was taken out from the vacuum chamber and annealed in a laboratory furnace at temperatures ranging from 575 °C to 1000 °C for different length of time (0 min to 30 min holding time).

For the vapour-solid reaction of  $\text{BaO}$  with  $\text{TiO}_2$ , the substrate was heated to the reaction temperature (575 °C-1000 °C) and kept constant at a desired temperature during the reaction. A complete deposition/reaction experiment required about 35 min. It should be noted that  $\text{BaCO}_3$  evaporates by decomposition, the vapour consists of  $\text{BaO}$  and  $\text{CO}_2$ . In view of the high volatility (low sticking coefficient) of  $\text{CO}_2$  at such high temperatures, the material reacting with the rutile substrate consists of  $\text{BaO}$  species. This is in agreement with thermodynamical calculations where the formation of  $\text{BaCO}_3$  by a reaction between  $\text{BaO}$  and  $\text{CO}_2$  at temperatures higher than 575 °C is suppressed by a positive value of Gibbs energy (Fig. 3.4).<sup>128</sup> The same conclusion is valid for the formation

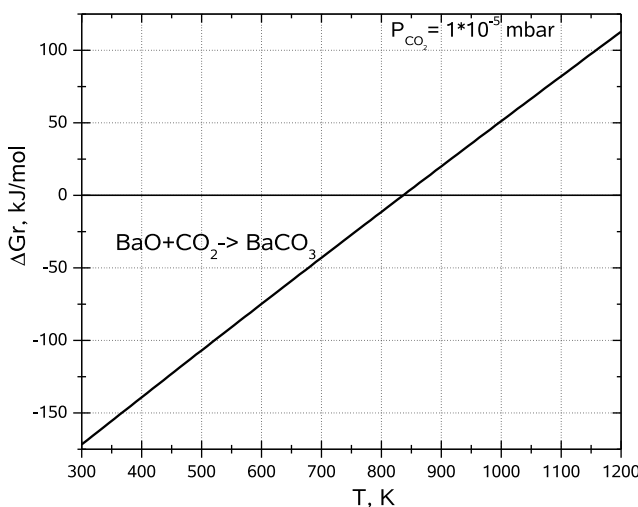


**Fig. 3.4.** The change in Gibbs free energy ( $\Delta G_r$ ) vs  $T$  for the formation of  $\text{BaCO}_3$  in vacuum of  $1 \times 10^{-5}$  mbar. Calculated using data from I. Barin.<sup>128</sup>

of  $\text{SrCO}_3$  or  $\text{CaCO}_3$  on hot  $\text{TiO}_2$  substrates by a reaction between  $\text{SrO}$  or  $\text{CaO}$  and  $\text{CO}_2$  since the thermodynamic estimations for the reactions  $\text{SrO} + \text{CO}_2 \rightarrow \text{SrCO}_3$  and  $\text{CaO} + \text{CO}_2 \rightarrow \text{CaCO}_3$  are close to the reaction  $\text{BaO} + \text{CO}_2 \rightarrow \text{BaCO}_3$ .

Several methods have been used to analyse the samples after solid state reactions. These methods are described in the next two chapters.

## 3.2 X-ray diffraction

Techniques based on X-ray probes dominate in the field of materials science mainly because of their simplicity, reliability, quantitative and nondestructive nature. Of these techniques, XRD plays a leading role, as a fundamental tool for material characterization.<sup>129</sup>

### 3.2.1 Basic principles

X-rays are electromagnetic radiation with typical photon energies in the range of 100 eV-100 keV. For diffraction applications, mainly short wavelength X-rays (hard X-rays) in the range of a few angstroms to 0.1 Å (1 keV-120 keV) are used. Because the wavelength of X-rays is comparable to the size of atoms, they are ideally suited for probing the structural arrangement of atoms and molecules in a wide range of materials. X-rays primarily interact with electrons in atoms. When X-ray photons collide with electrons, some photons from the incident beam will be deflected away from the direction of their original travel. If the wavelength of these scattered X-rays did not change (meaning that the X-ray photons did not lose any energy), the process is called elastic scattering in that only momentum has been transferred in the scattering process. These are the X-rays that we measure in diffraction experiments, as the scattered X-rays carry information about the electron distribution in materials. Diffracted waves from different atoms can interfere with each other and the resultant intensity distribution is strongly modulated by this interaction. If the atoms are arranged in a periodic fashion, as in crystalline solids, the diffracted waves will consist of sharp interference maxima (peaks) with the same symmetry as the distribution of atoms. The angles of peaks in a XRD pattern are directly related to the atomic distances. For a given set of lattice planes with an inter-plane distance of  $d$ , the condition for diffraction to occur can be simply written as:

$$2d\sin\theta = n\lambda, \quad (3.1)$$

which is known as Bragg's law. In the above equation  $\lambda$  is the wavelength of the X-ray,  $\theta$  is the scattering angle and  $n$  is an integer representing the order of the diffraction peak.

### 3.2.2 XRD analysis performed in this work

Powder XRD is perhaps the most widely used XRD technique for material characterisation. Powder diffraction data can be collected using either transmission or reflection geometry. Because

the particles in the powder sample are randomly oriented, these two methods will yield the same information.

Generally speaking thin film diffraction refers not to a specific technique but rather a collection of XRD techniques used to investigate thin film samples grown on single crystalline substrates. There are several special considerations for using XRD to characterise thin film samples. First, a reflection geometry is used for these measurements, as the substrates are generally too thick for transmission. Second, high angular resolution is required.

A four-circle Material Research Diffractometer was used in the present work (Philips X'Pert MRD, type 3050/65, 50 kV and 30 mA,  $\text{CuK}_\alpha$  radiation). The axes of a four-circle diffractometer are shown in Fig. 3.5.

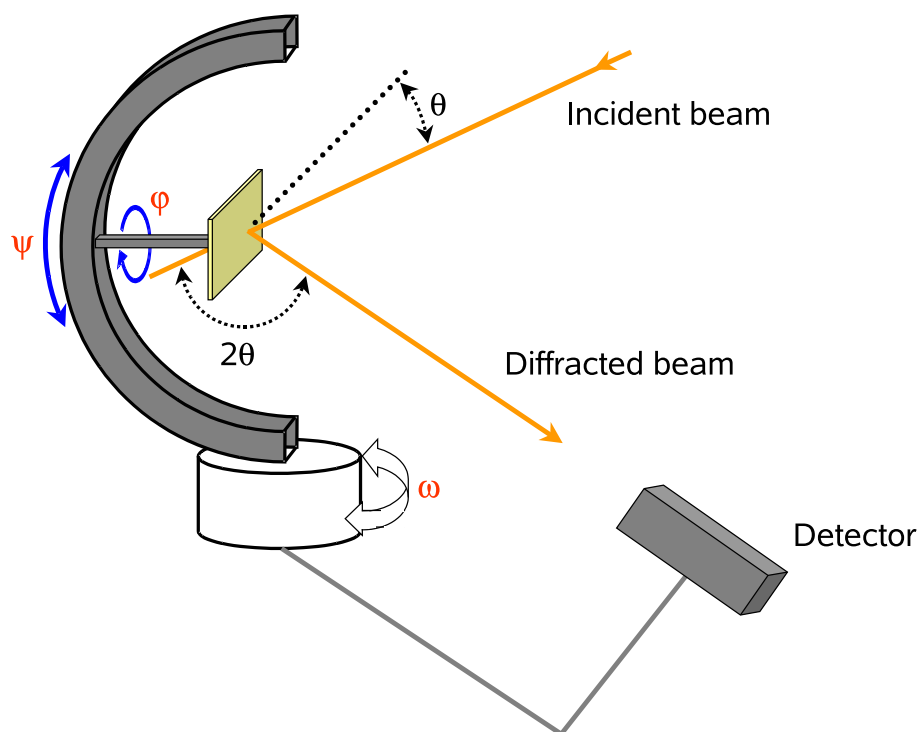


**Fig. 3.5.** Scheme of a four-circle diffractometer. The  $\phi$  axis is always parallel to the sample surface normal. The  $\psi$  axis is always in the plane of diffraction.

A parallel-beam optics geometry was used for the investigations (Fig. 3.6). In this geometry, the diffracted-beam optics is modified to parallel-beam optics, and a flat plate graphite monochromator is incorporated in front of the detector.

Standard  $\theta$ - $2\theta$  scans were made for phase analysis and to investigate a preferential orientation of the films. The  $\theta$ - $2\theta$  scan is also called  $\omega$ - $2\theta$  scan. In a four-circle diffractometer, an  $\omega$ - $2\theta$  scan runs on two axes of the diffraction system which are driven by two different motors ( $\omega$  motor: sample holder and  $2\theta$  motor: detector). In this Ph.D. work, the  $\omega$  axis is referred to as  $\theta$  one. In Fig. 3.5,  $\theta$  (the angle of incidence) represents the angle between the incident X-ray beam and the plane of the sample holder while  $2\theta$  (the angle of reflection) is the angle between the viewing direction of the detector (or scattered X-ray beam) and the incident X-ray beam. In a normal  $\theta$ - $2\theta$  scan these two angles are varied simultaneously from  $\theta_{\min}$  to  $\theta_{\max}$  and  $2\theta_{\min}$  to  $2\theta_{\max}$ . In this work, the samples

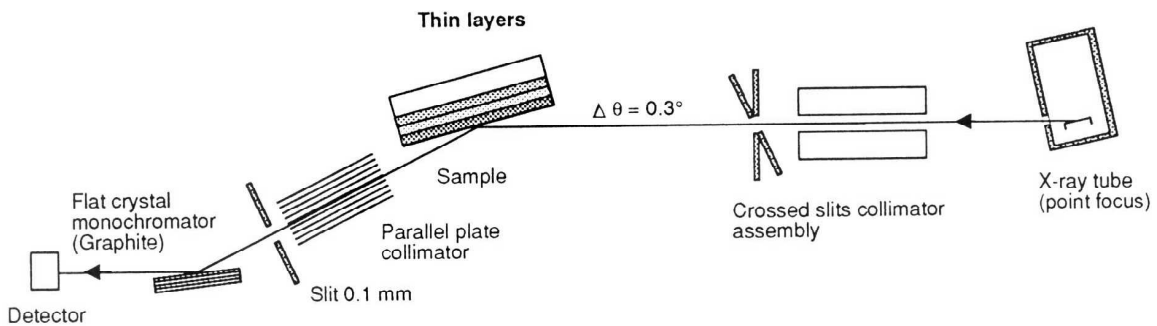


**Fig. 3.6.** Scheme of a parallel-beam optics geometry according to the User Guide for Philips X'Pert MRD Systems (1995). The  $2\theta$  resolution of the parallel plate collimator is  $0.09^\circ$ .

were mounted on a (001)-oriented silicon wafer in an open Eulerian cradle. After that, the  $\phi$  and  $\psi$  angles were optimised for a weak reflection of the substrate (e.g. for a (110)-oriented  $\text{TiO}_2$  (rutile) substrate the reflection (220) was used) in order to record the well-oriented contribution from the film. Fixing these two angles, the sample will then be rotated only in one direction by the variation of the  $\theta$  angle. Thus,  $\theta$ - $2\theta$  scans are only scans along one direction in reciprocal space. It is therefore a one-dimensional scan in the reciprocal space. If a film that covers the substrate crystal was grown with a certain orientation (i.e. in the case of epitaxy or topotaxy), the diffractogram of the sample will show the reflections of the single crystal substrate and reflections of those film planes which are parallel to the sample holder plane (substrate surface).

A  $2\theta$  scan was performed to study the polycrystalline or unoriented reaction products. The  $\theta$ - $2\theta$  scan is not useful for the study of polycrystalline thin films on single crystalline substrates, because of the presence of the interfering effect of the strong substrate reflections. A useful geometry is a grazing-incidence diffraction that is based on a low angle of incidence of the X-rays. In this geometry, X-rays pass through a suitable slit system and are made to fall on the sample at a grazing angle while the detector on the  $2\theta$  axis scans the XRD pattern. In this work a fixed  $\theta$  value of  $5^\circ$  was used to attenuate the substrate reflections (the  $\phi$  and  $\psi$  angles were kept as optimised for the  $\theta$ - $2\theta$  scan).

Texture measurements are used to determine the orientation distribution of crystalline grains in the sample. In materials science, texture is the distribution of crystallographic orientations of a sample. A sample in which these orientations are fully random is said to have no texture. If the crystallographic orientations are not random, but have some preferred orientation, then the sample has a weak, moderate or strong texture. The degree is dependent on the percentage of crystals that have the preferred orientation. Texture measurements can provide a complete description of the preferred orientation of a material. This is because a texture scan is a two-dimensional scan in reciprocal space. The surface of a hemisphere in reciprocal space is scanned for the reflections  $\{hkl\}$  off the sample/film. The possible reflections are selected by choosing the fixed value of  $2\theta$ . A texture measurement is also referred to as a pole figure (this definition is used in the present work) as it is plotted in polar coordinates consisting of the tilt and rotation angles with respect to a given orientation of the substrate surface. Thus, a pole figure is similar to a stereographic projection. This projection is used to represent graphically the orientation of planes in 3D space.

The pole figure analysis was performed using an open Eulerian cradle. A pole figure was measured at a fixed scattering angle  $2\theta$  (constant  $d$  spacing) and consists of a series of  $\phi$ -scans (in-plane rotation around the center of the sample) at different tilt  $\psi$  angles.  $\psi = 0^\circ$  (center of the plot) in the pole figures corresponds to the planes of the thin film being parallel to the substrate plane whereas  $\psi = 90^\circ$  (rim of the plot) corresponds to the planes of the thin film being perpendicular to the substrate plane. The full determination of the texture requires at least the measurements of two pole figures corresponding to planes that are not parallel and that do not have the same diffraction angle (different interplanar distances). In this work, to identify the orientation relationship between reaction products and the substrate, a series of pole figures were recorded with different  $2\theta$  values. The Ca.R.Ine Crystallography software was used to draw stereographic projections and 3D crystal structures.<sup>130</sup>

$\phi$  scans were performed in order to find-out the in plane orientation of the thin film with respect to the substrate. In this scan, the  $2\theta$  and  $\psi$  angles are fixed. For example, in the case of a (110) rutile  $\text{TiO}_2$  substrate a  $\phi$  scan with the  $\text{TiO}_2$  (200) reflection ( $2\theta = 39.2^\circ$ ) at  $\psi = 45^\circ$  could be done to determine the in-plane orientation of the substrate.

The XRD investigations in this work were performed outside the growth chamber at room temperature. The transfers of the samples were made through air.

## 3.3 Transmission electron microscopy

The electron microscopy methods are powerful techniques in the nanoscience world. Among them, cross-sectional TEM is essential for characterising of interfaces between thin films and substrates. TEM investigations were a significant part of this work. A conventional TEM CM20 Twin (Philips, Netherlands) at primary beam energy of 200 keV (point resolution 2.7 Å) and a HRTEM JEOL 4010 (JEOL, Japan) at primary beam energy of 400 keV (point resolution 1.8 Å) were used to study the reactive interfaces.

### 3.3.1 Basic concepts

A transmission electron microscope works on the same basic principles as a light microscope but uses electrons instead of light. The main principles of electron microscopy can be understood by use of optical ray diagrams as shown in Fig. 3.7.<sup>131</sup> As in the XRD, electron diffraction is an elastic scattering phenomenon with electrons being scattered by atoms in a regular array (crystal). When a crystal of lattice spacing  $d$  is irradiated with electrons of wavelength  $\lambda$ , diffracted waves will be produced at angles  $2\theta$ , satisfying the Bragg condition (3.1). The diffracted waves form diffraction spots on the back focal plane. In an electron microscope, the use of electron lenses allows the regular arrangement of the diffraction spots to be projected on a screen and the so-called electron diffraction pattern can then be observed. If the transmitted and the diffracted beams interfere on the image plane, a magnified image can be seen. The space where the diffraction pattern forms is called the reciprocal space, while the space at the image plane or at a specimen is called the real space.

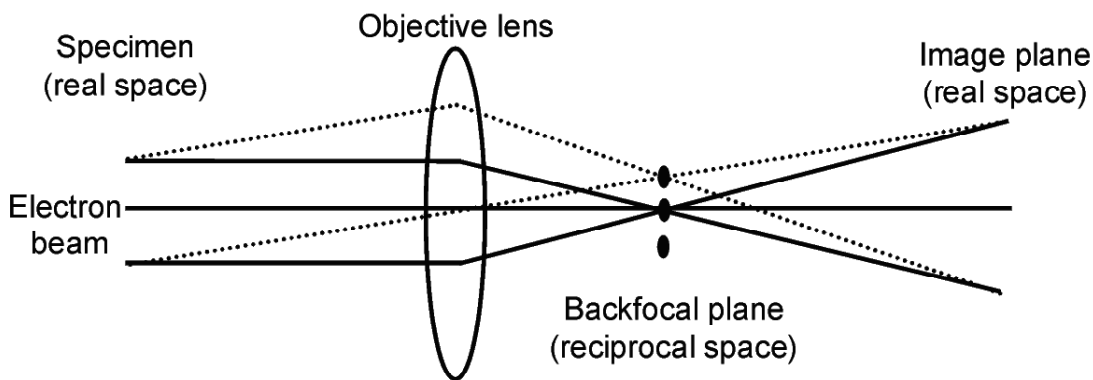


**Fig. 3.7.** Optical ray diagram with an optical objective lens showing the principle of the imaging process in a transmission electron microscope.

The transformation from the real space to the reciprocal space is mathematically given by the Fourier transform. By adjusting the electron lenses to obtain a diffraction image and inserting an aperture (selected area aperture) in a plane of the microscope containing an intermediate image, a specific area can be resolved and a diffraction pattern of the selected area (SAED) can be obtained. Because a SAED pattern can be obtained locally from different parts of the investigated material, crystal structure and mutual crystal orientation relationships of these parts can be identified.

Several types of observation modes in the electron microscope can be selected using an objective aperture. The observation mode using only the transmitted beam is called bright-field method and the image observed is a bright-field image (Fig. 3.8(a)). When one diffracted beam is selected, it is called dark-field method, and the image observed is a dark field image (Fig. 3.8(b)). It is also possible to form a TEM image by selecting multiple beams on the back focal plane using a large objective aperture. This observation is called high-resolution electron microscopy, and the image observed is a high-resolution image (HRTEM image) (Fig. 3.8(c)). HRTEM images can be classified into five groups: 1. lattice fringes; 2. one-dimensional structure images; 3. two-dimensional lattice images (showing the structural information at unit cell scale); 4. two-dimensional structure images (or crystal structure images, showing the structural information at atomic scale) and 5. special images.<sup>133</sup>

### 3.3.2 TEM sample preparation

A cross-sectional TEM investigation can only be performed, if a specimen is sufficiently thin (thinner than  $\approx 100$  nm). The samples for these investigations were prepared by standard methods of mechanical polishing and ion milling.<sup>134</sup>

The first step is to cut the substrate with the grown thin film into two parts of the same size using a diamond wire saw and then glue them face-to-face. In this work M-Bond 610 epoxy resin that has a very low viscosity was used. The glued sample is compressed by a uniformly distributed pressure during the curing time (1.5 h at curing temperature of 150 °C). The glue layer should be

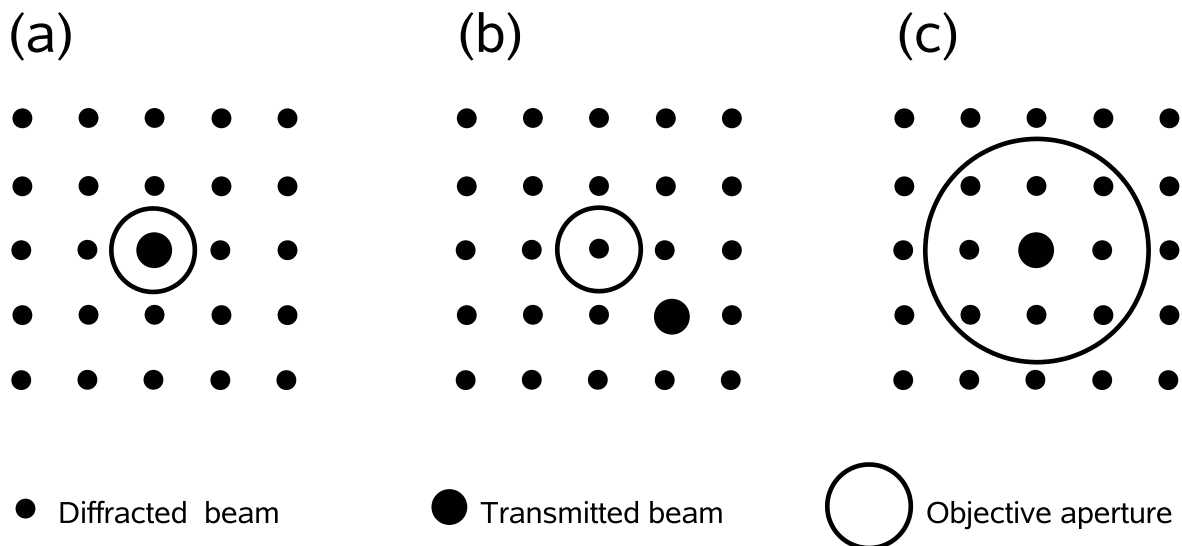


**Fig. 3.8.** Three observation modes in electron microscope using an objective aperture. The center of the objective aperture is on the optical axis. (a) Bright-field method, (b) Dark-field method and (c) High-resolution electron microscopy.<sup>133</sup>

as thin as possible. The glued sample is cut into slices normal to the interfaces with a thickness of 0.5 mm. Then, this slice was polished manually on grinding and polishing paper until the thickness is less than 70  $\mu\text{m}$ . A Gatan Model 656 dimple grinder was used to dimple and polish from one side at the center of the slice (the interface region) by a copper wheel with a radius of 15 mm. Hot wax was used to mount the slice onto a glass cylinder. After dimpling, the specimen was glued to a metallic Cu grid. The wax attached on the slice was cleaned by acetone. At the end of this step, the thickness at the dimpled area is in the range of 15  $\mu\text{m}$ -20  $\mu\text{m}$ .

The next step was thinning the slice at the center of the dimple by ion sputtering until a transparent hole is formed. A Gatan PIPS 691 was used to do the work. Two  $\text{Ar}^+$  ion guns bombard the up- and down-side of the specimen alternatively. The incident angles were set to  $6^\circ$ . A varying ion energy method has been used to quicken the specimen preparation. At the beginning of the ion milling process, the ion energy was set to 4 keV. Several hours later when the specimen was nearly transparent, the ion energy was reduced to 3 keV. After the transparent hole was formed, the milling was terminated. After a careful investigation of the sample by an optical microscope, the last step consisted of a fine polish for several minutes at incident angles of  $10^\circ$ - $15^\circ$  with respect to the surface using a decreasing accelerating voltage of 4 kV to 2 kV. A Duomill (Dual Ion Mill, Gatan) was used to perform the last step. This step completes the cross-section specimen preparation for TEM investigations.

## 3.4 Atomic force microscopy

An atomic force microscope (AFM) was used in this work to get information on the sample topography. AFM is a scanning probe microscope that probes the surface of a sample by moving the sample beneath a tip attached to a weak cantilever while the tip is in contact, or near contact,

with the surface. An AFM comprises two main components: the scanner and the AFM detection system. An AFM can operate in two principal modes, viz. tapping (non-contact) mode and contact mode, depending on the interaction between the tip and the sample.

In the contact mode, the tip adheres to the sample surface with a finite force as it is dragged across the surface. The finite adhesion forces deform the tip and sample so that contact occurs over a finite area. This area is greatly influenced by the tip sharpness and is increased by any additional spring force. In the tapping mode, long-range van der Waals forces deflect the tip. The strength of the van der Waals interaction depends on the tip sharpness and the amount of spring deflection is fixed by the spring constant. More information about AFM can be found in Ref.<sup>135</sup>.

In this study, the surfaces of substrates and thin films were studied by a Digital Instruments 5000 microscope working in tapping mode and using ultrasharp Si tips.

# 4 Results

## 4.1 Solid state reactions of $\text{BaCO}_3$ and $\text{BaO}$ with $\text{TiO}_2$ (rutile)

### 4.1.1 Solid-solid reaction of $\text{BaCO}_3$ with $\text{TiO}_2$ (rutile)

#### A. Some properties of $\text{BaCO}_3$ thin films

It is well-known that the substrate temperature has a primary role in controlling structure and composition of a growing thin film. Effects of the substrate temperature appear to be very important in obtaining a particular crystal structure and orientation of a thin film. A desired temperature should be below the temperature at which a reaction of the deposited film with the substrate occurs. The optimal temperature for  $\text{BaCO}_3$  deposition was first found by using the (110)  $\text{TiO}_2$  (rutile) substrates. Furthermore, this temperature was used for the deposition of  $\text{BaCO}_3$  on (100)  $\text{TiO}_2$  (rutile) substrates and  $\text{TiO}_2$  (anatase) thin films.

Deposition of  $\text{BaCO}_3$  at temperatures between 300 °C and 500 °C resulted in the growth of a single  $\text{BaCO}_3$  phase (JCPDS 45-1471,<sup>†</sup> barium carbonate) as indicated by the XRD  $\theta$ - $2\theta$ ,  $2\theta$  and pole figure measurements. However, the orientation relationship of the  $\text{BaCO}_3$  with respect to the (110) rutile substrates was dependent on the substrate temperature.  $\text{BaCO}_3$  films with a poor orientation quality were growing at a deposition temperature of 300 °C or 400 °C. The optimum temperature for the  $\text{BaCO}_3$  deposition was found at 500 °C. At this temperature the orientation relationship between the barium carbonate and the substrate was well-defined. Fig. 4.1(left) shows a XRD  $\theta$ - $2\theta$  scan of a  $\text{BaCO}_3$  thin film deposited at a substrate temperature of 500 °C. The peak position at  $2\theta = 34.3^\circ$  in Fig. 4.1(left) is from the (202) reflection of  $\text{BaCO}_3$  which means that the (101) plane of  $\text{BaCO}_3$  is parallel to the (110) substrate plane. The in-plane orientation was determined by pole figures taken at 23.9°, 24.2° and 34.3° (one of them is shown in Fig. 4.1(right)) and  $\phi$  scans of the  $\text{TiO}_2$  (200) reflection taken at  $\psi = 45^\circ$ . The  $\phi$  positions corresponding to the (001) and (00 $\bar{1}$ ) substrate planes are denoted A and B, respectively. The main orientation relationship at 500 °C was derived as:

$$(101) \text{ BaCO}_3 \parallel (110) \text{ TiO}_2; [10\bar{1}] \text{ BaCO}_3 \parallel [001] \text{ TiO}_2. \quad (4.1)$$

A second orientation relation was determined as:

$$(21\bar{1}) \text{ BaCO}_3 \parallel (110) \text{ TiO}_2; [2\bar{3}1] \text{ BaCO}_3 \parallel [001] \text{ TiO}_2. \quad (4.2)$$

---

<sup>†</sup>Lattice parameters:  $a = 0.643$  nm,  $b = 0.531$  nm,  $c = 0.89$  nm; space group Pnma (62).

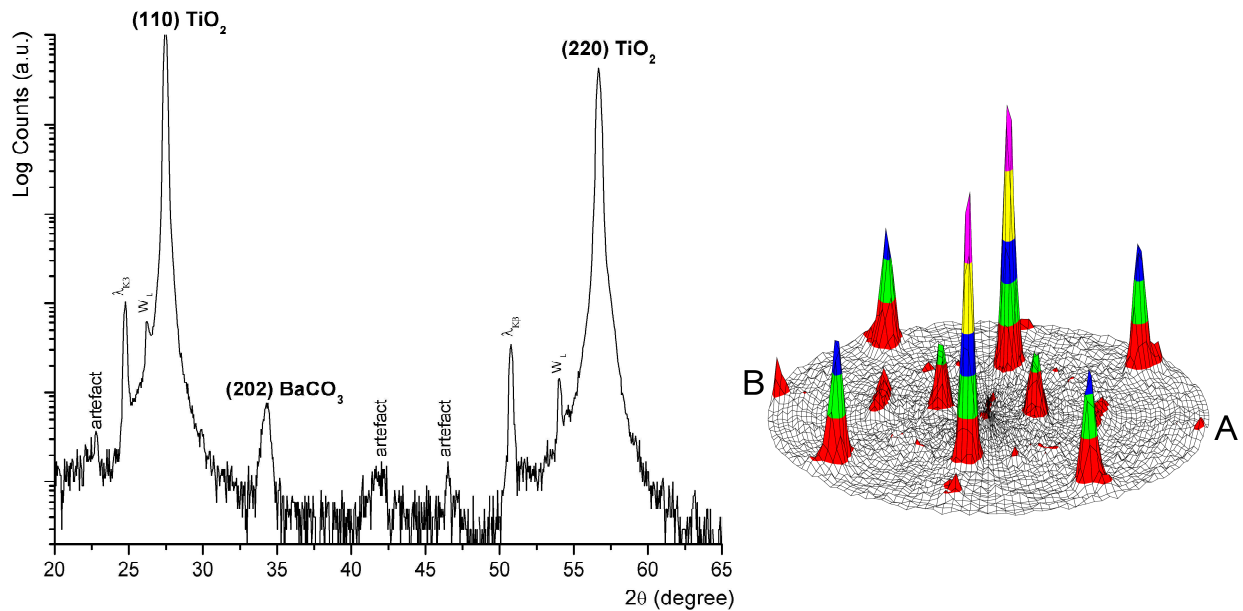


**Fig. 4.1.** (left) XRD  $\theta$ - $2\theta$  scan of a  $\text{BaCO}_3$  thin film deposited at  $500\text{ }^\circ\text{C}$  on a (110) rutile substrate. The  $\lambda_{\text{K}_\beta}$  lines are the substrate peaks originating from the remaining  $\text{Cu-K}_\beta$  radiation, and the  $\text{W}_\text{L}$  lines are coming from the tungsten contamination of the X-ray target by the tungsten cathode filament. The "artefact" peaks are substrate-induced artefacts. (right)  $\text{BaCO}_3$  (111) ( $2\theta = 23.9^\circ$ ) pole figure of a sample deposited on (110)  $\text{TiO}_2$  at  $500\text{ }^\circ\text{C}$ . The positions of marks A and B correspond to the  $\phi$  values of the (001) and (00 $\bar{1}$ ) substrate planes, respectively.

The crystallite size determined from the broadening of the (202) reflection of  $\text{BaCO}_3$  using Scherrer's equation<sup>†</sup> (see footnote) was  $\approx 20\text{ nm}$ .

The  $\text{BaCO}_3$  thin films were found to be unstable and decomposed when extensively exposed to the 200 keV electron beam for a few minutes, most probably to  $\text{BaO}$  and  $\text{CO}_2$ . Recently, a similar decomposition of  $\text{BaCO}_3$  particles was observed in Ref.<sup>136</sup>.

The  $\text{BaCO}_3$  thin films deposited on (100)  $\text{TiO}_2$  at a substrate temperature of  $500\text{ }^\circ\text{C}$  formed also with a defined orientation to the substrate. A XRD  $\theta$ - $2\theta$  scan indicated that the (100) plane of  $\text{BaCO}_3$  ( $2\theta = 27.7^\circ$ ) is parallel to the (100) substrate surface (Fig. 4.2(left)). A pole figure recorded at  $2\theta = 23.9^\circ$  of the sample prepared at a substrate temperature of  $500\text{ }^\circ\text{C}$  is shown in Fig. 4.2(right). This figure displays rather broad reflections of  $\text{BaCO}_3$  both in  $\phi$  and  $\psi$  directions. The X-ray intensity of this phase was also low in Fig. 4.2(left). In addition, some weak peaks were observed in a  $2\theta$  scan which means that the film contained unoriented parts. The mean orientation of most of the  $\text{BaCO}_3$  grains determined by pole figure measurements and a  $\phi$  scan of the (110)  $\text{TiO}_2$  reflection ( $\psi = 45^\circ$ ,  $2\theta = 27.45^\circ$ ) was derived as:

$$(100) \text{ BaCO}_3 \parallel (100) \text{ TiO}_2; [001] \text{ BaCO}_3 \parallel [001] \text{ TiO}_2. \quad (4.3)$$

The crystallite size determined from the broadening of the (100) peak of  $\text{BaCO}_3$  using Scherrer's

<sup>†</sup> $D_v = 0.9\lambda/B\cos\theta$ , where  $D_v$  - crystallite size,  $\lambda$  - wavelength of radiation, and  $B$  - FWHM of diffraction peak (in radians) and  $\theta$  is the diffraction angle. This approach does, however, neglect the effect that strain and defects can have on the width of the diffraction peaks.

equation was  $\approx 19$  nm.

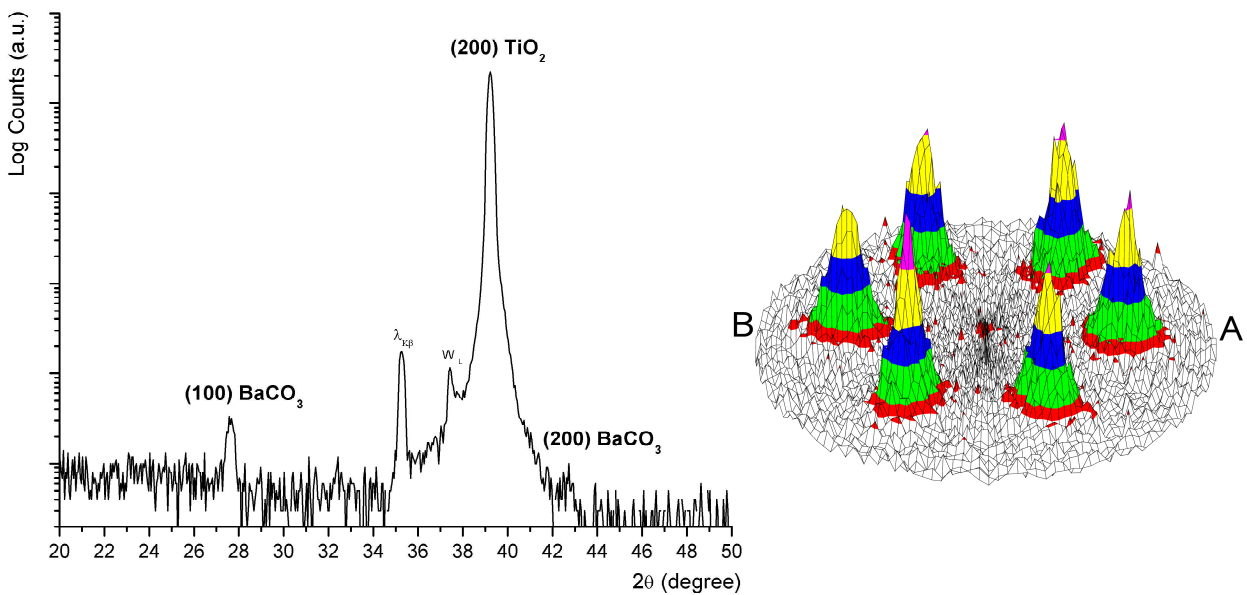


**Fig. 4.2.** (left) XRD  $\theta$ - $2\theta$  scan of a  $\text{BaCO}_3$  thin film deposited at  $500\text{ }^\circ\text{C}$  on a (100) rutile substrate. The  $\lambda_{\text{K}\beta}$  lines are the substrate peaks originating from the remaining  $\text{Cu-K}\beta$  radiation, and the  $\text{W}_L$  lines are coming from the tungsten contamination of the X-ray target by the tungsten cathode filament. (right)  $\text{BaCO}_3$  (111) ( $2\theta = 23.9^\circ$ ) pole figure of a sample deposited at  $500\text{ }^\circ\text{C}$  on (100)  $\text{TiO}_2$ . The positions of marks A and B correspond to the  $\phi$  values of the (001) and (001̄) substrate planes, respectively.

## B. Phase formation

### a. Reaction in vacuum ( $P_{\text{CO}_2} = 10^{-5}$ mbar)

#### X-ray diffraction

Most of the solid-solid reactions presented in this work were conducted on (110)  $\text{TiO}_2$  (rutile) substrates using  $\text{BaCO}_3$  layers grown at  $500\text{ }^\circ\text{C}$ .

The presence of  $\text{Ba}_2\text{TiO}_4$  (JCPDS 38-1481),  $\text{BaTiO}_3$  (JCPDS 89-2475) and Ti-rich phases depending on the reaction temperature was first investigated by XRD. A deposition of  $\text{BaCO}_3$  at  $500\text{ }^\circ\text{C}$  followed by solid-solid reaction at  $575\text{ }^\circ\text{C}$ - $600\text{ }^\circ\text{C}$  for 30 min produced a single  $\text{Ba}_2\text{TiO}_4$  phase (Fig. 4.3(b)). The reaction at temperatures between  $625\text{ }^\circ\text{C}$  and  $825\text{ }^\circ\text{C}$  lead to the formation of both  $\text{Ba}_2\text{TiO}_4$  and  $\text{BaTiO}_3$  phases (Figs. 4.3(c)-(d)) while the reaction at  $850\text{ }^\circ\text{C}$  for 30 min resulted in the formation of  $\text{BaTiO}_3$  without any evidence of remaining  $\text{Ba}_2\text{TiO}_4$ .

In order to evaluate the rate of the solid-solid reaction, the  $\text{BaCO}_3$ - $\text{TiO}_2$  system was annealed at constant temperature ( $575\text{ }^\circ\text{C}$ - $600\text{ }^\circ\text{C}$  and  $850\text{ }^\circ\text{C}$ ) for different length of times. The reaction proceeded from a  $\text{BaCO}_3$  layer to a mixture of  $\text{BaCO}_3$  and  $\text{Ba}_2\text{TiO}_4$ . As soon as all the  $\text{BaCO}_3$  has been consumed, the film consists only of  $\text{Ba}_2\text{TiO}_4$ . Both  $\text{BaCO}_3$  and  $\text{Ba}_2\text{TiO}_4$  phases were found immediately after heating the sample up to  $575\text{ }^\circ\text{C}$  (holding time null minutes) while only the  $\text{Ba}_2\text{TiO}_4$  phase was observed after annealing at  $600\text{ }^\circ\text{C}$  for one minute. The effect of a short holding time is mainly given by the heating during ramp up and ramp down (5 K/min). Increasing the

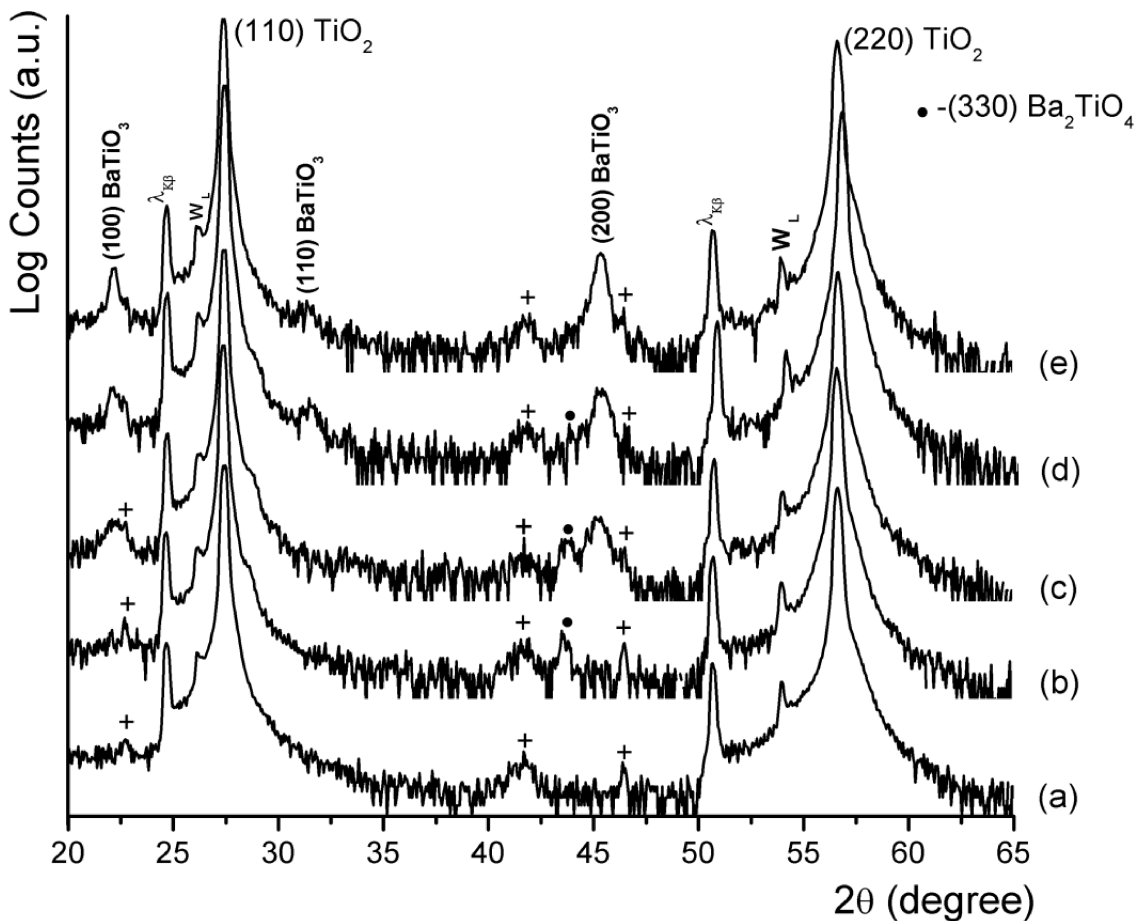


**Fig. 4.3.** XRD  $\theta$ - $2\theta$  scans for: (a) virginal (110) rutile substrate and for samples after solid-solid reaction of  $\text{BaCO}_3$  thin film deposited at 500 °C with the (110)  $\text{TiO}_2$  at (b) 600 °C, (c) 700 °C, (d) 800 °C and (e) 900 °C. The  $\lambda_{K\beta}$  lines are the substrate peaks originating from the remaining  $\text{Cu}-K\beta$  radiation, and the  $W_L$  lines are coming from the tungsten contamination of the X-ray target by the tungsten cathode filament. The peaks marked by "+" characters are substrate-induced artefacts.

reaction time up to 180 min at 600 °C resulted, together with the  $\text{Ba}_2\text{TiO}_4$  phase, in the formation of  $\text{BaTiO}_3$ . After the reaction at 850 °C for a short time (holding time null minutes), two phases ( $\text{Ba}_2\text{TiO}_4$  and  $\text{BaTiO}_3$ ) were identified.

The  $\text{Ba}_2\text{TiO}_4$  had an orthorhombic structure as indicated by pole figure analyses. This phase was found to be a chemically unstable compound and to decompose entirely after a storage for two weeks in air, most probably by reaction with  $\text{H}_2\text{O}$  and  $\text{CO}_2$ . This observation is in good agreement with the data obtained in Refs.<sup>55,56</sup>.

After reaction at 900 °C,  $\text{BaTiO}_3$  (Fig. 4.3(e)) and Ti-rich phases were observed on the (110)  $\text{TiO}_2$  substrate (detected by pole figures) while after the reaction at 1000 °C, only the  $\text{BaTi}_4\text{O}_9$  phase was detected by XRD. It should be noted that after reaction at 900 °C-1000 °C the samples became blue in colour. As was reported earlier,<sup>139</sup> heating  $\text{TiO}_2$  crystals in vacuum or under reducing conditions results in oxygen losses and corresponding change of the colour from yellowish to blue.

The phase sequence during solid-solid reaction on (100)  $\text{TiO}_2$  (rutile) substrates at temperatures between 600 °C and 1000 °C showed a process that is similar to the reaction on (110)  $\text{TiO}_2$ . An

example of a sample prepared by a solid-solid reaction between a  $\text{BaCO}_3$  film and (100)  $\text{TiO}_2$  substrate at 1000 °C for 30 min is shown in Fig. 4.4.

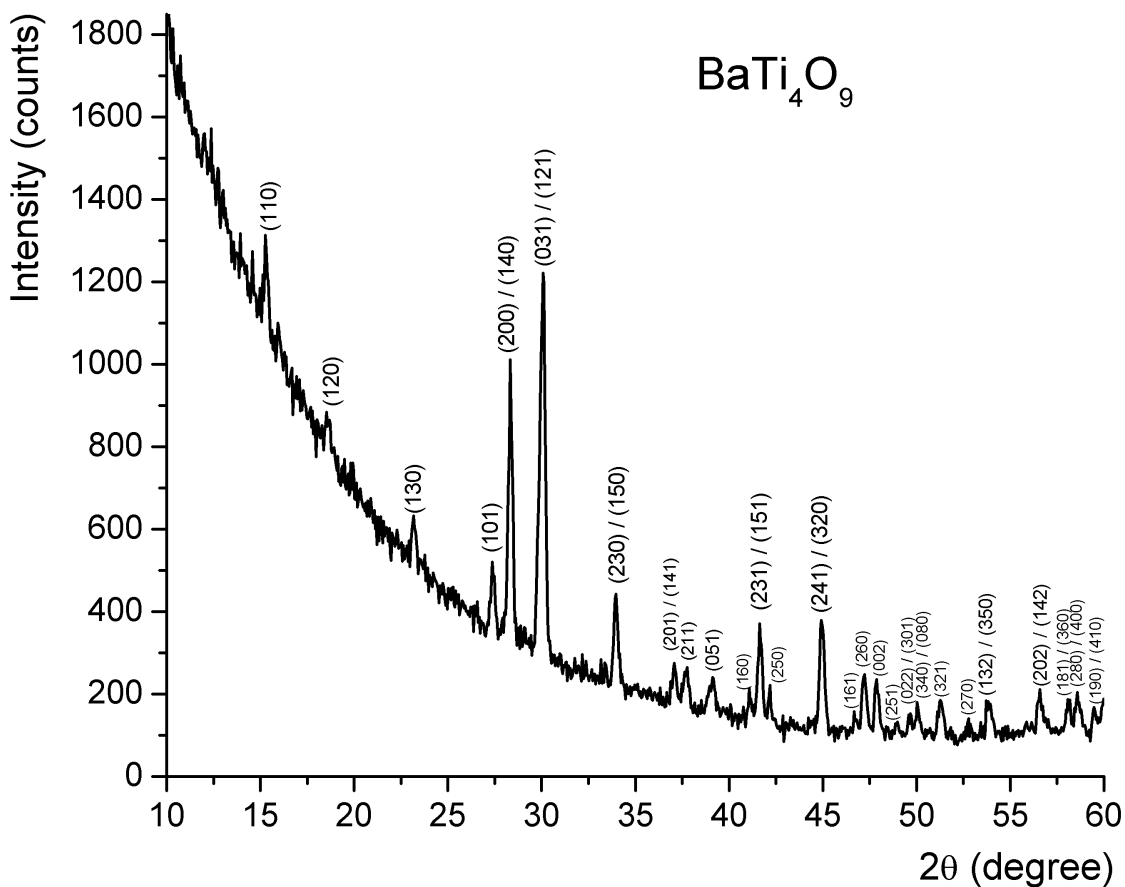


**Fig. 4.4.** XRD  $2\theta$  scan of a sample made by a solid-solid reaction in vacuum at 1000 °C for 30 min between a (100)  $\text{TiO}_2$  substrate and a  $\text{BaCO}_3$  thin film grown at 500 °C. The pattern was indexed according to JCPDS 77-1565. The scan speed was 0.0005 °/s.

### TEM and HRTEM investigations

As was shown above, only the  $\text{Ba}_2\text{TiO}_4$  phase was detected by XRD after solid-solid reaction at temperatures between 575 °C and 625 °C. To obtain more information about the presence of possible other phases formed in the films after the reactions on a nanometer scale, TEM and HRTEM were employed.

As was mentioned above, the  $\text{Ba}_2\text{TiO}_4$  phase is a very unstable compound and decomposed when exposed to air by reaction with  $\text{H}_2\text{O}$  and  $\text{CO}_2$ . To protect this phase, a  $\text{SiO}_2$  film was deposited at room temperature after a solid-solid reaction. This film protected  $\text{Ba}_2\text{TiO}_4$  from the influence of air and, thus, induced a stability of  $\text{Ba}_2\text{TiO}_4$  for several weeks, as shown by repeated X-ray diffraction measurements in air. Using such protected samples, cross-sectional samples with the  $\text{Ba}_2\text{TiO}_4$  phase were prepared for TEM investigations several times.

Fig. 4.5 shows a HRTEM image of a typical interface after solid-solid reaction of  $\text{BaCO}_3$  with (110)  $\text{TiO}_2$  in vacuum at 600 °C for 1 min. Small poorly-oriented  $\text{BaTiO}_3$  grains separated from each other by large distances were observed on the substrate surface after the reaction. However,

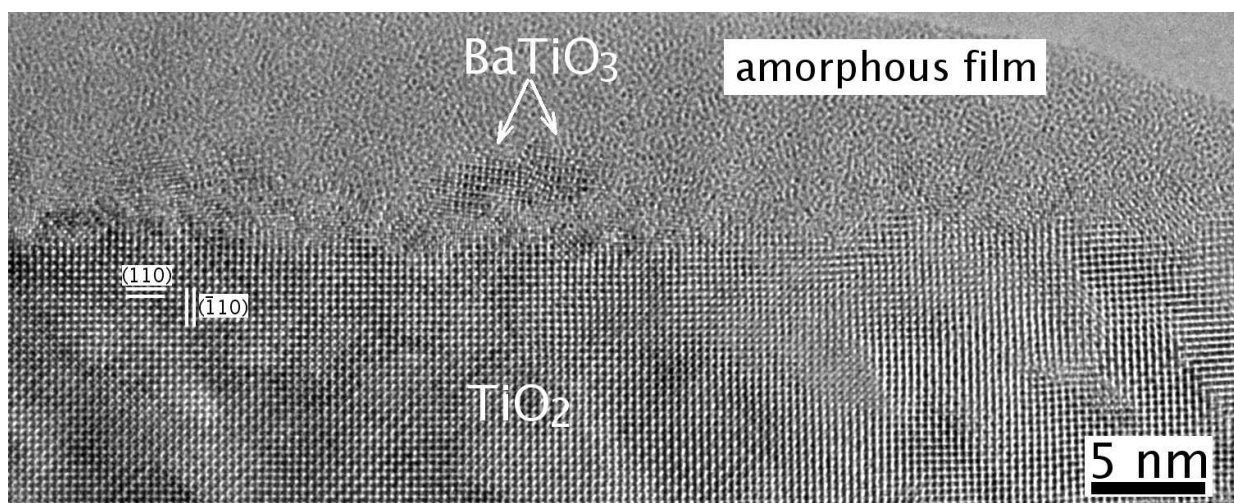


**Fig. 4.5.** Cross-sectional TEM image of the interface after solid-solid reaction of  $\text{BaCO}_3$  with (110)  $\text{TiO}_2$  in vacuum at 600 °C for 1 min. Viewing direction is [001]  $\text{TiO}_2$ .

their density was very low. The  $\text{Ba}_2\text{TiO}_4$  phase was not found in the sample. Instead, an amorphous film on the  $\text{TiO}_2$  substrate was observed in TEM. This film was converted into the crystalline  $\text{BaTiO}_3$  phase when extensively exposed to the 400 keV electron beam for a few minutes.

Fig. 4.6 shows a HRTEM image of a typical interface after solid-solid reaction of  $\text{BaCO}_3$  with (110)  $\text{TiO}_2$  in vacuum at 700 °C for 30 min. A thin layer consisting of oriented  $\text{BaTiO}_3$  grains was observed on the (110)  $\text{TiO}_2$  substrate surface after the reaction. The interface between the film and the substrate is rough. In addition, misfit dislocations were found at the  $\text{BaTiO}_3$ /(110)  $\text{TiO}_2$  interface (Fig. 4.7).

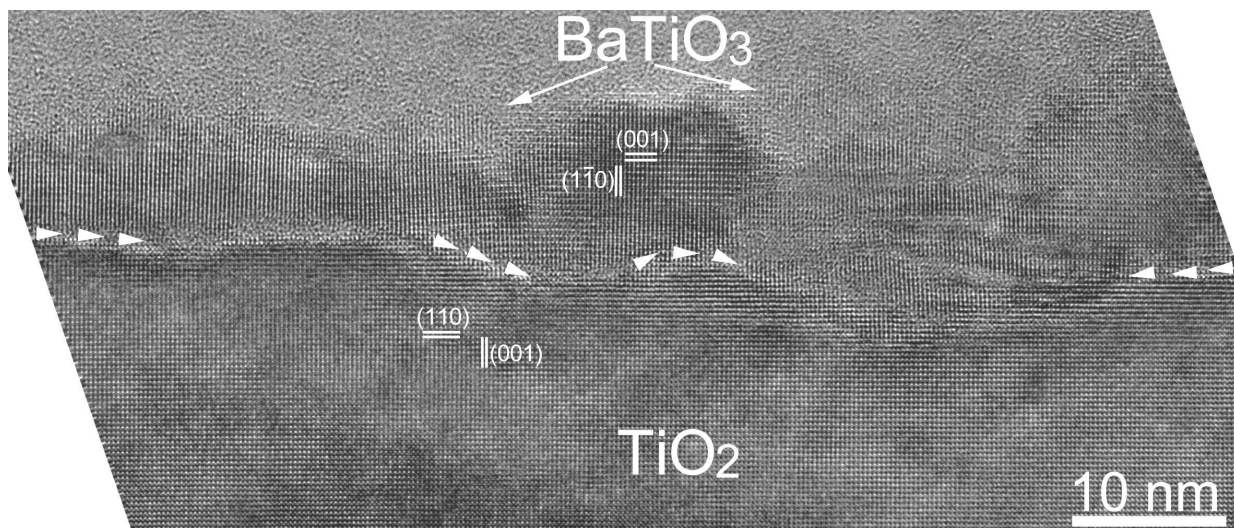


**Fig. 4.6.** Cross-sectional TEM image of a thin  $\text{BaTiO}_3$  layer grown by a solid-solid reaction in vacuum at 700 °C for 30 min between a (110)  $\text{TiO}_2$  (rutile) substrate and a  $\text{BaCO}_3$  layer grown at 500 °C. The rutile surface is marked by arrows. Viewing direction is [110]  $\text{BaTiO}_3$  || [1̄10]  $\text{TiO}_2$ .

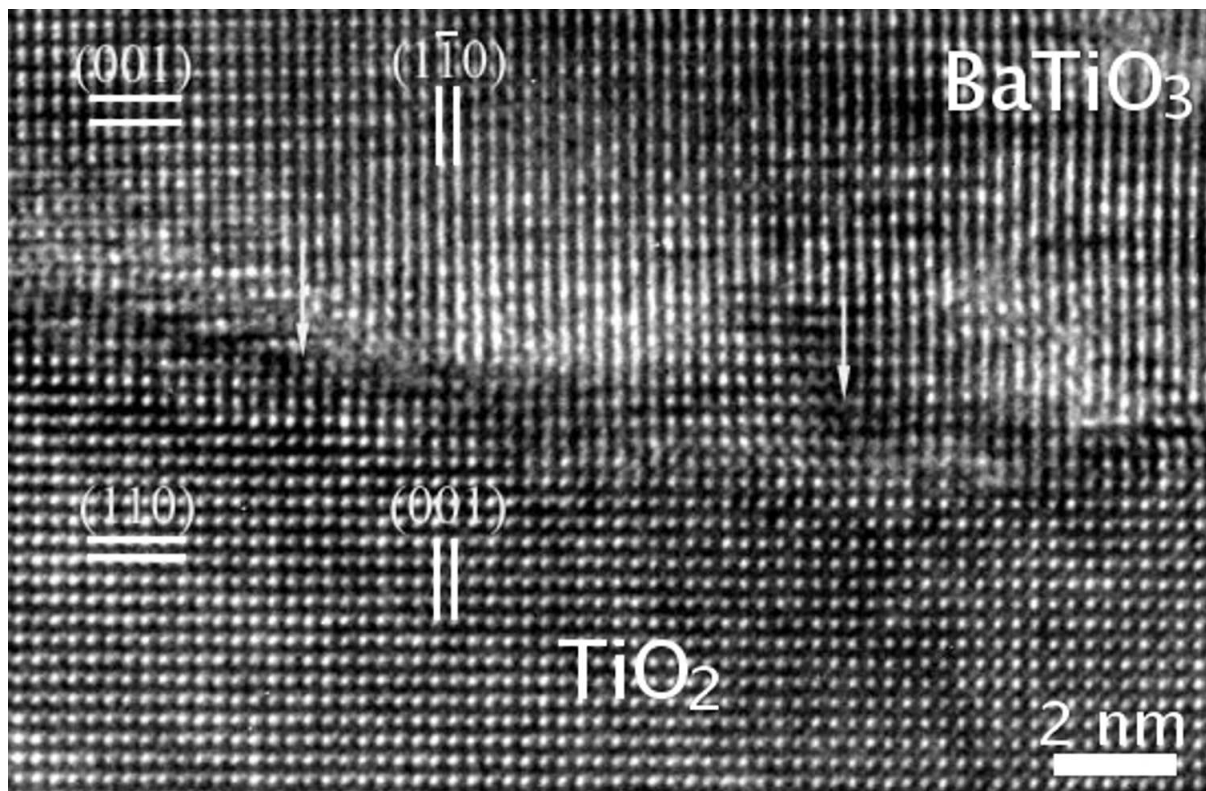


**Fig. 4.7.** Cross-sectional TEM image of the  $\text{BaTiO}_3/\text{TiO}_2$  reaction front. Interfacial dislocations are marked by arrows. Viewing direction is  $[110] \text{ BaTiO}_3 \parallel [\bar{1}10] \text{ TiO}_2$ .

### b. Reaction in air ( $P_{\text{CO}_2} = 0.381 \text{ mbar}$ )

The phase formation sequence after the solid-solid reaction of  $\text{BaCO}_3$  with the (110) and (100)  $\text{TiO}_2$  (rutile) substrates in air is different from the phase formation sequence in vacuum. Only the  $\text{BaTiO}_3$  phase was detected by XRD measurements after solid-solid reaction in air on (110) rutile substrates at substrate temperatures between 575 °C and 800 °C for 30 min. Fig. 4.8 gives an XRD  $\theta$ - $2\theta$  scan of a sample made by a solid-solid reaction of a  $\text{BaCO}_3$  thin film deposited at 500 °C with the (110)  $\text{TiO}_2$  substrate at 600 °C for 30 min, revealing the formation of only  $\text{BaTiO}_3$ .  $\text{Ba}_2\text{TiO}_4$  was not found in the thin films also by pole figure measurements. Even after the reaction for a short reaction time (holding time null minutes at 575 °C),  $\text{BaTiO}_3$  and  $\text{BaCO}_3$  phases were observed.

By contrast,  $\text{BaTiO}_3$  and non-reacted  $\text{BaCO}_3$  phases were found by XRD measurements after solid-solid reaction in air on (100)  $\text{TiO}_2$  (rutile) at substrate temperatures between 575 °C and 700 °C for 30 min. The reaction at 800 °C on (100)  $\text{TiO}_2$  resulted in the formation of  $\text{BaTiO}_3$  without any evidence of remaining  $\text{BaCO}_3$ . After a reaction at 900 °C,  $\text{BaTiO}_3$  and Ti-rich barium titanates were observed on both (110) and (100)  $\text{TiO}_2$  substrates while after reaction at 1000 °C, the  $\text{Ba}_4\text{Ti}_{13}\text{O}_{30}$  phase was formed on both substrates.

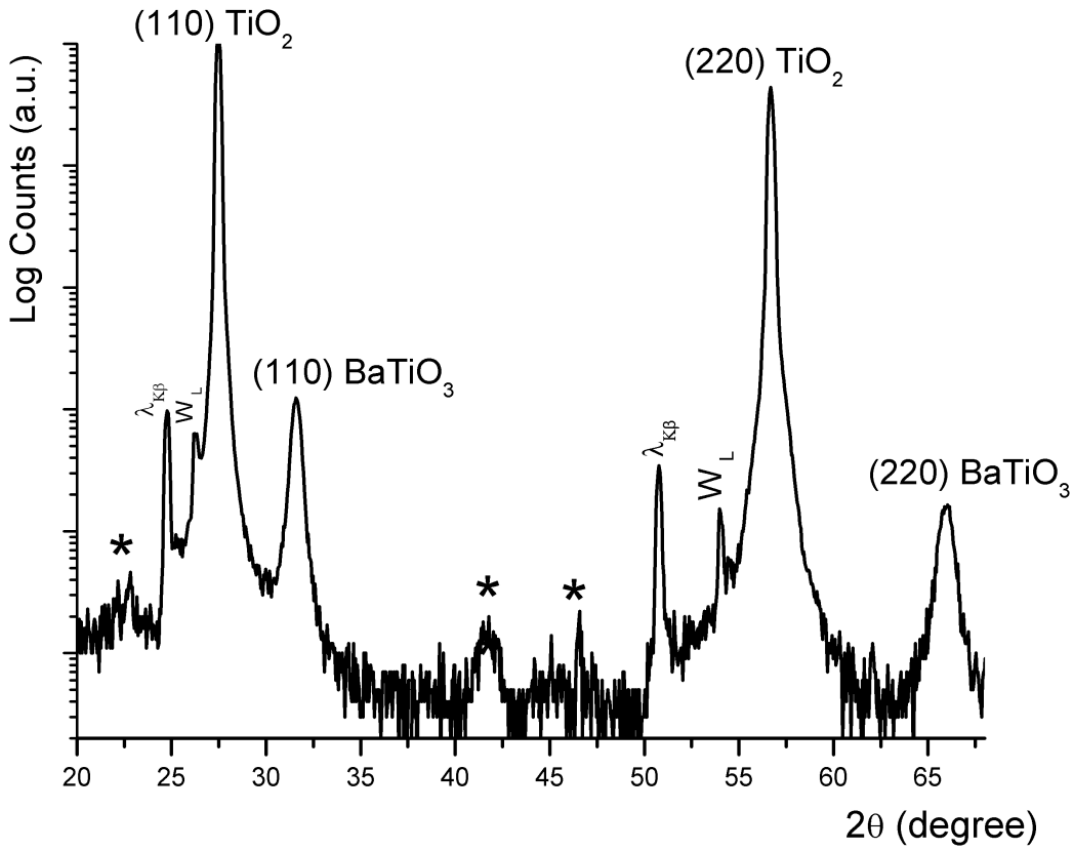


**Fig. 4.8.** XRD  $\theta$ - $2\theta$  scan of a sample made by a solid-solid reaction in air at 600 °C for 30 min between a (110)  $\text{TiO}_2$  substrate and a  $\text{BaCO}_3$  thin film deposited at 500 °C. The  $\lambda_{\text{K}\beta}$  lines are the substrate peaks originating from the remaining  $\text{Cu-K}\beta$  radiation, and the  $W_L$  lines are coming from the tungsten contamination of the X-ray target by the tungsten cathode filament. The peaks marked by "\*" characters are substrate-induced artefacts.

### 4.1.2 Vapour-solid reaction of $\text{BaO}$ with $\text{TiO}_2$ (rutile)

#### A. Phase formation

The vapour-solid experiments on (110)  $\text{TiO}_2$  (rutile) showed a reaction process that is similar to the solid-solid reaction with a shift of the temperatures of  $\text{BaTiO}_3$  formation.

At a reaction temperature of 575 °C, only the  $\text{Ba}_2\text{TiO}_4$  phase was identified, and between 600 °C and 850 °C two phases ( $\text{Ba}_2\text{TiO}_4$  and  $\text{BaTiO}_3$ ) were formed in contrast to the solid-solid reaction. But at 600 °C the  $\text{BaTiO}_3$  phase was contained in the thin film in a small amount only as shown by the very weak intensity in the pole figures. As in the solid-solid reaction, the barium orthotitanate obtained after vapour-solid reaction was also found to decompose when exposed to air for two weeks. Experiments at 900 °C resulted in the formation of  $\text{BaTiO}_3$  and Ti-rich grains in the thin film. Fig. 4.9 shows a cross-section HRTEM image of a typical reaction front developed after vapour-solid reaction of  $\text{BaO}$  with the (110)  $\text{TiO}_2$  surface at 900 °C. A thin film consisting of  $\text{BaTiO}_3$  and Ti-rich grains was formed after the reaction. The Ti-rich grains are located at the interface with the rutile substrate, whereas the  $\text{BaTiO}_3$  grains are located on top of the Ti-rich layer. The reaction interface is rough. In addition, large pores have developed during the reaction,

at the interface with the (110)  $\text{TiO}_2$  substrate. The walls of the pore in Fig. 4.9 are faceted by large  $\{100\}$  and  $\{110\}$   $\text{TiO}_2$  facets.

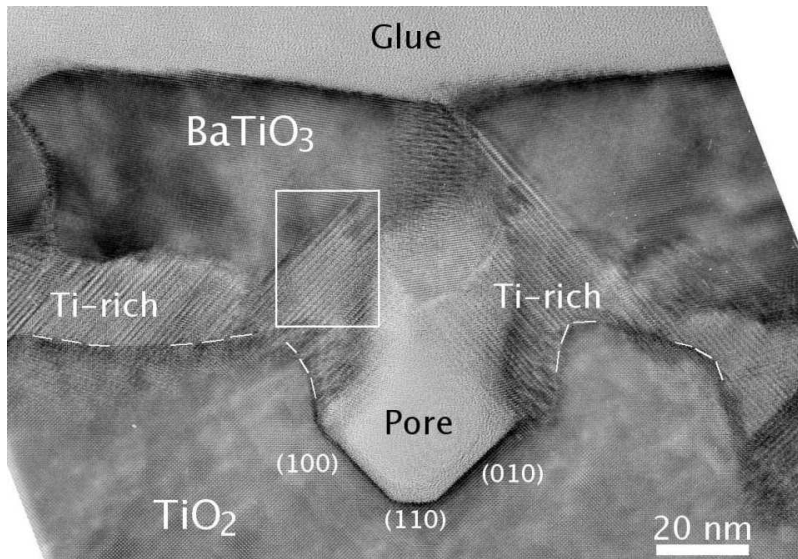


**Fig. 4.9.** TEM image of a typical reaction front after vapour-solid reaction of a  $\text{BaO}$  vapour with (110)  $\text{TiO}_2$  at  $900\text{ }^\circ\text{C}$ . The dashes mark the rutile surface.

The Ti-rich phase  $\text{Ba}_6\text{Ti}_{17}\text{O}_{40}$  (marked by a white rectangle in Fig. 4.9) was characterised by HRTEM investigation shown in Fig. 4.10. In this figure, the  $(\bar{2}00)$  and  $(002)$  interplanar distances of the Ti-rich phase are  $\sim 0.94\text{ nm}$  and  $\sim 0.49\text{ nm}$  (respectively), with an angle of  $98.8^\circ$  in between them. Thus, this Ti-rich grain was identified as the  $\text{Ba}_6\text{Ti}_{17}\text{O}_{40}$  phase. This phase was also found in other parts of the sample.

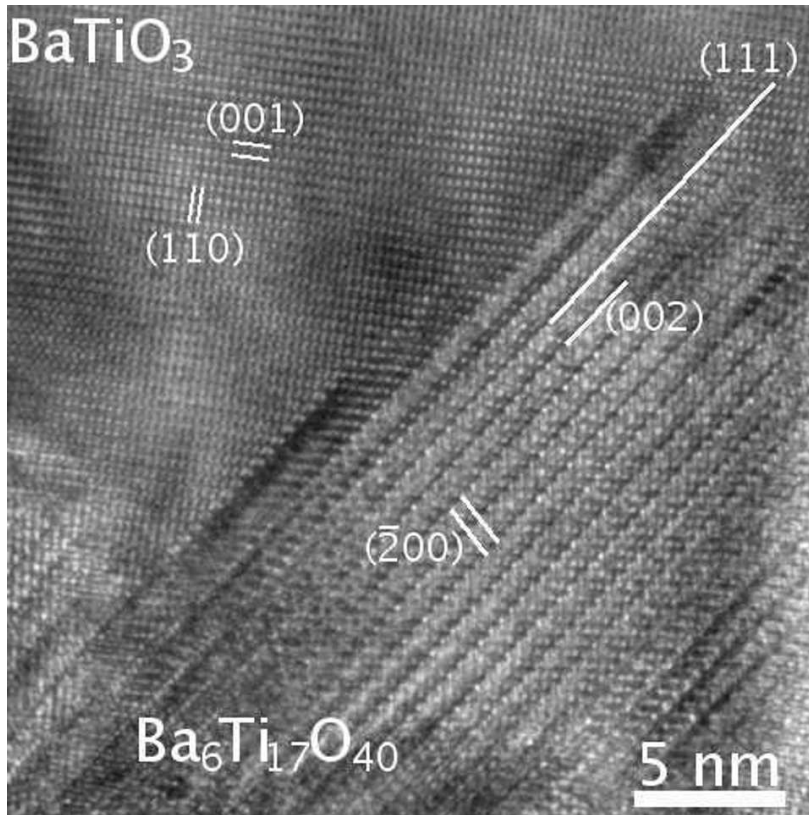


**Fig. 4.10.** Lattice plane image of  $\text{Ba}_6\text{Ti}_{17}\text{O}_{40}$  and  $\text{BaTiO}_3$  (magnified image of the white box shown in Fig. 4.9). Viewing direction is  $[010]\text{ Ba}_6\text{Ti}_{17}\text{O}_{40} \parallel [1\bar{1}0]\text{ BaTiO}_3$ .

After vapour-solid reaction at  $1000\text{ }^\circ\text{C}$ , only Ti-rich grains were found by XRD pole figure investigations. Fig. 4.11 shows a TEM image of the interface after reaction of  $\text{BaO}$  with (110)  $\text{TiO}_2$

at 1000 °C. Several large holes with {100} and {110}  $\text{TiO}_2$  facet walls were formed during the reaction.

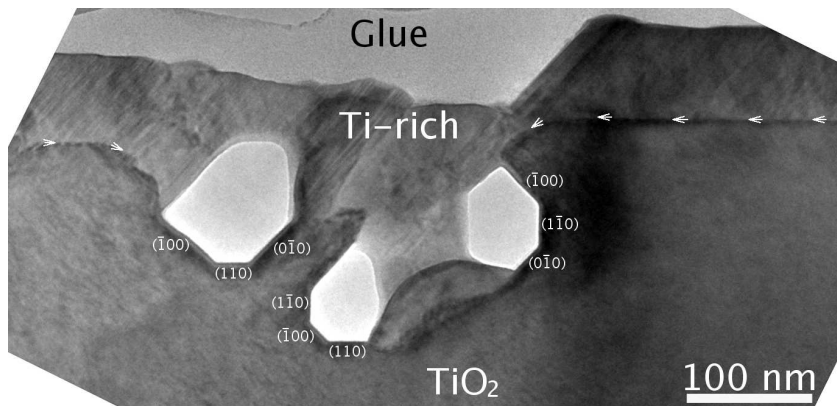


**Fig. 4.11.** Cross-sectional TEM image of a typical reaction front after vapour-solid reaction of  $\text{BaO}$  vapour with (110) rutile substrate at 1000 °C. Large holes with {100} and {110}  $\text{TiO}_2$  facet walls are visible in the image. The arrows mark the rutile surface.

The phase sequence during vapour-solid reaction on (100)  $\text{TiO}_2$  (rutile) substrates at temperatures between 600 °C and 1000 °C showed a process that is similar to the reaction on the (110)  $\text{TiO}_2$  substrate. A summary of the phase sequences after both solid-solid and vapour-solid reactions is given in Fig. 4.12.

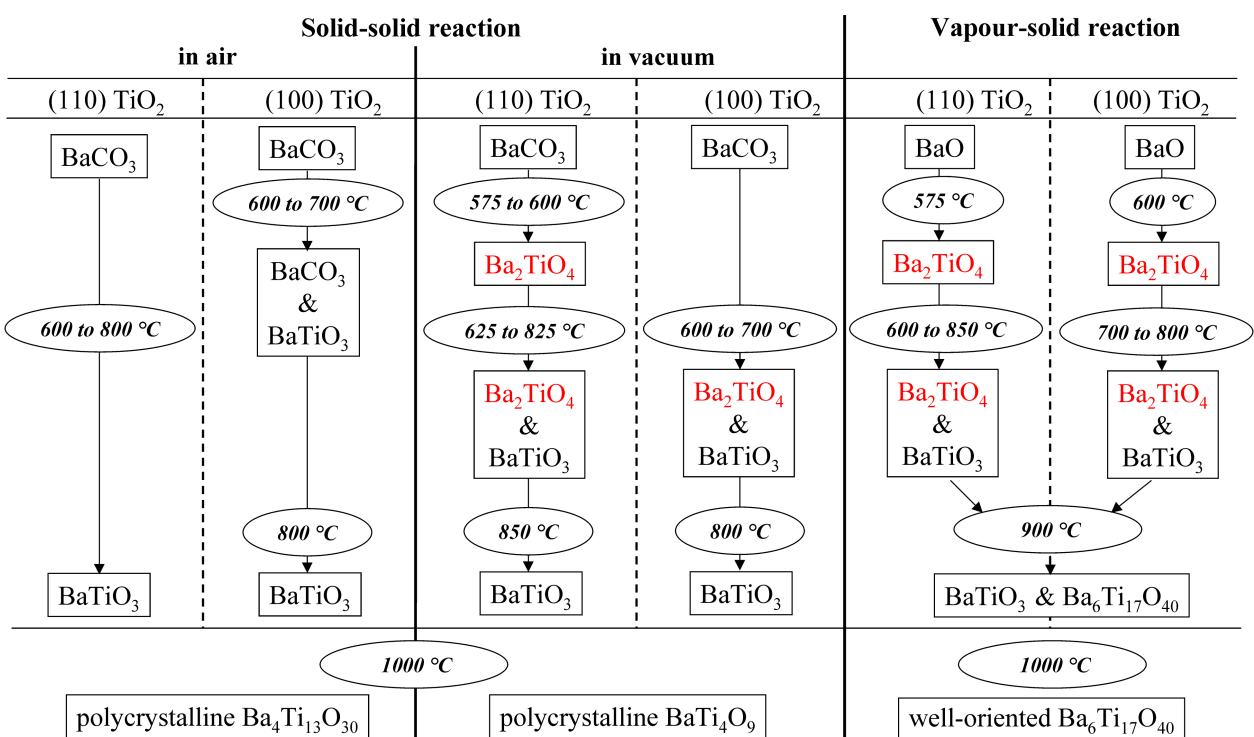
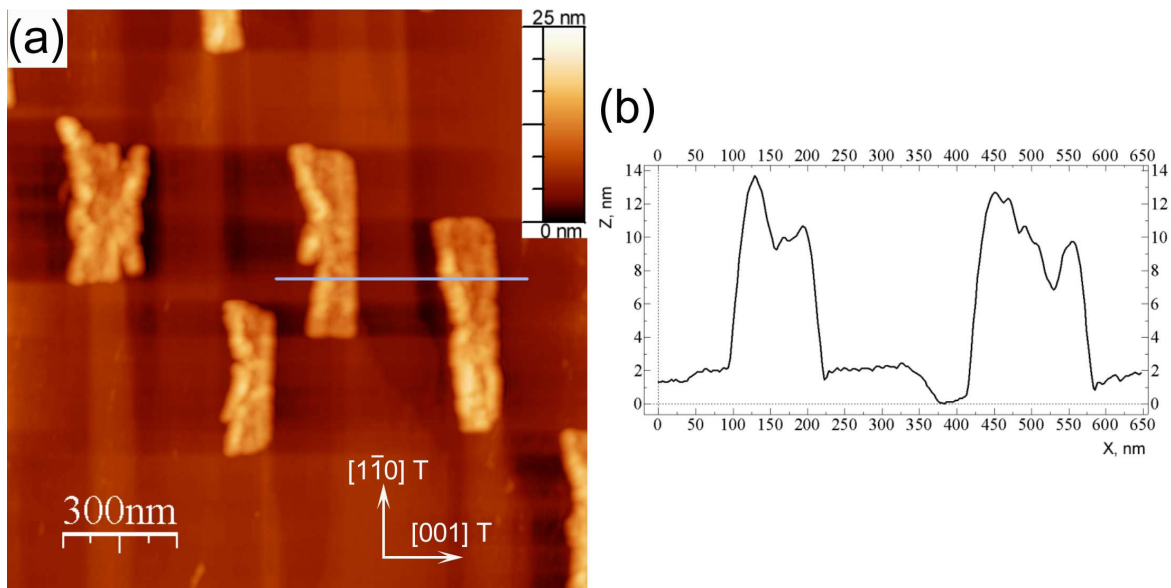


**Fig. 4.12.** Schematic representation of phase sequences after solid-solid (in air and in vacuum) and vapour-solid (in vacuum) reactions.

## B. Initial stage of vapour-solid reaction at 900 °C

This part of the work was performed to define which phase is nucleated first during a vapour-solid reaction at high reaction temperature. A very low amount of  $\text{BaO}$  was deposited on a (110)  $\text{TiO}_2$  substrate and on a (100)  $\text{TiO}_2$  substrate, both at 900 °C. The nominal thickness of  $\text{BaO}$  was varied from  $\approx 1$  nm to  $\approx 5$  nm.

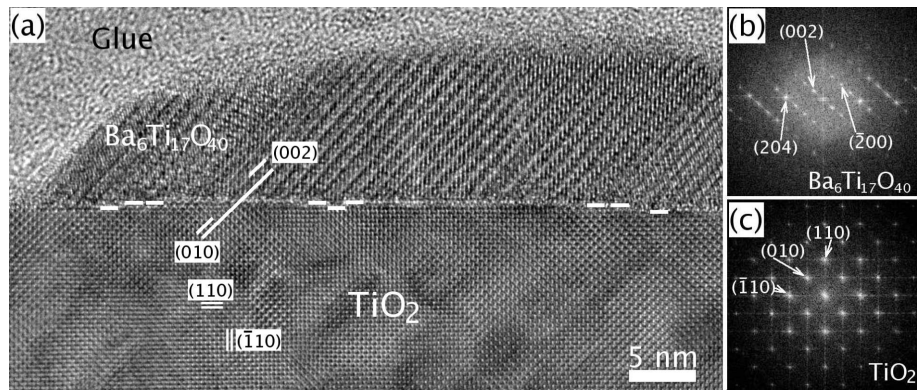
Fig. 4.13(a) shows a typical top-view AFM image and a line profile of Ba-Ti-O islands formed after vapour-solid reaction of a  $\text{BaO}$  quantity equivalent to a nominal film thickness of 1 nm with the (110)  $\text{TiO}_2$  surface at 900 °C. The line profile in Fig. 4.13(b) is along the blue line in



**Fig. 4.13.** (a) AFM image and (b) line profile of Ba-Ti-O islands formed by vapour-solid reaction on (110)  $\text{TiO}_2$  (T) surface at 900 °C. The height profile is along the blue line in image (a).

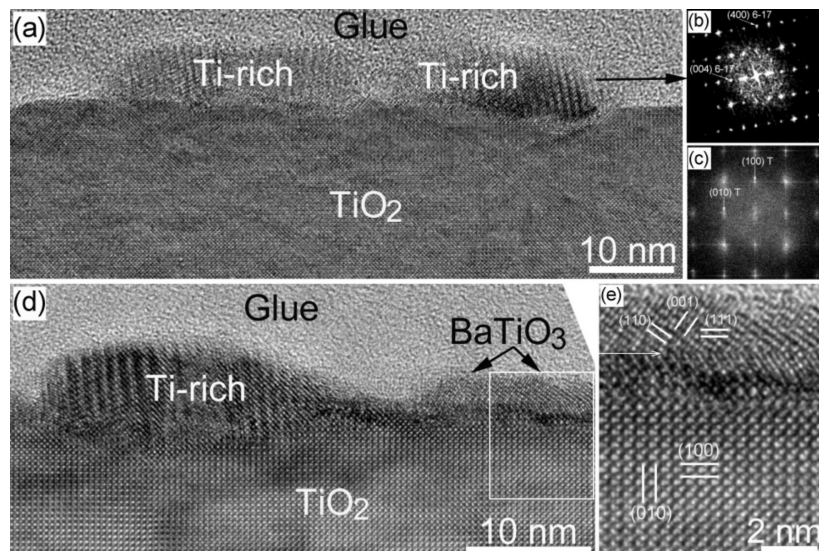
Fig. 4.13(a). The islands in Fig. 4.13(a) are elongated along the  $[1\bar{1}0]$  direction of  $\text{TiO}_2$  (the orientation of the substrate was confirmed by X-ray diffraction). The lateral sizes of the islands are in the range of 400 nm-600 nm in the  $[1\bar{1}0]$  direction of  $\text{TiO}_2$  while in the range of 100 nm-200 nm in the  $[001]$  direction of  $\text{TiO}_2$ . Their height varies from 10 nm to 15 nm (Fig. 4.13(b)). Each big island in Fig. 4.13(a) consists of several small grains. HRTEM investigations showed that the Ba-Ti-O grains consist of Ti-rich barium titanates.

Fig. 4.14 gives a typical cross-section HRTEM image of the sample shown in Fig. 4.13(a) in the  $[001]$  viewing direction of  $\text{TiO}_2$ . The reaction interface is flat. The grain in Fig. 4.14 is characterised by a large lattice constant and by stacking faults which are typical for Ti-rich phases formed by solid state reactions. The  $\text{Ba}_6\text{Ti}_{17}\text{O}_{40}$  Ti-rich phase was identified by the Fast Fourier Transformation (FFT) of the corresponding HRTEM image (Fig. 4.14(b)). Similar grains were observed in other parts of the TEM sample. No  $\text{BaTiO}_3$  grains or any wetting layer were found on the (110)  $\text{TiO}_2$  surface.



**Fig. 4.14.** HRTEM image of a sample after the reaction of a  $\text{BaO}$  vapour with a (110)  $\text{TiO}_2$  substrate at 900 °C. The nominal thickness of  $\text{BaO}$  was  $\approx 1$  nm. (a) Part of a Ti-rich island on the rutile substrate. The long white line in the image indicates  $(002) \text{Ba}_6\text{Ti}_{17}\text{O}_{40} \parallel (010) \text{TiO}_2$ . The dashes show steps on the  $\text{TiO}_2$  surface. (b) FFT image of a  $\text{Ba}_6\text{Ti}_{17}\text{O}_{40}$  Ti-rich grain. (c) FFT image of the rutile substrate. Viewing direction is [010]  $\text{Ba}_6\text{Ti}_{17}\text{O}_{40} \parallel [001] \text{TiO}_2$ . Magnified version of this figure see in the appendix, Fig. A.6.

Fig. 4.15 gives HRTEM images of the reaction products that have formed on the (100) rutile substrate after the initial stage of the reaction between a  $\text{BaO}$  vapour and the (100)  $\text{TiO}_2$  substrate at 900 °C. The nominal thickness of  $\text{BaO}$  was  $\approx 1$  nm.  $\text{BaTiO}_3$  and Ti-rich grains were found on



**Fig. 4.15.** HRTEM images of a sample after the reaction of a  $\text{BaO}$  vapour with a (100)  $\text{TiO}_2$  substrate at 900 °C. The nominal thickness of  $\text{BaO}$  was  $\approx 1$  nm. (a) Ti-rich islands on the rutile substrate. (b) FFT image of a  $\text{Ba}_6\text{Ti}_{17}\text{O}_{40}$  (6-17) Ti-rich grain. (c) FFT image of the rutile substrate (T). Viewing direction is [010]  $\text{Ba}_6\text{Ti}_{17}\text{O}_{40} \parallel [001] \text{TiO}_2$ . (d) Ti-rich and  $\text{BaTiO}_3$  grains on the rutile substrate. (e) Computer-processed lattice plane images of  $\text{BaTiO}_3$  and the rutile substrate (magnified section of image (d)). The arrow in image (e) marks a (111) twin boundary in  $\text{BaTiO}_3$ . Viewing direction is [1−10]  $\text{BaTiO}_3 \parallel [001] \text{TiO}_2$ . Magnified version of the figure see in the appendix, Fig. A.7.

the substrate surface after the reaction. The Ti-rich islands have an average size of about 10 nm in height and 25 nm in width. The  $\text{Ba}_6\text{Ti}_{17}\text{O}_{40}$  Ti-rich phase was identified by the FFT of the corresponding HRTEM images (Figs. 4.15(b)-(c)).  $\text{BaTiO}_3$  grains were also formed well-oriented with respect to the rutile substrate (Fig. 4.15(e)). They grew with a (111) orientation. However, their density was much lower than the density of the Ti-rich grains. Mainly, the (100) rutile surface

was covered by Ti-rich islands. No wetting layer was found on the substrate surface.

Increasing the nominal thickness of  $\text{BaO}$  up to  $\approx 5$  nm, the average size of the Ti-rich grains is increasing as shown in Fig. 4.16. In addition, cavities between the Ti-rich grains are formed (Fig. 4.16).

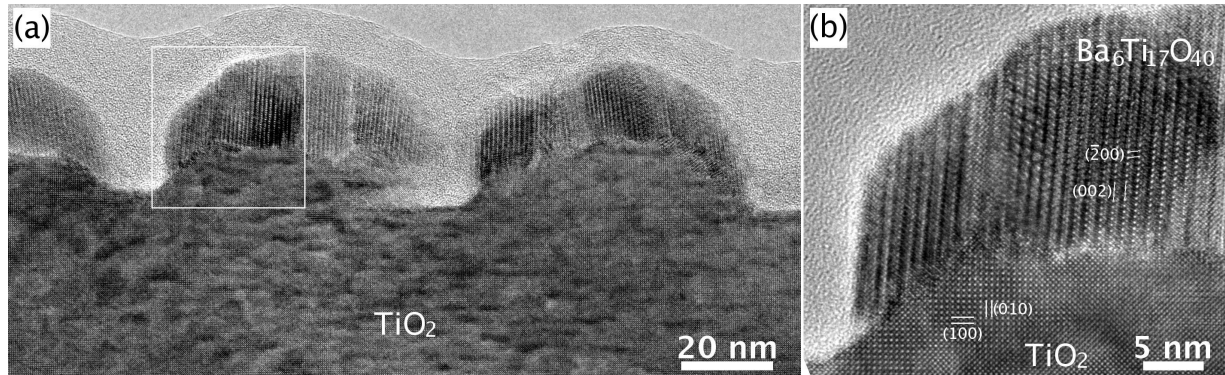


**Fig. 4.16.** HRTEM images of a sample made by a vapour-solid reaction on a (100)  $\text{TiO}_2$  substrate at 900 °C. The nominal thickness of  $\text{BaO}$  was  $\approx 5$  nm. a) Overview and b) lattice plane images of  $\text{Ba}_6\text{Ti}_{17}\text{O}_{40}$  and the rutile substrate (magnified section of image (a)). Viewing direction is  $[010] \text{Ba}_6\text{Ti}_{17}\text{O}_{40} \parallel [001] \text{TiO}_2$ . Magnified version of image (b) see in the appendix, Fig. A.8.

### 4.1.3 Orientation relationships

#### A. Orientation of $\text{Ba}_2\text{TiO}_4$

##### Solid-solid reaction

The orientation of  $\text{Ba}_2\text{TiO}_4$  after solid-solid reaction on (110)  $\text{TiO}_2$  substrates was dependent on the orientation quality of  $\text{BaCO}_3$ . A deposition of  $\text{BaCO}_3$  at 300 °C followed by solid-solid reaction at 575 °C-700 °C for 30 min produced  $\text{Ba}_2\text{TiO}_4$  with a low orientation quality (Fig. 4.17(left)).

On the other hand, a deposition of  $\text{BaCO}_3$  at 500 °C followed by solid-solid reaction at 575 °C-850 °C for 30 min produced a well-oriented  $\text{Ba}_2\text{TiO}_4$ . The peaks at  $2\theta = 43.8^\circ$  in Figs. 4.3(b)-(d) are from (330)  $\text{Ba}_2\text{TiO}_4$ . Several pole figures were recorded at different  $2\theta$  values to find out which plane of  $\text{Ba}_2\text{TiO}_4$  is parallel to the  $\text{TiO}_2$  substrate. Fig. 4.17(right) shows a pole figure taken at  $2\theta = 29.24^\circ$  ( $\text{Ba}_2\text{TiO}_4$  (031)/(002)) of the sample prepared after solid-solid reaction at 700 °C. The orientation relationship of  $\text{Ba}_2\text{TiO}_4$  with respect to the (110) rutile surface was found as follows:

$$(110) \text{Ba}_2\text{TiO}_4 \parallel (110) \text{TiO}_2; [001] \text{Ba}_2\text{TiO}_4 \parallel [001] \text{TiO}_2. \quad (4.4)$$

This orientation relationship was also observed for the samples prepared after the reaction at temperatures between 575 °C and 850 °C.

The orientation quality of  $\text{Ba}_2\text{TiO}_4$  after the solid-solid reaction on (100) rutile substrates was also dependent on the orientation quality of  $\text{BaCO}_3$ . A deposition of  $\text{BaCO}_3$  at 300 °C followed by solid-solid reaction at 700 °C for 30 min produced  $\text{Ba}_2\text{TiO}_4$  with a poor orientation quality while a deposition of  $\text{BaCO}_3$  at 500 °C followed by solid-solid reaction at 600 °C-700 °C for 30 min produced a well-oriented  $\text{Ba}_2\text{TiO}_4$ .

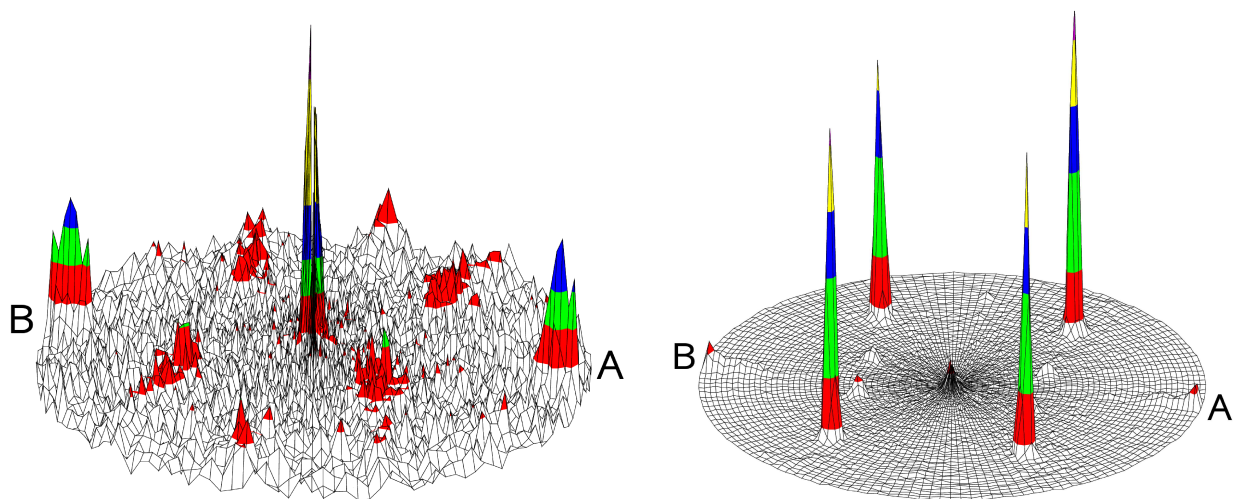


**Fig. 4.17.** Pole figures of samples grown by a solid-solid reaction recorded with  $\{103\}/\{200\}$   $\text{Ba}_2\text{TiO}_4$  reflections ( $2\theta = 29.24^\circ$ ). The samples were made by a reaction at  $700\text{ }^\circ\text{C}$  for 30 min between (110)  $\text{TiO}_2$  substrate and  $\text{BaCO}_3$  layer grown at: (left)  $300\text{ }^\circ\text{C}$  and (right)  $500\text{ }^\circ\text{C}$ . In the right figure, peaks are situated at  $\psi = 0^\circ, 60^\circ$  and  $90^\circ$  and thus correspond to a (110) orientation of  $\text{Ba}_2\text{TiO}_4$ . Weak peaks situated at  $\psi = 34^\circ$  are from  $\{211\}$  and  $\{2\bar{1}\bar{1}\}$   $\text{Ba}_2\text{TiO}_4$  which correspond to  $2\theta = 28.78^\circ$  of  $\text{Ba}_2\text{TiO}_4$ . They appear in the figure because the intensity of these peaks are rather strong (Int= 82% according to JCPDS 38-1481) and they are very close to  $2\theta = 29.24^\circ$  (Int= 100% according to JCPDS 38-1481).

Fig. 4.18 shows a pole figure recorded at  $2\theta = 29.24^\circ$  ( $\text{Ba}_2\text{TiO}_4$  (031)/(002)) of the sample made by solid-solid reaction at  $700\text{ }^\circ\text{C}$  for 30 min between (100)  $\text{TiO}_2$  substrate and  $\text{BaCO}_3$  layer grown at  $500\text{ }^\circ\text{C}$ . The orientation relationship of  $\text{Ba}_2\text{TiO}_4$  with respect to the (100) rutile surface was found as follows:

$$(100) \text{ Ba}_2\text{TiO}_4 \parallel (100) \text{ TiO}_2; [001] \text{ Ba}_2\text{TiO}_4 \parallel [001] \text{ TiO}_2. \quad (4.5)$$

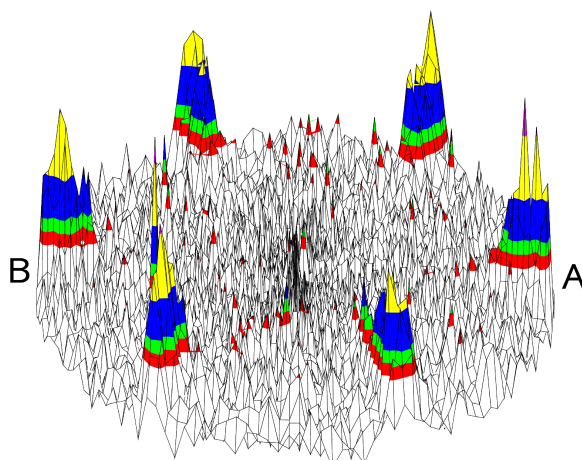


**Fig. 4.18.** Pole figure of a sample grown by a solid-solid reaction at  $700\text{ }^\circ\text{C}$  for 30 min between a (100)  $\text{TiO}_2$  substrate and a  $\text{BaCO}_3$  layer grown at  $500\text{ }^\circ\text{C}$ . The figure was recorded with  $\{031\}/\{002\}$   $\text{Ba}_2\text{TiO}_4$  reflections ( $2\theta = 29.24^\circ$ ). Peaks are situated at  $\psi = 0^\circ$  and  $90^\circ$  and, thus, correspond to a (100) orientation of  $\text{Ba}_2\text{TiO}_4$ .

### Vapour-solid reaction

After vapour-solid reaction on the (110)  $\text{TiO}_2$  surface, the orientation relationship of the  $\text{Ba}_2\text{TiO}_4$  phase is different compared to the solid-solid reactions. In the temperature range between  $575\text{ }^\circ\text{C}$

and 700 °C, most of the  $\text{Ba}_2\text{TiO}_4$  grains grew according to the following relation:

$$(100) \text{ Ba}_2\text{TiO}_4 \parallel (110) \text{ TiO}_2; [001] \text{ Ba}_2\text{TiO}_4 \parallel [001] \text{ TiO}_2. \quad (4.6)$$

At a substrate temperature of 800 °C no well-defined orientation was deduced because a XRD pole figure taken at  $2\theta = 29.24^\circ$  showed broad reflections of  $\text{Ba}_2\text{TiO}_4$  both in  $\phi$  and  $\psi$  directions. On the other hand, the orientation relationship of the  $\text{Ba}_2\text{TiO}_4$  phase after vapour-solid reaction on (100)  $\text{TiO}_2$  did not change compared to the solid-solid reactions. In the temperature range between 575 °C and 800 °C, the  $\text{Ba}_2\text{TiO}_4$  grains grew according to the relation (4.5).

## B. Orientation of $\text{BaTiO}_3$

### Solid-solid reaction

#### (110) $\text{TiO}_2$ (rutile)

After the solid-solid reaction in vacuum,  $\text{BaTiO}_3$  grains were formed with a defined orientation with respect to the (110)  $\text{TiO}_2$  substrates. Figs. 4.19(a)-(c) show typical pole figures taken at  $2\theta = 31.4^\circ$  for samples prepared on (110)  $\text{TiO}_2$  at 700 °C, 800 °C and 900 °C, respectively. The figures display extended reflections of the  $\text{BaTiO}_3 \{101\}$  family with a shape like a fin, which means that the  $\text{BaTiO}_3$  film consists of several kinds of tilted grains with a common tilt axis.

A pole figure after solid-solid reaction at 700 °C is shown in Fig. 4.19(a). For this temperature most of the  $\text{BaTiO}_3$  grains were grown with a mean orientation relationship (001)  $\text{BaTiO}_3 \parallel$  (110)  $\text{TiO}_2$  (see also Figs. 4.6-4.7).

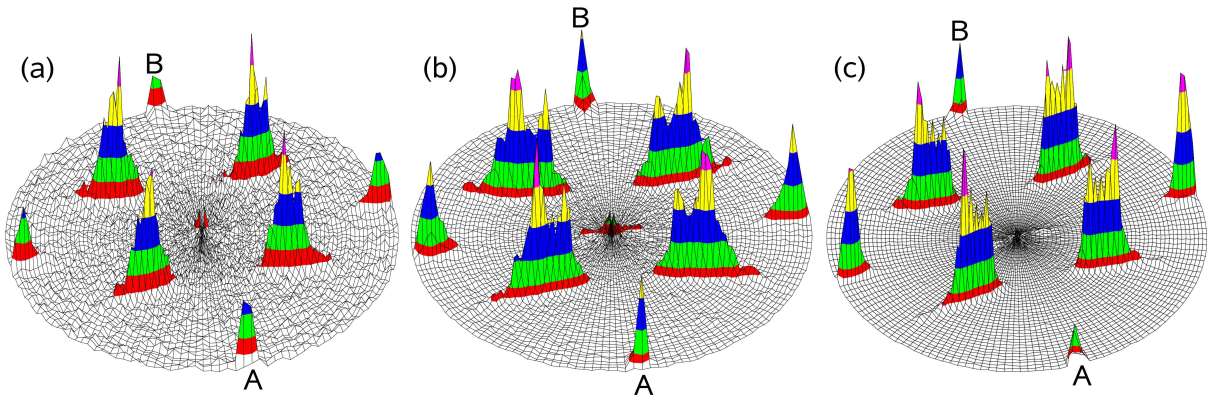


**Fig. 4.19.** Pole figures of samples produced on (110)  $\text{TiO}_2$  substrates by a solid-solid reaction in vacuum at: (a) 700 °C, (b) 800 °C and (c) 900 °C. The figures were taken at  $2\theta = 31.4^\circ$  ( $\text{BaTiO}_3 \{101\}$ ). The peaks are situated at  $\psi = 40^\circ$  to  $60^\circ$  and  $90^\circ$  in all the figures. Additional weak peaks in Figs. 4.16(b)-(c) are situated at  $\psi = 0^\circ$ ,  $11^\circ$  and  $82^\circ$ . The  $\psi$  values of  $40^\circ$ ,  $50^\circ$ ,  $82^\circ$  and  $90^\circ$  correspond to a (119) orientation of  $\text{BaTiO}_3$  while the  $\psi$  values of  $11^\circ$ ,  $50^\circ$ ,  $70^\circ$  and  $90^\circ$  correspond to a (441) orientation of  $\text{BaTiO}_3$  and the  $\psi$  value of  $45^\circ$  corresponds to a (001) orientation of  $\text{BaTiO}_3$ .

With increasing reaction temperature, the number of tilted grains is increasing. After reaction between 800 °C and 900 °C XRD  $\theta$ - $2\theta$  scans (Figs. 4.3(d)-(e)) and pole figure measurements (Figs. 4.19(b)-(c)) revealed additional orientations of  $\text{BaTiO}_3$  such as (110)  $\text{BaTiO}_3 \parallel$  (110)  $\text{TiO}_2$ ,

(119)  $\text{BaTiO}_3 \parallel (110) \text{TiO}_2$  and (441)  $\text{BaTiO}_3 \parallel (110) \text{TiO}_2$ . From a series of pole figures,  $\phi$  scans and HRTEM investigations, the in-plane orientation was found to be  $[1\bar{1}0] \text{BaTiO}_3 \parallel [001] \text{TiO}_2$  for all orientations of  $\text{BaTiO}_3$  grown by a solid-solid reaction in vacuum on (110)  $\text{TiO}_2$  substrates.

In contrast to the formation of  $\text{Ba}_2\text{TiO}_4$ ,  $\text{BaTiO}_3$  formed also with (001)  $\text{BaTiO}_3 \parallel (110) \text{TiO}_2$  after reaction at 700 °C for 30 min if a  $\text{BaCO}_3$  film with low orientation quality grown at 300 °C was used.

A deposition of  $\text{BaCO}_3$  at 500 °C followed by the reaction in air produced well-oriented  $\text{BaTiO}_3$ . Fig. 4.20 shows a X-ray pole figure of a sample made on a (110)  $\text{TiO}_2$  substrate by a solid-solid reaction in air at 700 °C for 30 min. The orientation relationship of  $\text{BaTiO}_3$  was identified as:

$$(110) \text{BaTiO}_3 \parallel (110) \text{TiO}_2; [1\bar{1}0] \text{BaTiO}_3 \parallel [001] \text{TiO}_2. \quad (4.7)$$

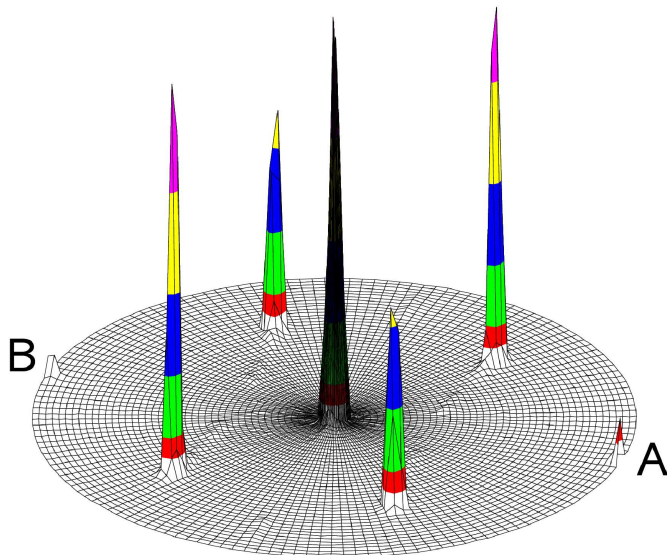


**Fig. 4.20.** Pole figure of a sample made on a (110)  $\text{TiO}_2$  substrate by a solid-solid reaction in air at 700 °C for 30 min. The pole figure was recorded at  $2\theta = 31.4^\circ$  ( $\text{BaTiO}_3 \{101\}$ ). The peaks are situated at  $\psi = 0^\circ, 60^\circ$  and  $90^\circ$  and thus correspond to a (110) orientation of  $\text{BaTiO}_3$ .

Such an orientation relationship was also observed for the samples after solid-solid reaction at temperatures between 600 °C and 900 °C in air. No tilted grains were found in the thin films. This is in contrast to the orientation of  $\text{BaTiO}_3$  grains grown by solid-solid reaction on (110) rutile substrates in vacuum.

### (100) $\text{TiO}_2$ (rutile)

The  $\text{BaTiO}_3$  grains grown on (100)  $\text{TiO}_2$  surfaces are also crystallographically well-oriented.

Fig. 4.21 gives the pole figure taken at  $2\theta = 31.4^\circ$  of the sample prepared on (100)  $\text{TiO}_2$  by a solid-solid reaction in vacuum at 700 °C for 30 min. The orientation relationship of  $\text{BaTiO}_3$  was found as:

$$(111) \text{BaTiO}_3 \parallel (100) \text{TiO}_2; [1\bar{1}0] \text{BaTiO}_3 \parallel [001] \text{TiO}_2. \quad (4.8)$$

Such an orientation relationship was also observed for the samples after solid-solid reaction at temperatures between 600 and 900 °C in vacuum and in air. Noticeably, the (111)  $\text{BaTiO}_3$  ( $2\theta = 38.8^\circ$ ) reflection could not be detected in XRD  $\theta$ - $2\theta$  scans because it is completely hidden by the strong  $\text{TiO}_2$  (200) peak ( $2\theta = 39.2^\circ$ ).

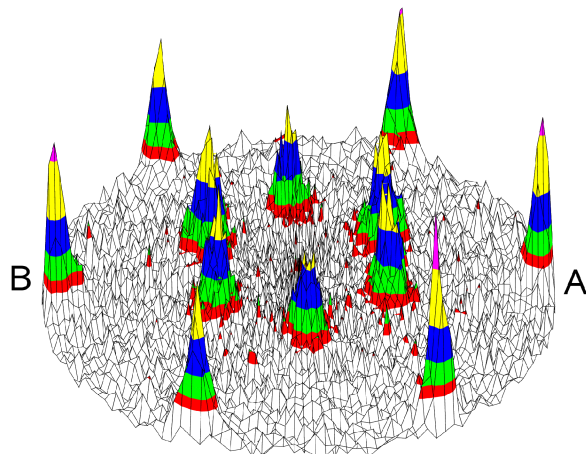


**Fig. 4.21.** Pole figure of a sample produced on a (100)  $\text{TiO}_2$  substrate by a solid-solid reaction at 700 °C. The peaks are situated at  $\psi = 35^\circ$  and  $90^\circ$  and thus correspond to a (111) orientation of  $\text{BaTiO}_3$ .

### Vapour-solid reaction

#### (110) $\text{TiO}_2$ (rutile)

After vapour-solid reaction, the  $\text{BaTiO}_3$  grains grew with a well-defined orientation with respect to the (110)  $\text{TiO}_2$  substrates. However, their tilt distribution is sharper compared to the solid-solid reaction in vacuum.

Figs. 4.22(a)-(b) give typical pole figures taken at  $2\theta = 31.4^\circ$  for samples prepared on (110)  $\text{TiO}_2$  at 800 °C and 900 °C, respectively. Compared to the reflections of  $\text{BaTiO}_3$  in Figs. 4.19(a)-(c), the peaks from the  $\text{BaTiO}_3$  {101} planes in Figs. 4.22(a)-(b) are stronger and sharper, indicating the growth of  $\text{BaTiO}_3$  grains with well-defined orientations.

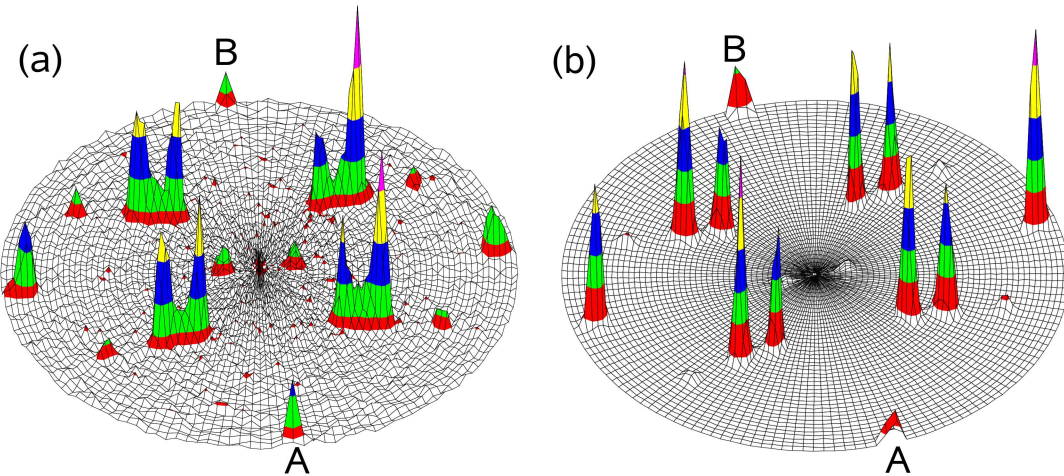


**Fig. 4.22.** Pole figures of samples made on (110)  $\text{TiO}_2$  substrates by a vapour-solid reaction at: (a) 800 °C and (b) 900 °C. The figures were taken at  $2\theta = 31.4^\circ$  ( $\text{BaTiO}_3$  {101}). The peaks are situated at  $\psi = 11^\circ$ ,  $40^\circ$ ,  $50^\circ$ ,  $70^\circ$ ,  $82^\circ$  and  $90^\circ$  in the Figs. (a)-(b), while there are additional reflections at  $\psi = 45^\circ$  in Fig. (a). The  $\psi$  values of  $40^\circ$ ,  $50^\circ$ ,  $82^\circ$  and  $90^\circ$  correspond to a (119) orientation of  $\text{BaTiO}_3$  while the  $\psi$  values of  $11^\circ$ ,  $50^\circ$ ,  $70^\circ$  and  $90^\circ$  correspond to a (441) orientation of  $\text{BaTiO}_3$  and the  $\psi$  value of  $45^\circ$  corresponds to a (001) orientation of  $\text{BaTiO}_3$ .

Fig. 4.23 gives a HRTEM image of an interface after vapour-solid reaction of  $\text{BaO}$  with (110)  $\text{TiO}_2$  in vacuum at 800 °C. The reaction interface is rough. Looking along the [001] direction of

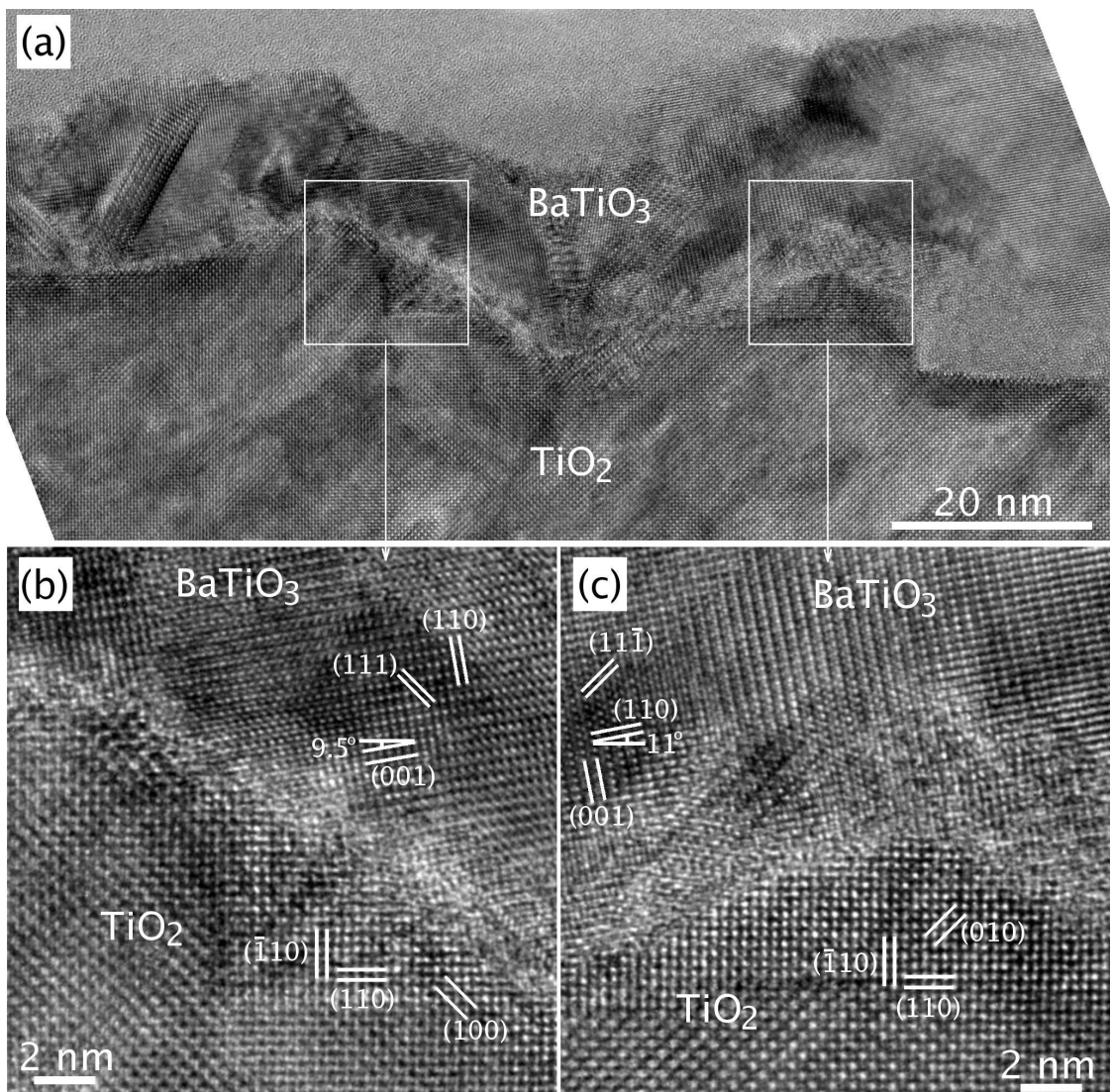


**Fig. 4.23.** HRTEM images of a sample made on a (110)  $\text{TiO}_2$  substrate by a vapour-solid reaction at 800 °C: (a) thin film-substrate interface, (b) and (c) lattice plane images of  $\text{BaTiO}_3$  grains and the substrate (magnified sections of image (a)). Viewing direction is  $[1\bar{1}0] \text{ BaTiO}_3 \parallel [001] \text{ TiO}_2$ .

$\text{TiO}_2$ , (100), (010), (110) and  $(\bar{1}10)$   $\text{TiO}_2$  facets are seen. The orientation relationships of  $\text{BaTiO}_3$  found by HRTEM (Fig. 4.23) as well as by pole figure measurements (Fig. 4.22) are: (119)  $\text{BaTiO}_3 \parallel (110) \text{ TiO}_2$  (major) and (441)  $\text{BaTiO}_3 \parallel (110) \text{ TiO}_2$  (minor). It should be noted that the (441) orientation of  $\text{BaTiO}_3$  is rather close to the (331) orientation of  $\text{BaTiO}_3$  ( $\angle(441);(331) \text{ BaTiO}_3 = 3.24^\circ$ ). HRTEM investigations (Figs. 4.23(b)-(c)) showed that (119)- and (441)-oriented  $\text{BaTiO}_3$  grains are located on (100) and (010) facets of  $\text{TiO}_2$ , respectively. Both orientations can be understood as a result of a systematic tilt around a unique tilt axis starting from low index orientations with (001)  $\text{BaTiO}_3 \parallel (110) \text{ TiO}_2$  ( $\angle \text{BaTiO}_3 (001);(119) = 8.9^\circ$ , see also Fig. 4.23(b)) and (110)  $\text{BaTiO}_3 \parallel (110) \text{ TiO}_2$  ( $\angle \text{BaTiO}_3 (110);(441) = 10^\circ$ , see also Fig. 4.23(c)), respectively. It is worth to note that the (119) and (441) orientations of  $\text{BaTiO}_3$  have one of the  $\{111\}$   $\text{BaTiO}_3$  planes almost parallel to one of the  $\{100\}$   $\text{TiO}_2$  planes in the viewing direction  $[1\bar{1}0] \text{ BaTiO}_3 \parallel [001] \text{ TiO}_2$ :  $\angle \text{BaTiO}_3 (119);(111) = 45.8^\circ$  and  $\angle \text{BaTiO}_3 (441);(11\bar{1}) = 45.3^\circ$  while  $\angle \text{TiO}_2 (110);(100) = 45^\circ$  and  $\angle \text{TiO}_2 (110);(010) = 45^\circ$ . This is in agreement with HRTEM observations. The main (119)

orientation of  $\text{BaTiO}_3$  deviates from the minor (441) one by a tilt of  $71^\circ$  around the  $[1\bar{1}0] \text{ BaTiO}_3 \parallel [001] \text{ TiO}_2$  tilt axis. In addition, pole figure measurements revealed a second minor orientation of  $\text{BaTiO}_3$  at  $800^\circ\text{C}$  as  $(001) \text{ BaTiO}_3 \parallel (110) \text{ TiO}_2$ .

After vapour-solid reaction at  $900^\circ\text{C}$ ,  $\text{BaTiO}_3$  grains were found on top of  $\text{Ba}_6\text{Ti}_{17}\text{O}_{40}$  grains. They formed exactly with  $(119) \text{ BaTiO}_3 \parallel (110) \text{ TiO}_2$  (major) and  $(441) \text{ BaTiO}_3 \parallel (110) \text{ TiO}_2$  (minor) orientations as was found by pole figure measurements (Fig. 4.22(b)). The in-plane orientation relationship was found to be  $[1\bar{1}0] \text{ BaTiO}_3 \parallel [001] \text{ TiO}_2$  for all these orientations.

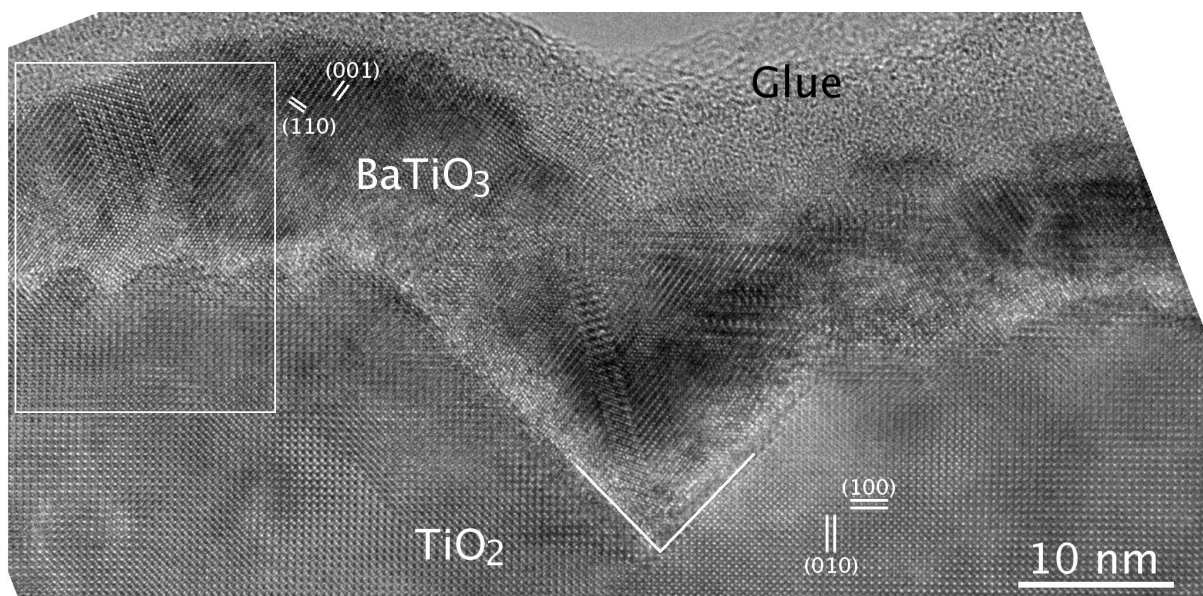
Fig. 4.9 shows a HRTEM image of the interface region after the reaction between a  $\text{BaO}$  vapour and a  $(110) \text{ TiO}_2$  (rutile) substrate of a sample prepared at a substrate temperature of  $900^\circ\text{C}$ . The reaction layer consisted of  $\text{BaTiO}_3$  and  $\text{Ba}_6\text{Ti}_{17}\text{O}_{40}$  grains. The latter were located between the  $\text{TiO}_2$  substrate and the  $\text{BaTiO}_3$  phase. The crystallographic orientation relationship found by HRTEM (Fig. 4.10) between the  $\text{BaTiO}_3$  and  $\text{Ba}_6\text{Ti}_{17}\text{O}_{40}$  grains was:

$$(001) \text{ Ba}_6\text{Ti}_{17}\text{O}_{40} \parallel (111) \text{ BaTiO}_3; [010] \text{ Ba}_6\text{Ti}_{17}\text{O}_{40} \parallel [1\bar{1}0] \text{ BaTiO}_3. \quad (4.9)$$

This orientation relationship indicates a topotaxial reaction between  $\text{BaTiO}_3$  and  $\text{Ba}_6\text{Ti}_{17}\text{O}_{40}$  and is in agreement to the relation (2.23).

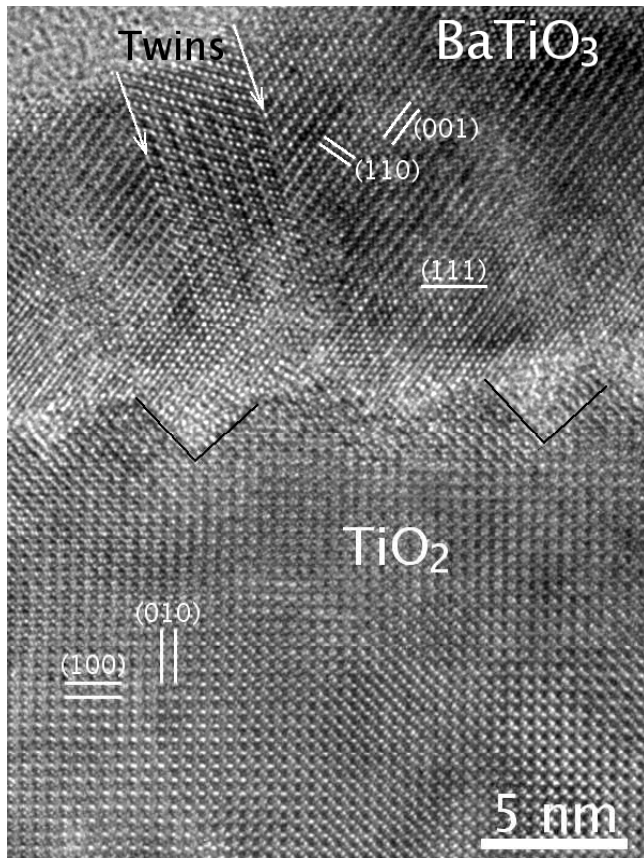
### (100) $\text{TiO}_2$ (rutile)

Fig. 4.24 shows a HRTEM image of the interface region between a  $\text{BaTiO}_3$  thin film and a  $(100) \text{ TiO}_2$  substrate of a sample made after vapour-solid reaction at  $700^\circ\text{C}$ . In Fig. 4.24, the interface between the thin film and the substrate is not flat. Large  $(110)$  and  $(1\bar{1}0)$  rutile facets are clearly visible.



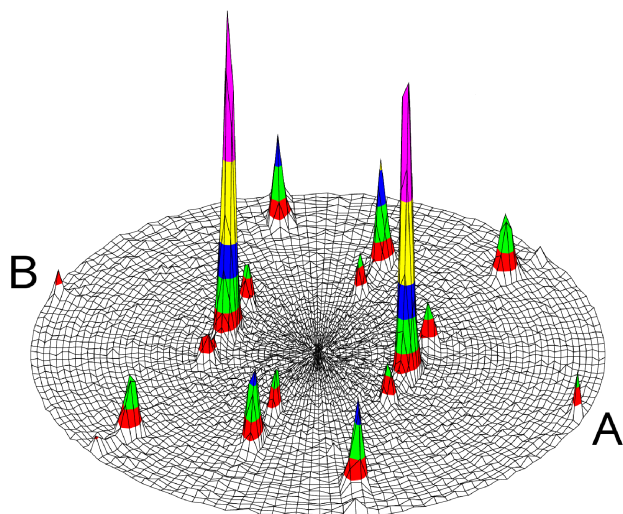
**Fig. 4.24.** HRTEM micrograph of a sample made after vapour-solid reaction on  $(100) \text{ TiO}_2$  at  $700^\circ\text{C}$ . Large  $(110)$  and  $(1\bar{1}0)$   $\text{TiO}_2$  facets were formed after the reaction (marked by white lines). Viewing direction is  $[1\bar{1}0] \text{ BaTiO}_3 \parallel [001] \text{ TiO}_2$ . A TEM image taken from a larger area by conventional TEM can be seen in the appendix, Fig. A.9.

Fig. 4.25 shows lattice plane images of  $\text{BaTiO}_3$  grains and a  $\text{TiO}_2$  substrate. From Fig. 4.25, it was found that the  $\text{BaTiO}_3$  grains grew according to the relation (4.8). In addition,  $(11\bar{1})$  twins were found within  $\text{BaTiO}_3$  grains.



**Fig. 4.25.** Lattice plane images of  $\text{BaTiO}_3$  in the  $[1\bar{1}0]$  viewing direction and the  $\text{TiO}_2$  substrate in the  $[001]$  viewing direction (magnified image of the white box shown in Fig. 4.24). Small  $(110)$  and  $(1\bar{1}0)$   $\text{TiO}_2$  facets are marked by black lines.  $(11\bar{1})$  twins in  $\text{BaTiO}_3$  were also observed.

A XRD  $\theta$ - $2\theta$  scan of the sample made on (100)  $\text{TiO}_2$  substrate by vapour-solid reaction at 800 °C showed the appearance of the characteristic reflection of (112)  $\text{BaTiO}_3$  ( $2\theta = 56.2^\circ$ ) beside the substrate reflections which means that the (112) plane of  $\text{BaTiO}_3$  is parallel to the (100) substrate plane. Fig. 4.26 gives a pole figure for a sample prepared by vapour-solid reaction at 800 °C using (100)  $\text{TiO}_2$  substrate. At this temperature two orientation relations for  $\text{BaTiO}_3$  were found.



**Fig. 4.26.** Pole figure of a sample grown on a (100)  $\text{TiO}_2$  substrate by a vapour-solid reaction at 800 °C. The figure was recorded at  $2\theta = 31.4^\circ$  ( $\text{BaTiO}_3 \{101\}$ ). The peaks are situated at  $\psi = 30^\circ, 55^\circ, 74^\circ$  and  $90^\circ$ .

While the peaks in Fig. 4.26 at  $\psi = 30^\circ, 55^\circ, 74^\circ$  and  $90^\circ$  are from the major orientation relationship  $(112) \text{ BaTiO}_3 \parallel (100) \text{ TiO}_2$  those at  $\psi = 0^\circ, 35^\circ$  and  $90^\circ$  are from the minor orientation relationship  $(111) \text{ BaTiO}_3 \parallel (100) \text{ TiO}_2$ . The in-plane orientation relationship is found to be  $[1\bar{1}0] \text{ BaTiO}_3 \parallel [001] \text{ TiO}_2$  for all these orientations. The main  $(112)$  orientation of  $\text{BaTiO}_3$  deviates from the minor  $(111)$  one by a tilt of  $19.5^\circ$  around the  $[1\bar{1}0] \text{ BaTiO}_3 \parallel [001] \text{ TiO}_2$  tilt axis.

Fig. 4.27(a) shows a cross sectional bright field TEM image of a reaction layer prepared by vapour-solid reaction on a  $(100)$   $\text{TiO}_2$  substrate at  $800$   $^\circ\text{C}$ . In Fig. 4.27(a), the interface between the thin film and the substrate is rough and faceted. Well-oriented  $\text{BaTiO}_3$  grains were formed after the reaction. This was confirmed by selected area electron diffraction (Fig. 4.27(b)). The  $(112)$  orientation relationship of  $\text{BaTiO}_3$  found by XRD texture measurements is in agreement with the one deduced by selected area electron diffraction (Fig. 4.27(b)).

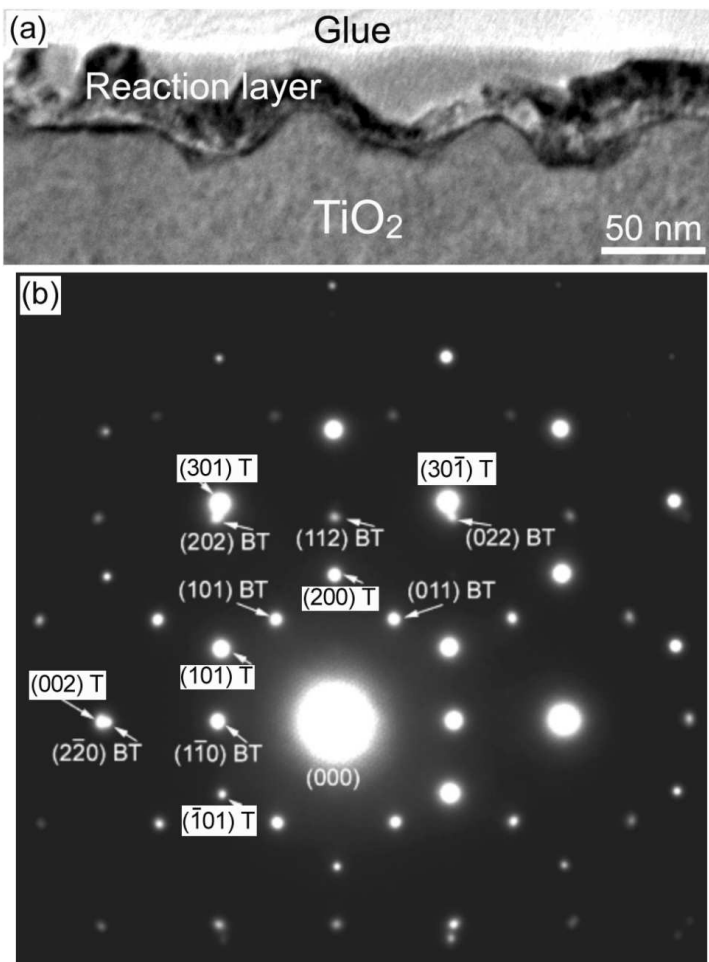


**Fig. 4.27.** (a) Bright-field TEM image of a reaction layer formed by vapour-solid reaction on the  $(100)$  rutile surface at  $800$   $^\circ\text{C}$ , and (b) electron diffraction pattern taken from the surface region between the rutile substrate (T) and the reaction layer. Well-oriented  $\text{BaTiO}_3$  (BT) grains were found in the thin film. Viewing direction is  $[11\bar{1}] \text{ BaTiO}_3 \parallel [010] \text{ TiO}_2$ .

Fig. 4.28 shows a HRTEM image of the interface region after the reaction between a  $\text{BaO}$  vapour and the  $(100)$   $\text{TiO}_2$  (rutile) single crystal of a sample prepared at a substrate temperature of  $900$   $^\circ\text{C}$ . The reaction layer consists of  $\text{BaTiO}_3$  and  $\text{Ba}_6\text{Ti}_{17}\text{O}_{40}$  grains. The latter were again observed between the  $\text{TiO}_2$  substrate and the  $\text{BaTiO}_3$  phase. The crystallographic orientation relationship found by HRTEM between the  $\text{BaTiO}_3$  and  $\text{Ba}_6\text{Ti}_{17}\text{O}_{40}$  grains corresponds to the relation (4.9).

The  $\text{BaTiO}_3$  grains have also a well-defined orientation to the  $(100)$   $\text{TiO}_2$  substrate. Several orientations of the  $\text{BaTiO}_3$  phase were found by XRD pole figures and HRTEM investigations

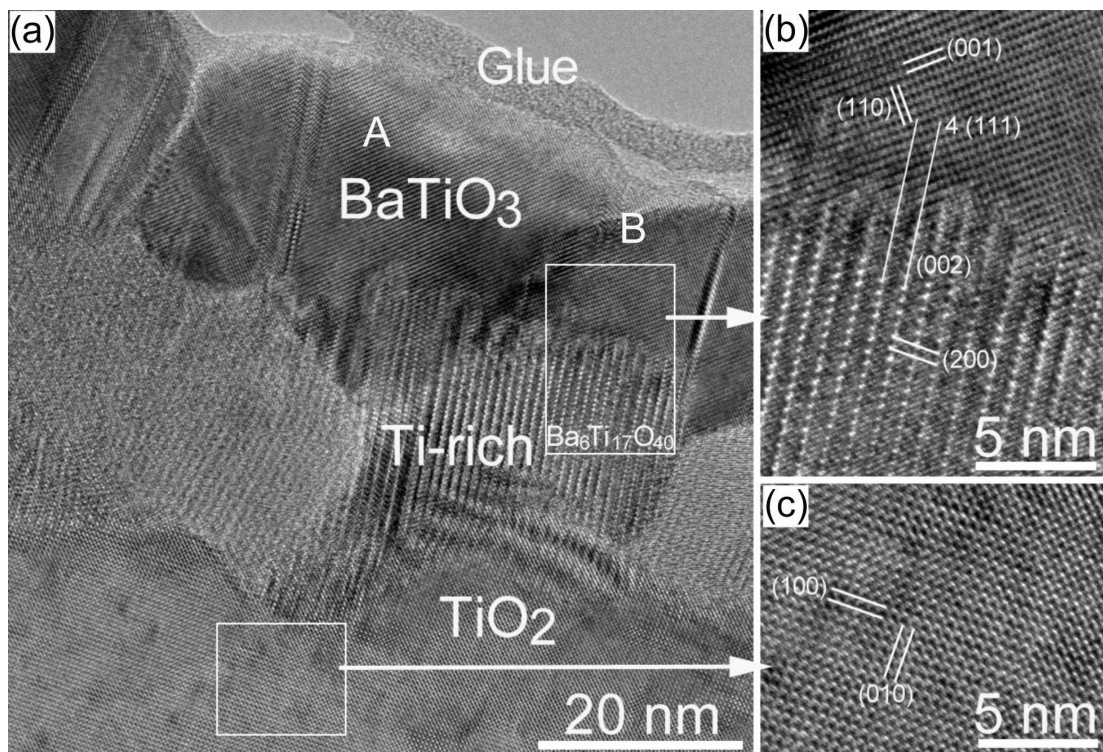


**Fig. 4.28.** HRTEM cross-section images of reaction products grown between  $\text{BaO}$  vapour and (100)  $\text{TiO}_2$  at 900 °C: (a) thin film-substrate interface; (b) lattice plane images of  $\text{BaTiO}_3$  and  $\text{Ba}_6\text{Ti}_{17}\text{O}_{40}$  grains and (c) the rutile substrate. The long white lines in image (b) mark the  $(001) \text{Ba}_6\text{Ti}_{17}\text{O}_{40} \parallel (111) \text{BaTiO}_3$  lattice planes. Viewing direction is  $[010] \text{Ba}_6\text{Ti}_{17}\text{O}_{40} \parallel [1\bar{1}0] \text{BaTiO}_3 \parallel [001] \text{TiO}_2$ .

at 900 °C. Fig. 4.29 gives a pole figure for a sample made at a substrate temperature of 900 °C. The observed orientations of  $\text{BaTiO}_3$  are: (223)  $\text{BaTiO}_3 \parallel (100) \text{TiO}_2$  (grain A in Fig. 4.28);

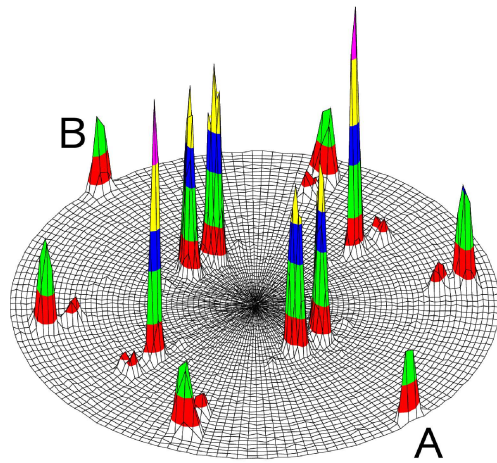


**Fig. 4.29.** Pole figure of a sample grown on a (100)  $\text{TiO}_2$  substrate by a vapour-solid reaction at 900 °C. The figure was taken at  $2\theta = 31.4^\circ$  ( $\text{BaTiO}_3 \{101\}$ ). The peaks are situated at  $\psi = 30^\circ, 35^\circ, 48^\circ, 60^\circ, 68^\circ, 78^\circ$  and  $90^\circ$ . The  $\psi$  values of  $30^\circ, 48^\circ, 78^\circ$  and  $90^\circ$  correspond to a (223) orientation of  $\text{BaTiO}_3$  while the  $\psi$  values of  $30^\circ, 60^\circ, 68^\circ$  and  $90^\circ$  correspond to a (225) orientation of  $\text{BaTiO}_3$  and the  $\psi$  values of  $35^\circ$  and  $90^\circ$  correspond to a (111) orientation of  $\text{BaTiO}_3$ .

(335)  $\text{BaTiO}_3 \parallel (100) \text{TiO}_2$  (grain B in Fig. 4.28); (225)  $\text{BaTiO}_3 \parallel (100) \text{TiO}_2$ ; (111)  $\text{BaTiO}_3 \parallel (100) \text{TiO}_2$ . The in-plane orientation relationship is found to be  $[1\bar{1}0] \text{BaTiO}_3 \parallel [001] \text{TiO}_2$  for all these orientations. The (223)  $\text{BaTiO}_3 \parallel (100) \text{TiO}_2$  and (335)  $\text{BaTiO}_3 \parallel (100) \text{TiO}_2$  orientations can be understood as a result of a systematic tilt around the  $[1\bar{1}0] \text{BaTiO}_3 \parallel [001] \text{TiO}_2$  tilt axis starting from the low-index orientation (111)  $\text{BaTiO}_3 \parallel (100) \text{TiO}_2$ :  $\angle \text{BaTiO}_3 (111); (223) = 11.4^\circ$ ,  $\angle \text{BaTiO}_3 (111); (335) = 14.4^\circ$ ,  $\angle \text{BaTiO}_3 (111); (225) = 25.2^\circ$ .

Table 4.1 summarises the orientation relationships and the misfit values for  $\text{BaTiO}_3$  grown on the (100) and (110)  $\text{TiO}_2$  substrates by solid-solid reaction in vacuum (ss(v)), solid-solid reaction in air (ss(a)) and vapour-solid reaction (vs) at different substrate temperatures. The misfits were calculated by using the equation adopted in the near-coincidence site lattice theory (NCSL):<sup>137,138</sup>

$$F = 2(nd_1 - md_2)/(nd_1 + md_2), \quad (4.10)$$

where  $d_1$  and  $d_2$  are lattice spacings of the two materials in the interface plane and  $n$  and  $m$  are integers.

**Table 4.1.** Orientation relationships and NCSL misfit values ( $F_1$  (in-plane) and  $F_2$  (in-plane rotated by  $90^\circ$ )) for  $\text{BaTiO}_3$  (BTO) thin films grown on (110) and (100)  $\text{TiO}_2$  rutile (T) substrates at different temperatures.

T, °C	Parallel planes	Parallel direction	$F_1$ , %	$F_2$ , %
(110) $\text{TiO}_2$ (rutile)				
ss(v)700–900& vs700 – 800	(001) BTO  (110) T	[1̄10] BTO  [001] T	$2(8d(001)\text{BTO} - 7d(\bar{1}10)\text{T})/(8d(001)\text{BTO} + 7d(\bar{1}10)\text{T}) = -0.2$	$2(d(1\bar{1}0)\text{BTO} - d(001)\text{T})/(d(1\bar{1}0)\text{BTO} + d(001)\text{T}) = -4.1$
ss(v)800–900& vs700 – 900	(119) BTO  (110) T	[1̄10] BTO  [001] T	$2(10d(99\bar{2})\text{BTO} - d(\bar{1}10)\text{T})/(10d(99\bar{2})\text{BTO} + d(\bar{1}10)\text{T}) = -4.3$	$2(d(1\bar{1}0)\text{BTO} - d(001)\text{T})/(d(1\bar{1}0)\text{BTO} + d(001)\text{T}) = -4.1$
ss(v)800–900& vs800 – 900	(441) BTO  (110) T	[1̄10] BTO  [001] T	$2(7d(11\bar{8})\text{BTO} - d(\bar{1}10)\text{T})/(7d(11\bar{8})\text{BTO} + d(\bar{1}10)\text{T}) = +6.1$	$2(d(1\bar{1}0)\text{BTO} - d(001)\text{T})/(d(1\bar{1}0)\text{BTO} + d(001)\text{T}) = -4.1$
ss(v)800–900& ss(a)700 – 900	(110) BTO  (110) T	[1̄10] BTO  [001] T	$2(4d(001)\text{BTO} - 5d(\bar{1}10)\text{T})/(4d(001)\text{BTO} + 5d(\bar{1}10)\text{T}) = -1.2$	$2(d(1\bar{1}0)\text{BTO} - d(001)\text{T})/(d(1\bar{1}0)\text{BTO} + d(001)\text{T}) = -4.1$
(100) $\text{TiO}_2$ (rutile)				
ss(v&a)&vs 700 – 900	(111) BTO  (100) T	[1̄10] BTO  [001] T	$2(3d(11\bar{2})\text{BTO} - d(010)\text{T})/(3d(11\bar{2})\text{BTO} + d(010)\text{T}) = +6.9$	$2(d(1\bar{1}0)\text{BTO} - d(001)\text{T})/(d(1\bar{1}0)\text{BTO} + d(001)\text{T}) = -4.1$
vs800	(112) BTO  (100) T	[1̄10] BTO  [001] T	$2(2d(11\bar{1}0)\text{BTO} - d(010)\text{T})/(2d(11\bar{1}0)\text{BTO} + d(010)\text{T}) = +0.7$	$2(d(1\bar{1}0)\text{BTO} - d(010)\text{T})/(d(1\bar{1}0)\text{BTO} + d(010)\text{T}) = -4.1$
vs900	(223) BTO  (100) T	[1̄10] BTO  [001] T	$2(7d(33\bar{4})\text{BTO} - d(010)\text{T})/(7d(33\bar{4})\text{BTO} + d(010)\text{T}) = +4.7$	$2(d(1\bar{1}0)\text{BTO} - d(001)\text{T})/(d(1\bar{1}0)\text{BTO} + d(001)\text{T}) = -4.1$
	(335) BTO  (100) T	[1̄10] BTO  [001] T	$2(10d(55\bar{6})\text{BTO} - d(010)\text{T})/(10d(55\bar{6})\text{BTO} + d(010)\text{T}) = -6$	$2(d(1\bar{1}0)\text{BTO} - d(001)\text{T})/(d(1\bar{1}0)\text{BTO} + d(001)\text{T}) = -4.1$
	(225) BTO  (100) T	[1̄10] BTO  [001] T	$2(9d(55\bar{4})\text{BTO} - d(010)\text{T})/(9d(55\bar{4})\text{BTO} + d(010)\text{T}) = -3.6$	$2(d(1\bar{1}0)\text{BTO} - d(001)\text{T})/(d(1\bar{1}0)\text{BTO} + d(001)\text{T}) = -4.1$

Most remarkably, the relation  $[1\bar{1}0] \text{BaTiO}_3 \parallel [001] \text{TiO}_2$  holds for all the different orientation relationships in Table 4.1, independently of the experimental conditions and substrate orientation. The various orientation relationships differ from each other by a tilt around the  $[1\bar{1}0] \text{BaTiO}_3 \parallel [001] \text{TiO}_2$  axis. The parallel orientation of the  $(1\bar{1}0)$  plane of  $\text{BaTiO}_3$  to the  $(001)$  plane of  $\text{TiO}_2$  (rutile) seems thus to be the principal orientation relation in this system.

### C. Orientations of Ti-rich phases

Ti-rich phases were identified after both types of solid state reactions at high reaction temperatures in vacuum and in air but with quite different textures. At 1000 °C, a polycrystalline  $\text{BaTi}_4\text{O}_9$  phase was formed after the solid-solid reaction in vacuum while a polycrystalline  $\text{Ba}_4\text{Ti}_{13}\text{O}_{30}$  phase with fiber texture was grown after the reaction in air at temperatures between 900 °C (see Fig. A.10 in the appendix) and 1000 °C. The XRD pattern showed all reflections of the  $\text{Ba}_4\text{Ti}_{13}\text{O}_{30}$  phase as in the standard powder diffractogram but the intensity relations of the peaks were changed due to a preferred orientation of the  $\text{Ba}_4\text{Ti}_{13}\text{O}_{30}$  phase.

Contrary to the solid-solid reaction, a vapour-solid reaction at 900 °C and 1000 °C produced well-oriented  $\text{Ba}_6\text{Ti}_{17}\text{O}_{40}$  grains on both (110) and (100)  $\text{TiO}_2$  (rutile) surfaces. The examples for 900 °C are shown in Figs. 4.14-4.16, A.8 and 4.28. The crystallographic orientation relationship found by HRTEM between the  $\text{TiO}_2$  substrates and the  $\text{Ba}_6\text{Ti}_{17}\text{O}_{40}$  grains can be written as:

$$(001) \text{ Ba}_6\text{Ti}_{17}\text{O}_{40} \parallel (010) \text{ TiO}_2; [010] \text{ Ba}_6\text{Ti}_{17}\text{O}_{40} \parallel [001] \text{ TiO}_2, \quad (4.11)$$

which is, however, not exactly fulfilled. By analysing many HRTEM images, it was found that the (001) plane of  $\text{Ba}_6\text{Ti}_{17}\text{O}_{40}$  can form an angle between 0° and  $\approx 6^\circ$  with the (010) plane of the substrate for Ti-rich grains grown on (110)  $\text{TiO}_2$ , and between 0° and  $\approx 9^\circ$  with the (010) plane of the substrate for Ti-rich grains grown on (100)  $\text{TiO}_2$ . Thus, a deviation (tilt) from 0° to  $\approx 9^\circ$  around the  $[010] \text{ Ba}_6\text{Ti}_{17}\text{O}_{40} \parallel [001] \text{ TiO}_2$  tilt axis is possible for  $\text{Ba}_6\text{Ti}_{17}\text{O}_{40}$  grains in the above orientation.

Because of the monoclinic distortion of the  $\text{Ba}_6\text{Ti}_{17}\text{O}_{40}$  unit cell, there is no low-index plane exactly parallel to the substrate surface plane (110)  $\text{TiO}_2$ . However, from HRTEM and FFT images it was found that the (102) plane of  $\text{Ba}_6\text{Ti}_{17}\text{O}_{40}$  can approximately be parallel to (110)  $\text{TiO}_2$ . The angle between the (102) and (001) planes of  $\text{Ba}_6\text{Ti}_{17}\text{O}_{40}$  is  $47.88^\circ$  in the [010] viewing direction of  $\text{Ba}_6\text{Ti}_{17}\text{O}_{40}$ , whereas the angle between (110) and (010) planes of  $\text{TiO}_2$  is  $45^\circ$  in the [001] viewing direction of  $\text{TiO}_2$ . The orientation of the (001)  $\text{Ba}_6\text{Ti}_{17}\text{O}_{40}$  plane parallel to one of the {010}  $\text{TiO}_2$  planes in the viewing direction  $[010] \text{ Ba}_6\text{Ti}_{17}\text{O}_{40} \parallel [001] \text{ TiO}_2$  results in two positions (growth twins) of the  $\text{Ba}_6\text{Ti}_{17}\text{O}_{40}$  grains on the (110)  $\text{TiO}_2$  surface (see Fig. 4.9). Thus, there are two subsets of  $\text{Ba}_6\text{Ti}_{17}\text{O}_{40}$  grains belonging to two different (010) and (100) planes of  $\text{TiO}_2$ , any of which has the (102) plane of  $\text{Ba}_6\text{Ti}_{17}\text{O}_{40}$  almost parallel to (110)  $\text{TiO}_2$ . In the case of a (100)  $\text{TiO}_2$  surface, it was found that the (100) plane of  $\text{Ba}_6\text{Ti}_{17}\text{O}_{40}$  can approximately be parallel to the rutile surface.

## 4.2 Solid state reactions of $\text{BaCO}_3$ and $\text{BaO}$ with $\text{TiO}_2$ (anatase)

### 4.2.1 Epitaxial growth of $\text{TiO}_2$ anatase thin films

$\text{TiO}_2$  (anatase) single crystals are more difficult to obtain with appropriate size than rutile.<sup>40,140–142</sup> This problem has been addressed by growing epitaxial  $\text{TiO}_2$  (anatase) thin films<sup>143</sup> or by using mineral samples.<sup>144</sup> Epitaxial  $\text{TiO}_2$  (anatase) films could be prepared by several physical and chemical deposition techniques. Various substrates with different lattice misfits were used. Yamamoto *et al.* have used pulsed laser deposition (PLD) to grow  $\text{TiO}_2$  thin films on  $\text{SrTiO}_3$ ,  $\text{LaAlO}_3$  and Y-stabilised  $\text{ZrO}_2$  substrates.<sup>145</sup> They found that no epitaxial  $\text{TiO}_2$  thin films can be obtained on (110)  $\text{SrTiO}_3$  and (110)  $\text{LaAlO}_3$ . (001)  $\text{TiO}_2$  (anatase) films can be grown on (100)  $\text{SrTiO}_3$  even at a substrate temperature of 1000 °C.<sup>146</sup> Single crystal epitaxial (001)  $\text{TiO}_2$  (anatase) films were also obtained on (100)  $\text{LaAlO}_3$  by PLD.<sup>147</sup> Thus, only the (001) crystallographic surface of anatase can be grown by PLD with high quality.

The deposition of  $\text{TiO}_2$  thin films on fused silica and titanium-coated fused silica by reactive electron beam evaporation has been reported previously.<sup>148</sup> The structure and properties of thin films under different conditions such as oxygen partial pressure and substrate temperature were investigated. The structure of the obtained film depends on the oxygen partial pressure and on the substrate used.

In this Ph.D. work, the growth of epitaxial  $\text{TiO}_2$  thin films was carried out by reactive electron beam evaporation of titanium (IV) oxide ( $\text{TiO}_2$ ) powder tablets (Merck, Germany) as described in **Chapter 3**. The influence of substrate orientation and substrate temperature on formation and phase contents of  $\text{TiO}_2$  films is investigated. The typical thicknesses of the thin films were  $\approx 100$  nm and  $\approx 200$  nm. The substrates were heated to temperatures between 400 °C and 1200 °C during deposition. After deposition the samples were kept in the vacuum chamber and allowed to cool to room temperature.

One-side polished (100) and (110) surfaces of commercial  $\text{SrTiO}_3$  as well as (100) and (110) surfaces of  $\text{LaAlO}_3$  single crystals were used as substrate materials. Before the experiments the (100)  $\text{SrTiO}_3$  substrates were chemically cleaned in buffered HF solution and thermally treated in air at 950 °C. (110)  $\text{SrTiO}_3$  substrates were heated in air at 1100 °C for 60 min while (100) and (110)  $\text{LaAlO}_3$  were thermally treated in air at 900 °C for 10 min.

#### A. $\text{TiO}_2$ film growth on (100) $\text{SrTiO}_3$ and (100) $\text{LaAlO}_3$

Pure  $\text{TiO}_2$  (anatase) thin films were obtained on (100)  $\text{SrTiO}_3$  and (100)  $\text{LaAlO}_3$  substrates at substrate temperatures ranging from 500 °C to 1000 °C. XRD  $\theta$ - $2\theta$  scans (Fig. 4.30) and pole figure measurements revealed the epitaxial nature of the  $\text{TiO}_2$  (anatase) films.

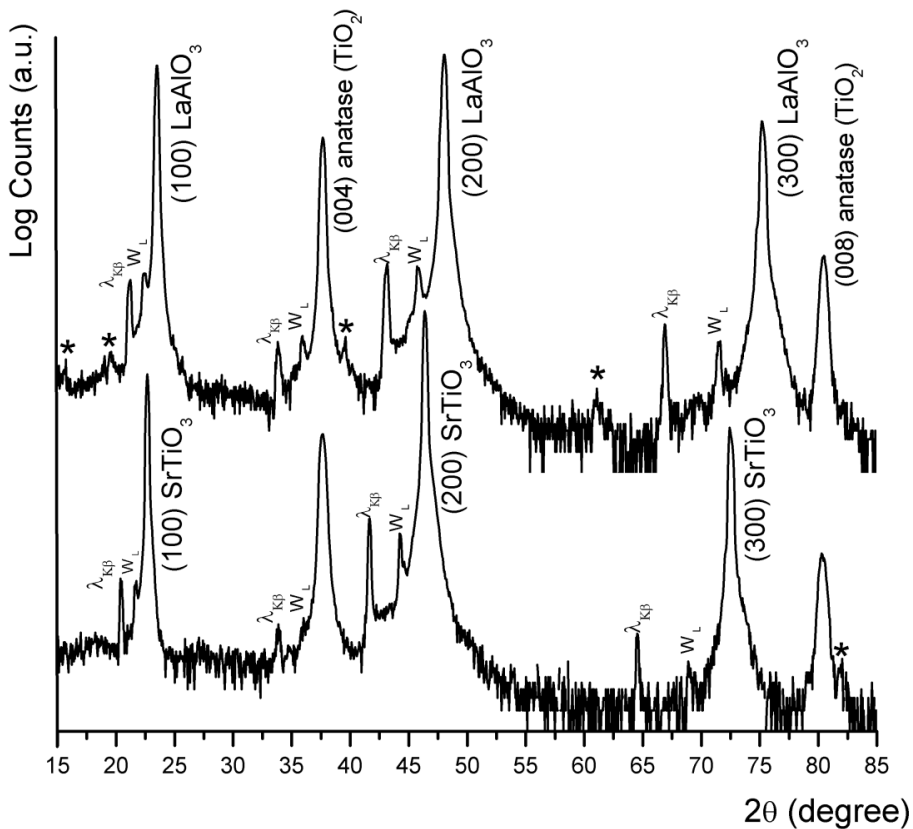


**Fig. 4.30.** XRD  $\theta$ - $2\theta$  scans of epitaxial  $\text{TiO}_2$  (anatase) thin films grown on (100)  $\text{SrTiO}_3$  and (100)  $\text{LaAlO}_3$  substrates. The films were deposited at  $700\text{ }^\circ\text{C}$ . The  $\lambda_{\text{K}\beta}$  lines are the substrate and thin film peaks originating from the remaining  $\text{Cu-K}\beta$  radiation, and the  $W_L$  lines are coming from the tungsten contamination of the X-ray target by the tungsten cathode filament. The peaks marked by "\*" characters are substrate-induced artefacts.

Fig. 4.31 shows a TEM micrograph of the film made on (100)  $\text{SrTiO}_3$  at a substrate temperature of  $600\text{ }^\circ\text{C}$ . Columnar grains are clearly seen in the film.

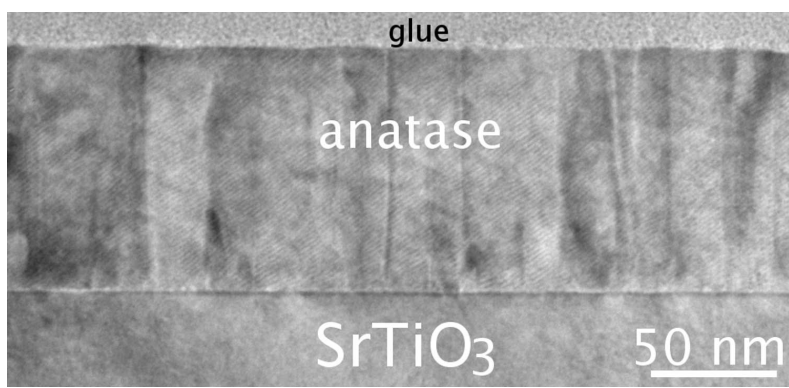


**Fig. 4.31.** Cross-sectional TEM micrograph of a  $\text{TiO}_2$  (anatase) thin film grown on (100)  $\text{SrTiO}_3$  at  $600\text{ }^\circ\text{C}$ .

HRTEM images of the  $\text{TiO}_2$  (anatase)/ $\text{SrTiO}_3$  interface are shown in Fig. 4.32. The interface between substrate and film is sharp. Low angle grain boundaries are seen in the film showing a rather perfect microstructure of the  $\text{TiO}_2$  (anatase) film ( $\text{TiO}_2$  (a)). The epitaxial orientation relationship obtained from TEM and XRD investigations is:

$$(001) \text{TiO}_2 \text{ (a)} \parallel (100) \text{SrTiO}_3; [100] \text{TiO}_2 \text{ (a)} \parallel [001] \text{SrTiO}_3. \quad (4.12)$$

This orientation relationship was also observed on (100)  $\text{LaAlO}_3$ .

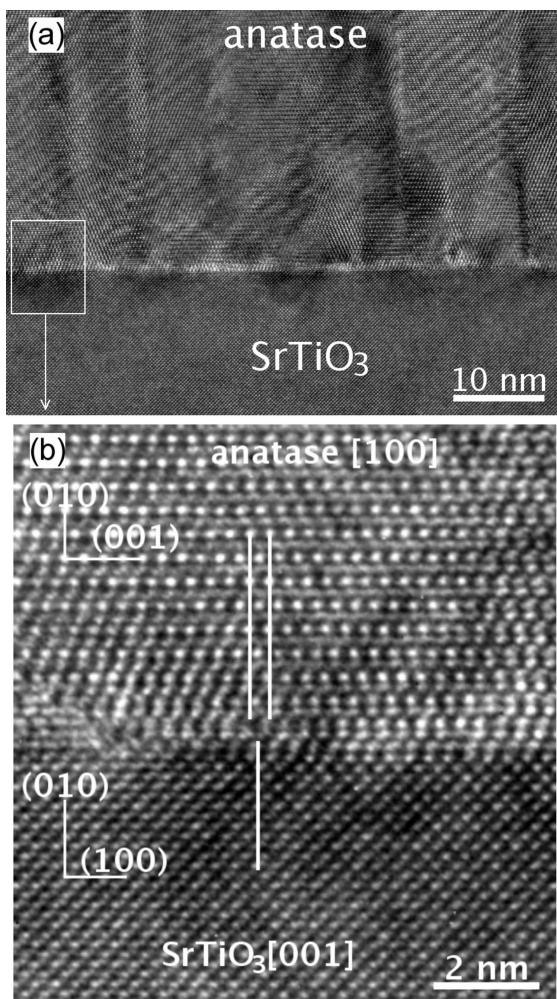


**Fig. 4.32.** HRTEM images of an anatase thin film grown at 600 °C: (a) overview of the (001)  $\text{TiO}_2$  (anatase)/(100)  $\text{SrTiO}_3$  interface and (b) lattice plane image of the  $\text{TiO}_2$  (anatase) and the substrate. A misfit dislocation is marked by white lines.

The crystal quality of the prepared  $\text{TiO}_2$  (anatase) thin films was analysed by rocking curves. The corresponding full-width at half maximum (FWHM) values of the (004)  $\text{TiO}_2$  (anatase) peaks for the films prepared on (100)  $\text{SrTiO}_3$  at substrate temperatures up to 900 °C ranged from 0.54° to 0.69°. The FWHM of the  $K_\beta$  line of the (100)  $\text{SrTiO}_3$  substrate was 0.13°. At a substrate temperature of 1000 °C, a relatively broad peak, split into three peaks, was observed in the  $\theta$  scan which means that the  $\text{TiO}_2$  (anatase) film consisted of three kinds of tilted domains. For the thin films deposited on (100)  $\text{LaAlO}_3$ , the FWHM values of the rocking curves were about 0.2° showing a better crystallinity of the  $\text{TiO}_2$  (anatase) films grown on (100)  $\text{LaAlO}_3$  compared to those on (100)  $\text{SrTiO}_3$ . It should be noted that  $\text{LaAlO}_3$  substrates usually consist of several twin domains. The rocking curve of the (200)  $\text{LaAlO}_3$  peak measured by high-resolution XRD with a Ge (220) monochromator showed a broad peak and the FWHM was estimated to be about 0.1°.

AFM images of thin films deposited on (100)  $\text{SrTiO}_3$  and (100)  $\text{LaAlO}_3$  at a substrate temperature of 800 °C are shown in Figs. 4.33(a)-(b), respectively. The surface morphology shows an average island diameter of about 180 nm in Fig. 4.33(a), and of about 450 nm in Fig. 4.33(b). The islands in Figs. 4.33(a)-(b) are square-shaped. The surface of each island consists of spiral terraces due to a spiral growth mechanism.

To study the stability of  $\text{TiO}_2$  (anatase) thin films made on (100)  $\text{SrTiO}_3$ , a film deposited on

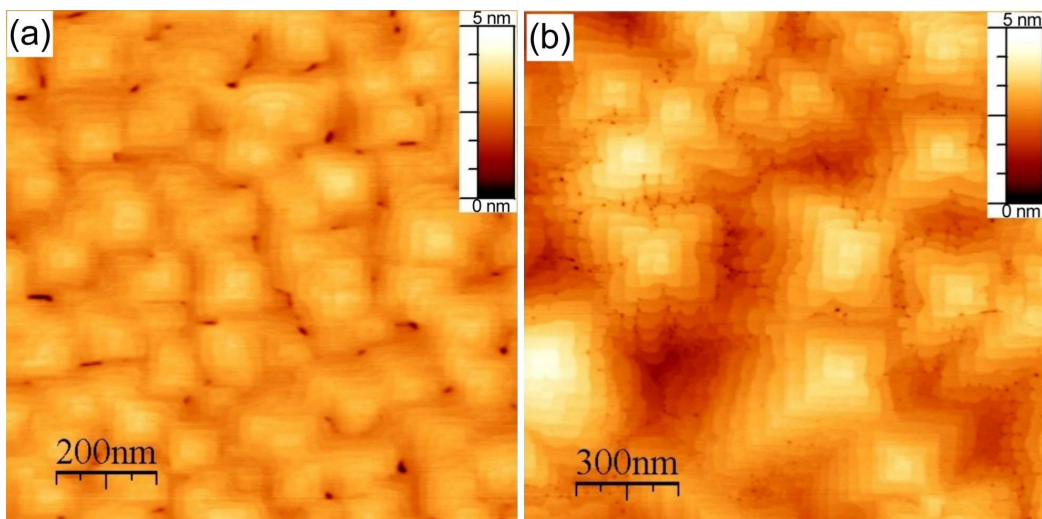


**Fig. 4.33.** AFM images of (001)  $\text{TiO}_2$  (anatase) thin films grown on (a) (100)  $\text{SrTiO}_3$  and (b) (100)  $\text{LaAlO}_3$  at a substrate temperature of 800 °C.

the  $\text{SrTiO}_3$  at a substrate temperature of 800 °C was annealed in air or in vacuum at 900 °C for 60 min. After this postannealing step, XRD analysis showed that no transformation from the anatase structure to the rutile structure had occurred.

At a substrate temperature of 1100 °C the films grown on (100)  $\text{SrTiO}_3$  consisted of a mixture of (110)  $\text{TiO}_2$  (rutile) and (001)  $\text{TiO}_2$  (anatase) grains. A splitting of the {101}  $\text{TiO}_2$  (anatase) peaks in pole figures into two peaks occurred, which means that the  $\text{TiO}_2$  (anatase) film consisted of two kinds of tilted domains.

## B. $\text{TiO}_2$ film growth on (110) $\text{SrTiO}_3$ and (110) $\text{LaAlO}_3$

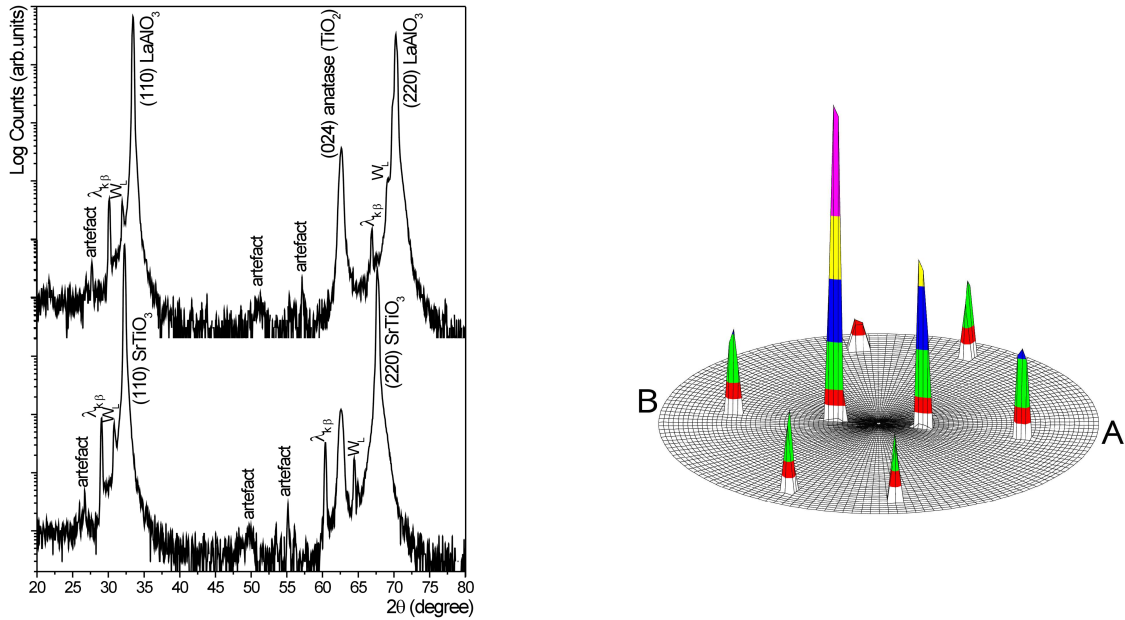
In the case of (110)  $\text{SrTiO}_3$  and (110)  $\text{LaAlO}_3$ , pure epitaxial  $\text{TiO}_2$  (anatase) films were obtained at substrate temperatures between 500 °C and 750 °C, and 500 °C and 900 °C, respectively.

Fig. 4.34(left) shows XRD  $\theta$ -2 $\theta$  scans of epitaxial  $\text{TiO}_2$  (anatase) films grown at 700 °C on (110)  $\text{SrTiO}_3$  and (110)  $\text{LaAlO}_3$ . The peaks at 62.6° in Figs. 4.34(a)-(b) correspond to (024)  $\text{TiO}_2$ . Fig. 4.34(right) shows a pole figure recorded at fixed  $2\theta = 25.3^\circ$  of the sample grown on (110)  $\text{LaAlO}_3$  at a substrate temperature of 800 °C. The epitaxial orientation relationship between the thin film and (110)  $\text{LaAlO}_3$  is:

$$(012) \text{TiO}_2 \text{ (a)} \parallel (110) \text{LaAlO}_3; [100] \text{TiO}_2 \text{ (a)} \parallel [001] \text{LaAlO}_3. \quad (4.13)$$

This orientation relationship was also observed on (110)  $\text{SrTiO}_3$ .

In rocking curves of the  $\text{TiO}_2$  (anatase) films grown on (110)  $\text{SrTiO}_3$  the FWHM values of the (024)  $\text{TiO}_2$  (anatase) peak varied from 0.56° to 0.72°. The crystal quality of the films obtained on (110)  $\text{LaAlO}_3$  was better than on (110)  $\text{SrTiO}_3$ . The FWHM values of the (024)  $\text{TiO}_2$  (anatase) peak were 0.4° for the films prepared at substrate temperatures up to 700 °C and 0.2° for the films prepared at substrate temperatures higher than 800 °C, showing the good crystallinity of the thin films.



**Fig. 4.34.** (left) XRD  $\theta$ - $2\theta$  scans of epitaxial  $\text{TiO}_2$  (anatase) thin films grown on (110)  $\text{SrTiO}_3$  and (110)  $\text{LaAlO}_3$  substrates. The films were deposited at 700 °C. The  $\lambda_{K\beta}$  lines are the substrate and thin film peaks originating from the remaining Cu- $K\beta$  radiation, and the  $W_L$  lines are coming from the tungsten contamination of the X-ray target by the tungsten cathode filament. The "artefact" peaks are substrate-induced artefacts. (right) X-ray pole figure recorded at  $2\theta = 25.3^\circ$  ( $\{101\}$   $\text{TiO}_2$ ) of the  $\text{TiO}_2$  (anatase) film deposited on (110)  $\text{LaAlO}_3$  at 800 °C. Peaks are situated at  $\psi = 16^\circ, 61^\circ$  and  $75^\circ$  and correspond to a (012) orientation of  $\text{TiO}_2$  (anatase). The positions of marks A and B correspond to the  $\phi$  values of the (110) and (110) substrate planes, respectively.

Fig. 4.35 shows a HRTEM image of the film deposited on (110)  $\text{SrTiO}_3$  substrate at a substrate temperature of 700 °C. The above orientation relationship is in good agreement with the one de-

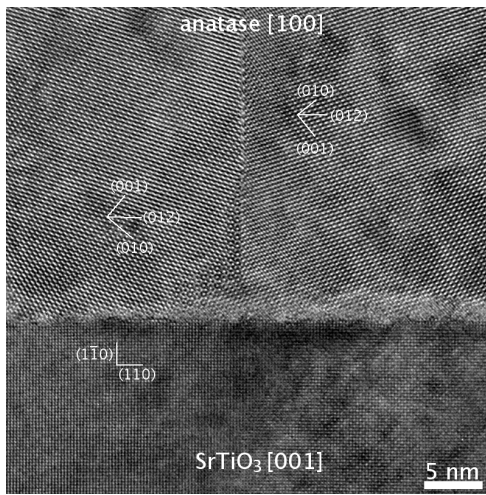


**Fig. 4.35.** HRTEM image of an epitaxial  $\text{TiO}_2$  (anatase) thin film grown on (110)  $\text{SrTiO}_3$  substrate at 700 °C. Magnified version of the image see in the appendix, Fig. A.11.

duced from HRTEM. Low angle grain boundaries are seen in the film showing a rather perfect microstructure of the anatase film.

The anatase film was converted into a cubic phase similar to  $\text{TiO}$  when extensively exposed to the 400 keV electron beam for a few minutes. Fig. 4.36 shows a HRTEM micrograph of a place after exposure of the anatase film under the electron beam for a few minutes. The film shows strong black and white contrast indicating the instability of the film under the electron beam.

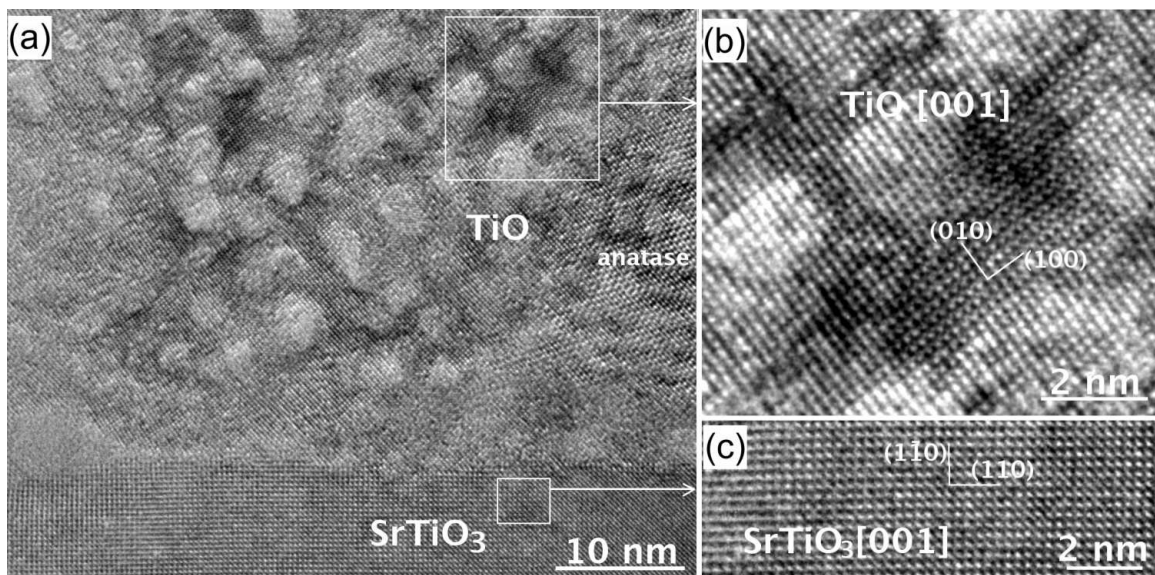


**Fig. 4.36.** TEM cross-section micrographs of  $\text{TiO}_2$  (anatase) film and (110)  $\text{SrTiO}_3$  substrate after extended exposure to the electron beam: (a) interface between the damaged film and (110)  $\text{SrTiO}_3$ ; (b) and (c) lattice plane images of  $\text{TiO}$  and the  $\text{SrTiO}_3$  substrate, respectively.

Damaged parts (white areas) are clearly seen in Fig. 4.36(a). At the same time, the contrast of the substrate is uniform showing that no distortions occur. Fig. 4.36(b) shows an enlarged image of the damaged part of Fig. 4.36(a). The angle between the lattice planes of the converted phase is  $90^\circ$ , with a spacing of 0.42 nm. This phase can thus be attributed to a cubic phase similar to titanium monoxide ( $\text{TiO}$ ).

An AFM image of the thin film deposited on (110)  $\text{LaAlO}_3$  at a substrate temperature of 800 °C is shown in Fig. 4.37. The islands are elongated in the  $[1\bar{1}0]$  direction of  $\text{LaAlO}_3$  (the orientation

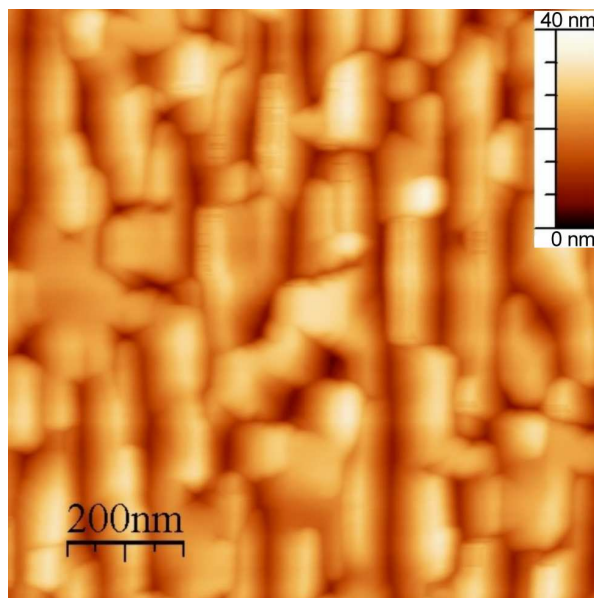


**Fig. 4.37.** AFM image of a (012)-oriented  $\text{TiO}_2$  (anatase) thin film grown on a (110)  $\text{LaAlO}_3$  substrate at a substrate temperature of 800 °C.

of the substrate was confirmed by XRD), with an average grain size of about 100 nm  $\times$  200 nm. The same surface morphology of the anatase islands was observed on (110)  $\text{SrTiO}_3$ . As shown by AFM, most of the surface of large (012)-oriented  $\text{TiO}_2$  (anatase) grains is planar and parallel to the

substrate surface, so that it could represent a crystallographic (012) plane.

A small amount of the  $\text{TiO}_2$  (rutile) phase was detected after deposition on (110)  $\text{SrTiO}_3$  at temperatures of 800 °C and 900 °C, as shown by one very weak peak in the pole figures recorded at  $2\theta = 27.4^\circ$ . The amount of  $\text{TiO}_2$  (rutile) grains was about the same at a temperature of 1000 °C but its orientation quality was improved. The maximum intensity of the  $\text{TiO}_2$  (rutile) phase at this temperature taken from a pole figure with  $2\theta = 27.4^\circ$  was 38 cps. This is a very low value compared to the intensity of  $\text{TiO}_2$  (anatase) taken from a pole figure with  $2\theta = 25.3^\circ$ , which was 9216 cps. The orientation quality and the amount of the  $\text{TiO}_2$  (anatase) phase decreased at a substrate temperature of 1100 °C. However, the total intensity obtained from  $\text{TiO}_2$  (anatase) was 3516 cps while from rutile it was 85 cps. At a substrate temperature of 1200 °C the  $\text{TiO}_2$  (anatase) phase was not present any more in the films. Now the film consisted mainly of tilted  $\text{TiO}_2$  (rutile) grains.

### C. Origin of the epitaxy between $\text{TiO}_2$ (anatase) and $\text{SrTiO}_3/\text{LaAlO}_3$

Although the growth of the  $\text{TiO}_2$  (anatase) thin film was not the major aim of this Ph.D. work, it is worth to analyse the results on the epitaxial growth of  $\text{TiO}_2$  (anatase) on the  $\text{SrTiO}_3$  and  $\text{LaAlO}_3$  substrates.

As was mentioned above, rutile is the most stable form of  $\text{TiO}_2$  whereas anatase and brookite are metastable and transform to the rutile phase on heating. Experimental data<sup>149</sup> and theoretical analysis<sup>149,150</sup> show that anatase becomes more stable with respect to rutile at very small crystallite sizes (10 nm - 14 nm). These findings are not directly applicable to the results shown above. The pure  $\text{TiO}_2$  (anatase) films deposited on  $\text{SrTiO}_3$  and on  $\text{LaAlO}_3$  have an average grain size from 100 nm to 600 nm depending on the substrate temperature used. In addition, the stability of  $\text{TiO}_2$  (anatase) depends strongly on the substrate temperature, the substrate orientation, and the kind of substrate used. Previous discussions on the stability of the  $\text{TiO}_2$  (anatase) phase and on the epitaxial growth were focused on the similarities between the local atomic arrangements in the grown layer and the substrate materials.<sup>146,151</sup> Here, we will apply a fundamental building block approach in order to better understand the epitaxial relations between  $\text{TiO}_2$  (anatase) and the substrates - an approach that was formerly adopted by Banfield *et al.*<sup>152</sup> to understand epitaxial relations among the  $\text{TiO}_2$  minerals.  $\text{TiO}_2$  and perovskite structures can be constructed from  $\text{AO}_6$  octahedra (in our case A= Ti, Al). Figs. 4.38(a)-(b) show a schematic representation of building blocks ( $\text{TiO}_6$  octahedra) for (001)  $\text{TiO}_2$  (anatase)/(100)  $\text{SrTiO}_3$  and (012)  $\text{TiO}_2$  (anatase)/(110)  $\text{SrTiO}_3$  interfaces, respectively. The similarities between the orientations of the  $\text{TiO}_6$  octahedra of  $\text{SrTiO}_3$  and  $\text{TiO}_2$  (anatase) are clearly visible.

It should be noted that the (100) surface of  $\text{SrTiO}_3$  presented in Fig. 4.38(a) is SrO-terminated. According to the work of Ohnishi *et al.*,<sup>153</sup> the experimental treatment of the (100)  $\text{SrTiO}_3$  substrates performed in our work (heating in air and then in vacuum of  $10^{-5}$  mbar), however, results in mixed SrO- and  $\text{TiO}_2$ -terminated surfaces of  $\text{SrTiO}_3$ . The substrate termination is important for the interface because the  $\text{TiO}_2$ -terminated (100)  $\text{SrTiO}_3$  surface contains truncated  $\text{TiO}_6$  octahedra. On the other hand, the (100) surface of  $\text{LaAlO}_3$  is terminated by a La-O layer at high temperatures (above 523 K)<sup>154,155</sup> and thus contains complete  $\text{AlO}_6$  octahedra. The  $\text{AO}_6$  octahedra (A= Ti,Al)

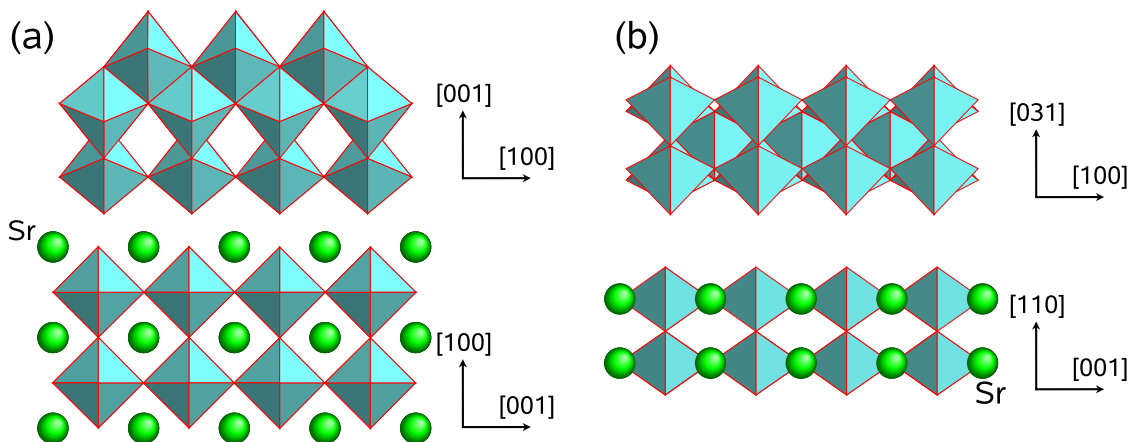


**Fig. 4.38.** Representation of the  $\text{TiO}_6$  octahedra of (a) the (001)  $\text{TiO}_2$  (anatase) (top)/(100)  $\text{SrTiO}_3$  (bottom) interface and (b) the (012)  $\text{TiO}_2$  (anatase) (top)/(110)  $\text{SrTiO}_3$  (bottom) interface, respectively. Similarities can be found in the orientations of  $\text{TiO}_6$  octahedra of  $\text{SrTiO}_3$  and anatase structures.

are assumed to be important in determining the final phase formation and the epitaxial growth of the thin films. Moreover, the  $\text{SrTiO}_3$  surfaces show a good lattice match with the  $\text{TiO}_2$  (anatase) surfaces. The in-plane lattice mismatch between (100)  $\text{TiO}_2$  (anatase) and (100)  $\text{SrTiO}_3$  is -3.04 % while the lattice mismatch between (01 $\bar{3}$ )  $\text{TiO}_2$  ( $d = 0.243$  nm) and (1 $\bar{1}$ 0)  $\text{SrTiO}_3$  ( $d = 0.275$  nm) is -11.6 %. It should be noted that the angle between the (01 $\bar{3}$ ) and (012) planes of anatase is not exactly 90°. A calculation results in the value of 88.5°. This means that the (01 $\bar{3}$ ) plane of a perfectly (012)-oriented anatase grain would deviate from the (1 $\bar{1}$ 0)  $\text{SrTiO}_3$  plane by 1.5°, resulting in a kink by 1.5° at the anatase/ $\text{SrTiO}_3$  interface. In the same scenario the epitaxial formation of anatase films on (100)  $\text{LaAlO}_3$  and (110)  $\text{LaAlO}_3$  surfaces can be explained. The only difference is the better lattice match of (001)/(012) anatase with (100)/(110)  $\text{LaAlO}_3$  surfaces. The lattice mismatch is -0.01 % between (100)  $\text{TiO}_2$  (anatase) and (001)  $\text{LaAlO}_3$  and -9.4 % between (01 $\bar{3}$ )  $\text{TiO}_2$  and (1 $\bar{1}$ 0)  $\text{LaAlO}_3$  ( $d = 0.268$  nm).

It was found that the irradiation of  $\text{TiO}_2$  (anatase) cross-section TEM specimens by the electron beam results in a transformation into a cubic phase. A similar transformation was observed by Hengerer *et al.*<sup>40,156</sup> by secondary-electron imaging and low energy electron diffraction. The authors found that sputtering with 500 eV  $\text{Ne}^+$  ions of a (001)  $\text{TiO}_2$  (anatase) surface leads to a transformation from tetragonal  $\text{TiO}_2$  (anatase) to the face-centered cubic titanium monoxide (TiO). Our TEM investigations also showed this phenomenon. The new transformed structure is topotaxial with  $\text{TiO}_2$  (anatase). A comparison of  $\text{TiO}_2$  (anatase) and TiO is shown in Figs. 4.39(a)-(b). The building blocks of the  $\text{TiO}_2$  (anatase) structure are distorted  $\text{TiO}_6$  octahedra in a zig-zag alignment (Fig. 4.39(a)) whereas the  $\text{TiO}_6$  octahedra in TiO are highly symmetric and without distortions (Fig. 4.39(b)). The cubic NaCl type lattice of TiO is known to be stable with very strong deviations from an ideal 1:1 stoichiometric ratio. Comparing one  $\text{TiO}_2$  (anatase) unit cell with two TiO unit cells, the authors of Ref.<sup>156</sup> found that filling interstitial sites in the anatase structure with titanium ions would lead to the TiO structure (see Fig. 6 in Ref.<sup>156</sup>). Thus,  $\text{TiO}_2$  (anatase) can be considered as an ordered phase similar to  $\text{Ti}_{0.5}\text{O}_{1.0}$  with missing octahedra. The electron beam induced disorder in  $\text{TiO}_2$  (anatase) results in a cubic oxide with an intermediate composition in the

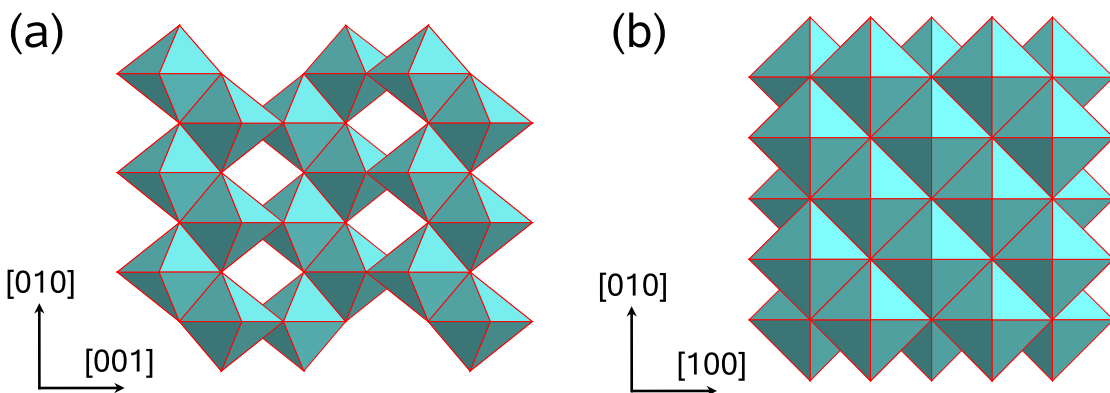


**Fig. 4.39.** Representation of the  $\text{TiO}_6$  octahedra of (a) the  $\text{TiO}_2$  (anatase) cell and (b) the  $\text{TiO}$  cell, respectively.

neighbourhood of  $\text{Ti}_{0.5}\text{O}_{1.0}$ . A transition from  $\text{TiO}_2$  (anatase) to ideal  $\text{TiO}$  would require a strong shrinkage since the densities are very different ( $\rho_{\text{anatase}} = 3.9 \text{ g/cm}^3$ ,  $\rho_{\text{TiO}} = 5.84 \text{ g/cm}^3$ ).

## 4.2.2 Phase formation and orientation relationships

For the reaction experiments anatase thin films grown on  $\text{SrTiO}_3$  and  $\text{LaAlO}_3$  substrates at a substrate temperature of  $800^\circ\text{C}$  were used.

### A. Phase formation

The phase sequences after solid-solid reactions in vacuum and in air at temperatures between  $575^\circ\text{C}$  and  $900^\circ\text{C}$  as well as after vapour-solid reaction at temperatures between  $575^\circ\text{C}$  and  $900^\circ\text{C}$  on epitaxial (001)- and (012)-oriented  $\text{TiO}_2$  (anatase) thin films indicate a process that is similar to the reaction on the  $\text{TiO}_2$  (rutile) substrates. It can be summarised as follows:

- At a substrate temperature of  $500^\circ\text{C}$  a single  $\text{BaCO}_3$  phase is present, as detected by XRD.
- The formation of  $\text{BaTiO}_3$  is always preceded by an intermediate  $\text{Ba}_2\text{TiO}_4$  compound at temperatures between  $575^\circ\text{C}$  and  $750^\circ\text{C}$  in vacuum. After solid-state reaction in air, the  $\text{Ba}_2\text{TiO}_4$  phase was not detected by XRD. Fig. 4.40 shows a HRTEM image of the interface region after the reaction between a  $\text{BaCO}_3$  thin film and the epitaxial (012)-oriented anatase thin film of a sample after solid-solid reaction in air at  $600^\circ\text{C}$  for 30 min. The reaction layer consists of  $\text{BaTiO}_3$  and  $\text{BaCO}_3$  grains.

- After solid state reactions at  $900^\circ\text{C}$  Ti-rich phases were observed by XRD and TEM investigations in both types of the solid state reactions. Fig. 4.41 shows a TEM image of the interface region after the reaction between a  $\text{BaO}$  vapour and the epitaxial (001) anatase film of a sample prepared at a substrate temperature of  $900^\circ\text{C}$ . In Fig. 4.41 the reaction front is similar to the Ti-rich/(110)  $\text{TiO}_2$  one (see Fig. 4.9). The Ti-rich grains were found at the interface with the anatase film and pores were formed during the reaction. HRTEM investigations revealed the presence of  $\text{Ba}_6\text{Ti}_{17}\text{O}_{40}$  in this sample.

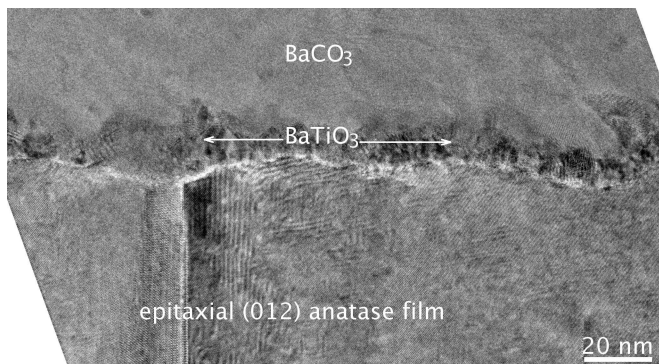


**Fig. 4.40.** Cross-sectional TEM image of the reaction front after solid-solid reaction of  $\text{BaCO}_3$  with an epitaxial (012)  $\text{TiO}_2$  (anatase) film. The reaction was performed in air at  $600^\circ\text{C}$  for 30 min.

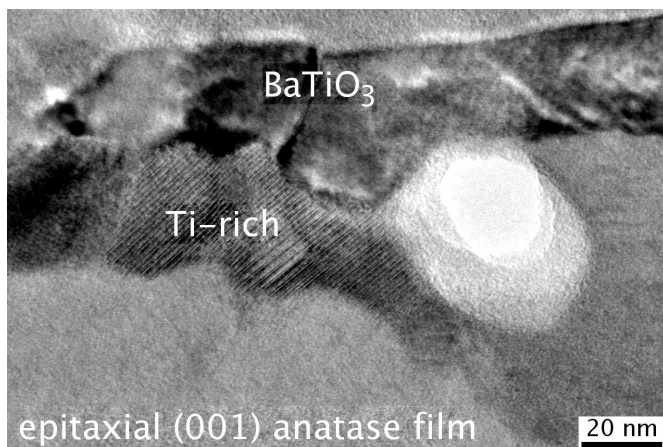


**Fig. 4.41.** Cross-sectional TEM image of the reaction front after vapour-solid reaction of  $\text{BaO}$  with an epitaxial (001)  $\text{TiO}_2$  (anatase) film at  $900^\circ\text{C}$ .

## B. Orientation relationships

### Orientation of $\text{Ba}_2\text{TiO}_4$

The orientation quality of  $\text{Ba}_2\text{TiO}_4$  grains after solid state reactions in vacuum with epitaxial anatase films is not as good as after the reactions with the rutile substrates. The solid state reactions with epitaxial anatase films lead to the formation of a polycrystalline  $\text{Ba}_2\text{TiO}_4$  phase with fiber texture. An example for a sample prepared after solid-solid reaction of  $\text{BaCO}_3$  with an epitaxial (001) anatase film is shown in Fig. 4.42.

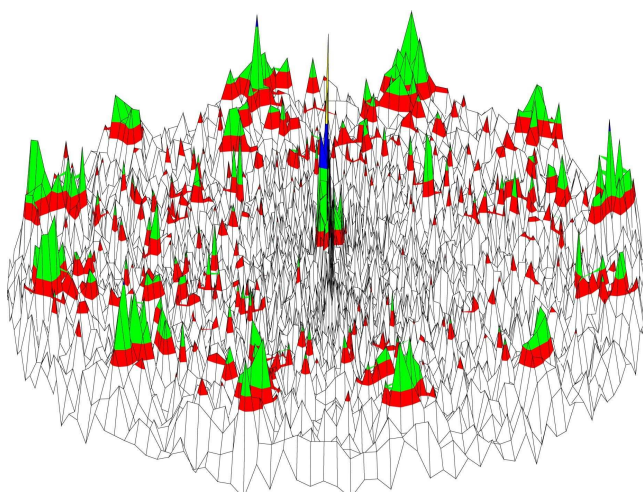


**Fig. 4.42.** Pole figure of a sample grown on an epitaxial (001)  $\text{TiO}_2$  (anatase) film by a solid-solid reaction in vacuum at  $700^\circ\text{C}$  for 30 min. The pole figure was recorded at  $2\theta = 29.34^\circ$  ( $\{031\}/\{002\}$   $\text{Ba}_2\text{TiO}_4$ ).

### Orientation of $\text{BaTiO}_3$

An X-ray pole figure analysis showed that the  $\text{BaTiO}_3$  grains grown on epitaxial (001) and (012)  $\text{TiO}_2$  (anatase) films after both types of the solid state reactions are crystallographically well-oriented.

Fig. 4.43 shows HRTEM images of the interface region after the reaction between a  $\text{BaO}$  vapour and the epitaxial (001) anatase film of a sample prepared at a substrate temperature of 900 °C. The reaction layer consists of  $\text{BaTiO}_3$  and  $\text{Ba}_6\text{Ti}_{17}\text{O}_{40}$  grains. The latter were observed between the epitaxial  $\text{TiO}_2$  (anatase) film and the  $\text{BaTiO}_3$  grains. The crystallographic orientation relationship found by HRTEM between the  $\text{BaTiO}_3$  and  $\text{Ba}_6\text{Ti}_{17}\text{O}_{40}$  grains corresponds to relation (4.9). The orientation relationship of  $\text{BaTiO}_3$  can be written from Fig. 4.43 as:

$$(001) \text{ BaTiO}_3 \parallel (001) \text{ TiO}_2 \text{ (a); } [1\bar{1}0] \text{ BaTiO}_3 \parallel [1\bar{1}0] \text{ TiO}_2 \text{ (a).} \quad (4.14)$$

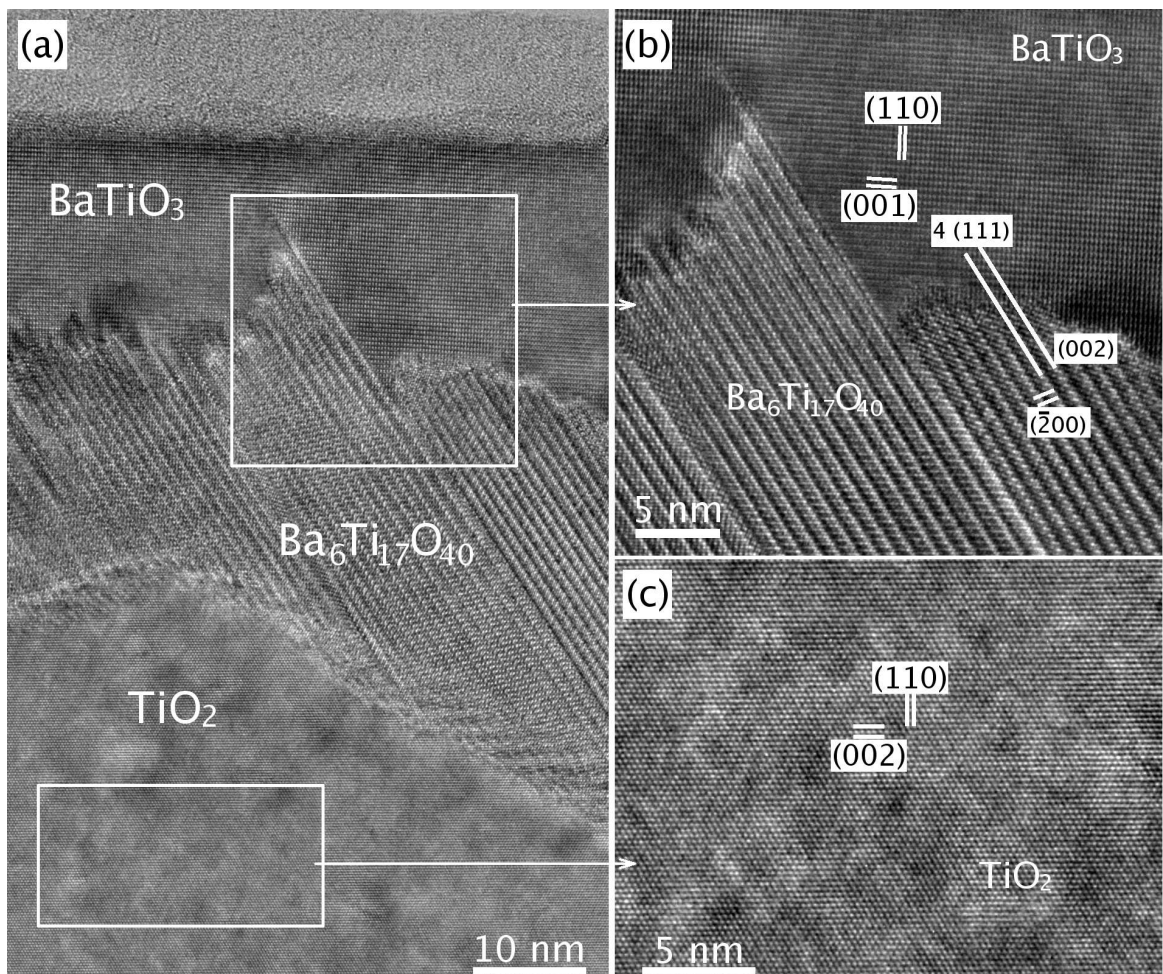


**Fig. 4.43.** HRTEM cross-section images of reaction products grown between a  $\text{BaO}$  vapour and an epitaxial (001)  $\text{TiO}_2$  (anatase) film at 900 °C: (a) thin film-substrate interface; (b) lattice plane images of  $\text{BaTiO}_3$  and  $\text{Ba}_6\text{Ti}_{17}\text{O}_{40}$  grains and (c) the  $\text{TiO}_2$  (anatase) film. The long white lines in the image (b) mark the  $(001) \text{ Ba}_6\text{Ti}_{17}\text{O}_{40} \parallel (111) \text{ BaTiO}_3$  lattice planes. Viewing direction is  $[010] \text{ Ba}_6\text{Ti}_{17}\text{O}_{40} \parallel [1\bar{1}0] \text{ BaTiO}_3 \parallel [1\bar{1}0] \text{ TiO}_2$  (anatase).

However,  $\text{BaTiO}_3$  grains show a small tilt of  $0^\circ$  to  $4^\circ$  around the  $[1\bar{1}0]$   $\text{BaTiO}_3 \parallel [1\bar{1}0]$   $\text{TiO}_2$  (anatase) tilt axis in the above orientation as was found by analysing many HRTEM images. Such an orientation relationship was also observed for the samples after vapour-solid reaction at temperatures between  $600^\circ\text{C}$  and  $900^\circ\text{C}$ , as well as after solid-solid reaction at temperatures between  $600^\circ\text{C}$  and  $900^\circ\text{C}$  in vacuum and in air.

Fig. 4.44 shows a HRTEM image of the interface region of a sample prepared by a solid-solid reaction in air at  $600^\circ\text{C}$  for 30 min between a  $\text{BaCO}_3$  film and the epitaxial (012)  $\text{TiO}_2$  (anatase) film. The  $\text{BaTiO}_3$  grains of Fig. 4.44 show the following orientation relationship:

$$(110) \text{ BaTiO}_3 \parallel (012) \text{ TiO}_2 \text{ (a); } [001] \text{ BaTiO}_3 \parallel [100] \text{ TiO}_2 \text{ (a).} \quad (4.15)$$

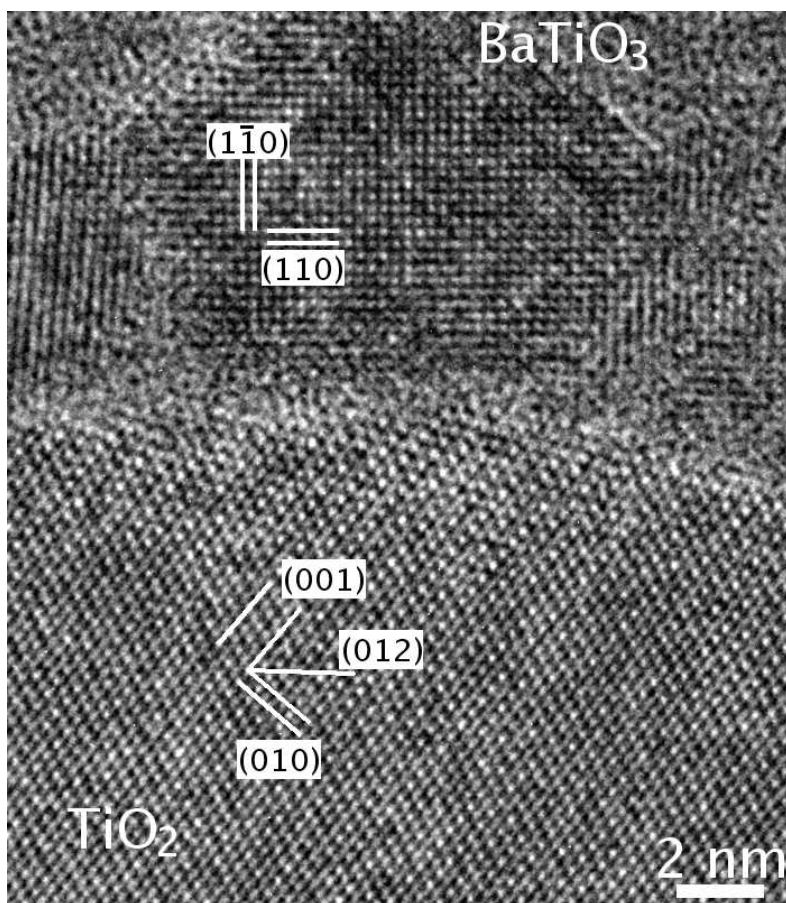


**Fig. 4.44.** Lattice plane image of an epitaxial (012)  $\text{TiO}_2$  (anatase) film and  $\text{BaTiO}_3$  grains. The sample was prepared by a solid-solid reaction in air at  $600^\circ\text{C}$  for 30 min. Viewing direction is  $[001] \text{ BaTiO}_3 \parallel [100] \text{ TiO}_2$  (anatase).

HRTEM investigations showed that the  $\text{BaTiO}_3$  grains were tilted by  $0^\circ$  to  $3^\circ$  around the  $[001] \text{ BaTiO}_3 \parallel [100] \text{ TiO}_2$  (anatase) tilt axis in the above orientation. This orientation relationship was also found for the samples after solid-solid reaction at temperatures between  $600^\circ\text{C}$  and  $900^\circ\text{C}$  in vacuum and in air, as well as after vapour-solid reaction at temperatures between  $600^\circ\text{C}$  and  $900^\circ\text{C}$ .

Table 4.2 summarises the orientation relationships at different substrate temperatures and the misfit values found for  $\text{BaTiO}_3$  films grown on epitaxial (001) and (012)  $\text{TiO}_2$  (anatase) films by solid state reactions.

**Table 4.2.** Orientation relationships and NCSL misfit values ( $F_1$  (in-plane) and  $F_2$  (in-plane rotated by 90°)) for  $\text{BaTiO}_3$  (BTO) thin films grown on epitaxial (001) and (012)  $\text{TiO}_2$  (anatase) films (A) after solid state reactions in vacuum and in air.

T, °C	Parallel planes	Parallel direction	$F_1$ , %	$F_2$ , %
(001) $\text{TiO}_2$ (anatase)				
600 – 900	(001) BTO    (001) A	[1 $\bar{1}$ 0] BTO    [1 $\bar{1}$ 0] A	$2(d(110)\text{BTO} - d(110)\text{A}) / (d(110)\text{BTO} + d(110)\text{A}) = +5.6$	$2(d(1\bar{1}0)\text{BTO} - d(1\bar{1}0)\text{A}) / (d(1\bar{1}0)\text{BTO} + d(1\bar{1}0)\text{A}) = +5.6$
(012) $\text{TiO}_2$ (anatase)				
600 – 900	(110) BTO    (012) A	[001] BTO    [100] A	$2(5d(1\bar{1}0)\text{BTO} - 6d(01\bar{3})\text{A}) / (5d(1\bar{1}0)\text{BTO} + 6d(01\bar{3})\text{A}) = -3$	$2(d(001)\text{BTO} - d(100)\text{A}) / (d(001)\text{BTO} + d(100)\text{A}) = +5.6$

### Orientation of Ti-rich phase

Fig. 4.43 shows a cross-section HRTEM image of a typical Ti-rich phase/ $\text{BaTiO}_3$  reaction front. The interplanar distances of the Ti-rich phase measured from Fig. 4.43 are 0.94 nm and 0.49 nm with an angle of 98.8° in between them. They correspond to the (200) and (002) planes of the  $\text{Ba}_6\text{Ti}_{17}\text{O}_{40}$  phase. In Fig. 4.43, the (002) plane of the  $\text{Ba}_6\text{Ti}_{17}\text{O}_{40}$  Ti-rich phase is parallel to the (111)  $\text{BaTiO}_3$  planes. The crystallographic orientation of the  $\text{Ba}_6\text{Ti}_{17}\text{O}_{40}$  follows a relation similar to (4.8).

Fig. 4.45 shows a HRTEM image of the  $\text{Ba}_6\text{Ti}_{17}\text{O}_{40}/\text{TiO}_2$  (anatase) interface of a sample prepared by vapour-solid reaction at 900 °C. The crystallographic orientation relationship found by

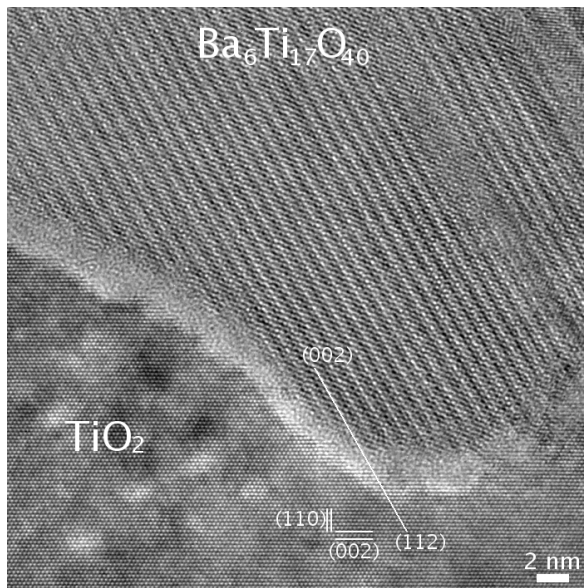


**Fig. 4.45.** Lattice plane image of an epitaxial (001)  $\text{TiO}_2$  anatase film and a  $\text{Ba}_6\text{Ti}_{17}\text{O}_{40}$  grain. The long white lines mark the (001)  $\text{Ba}_6\text{Ti}_{17}\text{O}_{40} \parallel$  (112)  $\text{TiO}_2$  (anatase) planes. Viewing direction is [010]  $\text{Ba}_6\text{Ti}_{17}\text{O}_{40} \parallel$  [1 $\bar{1}$ 0]  $\text{TiO}_2$  (anatase). The sample was prepared by a vapour-solid reaction at 900 °C. Magnified version of the image see in the appendix, Fig. A.12.

HRTEM between the  $\text{TiO}_2$  (anatase) and the  $\text{Ba}_6\text{Ti}_{17}\text{O}_{40}$  grain in Fig. 4.45 can be written as:

$$(002) \text{Ba}_6\text{Ti}_{17}\text{O}_{40} \parallel (112) \text{TiO}_2 \text{ (a)}; [010] \text{Ba}_6\text{Ti}_{17}\text{O}_{40} \parallel [1\bar{1}0] \text{TiO}_2 \text{ (a)}. \quad (4.16)$$

HRTEM investigations of other parts of this sample showed that the  $\text{Ba}_6\text{Ti}_{17}\text{O}_{40}$  grains were tilted by 0° to 3° around the [010]  $\text{Ba}_6\text{Ti}_{17}\text{O}_{40} \parallel$  [1 $\bar{1}$ 0]  $\text{TiO}_2$  tilt axis in the above orientation.

## 4.3 Solid state reactions of other alkaline-earth oxides with $\text{TiO}_2$ (rutile)

As was shown above, more than one orientation relationship was found for  $\text{BaTiO}_3$  grown on the rutile substrates, depending on the reaction temperature. X-ray texture investigations and high-resolution TEM images showed that all observed orientations of  $\text{BaTiO}_3$  grains on the  $\text{TiO}_2$  (rutile) substrates have a common  $[1\bar{1}0] \text{ BaTiO}_3 \parallel [001] \text{ TiO}_2$  tilt axis. In this part of the work, the experiments are extended to three other oxide systems, viz.  $\text{SrO-TiO}_2$ ,  $\text{CaO-TiO}_2$  and  $\text{MgO-TiO}_2$  which involve product phases containing  $\text{Sr}^{2+}$  ( $r_{\text{Sr}^{2+}} \approx 118 \text{ pm}$ ),  $\text{Ca}^{2+}$  ( $r_{\text{Ca}^{2+}} \approx 99 \text{ pm}$ ) and  $\text{Mg}^{2+}$  ( $r_{\text{Mg}^{2+}} \approx 75 \text{ pm}$ ) ions (respectively), the ionic radii ( $r$ ) of which are lower than that of  $\text{Ba}^{2+}$  ( $r_{\text{Ba}^{2+}} \approx 138 \text{ pm}$ ).

### 4.3.1 Vapour-solid reaction of $\text{SrO}$ with $\text{TiO}_2$ (rutile)

The reaction of  $\text{SrO}$  vapour with  $\text{TiO}_2$  (rutile) substrates was systematically investigated by XRD as a function of substrate temperature. Only  $\text{SrTiO}_3$  was found after vapour-solid reaction at temperatures between  $700 \text{ }^\circ\text{C}$  and  $900 \text{ }^\circ\text{C}$ .

Fig. 4.46 gives typical pole figures taken at  $2\theta = 32.4^\circ$  for samples prepared on (100)  $\text{TiO}_2$  at  $700 \text{ }^\circ\text{C}$ ,  $800 \text{ }^\circ\text{C}$  and  $900 \text{ }^\circ\text{C}$ , respectively. Fig. 4.46(a) shows that at  $700 \text{ }^\circ\text{C}$ , only the peaks

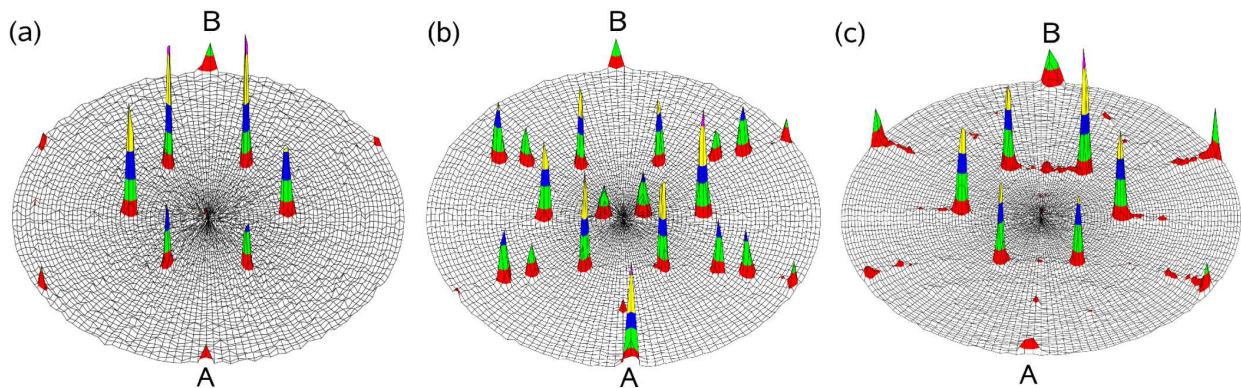


**Fig. 4.46.** Pole figures taken at  $2\theta = 32.4^\circ$ , corresponding to  $\text{SrTiO}_3 \{101\}$ , for samples made by vapour-solid reaction between  $\text{SrO}$  vapour and (100)  $\text{TiO}_2$  (rutile) substrates at three different temperatures (a)  $700 \text{ }^\circ\text{C}$ , (b)  $800 \text{ }^\circ\text{C}$  and (c)  $900 \text{ }^\circ\text{C}$ . For the full explanation see the text. Peaks situated at  $\psi = 58^\circ$  are from  $\{101\} \text{ TiO}_2$ . The positions of marks A and B correspond to the  $\phi$  values of the (001) and (00\bar{1}) substrate planes, respectively.

at  $\psi = 35^\circ$  and  $90^\circ$  are present. This is due to the first orientation relationship  $(111) \text{ SrTiO}_3 \parallel (100) \text{ TiO}_2$ . In Fig. 4.46(b) for a sample made at  $800 \text{ }^\circ\text{C}$ , in addition to the peaks at  $\psi = 35^\circ$  and  $90^\circ$ , there are peaks at  $\psi = 8^\circ$ ,  $54^\circ$  and  $67^\circ$  which are from the second orientation relationship  $(551) \text{ SrTiO}_3 \parallel (100) \text{ TiO}_2$ . Fig. 4.39(c) shows a pole figure of a sample made at a substrate temperature of  $900 \text{ }^\circ\text{C}$ . In Fig. 4.46(c), the strong peaks at  $\psi = 35^\circ$  and  $90^\circ$  are due to the (111) orientation of  $\text{SrTiO}_3$ , whereas the weak reflections at  $\psi = 30^\circ$ ,  $55^\circ$ ,  $73^\circ$  are coming from the third orientation relationship  $(112) \text{ SrTiO}_3 \parallel (100) \text{ TiO}_2$  and those at  $\psi = 30^\circ$ ,  $48.5^\circ$ ,  $79.5^\circ$  are due to the

fourth orientation relationship (558)  $\text{SrTiO}_3 \parallel (100) \text{TiO}_2$ .

The in-plane orientation was determined by pole figures recorded at  $2\theta = 32.4^\circ$  and  $2\theta = 46.5^\circ$  and a  $\phi$  scan of the  $\text{TiO}_2 \{110\}$  reflections taken at  $\psi = 45^\circ$ . The  $\phi$  positions corresponding to the (001) and (00 $\bar{1}$ ) substrate planes are denoted by marks A and B, respectively. Thus the in-plane orientation is always  $[1\bar{1}0] \text{SrTiO}_3 \parallel [001] \text{TiO}_2$  for all the orientations observed on the (100) rutile substrates. Notably, the (551) orientation of  $\text{SrTiO}_3$  deviates from the (111) one by a tilt of  $27.2^\circ$  around the  $[1\bar{1}0] \text{SrTiO}_3 \parallel [001] \text{TiO}_2$  axis, while the (112) and (558) orientations of  $\text{SrTiO}_3$  deviate from the (111) one by a tilt of  $19.4^\circ$  and  $13.2^\circ$ , respectively, around the same axis.

Fig. 4.47 shows typical pole figures taken at  $2\theta = 32.4^\circ$  for samples prepared on (110)  $\text{TiO}_2$  at  $700^\circ\text{C}$ ,  $800^\circ\text{C}$  and  $900^\circ\text{C}$ , respectively. Fig. 4.47(a) gives a pole figure for a sample made at

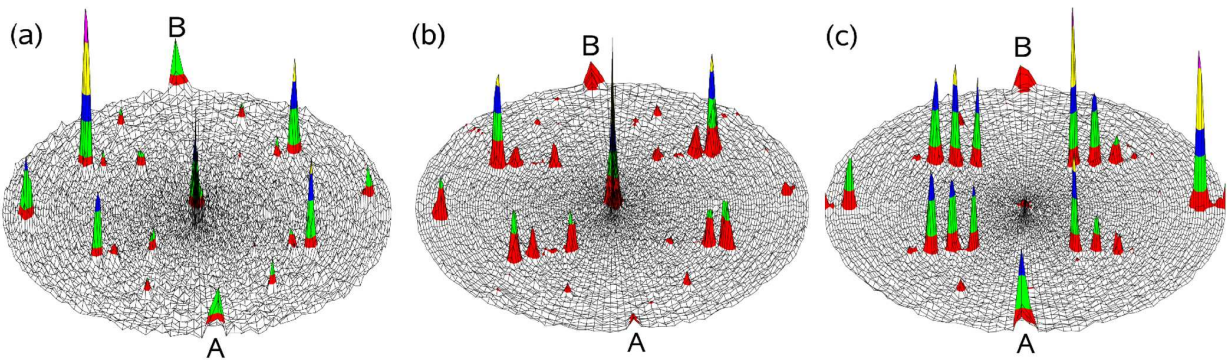


**Fig. 4.47.** Pole figures taken at  $2\theta = 32.4^\circ$ , corresponding to  $\text{SrTiO}_3 \{101\}$ , for samples after vapour-solid reaction of  $\text{SrO}$  with (110)  $\text{TiO}_2$  (rutile) substrates made at three different temperatures (a)  $700^\circ\text{C}$ , (b)  $800^\circ\text{C}$  and (c)  $900^\circ\text{C}$ . For more details see the text. Peaks situated at  $\psi = 67.5^\circ$  are from  $\{101\} \text{TiO}_2$ . The positions of marks A and B correspond to the  $\phi$  values of the (001) and (00 $\bar{1}$ ) substrate planes, respectively.

a substrate temperature of  $700^\circ\text{C}$ . At this temperature two orientation relations for  $\text{SrTiO}_3$  were found. Whereas the peaks in Fig. 4.47(a) at  $\psi = 0^\circ$ ,  $60^\circ$  and  $90^\circ$  are from the first orientation relationship (110)  $\text{SrTiO}_3 \parallel (110) \text{TiO}_2$ , those at  $\psi = 38.5^\circ$ ,  $52^\circ$ ,  $79.4^\circ$  and  $90^\circ$  are from the second orientation relationship (118)  $\text{SrTiO}_3 \parallel (110) \text{TiO}_2$ . For the samples made at temperatures between  $800^\circ\text{C}$  and  $900^\circ\text{C}$ , a third orientation relationship for this phase was found. The weak peaks situated at  $\psi = 45^\circ$  in Fig. 4.47(b) for the sample made at a substrate temperature of  $800^\circ\text{C}$  are due to the third orientation relationship (001)  $\text{SrTiO}_3 \parallel (110) \text{TiO}_2$ . The peak intensity from this orientation becomes stronger at  $900^\circ\text{C}$  (Fig. 4.47(c)). On the other hand, the peak intensity is getting much weaker for the first orientation.

From a series of pole figures and a  $\phi$  scan of the  $\text{TiO}_2 \{100\}$  reflections taken at  $\psi = 45^\circ$ , the in-plane orientation was found to be  $[1\bar{1}0] \text{SrTiO}_3 \parallel [001] \text{TiO}_2$  for all the orientations observed on the (110) rutile substrates. It should be noted that the (118) orientation of  $\text{SrTiO}_3$  deviates from the (110) one by a tilt of  $79.8^\circ$  around the  $[1\bar{1}0] \text{SrTiO}_3 \parallel [001] \text{TiO}_2$  axis, whereas the (001) orientation of  $\text{SrTiO}_3$  deviates from the (110) one by a tilt of  $90^\circ$  around the same axis.

Table 4.3 summarises the orientation relationships and the misfit values for  $\text{SrTiO}_3$  grown on the (100) and (110)  $\text{TiO}_2$  (rutile) substrates by vapour-solid reaction in vacuum at different substrate temperatures. As in the case of  $\text{BaTiO}_3$ , the relation  $[1\bar{1}0] \text{SrTiO}_3 \parallel [001] \text{TiO}_2$  holds independently of the substrate orientation.

**Table 4.3.** Orientation relationships and NCSL misfit values ( $F_1$  (in-plane) and  $F_2$  (in-plane rotated by 90°)) for  $SrTiO_3$  (STO) thin films grown on (100) and (110)  $TiO_2$  (rutile) substrates (T) at different temperatures.

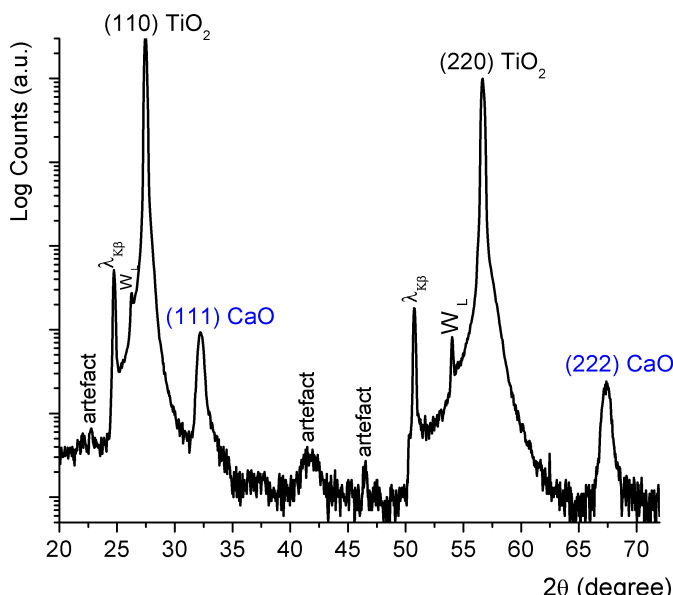
T, °C	Parallel planes	Parallel direction	$F_1$ , %	$F_2$ , %
(100) $TiO_2$ (rutile)				
700 – 900	(111) STO  (100) T	[1 $\bar{1}$ 0] STO  [001] T	$2(3d(11\bar{2})STO - d(010)T)/(3d(11\bar{2})STO + d(010)T) = +3.8$	$2(10d(1\bar{1}0)STO - 9d(001)T)/(10d(1\bar{1}0)STO + 9d(001)T) = +3.5$
800	(551) STO  (100) T	[1 $\bar{1}$ 0] STO  [001] T	$2(12d(11\bar{1}0)STO - d(010)T)/(12d(11\bar{1}0)STO + d(010)T) = +0.9$	$2(10d(1\bar{1}0)STO - 9d(010)T)/(10d(1\bar{1}0)STO + 9d(010)T) = +3.5$
900	(112) STO  (100) T	[1 $\bar{1}$ 0] STO  [001] T	$2(2d(11\bar{1})STO - d(010)T)/(2d(11\bar{1})STO + d(010)T) = -1.9$	$2(10d(1\bar{1}0)STO - 9d(001)T)/(10d(1\bar{1}0)STO + 9d(001)T) = +3.5$
	(558) STO  (100) T	[1 $\bar{1}$ 0] STO  [001] T	$2(9d(44\bar{5})STO - d(010)T)/(9d(44\bar{5})STO + d(010)T) = +1.4$	$2(10d(1\bar{1}0)STO - 9d(001)T)/(10d(1\bar{1}0)STO + 9d(001)T) = +3.5$
(110) $TiO_2$ (rutile)				
700 – 900	(110) STO  (110) T	[1 $\bar{1}$ 0] STO  [001] T	$2(5d(001)STO - 6d(\bar{1}10)T)/(5d(001)STO + 6d(\bar{1}10)T) = +0.06$	$2(10d(1\bar{1}0)STO - 9d(001)T)/(10d(1\bar{1}0)STO + 9d(001)T) = +3.5$
	(118) STO  (110) T	[1 $\bar{1}$ 0] STO  [001] T	$2(5d(44\bar{1})STO - d(\bar{1}10)T)/(5d(44\bar{1}) + d(\bar{1}10)T) = +4.4$	$2(10d(1\bar{1}0)STO - 9d(001)T)/(10d(1\bar{1}0)STO + 9d(001)T) = +3.5$
800 – 900	(001) STO  (110) T	[1 $\bar{1}$ 0] STO  [001] T	$2(7d(110)STO - 6d(\bar{1}10)T)/(7d(110)STO + 6d(\bar{1}10)T) = -0.9$	$2(10d(1\bar{1}0)STO - 9d(001)T)/(10d(1\bar{1}0)STO + 9d(001)T) = +3.5$

### 4.3.2 Vapour-solid reaction of $CaO$ with $TiO_2$ (rutile)

#### A. Phase formation

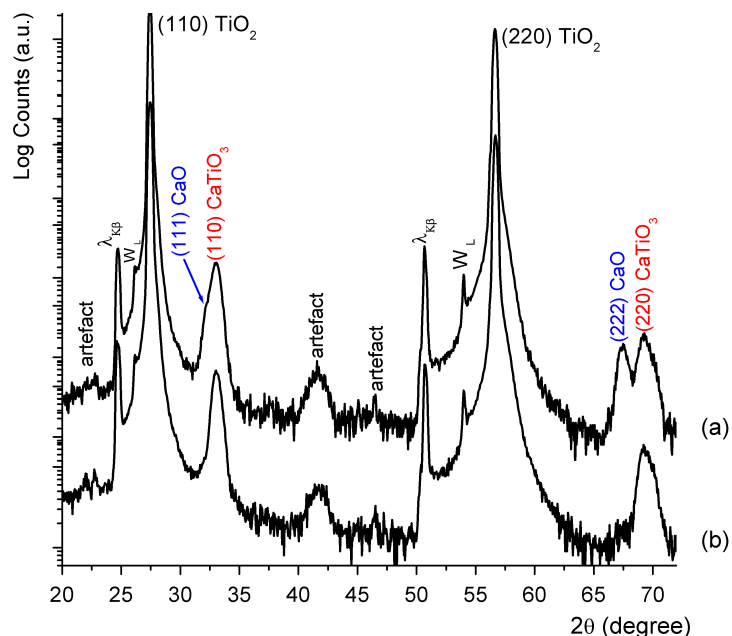
Vapour-solid reactions between  $CaO$  vapour and (110)  $TiO_2$  (rutile) substrates are different compared to the previous systems  $BaO-TiO_2$  (rutile) and  $SrO-TiO_2$  (rutile).  $CaTiO_3$  and non-reacted  $CaO$  phases were found in the thin films after vapour-solid reactions at temperatures between 600 °C and 900 °C by XRD investigations. The reaction time was  $\approx 32$  min.

Fig. 4.48 shows a XRD  $\theta$ - $2\theta$  scan of a sample prepared by vapour-solid reaction between  $CaO$  vapour and (110)  $TiO_2$  substrate at a substrate temperature of 600 °C. In Fig. 4.48, beside the



**Fig. 4.48.** XRD  $\theta$ - $2\theta$  scan of a sample made by vapour-solid reaction between  $CaO$  vapour and (110) rutile substrate at 600 °C. The  $\lambda_{K\beta}$  lines are the substrate peaks originating from the remaining  $Cu-K\beta$  radiation, and the  $W_L$  lines are coming from the tungsten contamination of the X-ray target by the tungsten cathode filament. The "artefact" peaks are substrate-induced artefacts.

substrate reflections, there are peaks at  $2\theta = 32.3^\circ$  and at  $2\theta = 67.4^\circ$ . They correspond to (111) and (222) reflections of CaO (JCPDS 78-0649), respectively. The CaTiO<sub>3</sub> phase is not seen in the XRD  $\theta$ - $2\theta$  pattern after the reaction at 600 °C because the phase was contained in the thin film in a small amount (I = 25 cps at  $\psi = 60^\circ$ ) as was shown by the weak intensity in the pole figure taken at  $2\theta = 33.1^\circ$  (CaTiO<sub>3</sub> (110)). With increasing reaction temperature the amount of the CaTiO<sub>3</sub> phase increased while the amount of CaO phase decreased. Fig. 4.49(a) gives a XRD  $\theta$ - $2\theta$  pattern of a sample made by vapour-solid reaction at 800 °C. While the peaks at  $2\theta = 32.3^\circ$  and at  $2\theta = 67.4^\circ$



**Fig. 4.49.** XRD  $\theta$ - $2\theta$  scans of a sample made by vapour-solid reaction between CaO vapour and (110) rutile substrate at 800 °C: (a) as deposited and (b) after storage in air for two days. The  $\lambda_{K\beta}$  lines are the substrate peaks originating from the remaining Cu- $K\beta$  radiation, and the  $W_L$  lines are coming from the tungsten contamination of the X-ray target by the tungsten cathode filament. The "artefact" peaks are substrate-induced artefacts.

are from (111) and (222) reflections of CaO, those at  $2\theta = 33.1^\circ$  and at  $2\theta = 69.3^\circ$  correspond to (110) and (220) reflections of CaTiO<sub>3</sub>. It is well-known that CaO is an unstable phase in air. In our work, the CaO phase was also found to be a very unstable compound and to react after storage for two days in air, most probably with H<sub>2</sub>O and CO<sub>2</sub>. Fig. 4.49(b) gives a XRD  $\theta$ - $2\theta$  scan which was taken from the sample shown in Fig. Fig. 4.49(a) after two days storage in air. The peaks at  $2\theta = 32.3^\circ$  and at  $2\theta = 67.4^\circ$  are not present any more in the XRD pattern, indicating the instability of the CaO phase in air. A vapour-solid reaction at 900 °C resulted in the formation of two phases (CaO and CaTiO<sub>3</sub>).

To define which phase is formed first during a vapour-solid reaction between CaO vapour with (110) TiO<sub>2</sub> (rutile) substrates, a low amount of CaO was deposited on a hot (110) TiO<sub>2</sub> substrate at 700 °C. The nominal thickness of CaO was  $\approx 3$  nm. Only CaTiO<sub>3</sub> was found in the thin film after the reaction by XRD  $\theta$ - $2\theta$  measurements as well as by pole figures. This was also confirmed by TEM investigations shown in Figs. 4.50-4.51.

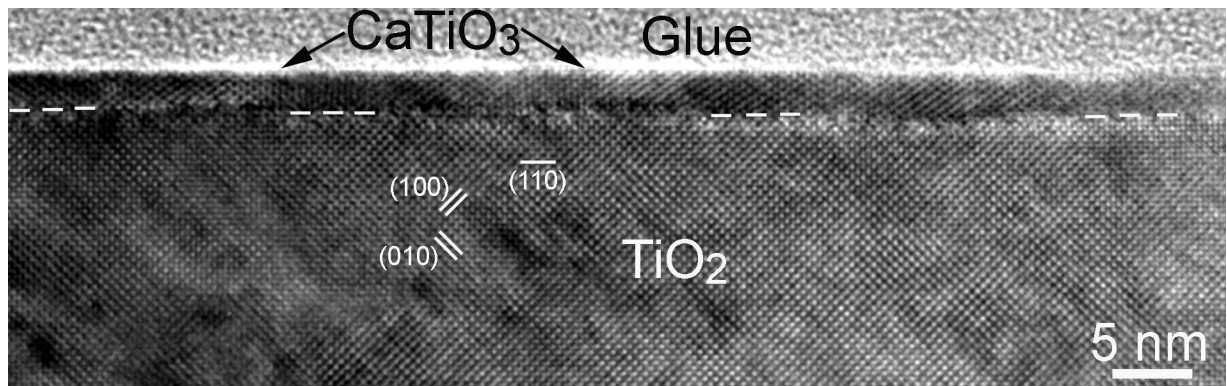


**Fig. 4.50.** Cross-sectional TEM image of a sample made by the reaction of CaO vapour with (110)  $TiO_2$  (rutile) substrate at 700 °C. The dashes mark the rutile substrate. Viewing direction is [001]  $TiO_2$ .

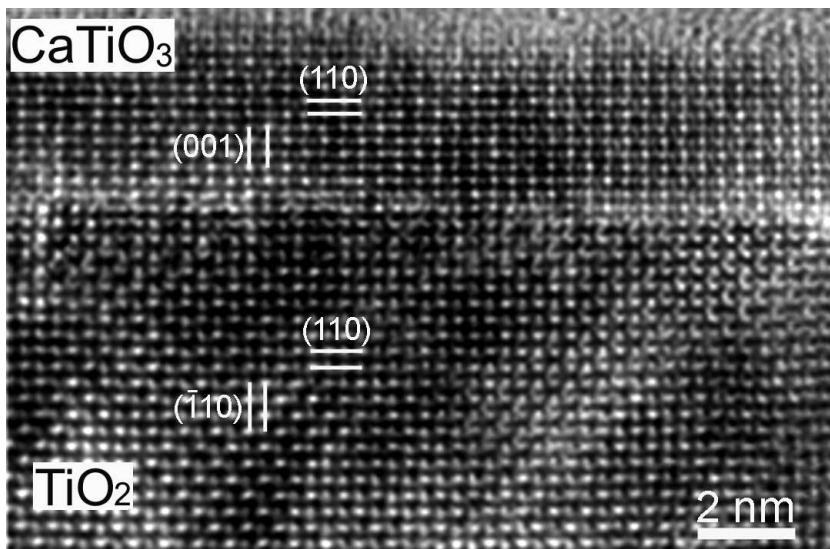


**Fig. 4.51.** Lattice plane image of the  $CaTiO_3/TiO_2$  reaction front. Viewing direction is  $[1\bar{1}0] CaTiO_3 \parallel [001] TiO_2$ .

## B. Orientation relationships

$CaTiO_3$  grew well-oriented with respect to the (110) rutile substrate. From Fig. 4.49 it can be concluded that the (110) plane of  $CaTiO_3$  is parallel to the (110)  $TiO_2$  surface. The orientation relationship of  $CaTiO_3$  found by HRTEM (Fig. 4.51) as well as by pole figure measurements was:

$$(110) CaTiO_3 \parallel (110) TiO_2; [1\bar{1}0] CaTiO_3 \parallel [001] TiO_2. \quad (4.17)$$

This orientation relationship was observed for the samples made at temperatures between 600 °C and 900 °C. No other orientations of  $CaTiO_3$  were found in the samples after the reaction. A rocking curve measurement with the (110) reflection of  $CaTiO_3$  resulted in a tilting FWHM of  $\approx 0.7^\circ$ . The FWHM of the (110)  $TiO_2$  substrate reflection was 0.1°.

To analyse the orientation of the CaO thin film, a number of pole figures were recorded at different  $2\theta$  values ( $32.2^\circ$ ,  $37.4^\circ$  and  $53.9^\circ$ ). Fig. 4.52 gives a pole figure recorded at  $2\theta = 37.4^\circ$  (CaO (200)). In the pole figure, six peaks are situated on the circle at  $\psi = 55^\circ$  ( $\Delta\phi = 60^\circ$ ) and correspond to the (111) orientation of CaO. For reasons of symmetry, these six reflection peaks can be related to two in-plane domain variants of the (111)-oriented CaO film, which are rotated in-

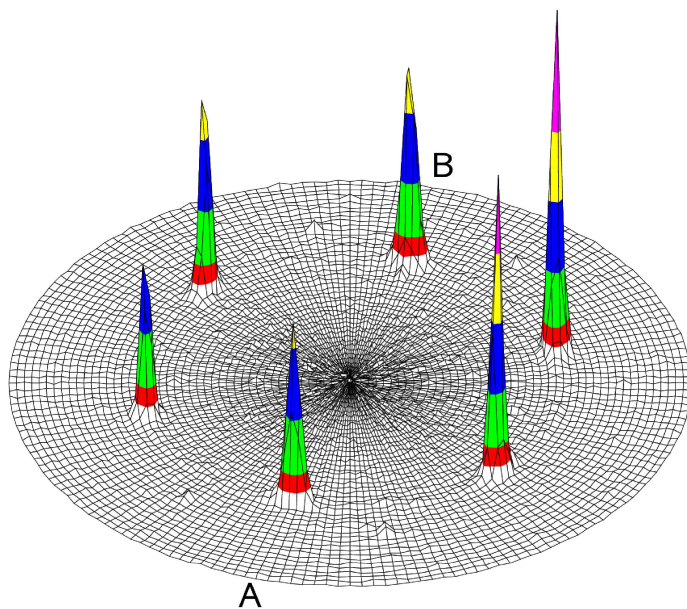


**Fig. 4.52.** Pole figure recorded with  $CaO$  (200) ( $2\theta = 37.4^\circ$ ) of a sample made at  $600\text{ }^\circ C$ . The positions of marks A and B correspond to the  $\phi$  values of the (001) and (00 $\bar{1}$ ) substrate planes, respectively.

plane by  $90^\circ$  relative to each other. From a series of pole figures,  $\phi$  and  $\theta$ - $2\theta$  scans, the orientation relationship of  $CaO$  with respect to (110)  $TiO_2$  was found to be:

$$(111) CaO \parallel (110) TiO_2; [1\bar{1}\bar{2}] CaO \parallel [001] TiO_2. \quad (4.18)$$

This orientation relationship was observed for the samples made at temperatures between  $600\text{ }^\circ C$  and  $900\text{ }^\circ C$ . A rocking curve measurement with the (111) planes of  $CaO$  resulted in a tilting FWHM of  $\approx 1.7^\circ$ . The FWHM of the (110)  $TiO_2$  substrate reflection was  $0.1^\circ$ .

From Eqs. (4.17) and (4.18), the orientation relationship between  $CaO$  and  $CaTiO_3$  can be written as follows:

$$(110) CaTiO_3 \parallel (111) CaO; [1\bar{1}0] CaTiO_3 \parallel [11\bar{2}] CaO. \quad (4.19)$$

Table 4.4 summarises the orientation relationships and NCSL misfit values observed for  $CaO$  and  $CaTiO_3$  thin films on (110)  $TiO_2$  substrates.

**Table 4.4.** Orientation relationships and NCSL misfit values ( $F_1$  (in-plane) and  $F_2$  (in-plane rotated by  $90^\circ$ )) for  $CaTiO_3$  (CT) and  $CaO$  (CO) thin films grown on (110) rutile substrates (T).

T, °C	Parallel planes	Parallel direction	$F_1$ , %	$F_2$ , %
600 – 900	(110) CT  (110) T	[1 $\bar{1}0$ ] CT  [001] T	$2(6d(001)CT - 5d(\bar{1}10)T)/(6d(001)CT + 5d(\bar{1}10)T) = -1.2$	$2(9d(\bar{1}10)CT - 8d(001)T)/(9d(\bar{1}10)CT + 8d(001)T) = +3.3$
600 – 900	(110) CT  (111) CO	[1 $\bar{1}0$ ] CT  [11 $\bar{2}$ ] CO	$2(8d(001)CT - 9d(\bar{1}10)CO)/(8d(001)CT + 9d(\bar{1}10)CO) = -0.5$	$2(3d(\bar{1}10)CT - 4d(11\bar{2})CO)/(3d(\bar{1}10)CT + 4d(11\bar{2})CO) = -2.7$

### 4.3.3 Vapour-solid reaction of $\text{MgO}$ with $\text{TiO}_2$ (rutile)

Only the phase  $\text{MgTiO}_3$  was observed after reaction of  $\text{MgO}$  vapour with the  $\text{TiO}_2$  (rutile) substrates at temperatures between 600 °C and 800 °C. X-ray diffractometry and pole figure analysis showed that the  $\text{MgTiO}_3$  films grown on (100) and (110)  $\text{TiO}_2$  substrates were crystallographically well-oriented.

XRD  $\theta$ - $2\theta$  scans of the films produced on the (100)  $\text{TiO}_2$  substrates showed the appearance of characteristic reflections of (11.0)  $\text{MgTiO}_3$  at  $2\theta = 35.5^\circ$  and (22.0)  $\text{MgTiO}_3$  at  $2\theta = 75.1^\circ$  beside the (200) and (400) substrate reflections. This means that the (11.0) plane of  $\text{MgTiO}_3$  is parallel to the (100) surface of  $\text{TiO}_2$ . A rocking curve measurement with the planes (11.0)  $\text{MgTiO}_3$  resulted in a tilting FWHM of 0.37°. The FWHM of the (200)  $\text{TiO}_2$  (rutile) substrate reflection was 0.1°.

Fig. 4.53(a) shows a cross sectional transmission electron micrograph of a  $\text{MgTiO}_3$  thin film grown by vapour-solid reaction on (100)  $\text{TiO}_2$  (rutile) at a substrate temperature of 700 °C. The

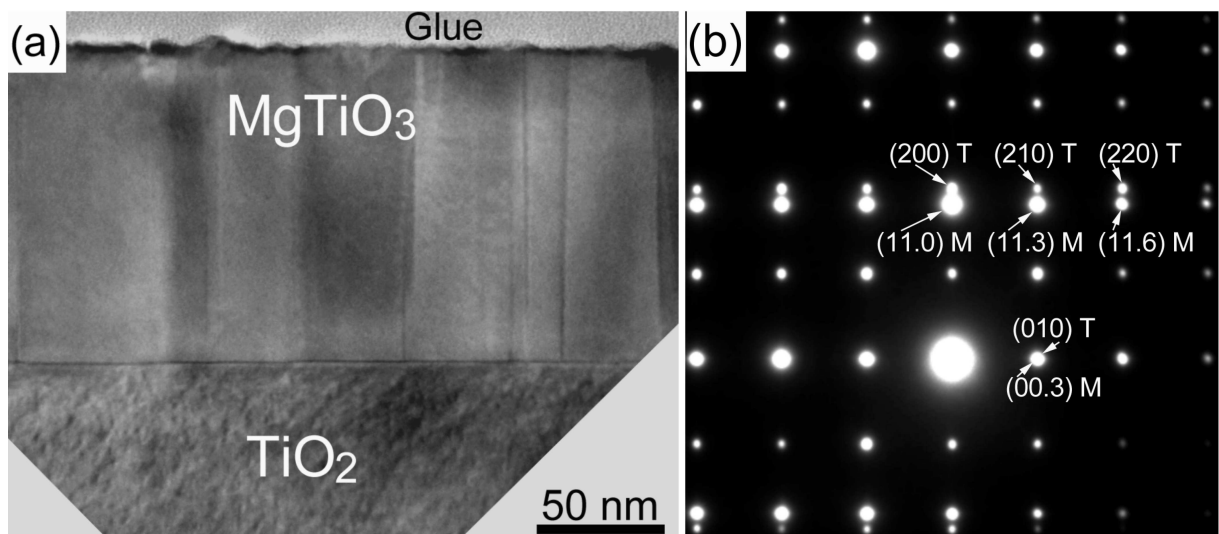


**Fig. 4.53.** (a) Bright field transmission electron micrograph of a  $\text{MgTiO}_3$  thin film produced by vapour-solid reaction between  $\text{MgO}$  vapour and (100)  $\text{TiO}_2$  at a substrate temperature of 700 °C. (b) Selected area electron diffraction pattern from the interface region between the  $\text{MgTiO}_3$  film (M) and the substrate (T). Viewing direction is  $[1\bar{1}.0] \text{ MgTiO}_3 \parallel [001] \text{ TiO}_2$ .

interface between the thin film and the substrate is flat. This is in contrast to the interface after reaction of  $\text{BaO}$  vapour with (100)  $\text{TiO}_2$ , where large and small (110) and (1 $\bar{1}$ 0)  $\text{TiO}_2$  facets of the (100) rutile surface were observed. Fig. 4.53(b) shows a selected area electron diffraction pattern taken from the substrate/film interface region of Fig. 4.53(a). The complete orientation relationship can be derived from Fig. 4.53(b) as:

$$(11.0) \text{ MgTiO}_3 \parallel (100) \text{ TiO}_2; [1\bar{1}.0] \text{ MgTiO}_3 \parallel [001] \text{ TiO}_2.$$

Fig. 4.54 gives a pole figure recorded at  $2\theta = 32.9^\circ$  ( $\{10.4\}/\{\bar{1}1.4\} \text{ MgTiO}_3$ ) for a sample prepared on (110)  $\text{TiO}_2$  at a substrate temperature of 600 °C. In Fig. 4.53, the peaks at  $\psi = 21^\circ$ ,  $56.5^\circ$  and  $80^\circ$  are due to a (22.11) orientation of  $\text{MgTiO}_3$  (cf.  $\angle \text{MgTiO}_3$  (22.11); (10.4) =  $20.8^\circ$ ,  $\angle \text{MgTiO}_3$  (22.11); (11.4) =  $56.4^\circ$  and  $\angle \text{MgTiO}_3$  (22.11); (01.4) =  $80^\circ$ ). The (22.11) orientation of  $\text{MgTiO}_3$  is rather close to the (11.6) orientation of  $\text{MgTiO}_3$  ( $\angle \text{MgTiO}_3$  (22.11); (11.6) =  $2.5^\circ$ ,

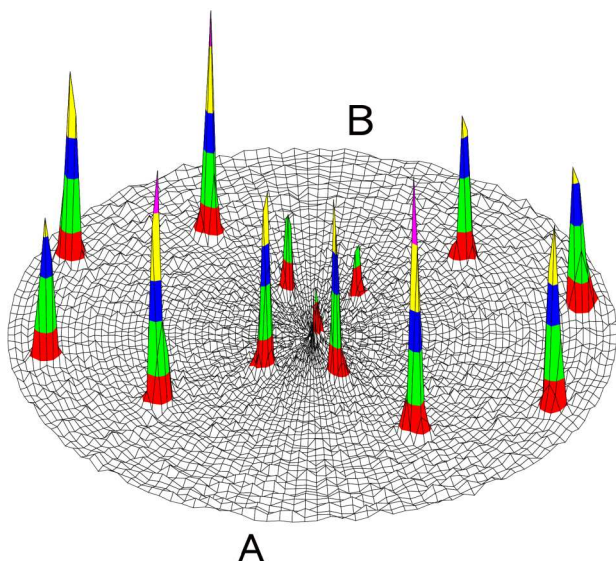


**Fig. 4.54.** X-ray pole figure measured at  $2\theta = 32.9^\circ$  ( $\{10.4\}/\{\bar{1}1.4\}$   $MgTiO_3$ ) of a sample prepared on (110)  $TiO_2$  at a substrate temperature of  $600^\circ C$ . Peaks are situated at  $\psi = 21^\circ, 56.5^\circ$  and  $80^\circ$ . The peak in the middle of the figure at  $\psi = 0^\circ$  marks the (110)  $TiO_2$  substrate surface. The positions of labels A and B correspond to the  $\phi$  values of the (001) and (001̄) substrate planes, respectively.

however,  $\angle MgTiO_3(11.6);(10.4) = 19.8^\circ$ ,  $\angle MgTiO_3(11.6);(\bar{1}1.4) = 54.8^\circ$  and  $\angle MgTiO_3(11.6);(0\bar{1}.4) = 77.7^\circ$ ). The peak at the center ( $\psi = 0^\circ$ ) in Fig. 4.54 is the (110)  $TiO_2$  peak (not fully suppressed) that results from the non-optimum wavelength selectivity of the secondary monochromator. From a series of pole figures and a  $\phi$  scan of the  $TiO_2\{200\}$  reflections taken at  $\psi = 45^\circ$ , the in-plane orientation was found to be  $[1\bar{1}.0] MgTiO_3 \parallel [001] TiO_2$ . It should be noted that the (110) orientation of  $MgTiO_3$  deviates from the (22.11) one by a tilt of  $45^\circ$  around the  $[1\bar{1}.0] MgTiO_3 \parallel [001] TiO_2$  axis.

Table 4.5 summarises the orientation relationships at different substrate temperatures and NCSL misfit values observed for  $MgTiO_3$  films on both (100) and (110)  $TiO_2$  substrates.

**Table 4.5.** Orientation relationships and NCSL misfit values ( $F_1$  (in-plane) and  $F_2$  (in-plane rotated by  $90^\circ$ )) for  $MgTiO_3$  (MTO) thin films grown on (100) and (110)  $TiO_2$  (rutile) substrates (T).

T, °C	Parallel planes	Parallel direction	$F_1$ , %	$F_2$ , %
(100) $TiO_2$ (rutile)				
600 – 800	$(11.0) MTO \parallel (100) T$	$[1\bar{1}.0] MTO \parallel [001] T$	$2(d(00.1)MTO - 3d(010)T)/$ $(d(00.1)MTO + 3d(010)T) = +0.9$	$2(2d(1\bar{1}.0)MTO - 3d(001)T)/$ $(2d(1\bar{1}.0)MTO + 3d(001)T) = -1.2$
(110) $TiO_2$ (rutile)				
600 – 800	$(22.11) MTO \parallel (110) T$	$[1\bar{1}.0] MTO \parallel [001] T$	$2(7d(11.\bar{5})MTO - 4d(\bar{1}10)T)/$ $(7d(11.5)MTO + 4d(\bar{1}10)T) = +1$	$2(2d(1\bar{1}.0)MTO - 3d(001)T)/$ $(2d(1\bar{1}.0)MTO + 3d(001)T) = -1.2$

# 5 Discussion

## 5.1 The reaction systems $\text{BaCO}_3\text{-TiO}_2$ and $\text{BaO}\text{-TiO}_2$

### 5.1.1 Phase formation

#### A. Solid-solid reaction of $\text{BaCO}_3$ with $\text{TiO}_2$

##### a. Reaction at low temperature (575 °C-800 °C)

The solid-solid reactions in vacuum and in air showed different processes to occur during  $\text{BaTiO}_3$  formation. The intermediate  $\text{Ba}_2\text{TiO}_4$  phase was observed always after reaction in vacuum. However,  $\text{Ba}_2\text{TiO}_4$  was not detected after a reaction in air. The formation of the observed phases was independent of the nature of  $\text{TiO}_2$  (rutile or anatase).

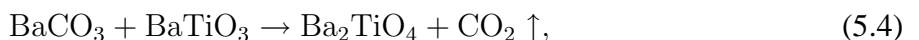
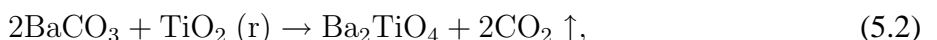
In the classical theory of nucleation, the rate of nucleation of a new nucleus is proportional to a term of the form  $\exp(-\sigma^3/\Delta G_r^2 kT)$ . Therefore, the nucleation of a new phase will occur rapid for compounds with high (more negative) values of  $\Delta G_r$  (reaction Gibbs energy). The  $\Delta G_r$  is usually defined as:

$$\Delta G_r = \sum G(\text{product}) - \sum G(\text{reactant}), \quad (5.1)$$

where  $G$  is the standard Gibbs energy of compound formation.

#### Thermodynamic analysis

The  $\Delta G_r$  values were calculated for the following reactions:



where  $\text{TiO}_2(r)$  is referred to the rutile modification of  $\text{TiO}_2$ . The  $G$  values for  $\text{TiO}_2(r)$ ,  $\text{BaTiO}_3$ ,  $\text{Ba}_2\text{TiO}_4$ ,  $\text{BaCO}_3$ , and  $\text{CO}_2$  were taken from I. Barin.<sup>128</sup> It should be noted that the  $G$  values for anatase  $\text{TiO}_2$  are rather close to those of  $\text{TiO}_2(r)$  and, thus, the calculations performed for reactions (5.2)-(5.5) with  $\text{TiO}_2(r)$  can be extrapolated to the anatase  $\text{TiO}_2$ . Below, the discussion will be always referred to  $\text{TiO}_2(r)$ .

$\Delta G_r$  values for reactions (5.2)-(5.5) are strongly dependent on the partial pressure of  $\text{CO}_2$  (in air  $P_{\text{CO}_2}$  is 0.381 mbar, in vacuum  $P_{\text{CO}_2}$  during the experiments was lower than  $1 \times 10^{-5}$  mbar) which is described as:<sup>157</sup>

$$G_{\text{CO}_2} = G + nRT \ln \frac{P_{\text{CO}_2}}{P_0}, \quad (5.6)$$

where  $G$  is the standard Gibbs energy of  $\text{CO}_2$  gas at  $P_{\text{CO}_2} = 1$  bar,  $n$  is the number of  $\text{CO}_2$  molecules released,  $R$  is the gas constant,  $T$  is the temperature,  $P_{\text{CO}_2}$  is a partial pressure of  $\text{CO}_2$  gas and  $P_0$  is the standard pressure of 1 bar. The results of the thermodynamic calculations for reactions (5.2)-(5.5) are shown in Figs. 5.1(a)-(d).

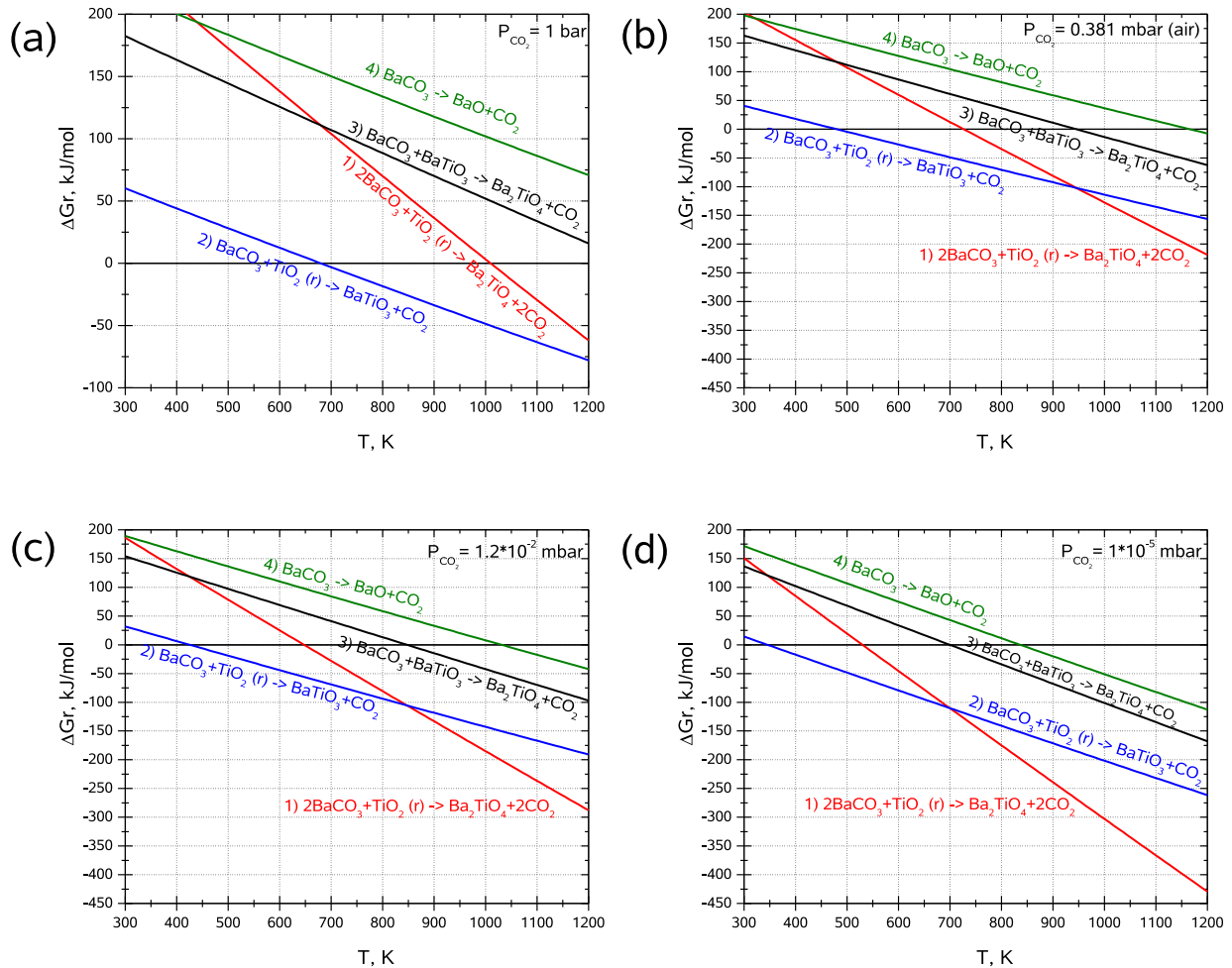


**Fig. 5.1.** Change in Gibbs free energy ( $\Delta G_r$ ) vs  $T$  during reactions under different partial pressures of  $\text{CO}_2$ : (a)  $P_{\text{CO}_2} = 1$  bar, (b)  $P_{\text{CO}_2} = 0.381$  mbar, (c)  $P_{\text{CO}_2} = 1.2 \times 10^{-2}$  mbar and (d)  $P_{\text{CO}_2} = 1 \times 10^{-5}$  mbar. Calculated from values given in I. Barin.<sup>128</sup>

As can be seen from Fig. 5.1, the preferred formation of either the  $\text{Ba}_2\text{TiO}_4$  or  $\text{BaTiO}_3$  phase by reaction between  $\text{BaCO}_3$  and  $\text{TiO}_2$  is a function of  $P_{\text{CO}_2}$ . The temperatures at which the formation of  $\text{Ba}_2\text{TiO}_4$  is more likely compared to the formation of  $\text{BaTiO}_3$  are lowered with a decreasing of  $P_{\text{CO}_2}$ .

### A possible mechanism of $\text{BaTiO}_3$ formation in vacuum

During the solid-solid reactions in vacuum the intermediate  $\text{Ba}_2\text{TiO}_4$  compound forms at the beginning of heating by direct reaction between barium carbonate grains and rutile single crystal. The time required for the formation of  $\text{Ba}_2\text{TiO}_4$  observed in this work is low compared to the decomposition time of  $\text{BaCO}_3$  reported by Judd *et al.*<sup>158</sup> or by L'vov.<sup>159</sup> Thus, a direct reaction of  $\text{BaCO}_3$  with  $\text{TiO}_2$  is expected. This is also supported by our thermodynamic calculations presented in Fig. 5.1(d). From these calculations, the decomposition of  $\text{BaCO}_3$  into  $\text{BaO}$  and  $\text{CO}_2$  (reaction (4) in Fig. 5.1(d)) or the formation of  $\text{Ba}_2\text{TiO}_4$  by a reaction between  $\text{BaTiO}_3$  and  $\text{BaCO}_3$  in vacuum at 575 °C is relatively unfavourable compared to the formation of  $\text{Ba}_2\text{TiO}_4$  or  $\text{BaTiO}_3$  by a reaction between  $\text{BaCO}_3$  and  $\text{TiO}_2$  (reaction (1) or (2) in Fig. 5.1(d)) due to an only small decrease in the Gibbs energy. The  $\Delta G_r$  values for the formation of  $\text{Ba}_2\text{TiO}_4$  (-205.9 kJ/mol) and  $\text{BaTiO}_3$  (-155.6 kJ/mol) at 575 °C are distinctly different, with a higher (more negative) value for  $\text{Ba}_2\text{TiO}_4$ . Thus, the phase  $\text{Ba}_2\text{TiO}_4$  will always nucleate and grow as the first phase in vacuum. This reaction will continue up to all  $\text{BaCO}_3$  is consumed. The formation of  $\text{BaTiO}_3$  by a direct reaction between  $\text{BaCO}_3$  and  $\text{TiO}_2$  in vacuum could be suppressed due to a  $\text{Ba}_2\text{TiO}_4$  diffusion barrier. Thus,  $\text{BaTiO}_3$  is formed by a reaction between  $\text{Ba}_2\text{TiO}_4$  and  $\text{TiO}_2$ .

Different formation mechanisms of  $\text{Ba}_2\text{TiO}_4$  and  $\text{BaTiO}_3$  can be assumed based on the differences in the orientations of both phases in dependence on the orientation of  $\text{BaCO}_3$  grown on the rutile substrates. The orientation of  $\text{Ba}_2\text{TiO}_4$  is strongly dependent on the orientation of  $\text{BaCO}_3$ , while the orientation of  $\text{BaTiO}_3$  grains is independent of the orientation of  $\text{BaCO}_3$ . Thus, the formation of  $\text{Ba}_2\text{TiO}_4$  might be dominated by diffusion of Ti ions into the  $\text{BaCO}_3$  matrix. In contrast,  $\text{BaTiO}_3$  grains might be formed by in-diffusion of Ba ions into the  $\text{TiO}_2$  lattice.

From the above discussion, it is clearly seen that neither the first scheme nor the second scheme proposed by Beauger *et al.*<sup>69</sup> to describe the phase formation sequence during  $\text{BaTiO}_3$  synthesis in vacuum is valid. The heating of nanocrystalline  $\text{BaCO}_3$  and  $\text{TiO}_2$  powders under pressure of 40 mbar at 740 °C performed by Buscaglia *et al.*<sup>18</sup> showed a significant formation of  $\text{Ba}_2\text{TiO}_4$  phase in the powder after the calcination. This results fits well to the description developed in this thesis.

### A possible mechanism of $\text{BaTiO}_3$ formation in air

During the solid-solid reactions in air the  $\text{BaTiO}_3$  compound forms at the beginning of heating (575 °C) by reaction between barium carbonate grains and rutile single crystal. Similar to the reaction in vacuum, a direct reaction between  $\text{BaCO}_3$  and  $\text{TiO}_2$  has occurred. The formation of  $\text{BaTiO}_3$  in air by direct reaction between  $\text{BaCO}_3$  and  $\text{TiO}_2$  was also proposed by Beauger *et al.*<sup>69</sup> and by Buscaglia *et al.*<sup>18</sup>. Thermodynamic estimations showed that  $\text{BaCO}_3$  is a stable phase in air until 880 °C due to positive values of the Gibbs free energy for the decomposition of  $\text{BaCO}_3$  (Fig. 5.1(b)).

In air, the  $\Delta G_r$  value for  $\text{BaTiO}_3$  formation at 575 °C (-82.9 kJ/mol) is more negative than for  $\text{Ba}_2\text{TiO}_4$  formation at 575 °C (-60.5 kJ/mol) while at temperatures higher than 657 °C the  $\Delta G_r$  values for  $\text{Ba}_2\text{TiO}_4$  formation become more negative than for  $\text{BaTiO}_3$  formation. Consequently,

$\text{BaTiO}_3$  can be nucleated during heating at 575 °C as the first phase in air. This description is supported by the results obtained by Buscaglia *et al.*<sup>14</sup> Initial formation of  $\text{BaTiO}_3$  was observed after heating of  $\text{BaCO}_3$  (core) -  $\text{TiO}_2$  (shell) powders at temperatures between 500 °C and 550 °C, in agreement with our observations and thermodynamic calculations (Fig. 5.1(b)). According to previous studies,<sup>12,18,69,70</sup> the formation of a  $\text{BaTiO}_3$  layer occurs at the interface  $\text{BaCO}_3\text{/TiO}_2$  by in-diffusion of Ba ions into  $\text{TiO}_2$ . In our case, the nucleation of  $\text{BaTiO}_3$  might also have occurred by in-diffusion of Ba into  $\text{TiO}_2$ .

The formation of the  $\text{Ba}_2\text{TiO}_4$  compound by direct reaction of  $\text{BaCO}_3$  with  $\text{TiO}_2$  substrates in air at temperatures higher than 575 °C may be suppressed due to a diffusion barrier induced by  $\text{BaTiO}_3$  grains which are nucleated on heating at 575 °C. However, the formation of  $\text{Ba}_2\text{TiO}_4$  in air is considered possible by a reaction between  $\text{BaCO}_3$  and beforehand formed  $\text{BaTiO}_3$  at its expense at temperatures above 800 °C. In this work,  $\text{Ba}_2\text{TiO}_4$  was not observed to form by the reaction between  $\text{BaCO}_3$  and  $\text{BaTiO}_3$  after heating in air at temperatures between 600 °C and 700 °C (see Table 1). From a thermodynamical point of view, the formation of  $\text{Ba}_2\text{TiO}_4$  by a reaction between  $\text{BaCO}_3$  and  $\text{BaTiO}_3$  up to temperatures 644 °C is hindered due to positive values of  $\Delta G_r$ . We used only a thin layer of  $\text{BaCO}_3$  (50 nm) and at a temperature of 650 °C this layer was reacted rapidly to  $\text{BaTiO}_3$ .

### **b. Reaction at high temperature (1000 °C)**

Ti-rich barium titanates were observed after solid-solid reaction in vacuum and in air at high temperature. In the bulk phase diagram of the  $\text{BaO}\text{-TiO}_2$  system, the compounds  $\text{BaTi}_4\text{O}_9$  and  $\text{Ba}_4\text{Ti}_{13}\text{O}_{30}$  exist between temperatures of about 900 °C and 1400 °C. The  $\text{BaTi}_4\text{O}_9$  and  $\text{Ba}_4\text{Ti}_{13}\text{O}_{30}$  compounds were observed in our experiments after reaction at 1000 °C.

## **B. Vapour-solid reaction of $\text{BaO}$ vapour with $\text{TiO}_2$**

### **a. Reaction at low temperature (575 °C-800 °C)**

During the vapour-solid reaction, a reaction between  $\text{BaO}$  and  $\text{TiO}_2$  has occurred. As can be seen from Fig. 5.2, the formation of  $\text{BaTiO}_3$  by a reaction between  $\text{BaO}$  and  $\text{TiO}_2$  at 575 °C is relatively unfavourable compared to the formation of  $\text{Ba}_2\text{TiO}_4$  by a reaction between  $\text{BaO}$  and  $\text{TiO}_2$  due to an only small decrease in the values of  $\Delta G_r$  with increasing temperature.

During the vapour-solid reaction, surface diffusion may be predominant, and independent nucleation events at surface defects may have occurred. Thus, a similar nucleation probability of  $\text{BaTiO}_3$  and  $\text{Ba}_2\text{TiO}_4$  during the vapour-solid reaction may have facilitated the initial formation of both phases at 600 °C observed in this work.

### **b. Reaction at high temperature (900 °C-1000 °C)**

The  $\text{Ba}_6\text{Ti}_{17}\text{O}_{40}$  Ti-rich phase was found after vapour-solid reaction at high temperature. However, the  $\text{BaO}\text{-TiO}_2$  phase diagram<sup>78</sup> permits the formation of several Ti-rich phases, some of which should form more easily than  $\text{Ba}_6\text{Ti}_{17}\text{O}_{40}$  at low temperatures. The occurrence and relative contribution of the different Ti-rich phases was investigated by Ritter *et al.*<sup>78</sup> who studied the

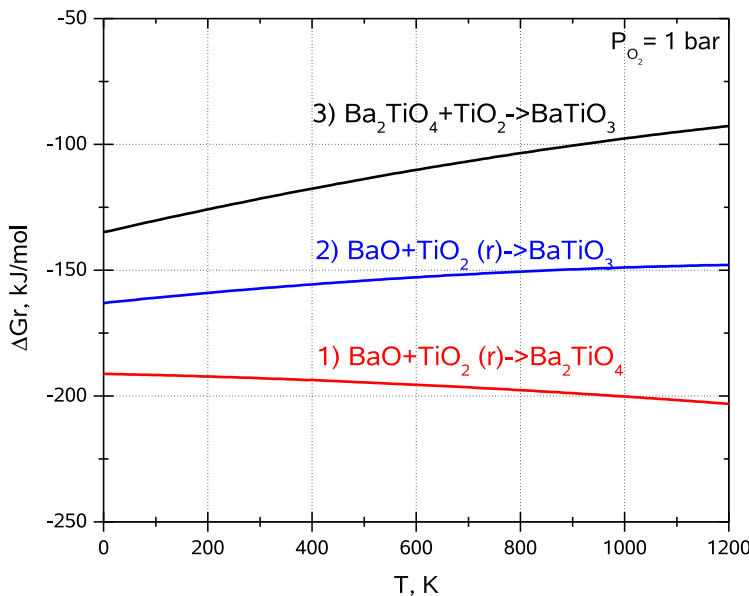


**Fig. 5.2.** Change in standard Gibbs free energy ( $\Delta G_r$ ) vs T during vapour-solid reaction. Calculated from values given in I. Barin.<sup>128</sup>

crystallisation of amorphous Ba-Ti-O compounds prepared by a metalorganic chemical precursor method at temperatures between 600 °C and 1500 °C in air. They found that the  $\text{Ba}_4\text{Ti}_{13}\text{O}_{30}$  phase is obtained most easily even at lower temperatures than the  $\text{Ba}_6\text{Ti}_{17}\text{O}_{40}$  phase. The latter crystallised only above  $\approx 1100$  °C and begins to decompose into  $\text{BaTi}_2\text{O}_5$  and  $\text{Ba}_4\text{Ti}_{13}\text{O}_{30}$  below  $\approx 1100$  °C. In the precursor prepared by Ritter *et al.*<sup>78</sup> the three elements Ba, Ti and O are already intermixed on an atomic scale and constraints for the nucleation of crystalline phases are quite different from a reaction between crystalline grains. Thus, the results obtained by Ritter *et al.*<sup>78</sup> do not fit directly to reactions between crystalline materials. In this work, the Ti-rich phases were formed always from crystalline phases. We have found that the  $\text{BaTi}_4\text{O}_9$  and  $\text{Ba}_4\text{Ti}_{13}\text{O}_{40}$  phases were formed after a solid-solid reaction in vacuum and in air (respectively) at 1000 °C for 30 min while  $\text{Ba}_6\text{Ti}_{17}\text{O}_{40}$  was found after a vapour-solid reaction at 900 °C-1000 °C. This difference might be explained by the geometrical nucleation conditions. The vapour-solid reaction allows a nucleation on the free surface of  $\text{TiO}_2$  and obeys the thermodynamic model (EHF) proposed by Pretorius *et al.*<sup>21,22</sup>. The  $\text{BaTiO}_3$ - $\text{TiO}_2$  phase diagram (Fig. 2.8 or Fig. A.1) shows the existence of the lowest eutectic at 1332 °C and an eutectic composition of 68.5 mole %  $\text{TiO}_2$ . Two phases  $\text{BaTiO}_3$  and  $\text{Ba}_6\text{Ti}_{17}\text{O}_{40}$  form an eutectic at this temperature. Thus, the  $\text{Ba}_6\text{Ti}_{17}\text{O}_{40}$  phase will be the first Ti-rich phase to grow at high temperature according to the EHF model. On the other hand, the reaction conditions during a solid-solid experiment are different. Ti diffuses out rapidly and nucleation of Ti-rich barium titanates occurred at  $\text{BaCO}_3$  grain boundaries or at the surface of  $\text{BaCO}_3$ . Unfortunately, the model of Pretorius *et al.*<sup>21,22</sup> cannot explain the formation of  $\text{BaTi}_4\text{O}_9$  or  $\text{Ba}_4\text{Ti}_{13}\text{O}_{30}$  Ti-rich phases observed after solid-solid reaction at high temperature in vacuum and in air, respectively.

## 5.1.2 Orientation relationships

### A. Orientation of $\text{Ba}_2\text{TiO}_4$ on $\text{TiO}_2$ (rutile)

The  $\text{Ba}_2\text{TiO}_4$  phase grew well-oriented with respect to the (110) and (100) rutile substrates. However, the similarity between these two structures is not so obvious. The fundamental structural building elements of  $\text{TiO}_2$  rutile are  $\text{TiO}_6$  octahedra which lie along the [001]  $\text{TiO}_2$  direction while the basic building elements of  $\text{Ba}_2\text{TiO}_4$  are  $\text{TiO}_4$  tetrahedra which lie along the [001]  $\text{Ba}_2\text{TiO}_4$  direction. Thus, there are no common structural elements in the  $\text{TiO}_2$  rutile and  $\text{Ba}_2\text{TiO}_4$  structures. The projections of the (110)  $\text{Ba}_2\text{TiO}_4$ /(110)  $\text{TiO}_2$  and (100)  $\text{Ba}_2\text{TiO}_4$ /(100)  $\text{TiO}_2$  interfaces based on their structural elements in the [001]  $\text{Ba}_2\text{TiO}_4$  || [001]  $\text{TiO}_2$  viewing direction are shown in Fig. 5.3. No features of the two lattices are recognisable that coincidence in this projection. Thus, the rutile structure cannot be taken over by the growing  $\text{Ba}_2\text{TiO}_4$ .

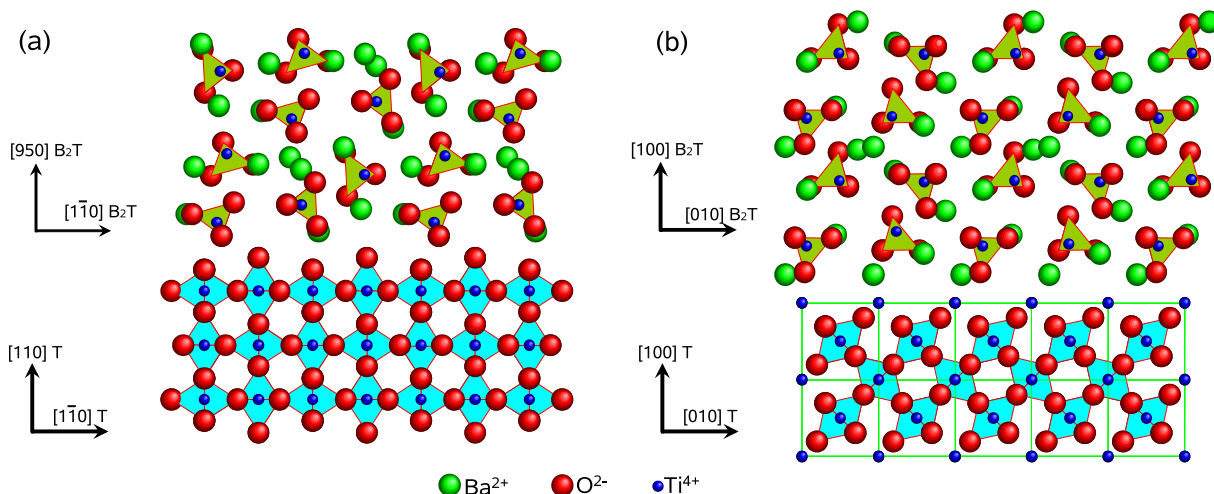


**Fig. 5.3.** Projections of the (110)  $\text{Ba}_2\text{TiO}_4$  ( $\text{B}_2\text{T}$ )/(110)  $\text{TiO}_2$  ( $\text{T}$ ) and (100)  $\text{Ba}_2\text{TiO}_4$ /(100)  $\text{TiO}_2$  interfaces based on their structural elements. Viewing direction is [001]  $\text{Ba}_2\text{TiO}_4$  || [001]  $\text{TiO}_2$ .

As was discussed above,  $\text{Ba}_2\text{TiO}_4$  formed by direct reaction between  $\text{BaCO}_3$  and  $\text{TiO}_2$ . Thus,  $\text{Ti}$  ions seem to be diffusing into the  $\text{BaCO}_3$  film. However, a transformation of  $\text{BaCO}_3$  into  $\text{Ba}_2\text{TiO}_4$  would require a strong shrinkage since the densities are different ( $\rho_{\text{BaCO}_3} = 4.3 \text{ g/cm}^3$ ,  $\rho_{\text{Ba}_2\text{TiO}_4} = 5.2 \text{ g/cm}^3$ ). The structural transformation could in principle occur through an intermediate phase like barium oxycarbonate<sup>160</sup> with a stoichiometry close to  $\text{Ba}_2\text{Ti}_2\text{O}_5(\text{CO}_3)$ . However, nothing is known about the crystal structure of the oxycarbonate phase. In addition, recently it was suggested that the phase commonly attributed in the literature to (Ba,Ti)-oxycarbonate is a barium oxycarbonate,<sup>161</sup> containing no titanium.

### B. Orientations of $\text{BaTiO}_3$ on $\text{TiO}_2$ (rutile)

It has been well established that the growth of films with preferred orientation on a substrate is closely related to surface free energy, film/substrate interface energy as well as misfit strain energy.<sup>162,163</sup> However, during solid state reactions nucleation and diffusion take place so that the system cannot immediately reach thermodynamic equilibrium conditions. Thus, the kinetic

effect of nucleation of thin films with preferred orientation should also be taken into account. The two different solid state reaction geometries used in the present study may lead to two different nucleation conditions.

In the case of a solid-solid reaction, the nucleation of  $BaTiO_3$  might have mainly occurred by diffusion of Ba ions into the  $TiO_2$  lattice. On the other hand, in the case of a vapour-solid reaction, the orientations of the product phases are a complex function of the reaction conditions such as substrate temperature and deposition rate. Surface diffusion may be dominant in the vapour-solid reaction, and a direct nucleation of  $BaTiO_3$  grains on the  $TiO_2$  surface may occur.

One and the same orientation relation of  $BaTiO_3$  on (100)  $TiO_2$  was found after solid-state reactions in vacuum and in air. On the other hand, different orientation relations between the  $BaTiO_3$  grains and the (100)  $TiO_2$  (rutile) substrates were observed after vapour-solid reaction. The orientations of  $BaTiO_3$  grains on the (110)  $TiO_2$  after solid-solid and vapour-solid reaction have similar features but with different sharpness of the tilt distributions. After vapour-solid reaction the orientations of  $BaTiO_3$  on (110)  $TiO_2$  are sharper than after solid-solid reaction in vacuum. Below, we will discuss first the orientation relationships of  $BaTiO_3$  after vapour-solid reaction.

### a. Vapour-solid reaction

#### Growth at low temperatures (575 °C-800 °C)

The  $BaTiO_3$  grains grew oriented with respect to the (110) and (100)  $TiO_2$  substrates. Different orientations were found for  $BaTiO_3$  depending on the substrate temperature and substrate orientation. However, the relation  $[1\bar{1}0] BaTiO_3 \parallel [001] TiO_2$  is ever standing and independent of the orientation of the substrate surface and substrate temperature used. This means that the [001]  $TiO_2$  axis is a common tilt axis for  $BaTiO_3$  grown on (110) and (10)  $TiO_2$  (rutile) surfaces. This is because the (110) and (100) planes of  $TiO_2$  are connected by a tilt of 45° around the [001]  $TiO_2$  axis. Thus, it is expected that the angles between crystal planes of  $BaTiO_3$  grown on (110) and (100)  $TiO_2$  substrates will also be close to 45°. The results of such a consideration are presented in Table 5.1. From Table 5.1, it can be seen that there are only small deviations from the value of 45° ( $\pm 0.8^\circ$ ). Thus, the growth of some  $BaTiO_3$  grains occurs with a three-dimensional orientation relationship with respect to the  $TiO_2$  substrates, irrespective of the orientation of the substrate surface.

**Table 5.1.** Angles between crystal planes observed for  $BaTiO_3$  thin films grown on (100) and (110)  $TiO_2$  substrates. The major orientations are marked by bold font while minors are marked by italic font.

(hkl) $BaTiO_3$ ( $B_1$ ) $\parallel$ (110) $TiO_2$	(hkl) $BaTiO_3$ ( $B_2$ ) $\parallel$ (100) $TiO_2$	$\angle(B_1); (B_2), (^\circ)$
<b>(119)</b>	<b>(111)</b>	45.8
<i>(441)</i>	<b>(112)</b>	44.7

Below, we describe factors influencing the nucleation of  $BaTiO_3$  on  $TiO_2$ . First, the structural similarities between  $TiO_2$  (rutile) and  $BaTiO_3$  (perovskite) will be considered. The fundamental

structural building elements of both the  $\text{TiO}_2$  and  $\text{BaTiO}_3$  structures are  $\text{TiO}_6$  octahedra linked in a three-dimensional network. The octahedra in the  $\text{TiO}_2$  rutile structure are both corner- and edge-shared and lie along the  $[001]$   $\text{TiO}_2$  direction while the octahedra in the perovskite structure are only corner-shared and lie along the  $[1\bar{1}0]$   $\text{BaTiO}_3$  direction. The structural considerations given below are based on a surface of the  $\text{TiO}_2$  (rutile) crystals obtained by simple cutting.

Fig. 5.4 shows a schematic projection of the  $\text{BaTiO}_3\text{/TiO}_2$  interfaces constructed from  $\text{TiO}_6$  octahedra for different orientations of  $\text{BaTiO}_3$  grown on  $(110)$   $\text{TiO}_2$  surfaces looking along the  $[1\bar{1}0]$   $\text{BaTiO}_3 \parallel [001]$   $\text{TiO}_2$  direction. The different types of linkage of  $\text{TiO}_6$  octahedra in the two

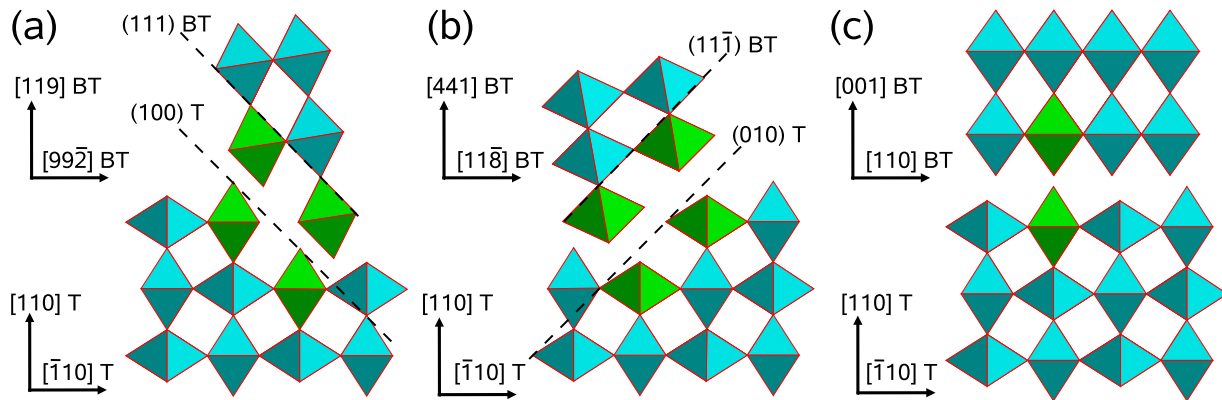


**Fig. 5.4.** Schematic representations of projections based on  $\text{TiO}_6$  octahedra for (a)  $(119)$   $\text{BaTiO}_3$  (BT)/(110)  $\text{TiO}_2$  (T), (b)  $(441)$   $\text{BaTiO}_3$ /(110)  $\text{TiO}_2$ , (c)  $(001)$   $\text{BaTiO}_3$ /(110)  $\text{TiO}_2$ . Viewing direction is  $[1\bar{1}0]$   $\text{BaTiO}_3 \parallel [001]$   $\text{TiO}_2$  for all projections. The highlighted octahedra are octahedra required for the nucleation of  $\text{BaTiO}_3$  (for more details see text). Both lattices are repeated perpendicular to the projection plane and thus the marked octahedra in 3D space make chains of octahedra parallel to the viewing direction.

structures are clearly seen in Fig. 5.4, making structural considerations easy. The presence of  $(119)$ - and  $(441)$ -oriented  $\text{BaTiO}_3$  grains on  $(110)$   $\text{TiO}_2$  substrates can be explained by the fact that the surface of  $(110)$   $\text{TiO}_2$  substrates has terraces which are separated by monoatomic step edges running predominantly along  $[001]$   $\text{TiO}_2$  and  $[1\bar{1}0]$   $\text{TiO}_2$  directions.<sup>164</sup> The step edges lying along the  $[001]$   $\text{TiO}_2$  direction may favour the nucleation of  $(119)$ -oriented  $\text{BaTiO}_3$  grains as shown in Fig. 5.4(a) as well as nucleation of  $(441)$ -oriented  $\text{BaTiO}_3$  grains as shown in Fig. 5.4(b). In both these cases, for the nucleation of  $(119)$ - and  $(441)$ -oriented  $\text{BaTiO}_3$  grains only two chains of substrate octahedra will be required (the octahedra required for the nucleation are highlighted and small octahedra misorientations are ignored). The nucleation would occur more easily if  $\{100\}$  or  $\{010\}$   $\text{TiO}_2$  facets would be present on the rutile surface. In this case, more than two chains of substrate octahedra can be taken for the nucleation of  $\text{BaTiO}_3$ . Such facets were observed after vapour-solid reaction at  $800$   $^\circ\text{C}$  by HRTEM investigations shown in Fig. 4.23. On these facets,  $(119)$ - and  $(441)$ -oriented  $\text{BaTiO}_3$  grains are found, confirming our suggestions. As was already pointed out above,  $(119)$ - and  $(441)$ -orientations of  $\text{BaTiO}_3$  have one of the  $\{111\}$   $\text{BaTiO}_3$  planes almost parallel to one of the  $\{100\}$   $\text{TiO}_2$  planes in the viewing direction  $[1\bar{1}0]$   $\text{BaTiO}_3 \parallel [001]$   $\text{TiO}_2$ . The highlighted octahedra of  $\text{BaTiO}_3$  in Fig. 5.4(a) show a  $(111)$  plane of  $\text{BaTiO}_3$  which is almost parallel to the  $(100)$  plane of  $\text{TiO}_2$  whereas the highlighted octahedra of  $\text{BaTiO}_3$  in Fig. 5.4(b) show a  $(11\bar{1})$  plane of  $\text{BaTiO}_3$  which is almost parallel to the  $(010)$  plane of  $\text{TiO}_2$ . Thus,

the growth of (119)- and (441)-orientations of  $\text{BaTiO}_3$  is obviously determined by the condition that one of its close-packed  $\{111\}$  planes of  $\text{BaTiO}_3$  is parallel to one of the rather close-packed  $\{100\}$  planes of the  $\text{TiO}_2$  substrate. The (111) orientation of  $\text{BaTiO}_3$  was observed on (100)  $\text{TiO}_2$  surfaces, details will be discussed below. In addition, the octahedra of a [001] monoatomic step edge of the (110)  $\text{TiO}_2$  surface are octahedra belonging to  $\{100\}$  planes of  $\text{TiO}_2$ . Consequently, the nucleation of (119)- and (441)-orientations of  $\text{BaTiO}_3$  on the [001] steps of the (110)  $\text{TiO}_2$  surface is plausible. However, the (001)-orientation of  $\text{BaTiO}_3$  cannot be explained by the reasons shown above. This case is illustrated in Fig. 5.4(c). Only one octahedron of  $\text{BaTiO}_3$  matches to the substrate octahedra. The nucleation of (001)-oriented  $\text{BaTiO}_3$  grains will be possible only if one chain of octahedra of  $\text{TiO}_2$  is taken over by the growing  $\text{BaTiO}_3$  (the octahedra required for the nucleation are highlighted). The octahedra of  $\text{BaTiO}_3$  belonging to the (111) plane of  $\text{BaTiO}_3$  deviate from the octahedra of  $\{100\}$  planes of  $\text{TiO}_2$  by  $9.7^\circ$  ( $\angle \text{BaTiO}_3 (001); (111) = 54.7^\circ$  while  $\angle \text{TiO}_2 (110); (100) = 45^\circ$ ). It is worth to mention that the nucleation of  $\text{BaTiO}_3$  on (110)  $\text{TiO}_2$  substrates will occur as line only in one  $[1\bar{1}0] \text{BaTiO}_3 \parallel [001] \text{TiO}_2$  direction. This is because  $\text{TiO}_6$  octahedra in  $\text{TiO}_2$  and  $\text{BaTiO}_3$  are connected with different topology. In  $\text{BaTiO}_3$ , the columns of edge-shared  $\text{TiO}_6$  octahedra are missing.

Fig. 5.5 shows a schematic projection of the  $\text{BaTiO}_3\text{/TiO}_2$  interfaces constructed from  $\text{TiO}_6$  octahedra for different orientations of  $\text{BaTiO}_3$  grown on (100)  $\text{TiO}_2$  surfaces, looking along the  $[1\bar{1}0] \text{BaTiO}_3 \parallel [001] \text{TiO}_2$  direction. Similarities in the alignment of the  $\text{TiO}_6$  octahedra can be

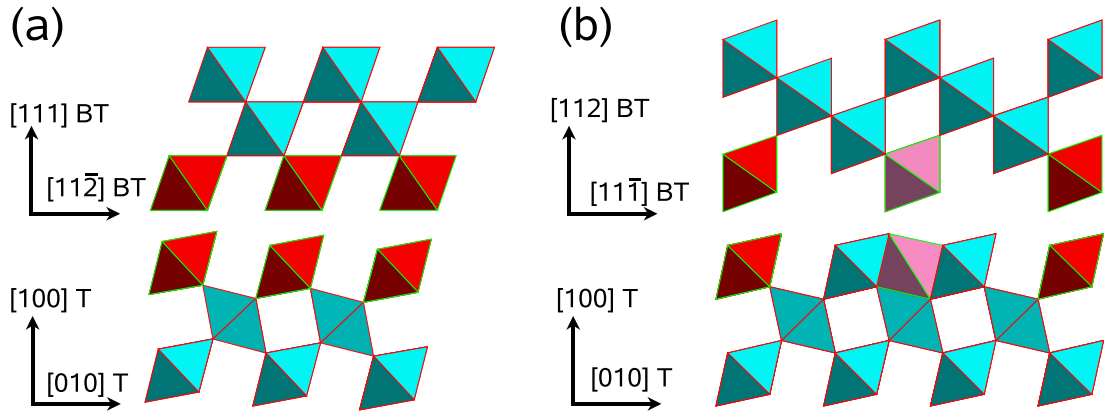


**Fig. 5.5.** Schematic representations of projections based on  $\text{TiO}_6$  octahedra for (a) (111)  $\text{BaTiO}_3$  (BT)/(100)  $\text{TiO}_2$  (T) and (b) (112)  $\text{BaTiO}_3$  (BT)/(100)  $\text{TiO}_2$  (T). Viewing direction is  $[1\bar{1}0] \text{BaTiO}_3 \parallel [001] \text{TiO}_2$  for all projections. The highlighted octahedra are octahedra required for the nucleation of  $\text{BaTiO}_3$  (for more details see text).

seen in Fig. 5.5(a) for the (111)  $\text{BaTiO}_3$  / (100)  $\text{TiO}_2$  interface. Ignoring small misorientations of the octahedra, the (111)-oriented  $\text{BaTiO}_3$  can be nucleated in such a way that the  $\text{TiO}_6$  octahedra of rutile in the surface layer can be taken over by the growing  $\text{BaTiO}_3$  (the octahedra required for the nucleation are highlighted). It should be noted that the situation illustrated in Fig. 5.5(a) is similar to that shown in Fig. 5.4(a). But compared to Fig. 5.5(a), the representation in Fig. 5.4(a) is rotated around the common [001]  $\text{TiO}_2$  axis by  $45^\circ$ , showing the three-dimensional orientation relationship of  $\text{BaTiO}_3$  with respect to the  $\text{TiO}_2$  substrates in the case of (111)- and (119)-oriented

$\text{BaTiO}_3$  grains. The presence of (112)-oriented  $\text{BaTiO}_3$  grains on (100)  $\text{TiO}_2$  substrates can be explained by the fact that the surface of (100)  $\text{TiO}_2$  reconstructs dramatically from (1×1) to (1×3) when heated in vacuum. However, the detailed surface geometry of the reconstruction is not well known. Two microfacet models are shown in Figs. A.13<sup>165</sup>-A.14<sup>166</sup> (see appendix). In addition, adsorption of Ba may influence the surface geometry of (100)  $\text{TiO}_2$ . Thus, one might speculate that the structural model of the (100) surface of  $\text{TiO}_2$  shown in Fig. 5.5(b) could exist. This surface structure may favour the nucleation of (112)-oriented  $\text{BaTiO}_3$  grains as shown in Fig. 5.5(b). It is worth to mention that the surface structure of the (100)  $\text{TiO}_2$  presented in Fig. 5.5(b) can be simply obtained from Fig. A.14(b) (see appendix) by removal of the top chain of  $\text{TiO}_6$  octahedra.

Thus, based on structural considerations the reasons for the nucleation of  $\text{BaTiO}_3$  grains on the  $\text{TiO}_2$  surfaces have been shown. On the other hand, the origin of all observed orientations of  $\text{BaTiO}_3$  seems to be determined by the initial stage of the solid state reaction, where the surface morphology of the  $\text{TiO}_2$  surfaces may influence the nucleation kinetics of the grains. As a model system, the (110) and (100) surfaces of  $\text{TiO}_2$  (rutile) are very well investigated. The  $\text{TiO}_2$  surfaces have been shown to exhibit various reconstructions upon annealing at elevated temperatures. The most commonly observed reconstruction of the (100)  $\text{TiO}_2$  surface has a (1×3) structure along the [001]  $\text{TiO}_2$  direction, which appears by annealing in ultrahigh vacuum ( $<10^{-6}$  mbar) at temperatures above 750 °C,<sup>164,167</sup> while the most frequently detected reconstruction on the (110)  $\text{TiO}_2$  surface has a (1×2) superstructure with features along the [001]  $\text{TiO}_2$  direction, which appear by annealing in ultrahigh vacuum ( $\sim 10^{-7}$  mbar) at temperatures higher than 730 °C.<sup>164,168</sup> These reconstructed surfaces are nonstoichiometric and oxygen-deficient. Our experiments were performed using an oxygen pressure of  $(1\text{-}4)\times 10^{-4}$  mbar. Thus, we expect that the temperatures of oxygen losses of the surface are shifted to higher temperatures compared to heating in ultrahigh vacuum. The interaction of different metals and metal oxides with the single crystalline  $\text{TiO}_2$  surfaces has also been investigated.<sup>164</sup> When a Ca overlayer formed by Ca metal vapour deposition (up to a monolayer (ML) coverage) or by precipitation from the bulk of (110)  $\text{TiO}_2$  crystals is annealed at  $\sim 800$  °C for several hours, well-ordered  $c(6\times 2)$  overlayers are formed.<sup>169</sup> At a calcium coverage of  $\approx 1.2$  ML, two coexisting structures (the ordered  $c(6\times 2)$  and a "disordered" structure) were observed. At higher calcium coverage, only a highly "disordered" structure was found and it completely covered the rutile substrate.<sup>169</sup> No experimental data on the influence of Sr or Ba on the reconstruction of rutile surfaces have been reported up to now. Since they are alkaline-earth metals, like Ca, the formation of various surface structures after adsorption of Ba or Sr on hot rutile substrates is expected. The nucleation kinetics and conditions on these changed  $\text{TiO}_2$  surfaces may be different. As a consequence, a nucleation of differently oriented  $\text{BaTiO}_3$  grains may occur with some of them being favoured during the initial stage of the nucleation.

### Growth at high reaction temperature (900 °C)

After vapour-solid reaction of BaO with (100)  $\text{TiO}_2$  substrates at 900 °C,  $\text{BaTiO}_3$  of several different orientations was observed on top of the  $\text{Ba}_6\text{Ti}_{17}\text{O}_{40}$  phase. The investigation of the initial stage of the vapour-solid reaction of a 1 nm thick BaO layer with the (100)  $\text{TiO}_2$  substrate at this

temperature showed that both  $\text{BaTiO}_3$  and  $\text{Ba}_6\text{Ti}_{17}\text{O}_{40}$  phases nucleate during the initial stage of the reaction. However, the density of the Ti-rich grains was much larger than that of the (111)-oriented  $\text{BaTiO}_3$  grains. Thus, with increasing reaction time (increasing amount of  $\text{BaO}$ ),  $\text{BaTiO}_3$  grains will nucleate on the as-formed  $\text{Ba}_6\text{Ti}_{17}\text{O}_{40}$  grains, which now play the role of a substrate for  $\text{BaTiO}_3$  growth. Thus, the orientations of  $\text{BaTiO}_3$  grains are mainly given by the orientation of the  $\text{Ba}_6\text{Ti}_{17}\text{O}_{40}$  grains. The topotaxial relationship of  $\text{BaTiO}_3$  with respect to  $\text{Ba}_6\text{Ti}_{17}\text{O}_{40}$  results in the orientation (111)  $\text{BaTiO}_3 \parallel$  (001)  $\text{Ba}_6\text{Ti}_{17}\text{O}_{40}$ . The tilt of the (001)  $\text{Ba}_6\text{Ti}_{17}\text{O}_{40}$  plane can be calculated from the tilt of the (100)  $\text{Ba}_6\text{Ti}_{17}\text{O}_{40}$  plane using the angle  $\beta = 98.7^\circ$  between them. The result of this calculation is a tilt of the (001)  $\text{Ba}_6\text{Ti}_{17}\text{O}_{40}$  plane around the [010]  $\text{Ba}_6\text{Ti}_{17}\text{O}_{40} \parallel$  [001]  $\text{TiO}_2$  axis by  $8.7^\circ$  to  $17.7^\circ$ . Corresponding tilts of  $\text{BaTiO}_3$  grains were indeed observed, confirming the above discussion.

### b. Solid-solid reaction

One orientation of  $\text{BaTiO}_3$  on (100)  $\text{TiO}_2$  was observed after solid-state reactions in vacuum and in air. The  $\text{BaTiO}_3$  grew with (111) orientation. It can be explained by the crystallographic reasons shown above.

The orientations of  $\text{BaTiO}_3$  grains on the (110)  $\text{TiO}_2$  surface after solid-solid reaction in vacuum were found to be similar to those observed after vapour-solid reaction. However, the tilt distributions of  $\text{BaTiO}_3$  grains in the thin films after the reaction in vacuum were not sharp. The number of (001)-oriented  $\text{BaTiO}_3$  grains in the thin films produced by a solid-solid reaction were higher than after a vapour-solid reaction. After vapour-solid reaction, (119)- and (441)-oriented  $\text{BaTiO}_3$  grains were observed on {100} facets of  $\text{TiO}_2$  which favour the nucleation of these two orientations. On the other hand, the frequently observed facets on the (110)  $\text{TiO}_2$  surface after solid-solid reaction are nearly {110}  $\text{TiO}_2$  facets (see Fig. A.15 in the appendix). Thus, the nucleation of  $\text{BaTiO}_3$  mainly occurred on {110} surfaces of  $\text{TiO}_2$  which favour the nucleation of (001)-oriented  $\text{BaTiO}_3$  grains. The structural considerations for the nucleation of (001)-oriented  $\text{BaTiO}_3$  grains as well as for the nucleation of (119)- and (441)-oriented  $\text{BaTiO}_3$  grains on (110)  $\text{TiO}_2$  were shown above (see Fig. 5.4). All observed orientation relationships of  $\text{BaTiO}_3$  on  $\text{TiO}_2$  (rutile) after both types of the solid state reactions can be explained in terms of a NCSL model (see Table 4.1).

## C. Orientations of $\text{BaTiO}_3$ on $\text{TiO}_2$ (anatase)

The observed orientation relationships between  $\text{BaTiO}_3$  and epitaxial  $\text{TiO}_2$  (anatase) thin films can be explained in terms of their crystal structures. As was mentioned above,  $\text{BaTiO}_3$  has a similar structure as  $\text{SrTiO}_3$ . Epitaxial  $\text{TiO}_2$  (anatase) thin films were obtained on  $\text{SrTiO}_3$  substrates. Epitaxial formation of  $\text{TiO}_2$  (anatase) on  $\text{SrTiO}_3$  is a result of a similar orientation of  $\text{TiO}_6$  octahedra at the  $\text{TiO}_2/\text{SrTiO}_3$  interface (see Subsection 4.2.1c of Section 4.2). The same crystallographic reason is valid for  $\text{BaTiO}_3$  produced by solid state reactions on epitaxial  $\text{TiO}_2$  (anatase) thin films since  $\text{BaTiO}_3$  has similar epitaxial orientation relationships with respect to  $\text{TiO}_2$  (anatase). The epitaxial orientation relationship between  $\text{BaTiO}_3$  and (001)  $\text{TiO}_2$  (anatase) thin films observed in this work is in agreement with the epitaxial relation obtained for  $\text{BaTiO}_3$  grown in alkaline

aqueous solutions using  $TiO_2$  (anatase) powder<sup>170</sup> or for  $BaTiO_3$  produced by solid-solid reaction between  $TiO_2$  (anatase) single crystals and a barium salt.<sup>171</sup> The observed orientation relationships of  $BaTiO_3$  on  $TiO_2$  (anatase) can be explained in terms of a NCSL model (see Table 4.2).

## D. Orientations of Ti-rich phases on $TiO_2$ (rutile)

### a. Solid-solid reaction

Ti-rich phases were grown in both types of solid state reactions at high reaction temperatures, but with quite different textures. Oriented  $Ba_6Ti_{17}O_{40}$  grains were formed after vapour-solid reaction at substrate temperatures between 900 °C and 1000 °C. Contrary to the vapour-solid reaction, polycrystalline  $BaTi_4O_9$  and  $Ba_4Ti_{13}O_{30}$  (with fiber texture) phases were found after the solid-solid reaction at 1000 °C in vacuum and in air, respectively. These differences are caused by the reaction conditions changing with reaction geometry. During the vapour-solid reaction, the  $BaO$  vapour directly reacts with the  $TiO_2$  rutile surfaces. In this case, the orientations of the reaction products are determined only by the orientation of the substrate. Thus, the nucleation directly on the rutile single crystal surface results in well-oriented Ti-rich grains (details are shown below). The initial reaction during solid-solid experiments seems to be dominated by Ti out-diffusion. At low reaction temperatures,  $Ba_2TiO_4$  with an orientation influenced by the orientation of  $BaCO_3$  was observed. If this behaviour is extrapolated to high temperatures, we can expect a more rapid Ti out-diffusion that results in a high Ti concentration at  $BaCO_3$  grain boundaries and on top of the  $BaCO_3$  layer. The nucleation of Ti-rich phases now occurs without a direct interface to the substrate surface and thus results in a random orientation of the Ti-rich phases.

### b. Vapour-solid reaction

$Ba_6Ti_{17}O_{40}$  grows well-oriented with respect to the (110)  $TiO_2$  substrate as well as to the (100)  $TiO_2$  substrate. This feature can be explained on the basis of the crystallographic similarity of the two lattices.

A schematic projection of the  $Ba_6Ti_{17}O_{40}$ / $TiO_2$  interface for the observed orientation of the Ti-rich phase on a (110)  $TiO_2$  substrate is shown in Fig. 5.6 looking along the [010]  $Ba_6Ti_{17}O_{40}$  || [001]  $TiO_2$  direction. Similarities can be found in the arrangements of oxygen sublattices of the  $Ba_6Ti_{17}O_{40}$  and  $TiO_2$  (rutile) structure. However, small deviations of the oxygen positions in  $Ba_6Ti_{17}O_{40}$  (Fig. 5.6(a)) from those in  $TiO_2$  (Fig. 5.6(b)) are seen. This is due to different types of linkage of the  $TiO_6$  octahedra in the two structures. In addition, the (001) and ( $\bar{1}02$ ) planes of  $Ba_6Ti_{17}O_{40}$  are joined by a tilt of 47.88° around the [010]  $Ba_6Ti_{17}O_{40}$  axis, whereas the (010) and (110) planes of  $TiO_2$  are aligned by a tilt of 45° around the [001]  $TiO_2$  axis. Thus, from these considerations, it is very probable that the growth of  $Ba_6Ti_{17}O_{40}$  on  $TiO_2$  rutile substrates is topotaxial. The small deviations from perfect orientation are a result of the monoclinic distortion of the  $Ba_6Ti_{17}O_{40}$  lattice.

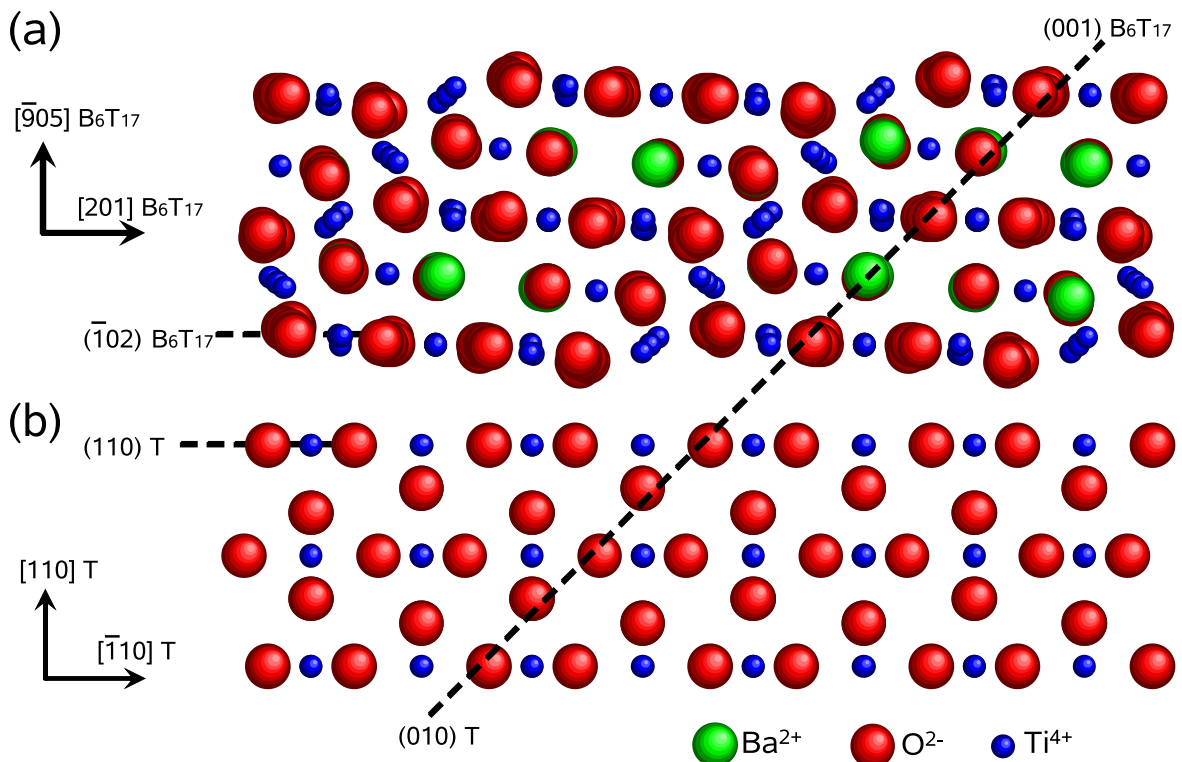


**Fig. 5.6.** Schematic cross-section representation of the interface between the  $\text{Ba}_6\text{Ti}_{17}\text{O}_{40}$  phase ( $\text{B}_6\text{T}_{17}$ ) and  $\text{TiO}_2$  (rutile) substrate (T) looking along the  $[010] \text{B}_6\text{T}_{17} \parallel [001] \text{T}$  direction. The orientation relationship is  $(001) \text{B}_6\text{T}_{17} \parallel (010) \text{T}$  and  $[010] \text{B}_6\text{T}_{17} \parallel [001] \text{T}$ . The dashed line indicates  $(001) \text{B}_6\text{T}_{17} \parallel (010) \text{T}$ .

### 5.1.3 Reaction of $\text{BaO}$ vapour with $\text{TiO}_2$ surfaces at 900 °C

#### A. Reaction mechanism

Based on TEM investigations and structural considerations, the following reaction mechanism between  $\text{BaO}$  vapour and  $\text{TiO}_2$  surfaces at 900 °C can be considered. The vapour-solid reaction starts with the surface diffusion of Ba-O species arriving on the hot  $\text{TiO}_2$  surface. The reaction leads to the nucleation and formation of small  $\text{Ba}_6\text{Ti}_{17}\text{O}_{40}$  grains. It is reasonable to assume that steps on the  $\text{TiO}_2$  surface (see the dashes in Fig. 4.14) are preferred sites for the nucleation of  $\text{Ba}_6\text{Ti}_{17}\text{O}_{40}$ . The height of one normal step of the  $(110) \text{TiO}_2$  surface is 0.32 nm while the height of one step of the  $(\bar{1}02) \text{Ba}_6\text{Ti}_{17}\text{O}_{40}$  surface (see Fig. 5.6(a)) is 0.17 nm. The nucleation could occur more easily if steps with lower heights would be present on the rutile surface. The presence of surface defects like crystallographic shear planes (CSPs) or added rows of  $\text{Ti}_2\text{O}_3$  forming on the  $(110) \text{TiO}_2$  surface after high-temperature annealing in ultrahigh-vacuum was reported by Bennet *et al.*<sup>172</sup> The height of one CSP is  $\approx 0.16$  nm which fits well to the height of one step of the  $\text{Ba}_6\text{Ti}_{17}\text{O}_{40}$  surface. Thus, the nucleation of  $\text{Ba}_6\text{Ti}_{17}\text{O}_{40}$  phase might have been favoured due to surface defects created on the  $(110)$  rutile substrates by heating in our high-vacuum chamber. The Ti-rich phase nucleates by Ba in-diffusion while the film growth proceeds mainly by surface diffusion. With increasing amount of  $\text{BaO}$ , the Ti-rich islands coalesce and form a nearly continuous thin film. This film induces a diffusion barrier for Ti out-diffusion. Thus, the concentration

of Ti ions on top of the  $\text{Ba}_6\text{Ti}_{17}\text{O}_{40}$  layer decreases. As a consequence,  $\text{BaTiO}_3$  grains nucleate on top of the film consisting of Ti-rich grains. Due to a certain similarity between the  $\text{BaTiO}_3$  and  $\text{Ba}_6\text{Ti}_{17}\text{O}_{40}$  lattices, a definite crystallographic orientation of  $\text{BaTiO}_3$  results. As is well-known, the (001) planes of  $\text{Ba}_6\text{Ti}_{17}\text{O}_{40}$  can be compatibly attached to the (111) planes of  $\text{BaTiO}_3$ , forming a topotactic boundary.<sup>98</sup> Here, we observed a similar topotaxial orientation relationship as the one published in Ref.<sup>98</sup>, confirming the above discussion. The topotaxial reaction involves the transformation of (111) planes of  $\text{BaTiO}_3$  into (001) planes of the Ti-rich phase by removal of BaO and insertion of  $\text{TiO}_2$ .

## B. Void formation

Large pores have been observed after vapour-solid reaction of a BaO quantity equivalent to a nominal film thickness of 50 nm at the  $\text{TiO}_2$  (rutile)/Ti-rich or  $\text{TiO}_2$  (anatase)/Ti-rich interface at 900 °C in this work, as well as after vapour-solid reaction of a BaO quantity equivalent to a nominal film thickness of 100 nm at the  $\text{TiO}_2$  (rutile)/Ti-rich interface at 900 °C in Ref.<sup>173</sup>. The formation of voids is usually attributed to the Kirkendall effect.<sup>174,175</sup> The latter was originally observed in bulk diffusion couples of Cu and CuZn ( $\alpha$ -brass or Cu-30wt% Zn). Mo-wire markers which were placed at the original Cu/CuZn interface had moved into the  $\alpha$ -brass, showing that the Zn flux was greater than that of Cu. Thus, different diffusion rates of the atoms moving in and out of the interface between two reacting materials caused a net flux of vacancies which may subsequently lead to the formation of voids at the interface of two materials. This phenomenon is completely general in metallic systems with a simple system of lattice sites. Recently, the Kirkendall effect was applied to explain the formation of hollow spherical nanocrystals<sup>176</sup> and monocrystalline  $\text{ZnAl}_2\text{O}_4$  spinel nanotubes.<sup>177</sup> Thermodynamic and kinetic aspects of this effect which might contribute to the design, fabrication route, and materials choice of hollow nanostructures were given by Tu and Gösele.<sup>178</sup>

Below, we propose a model describing the formation of void at the interface with the  $\text{TiO}_2$  (rutile) surfaces. After the initial stage of a vapour-solid reaction with a BaO quantity equivalent to a nominal film thickness of 1 nm the formation of  $\text{Ba}_6\text{Ti}_{17}\text{O}_{40}$  islands was observed (Fig. 5.7(a), see also Figs. 4.14-4.15). No voids are formed at the  $\text{TiO}_2$  (rutile)/Ti-rich interface at this stage of the reaction. The Ti-rich phase nucleates by Ba in-diffusion while the film growth proceeds mainly by surface diffusion. Thus, with increasing reaction time (amount of BaO), cavities are formed between neighbouring islands (Fig. 5.7(b), see also Fig. 4.16). Since surface diffusion of  $\text{TiO}_2$  species along the  $\text{TiO}_2$  surface is relatively easy and fast, the cavities are produced by out-diffusion of the  $\text{TiO}_2$ . Further reaction leads to the coalescence of the Ti-rich islands over the cavities (Fig. 5.7(c)). Consequently, voids are formed. We conclude that in our case the pores are produced mainly by surface diffusion of  $\text{TiO}_2$ .

When the reaction is continued, Ti is supplied to the surface by grain boundary diffusion. The concentration of Ti on the surface decreases and consequently  $\text{BaTiO}_3$  is formed (see Fig. 4.9).

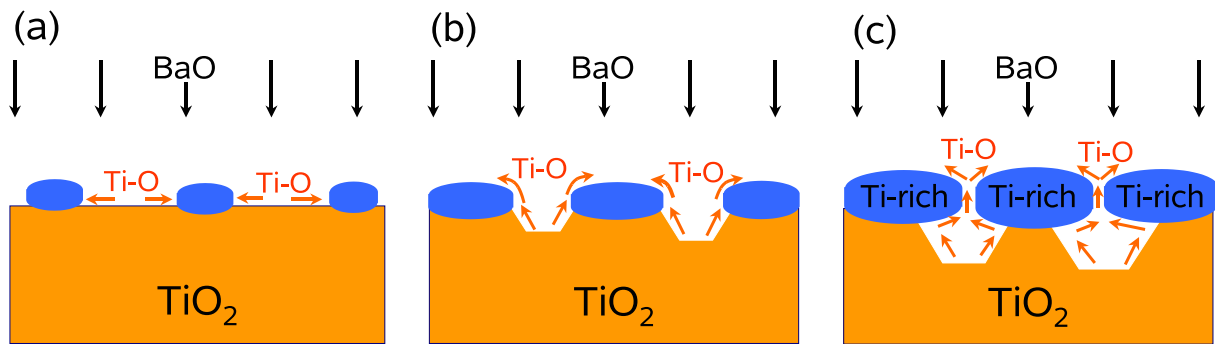


Fig. 5.7. Schematic diagram of void formation.

## 5.2 The reaction systems $\text{SrO}-\text{TiO}_2$ , $\text{CaO}-\text{TiO}_2$ and $\text{MgO}-\text{TiO}_2$

### 5.2.1 Orientation of $\text{SrTiO}_3$ on $\text{TiO}_2$ (rutile)

The orientations of  $\text{SrTiO}_3$  after vapour-solid reaction on the  $\text{TiO}_2$  substrates were found to be similar to those observed for  $\text{BaTiO}_3$ . By comparing the orientation relationships found for  $\text{BaTiO}_3$  with those observed for  $\text{SrTiO}_3$ , it can be concluded that the [001]  $\text{TiO}_2$  axis is a unique tilt axis for  $\text{BaTiO}_3$  and  $\text{SrTiO}_3$  grains grown on (100) and (110)  $\text{TiO}_2$  surfaces. The nucleation of  $\text{SrTiO}_3$  on  $\text{TiO}_2$  can be explained by the same scenario as was done above (Figs. 5.4-5.5) for  $\text{BaTiO}_3$  on  $\text{TiO}_2$  (rutile). This is because the crystal structures of  $\text{BaTiO}_3$  and  $\text{SrTiO}_3$  are very similar. All observed orientation relationships of  $\text{SrTiO}_3$  on  $\text{TiO}_2$  can be explained in terms of a NCSL model (see Table 4.3).

### 5.2.2 Orientation of $\text{CaTiO}_3$ on $\text{TiO}_2$ (rutile)

One orientation of  $\text{CaTiO}_3$  on (110)  $\text{TiO}_2$  was found after the reaction of  $\text{CaO}$  (vapour) with  $\text{TiO}_2$ . This is in contrast to the results obtained in the previous two systems  $\text{BaO}$  (vapour)- $\text{TiO}_2$  and  $\text{SrO}$  (vapour)- $\text{TiO}_2$  where more than one orientation relationship was identified for  $\text{BaTiO}_3$  as well as for  $\text{SrTiO}_3$  on (110)  $\text{TiO}_2$ . In addition, an unreacted  $\text{CaO}$  phase was observed in the thin films produced by vapour-solid reaction on (110)  $\text{TiO}_2$  substrates at temperatures between 600 °C and 900 °C. This is a somewhat surprising result. It seems that the reactivity of  $\text{CaO}$  with  $\text{TiO}_2$  is different from the reactivity of  $\text{SrO}$  or  $\text{BaO}$  with the rutile substrates.

Calcium is a common impurity of commercial  $\text{TiO}_2$  single crystals. The segregation of Ca impurities from the bulk to the surface of rutile  $\text{TiO}_2$  (110) has been previously studied by several groups.<sup>169,179,180</sup> Zhang *et al.*<sup>179</sup> have proposed the formation of a (110)-oriented  $\text{CaTiO}_3$ -like compound on the (110)  $\text{TiO}_2$  surface after annealing of the fresh (110) surface of  $\text{TiO}_2$  (rutile) at 700 °C for several hours. In our work, we observed the growth of (110)-oriented  $\text{CaTiO}_3$  on the (110)  $\text{TiO}_2$  surface.  $\text{CaTiO}_3$  was formed as the first phase on (110)  $\text{TiO}_2$  substrates as was shown by HRTEM for sample prepared by vapour-solid reaction of a  $\text{CaO}$  quantity equivalent to a nominal film thickness of  $\approx 3$  nm. The observed orientation relationship of  $\text{CaTiO}_3$  on the (110)  $\text{TiO}_2$

can be explained in terms of a NCSL model (see Table 4.4).

The formation of an unreacted  $\text{CaO}$  phase can be explained as follows. Initial stage of the reaction between  $\text{CaO}$  vapour and (110)  $\text{TiO}_2$  leads to the formation of a nearly continuous  $\text{CaTiO}_3$  thin film. This film induces a diffusion barrier for Ti out-diffusion and Ca in-diffusion. As a consequence, an un-reacted  $\text{CaO}$  film is formed on top of the perovskite layer.

### 5.2.3 Orientation of $\text{MgTiO}_3$ on $\text{TiO}_2$ (rutile)

The vapour-solid reaction between  $\text{MgO}$  vapour and  $\text{TiO}_2$  (rutile) substrates resulted in the nucleation and growth of well-oriented  $\text{MgTiO}_3$  thin films. This feature can be explained on the basis of crystallographic similarity of the two lattices.

The ilmenite  $\text{MgTiO}_3$  structure is based on a hexagonal close packing of oxygen ions with cations occupying two thirds of the available octahedral sites. This structure results from equal amounts of di- ( $\text{Mg}$ ) and tetravalent ( $\text{Ti}$ ) cations, which are ordered at the octahedral sites and alternate along the  $c$  axis of the unit cell. A pair of  $\text{MgO}_6$  and  $\text{TiO}_6$  octahedra share a (001) face. Each octahedron in the ilmenite structure shares an edge with the same type of octahedron and three edges with the other octahedra. On the other hand, the rutile  $\text{TiO}_2$  structure is based on a hexagonal close packing of oxygen ions with  $\text{Ti}$  cations in octahedral interstitials. Each  $\text{Ti}$  cation has six octahedral neighbours and each octahedron is connected to two neighbouring octahedra via an edge and 8 octahedra via a corner.

A projection of the  $\text{MgTiO}_3$ - $\text{TiO}_2$  interface based on the observed orientations of  $\text{MgTiO}_3$  on (100) and (110) rutile substrates is shown in Fig. 5.8. Similarities can be found in the arrangements of oxygen sublattices of the  $\text{MgTiO}_3$  and  $\text{TiO}_2$  (rutile) structures. However, small deviations of the oxygen positions in  $\text{TiO}_2$  from those in  $\text{MgTiO}_3$  (Figs. 5.8(a)-(c)) are seen. This is due to different types of linkage of  $\text{TiO}_6$  octahedra in the two structures. In addition, the (11.0) and (22.11) planes of  $\text{MgTiO}_3$  are joined by a tilt of  $45^\circ$  around the  $[1\bar{1}.0]$   $\text{MgTiO}_3$  axis, whereas the (100) and (110) planes of  $\text{TiO}_2$  are aligned by a tilt also of  $45^\circ$  around the  $[001]$   $\text{TiO}_2$  axis. Moreover, the  $\text{TiO}_2$  rutile surfaces show a good lattice match with the  $\text{MgTiO}_3$  (see Table 4.5). Thus, from these considerations, it can be concluded that the growth of  $\text{MgTiO}_3$  on  $\text{TiO}_2$  rutile substrates is topotaxial. The formation of  $\text{MgTiO}_3$  from  $\text{MgO}$  vapour and  $\text{TiO}_2$  crystals seems to have occurred via an in-diffusion of Mg cations into the  $\text{TiO}_2$  lattice, so that the oxygen sublattice of  $\text{TiO}_2$  (rutile) can be taken over by the growing  $\text{MgTiO}_3$  (geikielite) phase.

Our results can be compared with earlier experiments in the system  $\text{MgO}-\text{TiO}_2$ <sup>11,118-120,181</sup> where a  $\text{MgO}$  substrate was exposed to  $\text{TiO}_2$  vapour. The result was a topotaxial formation of a cubic  $\text{Mg}_2\text{TiO}_4$  spinel on the cubic rock-salt substrate. In this case the oxygen sublattice is also kept. Thus, a vapour-solid reaction in the system  $\text{MgO}-\text{TiO}_2$  leads to two different phases, depending on the crystallographic structure of the substrate.

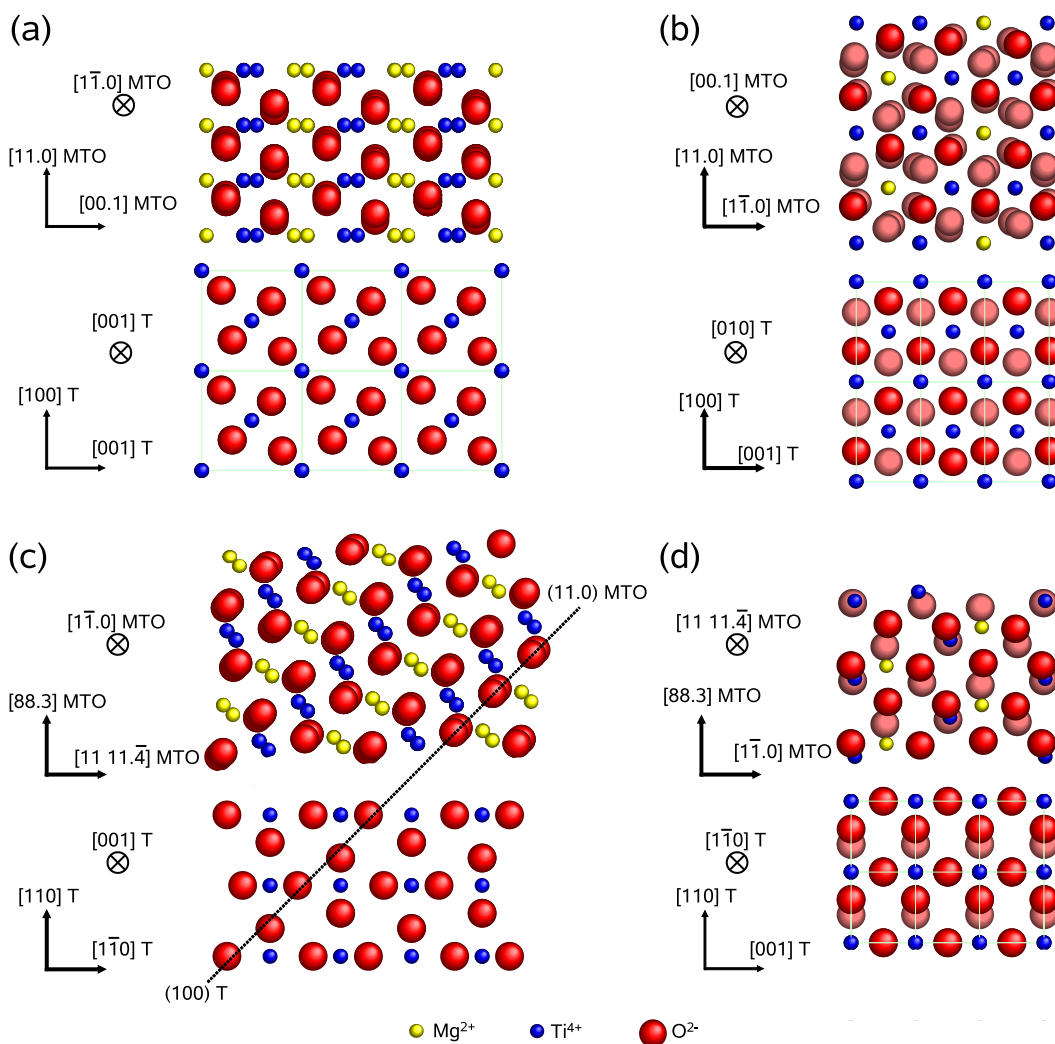


**Fig. 5.8.** Schematic cross-section representations of the interface between the  $\text{MgTiO}_3$  phase (MTO) and  $\text{TiO}_2$  (rutile) substrates (T). Orientation relationships are: (a)-(b)  $(11.0) \text{ MgTiO}_3 \parallel (100) \text{ TiO}_2$  and (c)-(d)  $(22.11) \text{ MgTiO}_3 \parallel (110) \text{ TiO}_2$ . Viewing directions are: (a) and (c)  $[1\bar{1}.0] \text{ MgTiO}_3 \parallel [001] \text{ TiO}_2$ , (b)  $[00.1] \text{ MgTiO}_3 \parallel [010] \text{ TiO}_2$  and (d)  $[1\bar{1} 1\bar{1}.4] \text{ MgTiO}_3 \parallel [1\bar{1}0] \text{ TiO}_2$ . The dashed line in (c) indicates  $(11.0) \text{ MgTiO}_3 \parallel (100) \text{ TiO}_2$ . Different colours for oxygen ions used in (b) and (d) show different height levels of the ions in the projections.

## 5.3 Factors influencing the first-phase selection in complex oxide thin film systems

The prediction of the first phase forming during a thin-film solid state reaction is of considerable interest since many years. Correspondingly, a number of models have been put forward, including kinetic, thermodynamic, and nucleation-controlled models. But these models mainly considered metal (thin film)-Si (substrate) systems. In the nucleation-controlled model,<sup>23</sup> it was shown that nucleation effects are dominant if  $\Delta G_r$  is small. The estimated limit of nucleation dominance  $\Delta g = \Delta G_r/V$  ( $V$  is the molar volume of the compound) is  $-400 \text{ J/cm}^3$ . Factors influencing the first-phase selection in oxide thin film systems have not been sufficiently considered so far. In this section, we analyse factors influencing the first-phase selection in complex oxides like  $\text{BaCO}_3$ -

$\text{TiO}_2$ ,  $\text{SrO-TiO}_2$ ,  $\text{CaO-TiO}_2$  and  $\text{MgO-TiO}_2$  on the base of experimental results obtained in this work.

In the system  $\text{BaCO}_3\text{-TiO}_2$ , the  $\Delta g$  values for the  $\text{Ba}_2\text{TiO}_4$  and  $\text{BaTiO}_3$  formation in air (see Fig. 5.9(a)) and in vacuum (see Fig. 5.9(b)) are beyond the limit. As was discussed above, the nucleation of the first phase in the system  $\text{BaCO}_3\text{-TiO}_2$  is determined by  $\Delta G_r$  values.

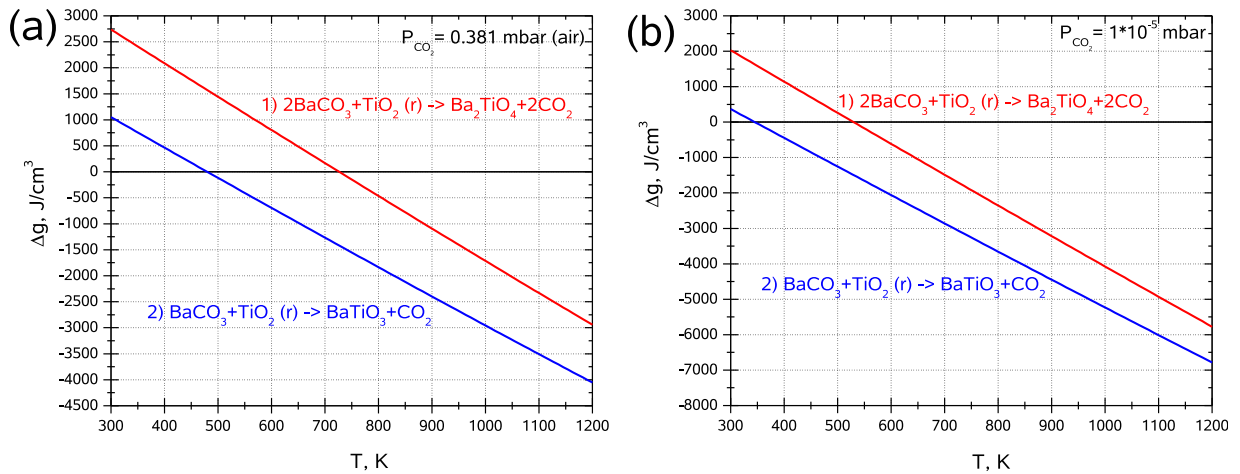
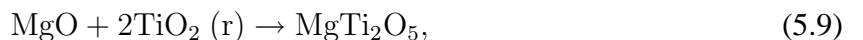
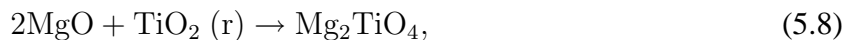


**Fig. 5.9.** a)  $\Delta g$  vs T for the formation of  $\text{Ba}_2\text{TiO}_4$  and  $\text{BaTiO}_3$  in air and (b)  $\Delta g$  vs T for the formation of  $\text{Ba}_2\text{TiO}_4$  and  $\text{BaTiO}_3$  in vacuum. Calculated from values given in I. Barin.<sup>128</sup>

In the systems  $\text{SrO-TiO}_2$  and  $\text{CaO-TiO}_2$ , the  $\Delta g$  values for the formation of  $\text{SrTiO}_3$  (ranging from  $-3805 \text{ J/cm}^3$  to  $-3875 \text{ J/cm}^3$  at temperatures between 300 K and 1200 K) and  $\text{CaTiO}_3$  (ranging from  $-2491 \text{ J/cm}^3$  to  $-2690 \text{ J/cm}^3$  at temperatures between 300 K and 1200 K) are beyond the limit. The formation of  $\text{SrTiO}_3$  or  $\text{CaTiO}_3$  as the first compound can be explained according to the EHF model.<sup>21,22</sup> The  $\text{SrO-TiO}_2$  phase diagram (Fig. 2.10 or Fig. A.3) and the  $\text{CaO-TiO}_2$  phase diagram (Fig. 2.11 or Fig. A.4) show the existence of the lowest eutectic at 1440 °C and at 1450 °C, respectively. The two phases  $\text{SrTiO}_3$  and  $\text{TiO}_2$  form an eutectic at 1440 °C (Fig. 2.10 or Fig. A.3) while  $\text{CaTiO}_3$  and  $\text{TiO}_2$  form an eutectic at 1450 °C (Fig. 2.11 or Fig. A.4). Thus, the  $\text{SrTiO}_3$  and  $\text{CaTiO}_3$  phase will be the first phase to grow in the systems  $\text{SrO-TiO}_2$  and  $\text{CaO-TiO}_2$ , respectively.

For the system  $\text{MgO-TiO}_2$ ,  $\Delta G_r$  was calculated for the following reactions:



where  $\text{TiO}_2 \text{ (r)}$  is referred to the rutile modification of  $\text{TiO}_2$ . The G values for  $\text{TiO}_2 \text{ (r)}$ ,  $\text{MgTiO}_3$ ,  $\text{Mg}_2\text{TiO}_4$  and  $\text{MgTi}_2\text{O}_5$  were taken from I. Barin<sup>128</sup>. The results of the thermodynamic calculations for reactions (5.7)-(5.9) are given in Fig. 5.10(a). As can be seen from Fig. 5.10(a), the  $\Delta G_r$  values for compounds in the system  $\text{MgO-TiO}_2$  are small and close to each other. The formation of  $\text{MgTiO}_3$  from simple oxides is less likely at temperatures higher than 530 °C. In this work,  $\text{MgTiO}_3$  was observed at temperatures between 600 °C and 800 °C. However, the formation of  $\text{Mg}_2\text{TiO}_4$

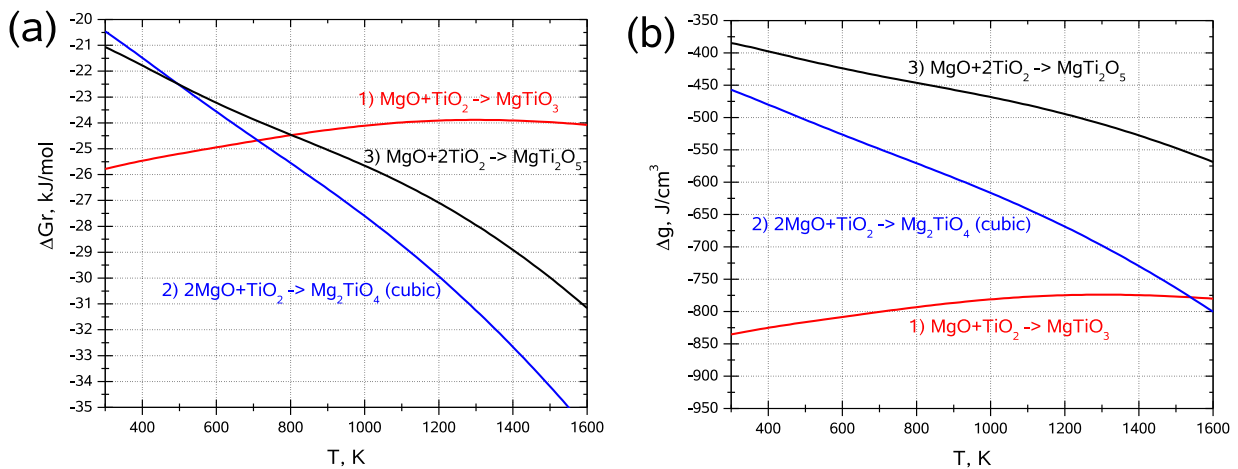


**Fig. 5.10.** a)  $\Delta G_r$  vs  $T$  for the formation of compounds in the system MgO-TiO<sub>2</sub> and (b)  $\Delta g$  vs  $T$  for the formation of compounds in the system MgO-TiO<sub>2</sub>. Calculated from values given in I. Barin.<sup>128</sup>

at these temperatures is more likely as shown by thermodynamical estimations (Fig. 5.10(a)). The  $\Delta g$  values for the MgTiO<sub>3</sub>, Mg<sub>2</sub>TiO<sub>4</sub> and MgTi<sub>2</sub>O<sub>5</sub> are presented in Fig. 5.10(b). They are also beyond the limit of -400 J/cm<sup>3</sup>.

Previous investigations of vapour-solid reactions in the system MgO-TiO<sub>2</sub> using (100) MgO substrates showed topotaxial formation of Mg<sub>2</sub>TiO<sub>4</sub> on MgO.<sup>11,118-120,181</sup> In this Ph.D. thesis, topotaxial formation of MgTiO<sub>3</sub> on TiO<sub>2</sub> (rutile) was found. Consequently, the choice in the nucleation and growth of the kind of first phase in the system MgO-TiO<sub>2</sub> is not determined by  $\Delta G_r$ , but instead is given by the crystallography of the substrate serving as reactant: For MgO, it is Mg<sub>2</sub>TiO<sub>4</sub>, whereas for TiO<sub>2</sub> (rutile), it is MgTiO<sub>3</sub>. Thus, crystallography obviously plays an important, if not dominant, role in the determination of the first growing phase in some topotaxial solid-state reactions. We propose the limit of  $\Delta g$  for oxides as -850 J/cm<sup>3</sup>. It should be noted that according to the EHF model,<sup>21,22</sup> either MgTiO<sub>3</sub> or MgTi<sub>2</sub>O<sub>5</sub> (see phase diagram in Fig. 2.12) should be the first phase forming in the system MgO-TiO<sub>2</sub>. Consequently, the EHF model is not suitable for the system MgO-TiO<sub>2</sub>. The phase MgTi<sub>2</sub>O<sub>5</sub> has a pseudobrookite structure. Thus, we can assume that MgTi<sub>2</sub>O<sub>5</sub> might be obtained using TiO<sub>2</sub> with brookite structure as substrate for the reaction.

## 6 Conclusions

In the present work, thin-film solid state reactions in the systems  $\text{BaCO}_3$  (thin film)- $\text{TiO}_2$  (rutile or anatase, substrate),  $\text{BaO}$  (vapour)- $\text{TiO}_2$  (rutile or anatase, substrate),  $\text{SrO}$  (vapour)- $\text{TiO}_2$  (rutile, substrate),  $\text{CaO}$  (vapour)- $\text{TiO}_2$  (rutile, substrate) and  $\text{MgO}$  (vapour)- $\text{TiO}_2$  (rutile, substrate) were experimentally studied. The substrates were one-side polished (110) and (100) surfaces of commercial  $\text{TiO}_2$  (rutile) (from CrysTec GmbH, Berlin, Germany) and (001) and (012) surfaces of epitaxial  $\text{TiO}_2$  (anatase) thin films grown on  $\text{SrTiO}_3$  or  $\text{LaAlO}_3$  substrates. The main findings of this Ph.D. thesis are summarised below.

- The formation of  $\text{BaTiO}_3$  thin films from  $\text{BaCO}_3$  (thin film) and (110)/(100)  $\text{TiO}_2$  (rutile) single crystals as well as from  $\text{BaCO}_3$  (thin film) and (001)/(012) epitaxial  $\text{TiO}_2$  (anatase) thin films by solid-solid reactions has been studied in vacuum and in air at temperatures between 575 °C and 1000 °C. The phase sequence during the reaction is independent of the structure of  $\text{TiO}_2$  (i.e. rutile or anatase). The solid-solid reactions in vacuum and in air showed different processes to occur during  $\text{BaTiO}_3$  formation. The  $\text{Ba}_2\text{TiO}_4$  compound is formed as the first phase after the reaction in vacuum at 575 °C while  $\text{BaTiO}_3$  is found as the first phase after a reaction in air at 575 °C. Thermodynamic factors favour the nucleation of  $\text{Ba}_2\text{TiO}_4$  in vacuum and of  $\text{BaTiO}_3$  in air. A mechanism of  $\text{BaTiO}_3$  formation in vacuum is proposed. This mechanism is in contrast to the model of Beauger *et al.*<sup>69</sup> Different formation mechanisms of  $\text{Ba}_2\text{TiO}_4$  and  $\text{BaTiO}_3$  are assumed. The  $\text{Ba}_2\text{TiO}_4$  is formed mainly by in-diffusion of Ti ions into  $\text{BaCO}_3$ , while  $\text{BaTiO}_3$  is nucleated mainly by in-diffusion of Ba ions into  $\text{TiO}_2$ .
- Ti-rich barium titanates were formed after solid-solid and vapour-solid reactions at high reaction temperatures, but with quite different textures. Oriented  $\text{Ba}_6\text{Ti}_{17}\text{O}_{40}$  phases were grown after vapour-solid reaction of  $\text{BaO}$  with the rutile substrates at temperatures between 900 °C and 1000 °C. Contrary to the vapour-solid reaction, polycrystalline  $\text{BaTi}_4\text{O}_9$  and  $\text{Ba}_4\text{Ti}_{13}\text{O}_{30}$  (with fiber texture) phases were found after the solid-solid reaction at 1000 °C in vacuum and in air, respectively. These differences are caused by the reaction conditions changing with reaction geometry.
- Vapour-solid reactions on the rutile surfaces at 900 °C were investigated at different reaction stages (using  $\text{BaO}$  vapour of different nominal thicknesses):
  - the initial stage of vapour-solid reaction of a  $\text{BaO}$  quantity equivalent to a nominal film thickness of 1 nm and 5 nm with the  $\text{TiO}_2$  substrates showed the formation of well-oriented  $\text{Ba}_6\text{Ti}_{17}\text{O}_{40}$  islands. A topotaxial orientation relationship between  $\text{Ba}_6\text{Ti}_{17}\text{O}_{40}$  and  $\text{TiO}_2$  was found. This topotaxy is facilitated by a certain similarity in the oxygen sublattices of  $\text{TiO}_2$  and  $\text{Ba}_6\text{Ti}_{17}\text{O}_{40}$ . The nucleation of the Ti-rich phase most probably occurs at surface steps

of the (110)  $\text{TiO}_2$  substrate via in-diffusion of Ba ions while the film growth proceeds mainly by surface diffusion.

-a thin film consisting of well-oriented  $\text{BaTiO}_3$  and  $\text{Ba}_6\text{Ti}_{17}\text{O}_{40}$  grains was observed after vapour-solid reaction of a BaO quantity equivalent to a nominal film thickness of 50 nm with the rutile substrates. The Ti-rich grains are located at the interface with the rutile substrates, whereas the  $\text{BaTiO}_3$  grains are located on top of the Ti-rich layer. Large pores were found after the reaction, at the interface with the  $\text{TiO}_2$  substrates. The pores have been formed by surface diffusion of  $\text{TiO}_2$ . The latter is the dominant diffusing species during vapour-solid reaction. Thus, the formation of the voids at the surface of the rutile substrates occurs by diffusion of one reactant, similar to the Kirkendall voids which are frequently observed after solid-solid reactions in planar reaction couples.

- More than one orientation relationship has been found for  $\text{BaTiO}_3$  and  $\text{SrTiO}_3$  after vapour-solid reaction of BaO (vapour) or SrO (vapour) with the  $\text{TiO}_2$  (rutile) substrates depending on the reaction temperature and substrate orientation, all of which imply, however, a common [001]  $\text{TiO}_2$  tilt axis. The crystallographic reason for the tilt axis are chains of  $\text{TiO}_6$  octahedra oriented along the [001] direction of  $\text{TiO}_2$  (rutile). Dominant orientations of  $\text{BaTiO}_3$  as well as  $\text{SrTiO}_3$  can be explained by common octahedra chains. The growth of the  $\text{BaTiO}_3$  and  $\text{SrTiO}_3$  grains with the observed various orientations are discussed in terms of the different nucleation kinetics and conditions which seem to be dependent on the surface structure and morphology of the  $\text{TiO}_2$  substrates.
- Only one orientation relationship has been found for  $\text{BaTiO}_3$  after vapour-solid reaction of BaO (vapour) with a  $\text{TiO}_2$  anatase thin film. This can be explained by a similar orientation of  $\text{TiO}_6$  octahedra in anatase and perovskite.
- Vapour-solid reaction between  $\text{MgO}$  (vapour) and  $\text{TiO}_2$  (rutile) single crystals resulted in the growth and topotaxial formation of the  $\text{MgTiO}_3$  phase. This is facilitated by similar oxygen sublattices of the  $\text{MgTiO}_3$  and  $\text{TiO}_2$  (rutile) structures. The nucleation of  $\text{MgTiO}_3$  occurred via in-diffusion of Mg cations into the  $\text{TiO}_2$  lattice, so that the oxygen sublattice of  $\text{TiO}_2$  (rutile) can be taken over by the growing  $\text{MgTiO}_3$ .
- Factors influencing the first-phase selection in complex oxide thin film systems are discussed. The nucleation of the first phase in the system  $\text{BaCO}_3\text{-TiO}_2$  is determined by the free energy change of the reaction  $\Delta G_r$ . The formation of  $\text{SrTiO}_3$  and  $\text{CaTiO}_3$  compounds in the systems  $\text{SrO-TiO}_2$  and  $\text{CaO-TiO}_2$ , can be explained according to the EHF model.<sup>21,22</sup> On the other hand, in the system  $\text{MgO-TiO}_2$  the phase forming first is neither determined by  $\Delta G_r$  nor by the EHF model,<sup>21,22</sup> but instead is determined by the crystallography of the substrate serving as reactant: For  $\text{MgO}$ , it is  $\text{Mg}_2\text{TiO}_4$ , whereas for  $\text{TiO}_2$  (rutile), it is  $\text{MgTiO}_3$ . The model by d'Heurle<sup>23</sup> describes phase formation as a nucleation controlled process. For silicide formation a limit of nucleation dominance ( $\Delta g = \Delta G_r/V$ ) was proposed as  $-400 \text{ J/cm}^3$ .<sup>23</sup> We propose the limit of  $\Delta g$  for oxides as  $-850 \text{ J/cm}^3$ .

- Although, the growth of epitaxial anatase  $\text{TiO}_2$  films on  $\text{SrTiO}_3$  and  $\text{LaAlO}_3$  substrates was not the main aim of the work, epitaxial (001)- and (012)-oriented  $\text{TiO}_2$  anatase films with a good microstructure were prepared and used for the solid state reactions. The (012) orientation of the  $\text{TiO}_2$  was most probably obtained for the first time. The mean orientation of the surface of (012)-oriented anatase grains is close to (012). The question, whether the (012) surface is stable or whether micro-faceting occurs, remains for further work. The similarities in the orientations of the  $\text{AO}_6$  ( $\text{A} = \text{Ti,Al}$ ) octahedra of  $\text{SrTiO}_3/\text{LaAlO}_3$  and anatase structures determine the final phase formation and the epitaxial growth of the thin films. The anatase films were transformed into a cubic phase similar to  $\text{TiO}$  when *in situ* exposed to an electron beam.
- It appears that solid state reactions in electroceramic systems as a rule are complex, and that their understanding requires the detailed consideration of thermodynamics, crystallographic, and nucleation-related conditions. As a rule, the oxygen sublattice, in particular the frame of octahedra of type  $\text{AO}_6$ , plays a dominating role for the crystallographic orientation relationships that are found after phase formation by solid state reactions, but it can also have a considerable impact on the phase formation sequence including first-phase selection.

# Bibliography

1. H. Schmalzried, *Solid state reactions*, Verlag Chemie, Weinheim, 1981.
2. H. Schmalzried, *Chemical Kinetics in Solids*, VCH-Verlag, Weinheim, 1995.
3. R. Röttger, H. Schmalzried, *Solid State Ionics*, **150**, 131 (2002).
4. V.V. Boldyrev, ed., *Reactivity of Solids: Past, Present and Future*, Blackwell Science, Oxford, 1996.
5. S. Senz, A. Graff, D. Hesse, H.-P. Abicht, *J. Eur. Ceram. Soc.*, **20**, 2469 (2000).
6. A. Graff, *Phasenbildung und Grenzflächenstruktur bei Festkörperreaktionen dünner Schichten auf Einkristallsubstraten:  $SnO_2$  auf  $MgO$  und  $SiO_2$  auf  $BaTiO_3$* , Dissertation, Martin-Luther-Universität Halle-Wittenberg (1999).
7. P.G. Kotula, C.B. Carter, *J. Am. Ceram. Soc.*, **81**, 2869 (1998).
8. P.G. Kotula, C.B. Carter, *J. Am. Ceram. Soc.*, **81**, 2877 (1998).
9. P.G. Kotula, C.B. Carter, *Phys. Rev. Lett.*, **77**, 3367 (1996).
10. C. Korte, B. Franz, D. Hesse, *Phys. Chem. Chem. Phys.*, **7**, 413 (2005).
11. D. Hesse, *Elektronenmikroskopische Untersuchungen zu Struktur und Funktion der Reaktionsfronten bei topotaktischen Festkörperreaktionen*, Habilitationsschrift, Martin-Luther-Universität Halle-Wittenberg (1997).
12. J.C. Nipce, G. Thomas, *Solid State Ionics*, **43**, 69 (1990).
13. S. Gablenz, C. Damm, F.W. Müller, G. Israel, M. Rössel, A. Röder, H.-P. Abicht, *Solid State Sci.*, **3**, 291 (2001).
14. M.T. Buscaglia, V. Buscaglia, R. Alessio, *Chem. Mater.*, **19**, 711 (2007).
15. M. Rössel, S. Gablenz, T. Müller, A. Röder, H.-P. Abicht, *Anal. Bioanal. Chem.*, **375**, 310 (2003).
16. S. Gablenz, *Sprühtröcknung und Sprühhydrolyse - neue Methoden zur Herstellung von Metalloxiden und zur Modifizierung von  $BaTiO_3$* , Dissertation, Martin-Luther-Universität Halle-Wittenberg (2001).
17. D.F.K. Hennings, B.S. Schreinemacher, H. Schreinemacher, *J. Am. Ceram. Soc.*, **84**, 2777 (2001).
18. M.T. Buscaglia, M. Bassoli, V. Buscaglia, *J. Am. Ceram. Soc.*, **88**, 2374 (2005).
19. T. Manabe, I. Yamaguchi, W. Kondo, S. Mizuta, T. Kumagai, T. Nagahama, T. Tsuchiya, *J. Am. Ceram. Soc.*, **82**, 2061 (1999).

20. D.C. Sun, S. Senz, D. Hesse, *J. Eur. Ceram. Soc.*, **26**, 3181 (2006).
21. R. Pretorius, T.K. Marais, C.C. Theron, *Mater. Sci. Eng.*, **10**, 1 (1993).
22. R. Pretorius, C.C. Theron, A. Vantomme, J.W. Mayer, *Reviews in Solid State and Materials Science*, **24(1)**, 1 (1999).
23. F.M. d'Heurle, *J. Mater. Res.*, **3**, 167 (1988).
24. A.E. Gershinkii, A.A. Khoromenko, E.I. Cherepov, *Phys. Status Solidi A*, **31**, 61 (1975).
25. C. Canali, F. Catellani, G. Ottaviana, M. Prudenziati, *Appl. Phys. Lett.*, **33**, 187 (1978).
26. Ya.Ye. Geguzin, Yu.S. Kaganovskiy, L.M. Paritskaya, V.I. Solunskiy, *Phys. Met. Metallogr.*, **47**, 127 (1980).
27. U. Gösele, K.N. Tu, *J. Appl. Phys.*, **53**, 3252 (1982).
28. *Materials interfaces: atomic-level structure and properties*, edited by D. Wolf and S. Yip, Chapman and Hall, London, 1992.
29. K.N. Tu, J. Meyer, *Thin films - Interdiffusion and Reactions*, edited by J.M. Poate, Wiley, New York, 1978.
30. J.F. Banfield, B.L. Bischoff, M.A. Anderson, *Chemical Geology*, **110**, 211 (1993).
31. *Semiconductor electrodes*, edited by H.O. Finklea, Elsevier, Amsterdam, 1988.
32. A.W. Czanderna, C.N.R. Rao, J.M. Honig, *Trans. Farad. Soc.*, **54**, 1069 (1958).
33. C.N.R. Rao, S.R. Yoganarasimhan, P.A. Faeth, *Trans. Farad. Soc.*, **57**, 504 (1961).
34. R. Rodriguez-Talavera, S. Vargas, R. Arroyo-Muirillo, R. Montiel-Campos, E. Haro-Poniatowski, *J. Mater. Res.*, **12**, 439 (1997).
35. F.C. Gennari, D.M. Pasquevich, *J. Mater. Sci.*, **33**, 1571 (1998).
36. A.A. Gribb, J.F. Banfield, *Am. Miner.*, **82**, 717 (1997).
37. H. Zhang, J.F. Banfield, *J. Mater. Chem.*, **8**, 2073 (1998).
38. R.D. Shannon, *J. Appl. Phys.*, **35**, 3414 (1964).
39. S. Morad, *Sedimentary Geology*, **46**, 77 (1986).
40. R. Hengerer, *Single crystal anatase TiO<sub>2</sub> - growth and surface investigations*, Dissertation, Swiss Federal Institute of Technology, Lausanne (2000).
41. M. Ramamoorthy, D. Vanderbilt, *Phys. Rev. B*, **49**, 16721 (1994).
42. M. Lazzeri, A. Vittadini, A. Selloni, *Phys. Rev. B*, **63**, 155409 (1994).
43. K.O. Strømme, *Acta. Chem. Scand. A*, **29**, 105 (1975).
44. <http://en.wikipedia.org/wiki/Perovskite> or <http://www.answers.com/perovskite>.
45. K.W. Kirby, B.A. Wechsler, *J. Am. Ceram. Soc.*, **74**, 1841 (1991).

46. R.M. Glaister, H.F. Kay, *Proc. Phys. Soc.*, **76**, 763 (1960).
47. R.W.G. Wyckoff, *Crystal structures*, Vol. 2, Interscience Publishers, 1964.
48. G.H. Kwei, A.C. Lawson, S.J.L. Billinge, S.-W. Cheong, *J. Phys. Chem.*, **97**, 2368 (1993).
49. J.A. Bland, *Acta. Cryst.*, **14**, 875 (1961).
50. K.K. Wu, I.D. Brown, *Acta. Cryst. B*, **29**, 2009 (1961).
51. J.R. Günter, G.B. Jameson, *Acta. Cryst. C*, **40**, 207 (1984).
52. H.F. McMurdie, M.C. Morris, E.H. Evans, B. Paretzkin, W. Wong-Ng, Y. Zhang, *Powder Diffraction*, **2**, 41 (1987).
53. G. Pfaff, *J. Mater. Sci. Lett.*, **10**, 1059 (1991).
54. T. Ahmad, A.K. Ganguli, *J. Mater. Res.*, **19**, 2905 (2004).
55. K.-H. Felgner, T. Müller, H.T. Langhammer, H.-P. Abicht, *Mater. Lett.*, **58**, 1943 (2004).
56. S.J. Lee, M.D. Biegalski, W.M. Kriven, *J. Mater. Res.*, **14**, 3001 (1999).
57. A. Beauger, J.C. Mutin, J.C. Niepce, *J. Mater. Sci.*, **19**, 195 (1984).
58. W. Trzebiatowski, J. Wojciechowska, J. Damm, *Experientia*, **6**, 138 (1950).
59. W. Trzebiatowski, J. Wojciechowska, J. Damm, *Roczniki Chemii*, **26**, 12 (1952).
60. T. Kubo, K. Shinriki, *J. Chem. Soc. Japan*, Ind. Chem. Sect. **55**, 49 (1952).
61. T. Kubo, K. Shinriki, *J. Chem. Soc. Japan*, Ind. Chem. Sect. **55**, 137 (1952).
62. T. Kubo, K. Shinriki, *J. Chem. Soc. Japan*, Ind. Chem. Sect. **57**, 612 (1954).
63. W. Freundlich, *C. R. Acad. Sci.*, **236**, 1895 (1953).
64. P. Turlier, L. Eyraud, C. Eyraud, M. Prettre, *C. R. Acad. Sci.*, **246**, 422 (1958).
65. L.K. Templeton, J.A. Pask, *J. Am. Ceram. Soc.*, **42**, 212 (1959).
66. Y. Suyama, A. Kato, *Ceramurgia International*, **1**, 5 (1975).
67. M. Cournil, M. Soustelle, G. Thomas, *Oxid. Met.*, **13**, 77 (1979).
68. M. Cournil, M. Soustelle, G. Thomas, *Oxid. Met.*, **13**, 89 (1979).
69. A. Beauger, J.C. Mutin, J.C. Niepce, *J. Mater. Sci.*, **18**, 3041 (1983).
70. A. Beauger, J.C. Mutin, J.C. Niepce, *J. Mater. Sci.*, **18**, 3543 (1983).
71. J.C. Mutin, J.C. Niepce, *J. Mater. Sci. Lett.*, **3**, 591 (1984).
72. E.I. Tochitsky, N.I. Romanova, *Thin Solids Films*, **110**, 55 (1983).
73. W.O. Statton, *J. Chem. Phys.*, **19**, 33 (1951).
74. D.E. Rase, R. Roy, *J. Am. Ceram. Soc.*, **38**, 102 (1955).

75. J. Schwarzbach, L. Plocek, *Silikaty*, **11**, 231 (1968).
76. H.M. O'Bryan, J. Thomson, *J. Am. Ceram. Soc.*, **57**, 522 (1974).
77. T. Negas, R.S. Roth, H.S. Parker, D. Minor, *J. Sol. State Chem.*, **9**, 297 (1974).
78. J.J. Ritter, R.S. Roth, J.E. Blendell, *J. Am. Ceram. Soc.*, **69**, 155 (1986).
79. E.I. Gindin, Yu.P. Kostikov, A.V. Motornyi, G.D. Rubalskii, *Translated from Izvestiya Akademii Nauk SSSR, Neorganicheskie Materialy*, **27**, 53 (1991).
80. D.S. Filimonov, Z.-K. Liu, C.A. Randall, *Mater. Res. Bull.*, **38**, 545 (2003).
81. T. Negas, G. Yeager, S. Bell, N. Coats, I. Minis, *Am. Ceram. Soc. Bull.*, **72**, 80 (1993).
82. E. Tillmanns, *Cryst. Struct. Commun.*, **1**, 1 (1972).
83. S. Andersson, A.D. Wadsley, *Acta Crystallogr.*, **15**, 194 (1962).
84. E. Tillmanns, W. Hofmeister, W.H. Baur, *J. Sol. State Chem.*, **58**, 14 (1985).
85. R.S. Roth, C.J. Rawn, C.G. Lindsay, W. Wong-Ng, *J. Sol. State Chem.*, **104**, 99 (1993).
86. E. Tillmanns, *Acta Crystallogr. B*, **30**, 2894 (1974).
87. W. Hofmeister, E. Tillmanns, W.H. Baur, *Acta Crystallogr. C*, **40**, 1510 (1984).
88. E. Tillmanns, W. Hofmeister, W.H. Baur, *J. Am. Ceram. Soc.*, **66**, 268 (1983).
89. G. Grzinic, L.A. Burcill, D.J. Smith, *J. Sol. State Chem.*, **47**, 151 (1983).
90. E. Tillmanns, *Acta Crystallogr. B*, **25**, 1444 (1969).
91. S. Möhr, H. Müller-Buschbaum, *J. Alloys and Compounds*, **199**, 203 (1993).
92. E. Tillmanns, *Inorg. Nucl. Chem. Lett.*, **7**, 1169 (1971).
93. E. Tillmanns, W. H. Baur, *Acta Crystallogr. B*, **26**, 1645 (1970).
94. V. Kraševac, D. Kolar, *J. Am. Ceram. Soc.*, **71**, C246 (1988).
95. R.S. Roth, J.J. Ritter, H.S. Parker, D.B. Minor, *J. Am. Ceram. Soc.*, **69**, 858 (1986).
96. R.S. Roth, L.D. Ettlinger, H.S. Parker, *J. Sol. State Chem.*, **68**, 330 (1987).
97. D. Hesse, A. Graff, S. Senz, N.D. Zakharov, *Materials Science Forum*, **294-296**, 597 (1999).
98. V. Kraševac, M. Drofenik, D. Kolar, *J. Am. Ceram. Soc.*, **70**, C193 (1987).
99. S. Senz, A. Graff, W. Blum, D. Hesse, *J. Am. Ceram. Soc.*, **81**, 1317 (1998).
100. M.-H. Lin, H.-Y. Lu, *Acta Mater.*, **50**, 605 (2002).
101. E.M. Levin, C.R. Robbins, H.F. McMurdie, *Phase diagrams for ceramists*, edited by M.K. Reser, American Ceramic Society, Columbus, OH, 1969.
102. H. Tagawa, K. Igarashi, *J. Am. Ceram. Soc.*, **69**, 310 (1986).

103. H.-Y. Chang, K.-S. Liu, *J. Mater. Res.*, **10**, 2052 (1995).
104. V. Berbenni, A. Marini, G. Bruni, *J. Alloys Comp.*, **329**, 230 (2001).
105. P.Y. Lesaicherre, H. Yamaguchi, H. Miyasaka, H. Watanabe, H. Ono, M. Yoshida, *Integrated Ferroelectrics*, **8**, 201 (1995).
106. N.D. Zakharov, D. Hesse, F. Nouvertné, J. Auge, H. Hoffschulz, J. Dreßen, H.G. Roskos, H. Kurz, G. Güntherodt, *Physica C*, **245**, 84 (1995).
107. H.N. Lee, D. Hesse, *Appl. Phys. Lett.*, **80**, 1040 (2002).
108. H. Zheng, J. Wang, S.E. Lofland, Z. Ma, L. Mohaddes-Ardabili, T. Zhao, L. Salamanca-Riba, S.R. Shinde, S.B. Ogale, F. Bai, D. Viehland, Y. Jia, D.G. Schlom, M. Wuttig, A. Roytburd, R. Ramesh, *Science*, **303**, 661 (2004).
109. Y. Watanabe, J.G. Bednorz, A. Bietsch, C. Gerber, D. Widmer, A. Beck, S.J. Wind, *Appl. Phys. Lett.*, **78**, 3738 (2001).
110. K. Szot, W. Speier, G. Bihlmayer, R. Waser, *Nature Mater.*, **5**, 312 (2006).
111. S.A.T. Redfern, *J. Phys. Condens. Matter.*, **8**, 8267 (1996).
112. V.V. Lemanov, A.V. Sotnikov, E.P. Smirnova, M. Weihnacht, R. Kunze, *Solid State Commun.*, **110**, 611 (1999).
113. J. Hao, W. Si, X.X. Xi, R. Guo, A.S. Bhalla, L.E. Cross, *Appl. Phys. Lett.*, **76**, 3100 (2000).
114. V.V. Lemanov, A.V. Sotnikov, E.P. Smirnova, M. Weihnacht, *Appl. Phys. Lett.*, **81**, 886 (2002).
115. K.L. Smith, N.J. Zaluzec, *J. Nucl. Mater.*, **336**, 261 (2005).
116. M. Manso, M. Langlet, J.M. Martinez-Duart, *Mater. Sci. Eng. C*, **23**, 447 (2003).
117. B.A. Wechsler, R.B. Dreele, *Acta Cryst. B*, **45**, 542 (1989).
118. D. Hesse, H. Bethge, *J. Crystal Growth*, **52**, 875 (1981).
119. H. Haefke, H.P. Lang, R. Sum, H.J. Güntherodt, L. Berthold, D. Hesse, *Appl. Phys. Lett.*, **61**, 2359 (1991).
120. D. Hesse, L. Berthold, H. Haefke, H.P. Lang, R. Sum, H.J. Güntherodt, *Physica C: Superconductivity*, **202**, 277 (1992).
121. K. Wakino, *Ferroelectrics*, **91**, 69 (1989).
122. X. Kuang, X. Jing, Z. Tang, *J. Am. Ceram. Soc.*, **89**, 241 (2006).
123. V.M. Ferreira, J.L. Baptista, *Mater. Res. Bull.*, **29**, 1017 (1994).
124. V.M. Ferreira, J.L. Baptista, S. Kamba, J. Petzelt, *J. Mater. Sci.*, **28**, 5894 (1993).
125. D.R. Lide, ed., *CRC handbook of chemistry and physics: a ready-reference book of chemical and physical data*. CRC Press, New York, 76. ed., 1995-1996.

126. Y.H. Choi, J. Lee, *Thin Solid Films*, **385**, 43 (2001).
127. Y.H. Choi, J. Lee, *Jpn. J. Appl. Phys.*, **38**, 3651 (1999).
128. I. Barin, *Thermochemical data of pure substances*, VCH Verlagsgesellschaft, Weinheim, 1995.
129. H.P. Klug, L.E. Alexander, *X-ray diffraction procedures*, Wiley-Interscience publication, New York, 1974.
130. CaRIne Crystallography software, version 3.0/3.1, Senlis/France (1996).
131. J.W. Edington, *Practical electron microscopy in materials science*, TechBooks, Herndon, 1976.
132. L.A. Bendersky, F.W. Gayle, *J. Res. Natl. Inst. Stand. Technol.*, **106**, 997 (2001).
133. D. Shido, K. Hiraga, *High-resolution electron microscopy for materials science*, Springer-Verlag, Tokyo, 1998.
134. P.J. Goodhew, *Specimen preparation for transmission electron microscopy of materials*, Oxford University Press, 1984.
135. S.N. Magonov, M.-N. Hwangbo, *Surface analysis with STM and AFM: experimental and theoretical aspects of image analysis*, VCH, Weinheim, 1996.
136. H. Nakano, K. Urabe, H. Ikawa, *J. Am. Ceram. Soc.*, **86**, 741 (2003).
137. H. Grimmer, W. Bollmann, D.H. Warrington, *Acta. Cryst. A*, **30**, 197 (1974).
138. T.X.T. Sayle, C.R.A. Catlow, D.C. Sayle, S.C. Parker, J.H. Harding, *Phil. Mag. A*, **68**, 565 (1993).
139. Y.W. Chung, W.J. Lo, G.A. Somorjai, *Surf. Sci.*, **64**, 588 (1977).
140. E. Wäsch, *Kristall und Technik*, **7**, 187 (1972).
141. F. Izumi, H. Kodama, A. Ono, *J. Crystal Growth*, **47**, 139 (1979).
142. H. Berger, H. Tang, F. Levy, *J. Crystal Growth*, **130**, 108 (1993).
143. G.S. Herman, Y. Gao, T.T. Tran, J. Osterwalder, *Surf. Sci.*, **447**, 201 (2000).
144. N. Ruzycki, G.S. Herman, L.A. Boatner, U. Diebold, *Surf. Sci. Lett.*, **529**, L239 (2003).
145. S. Yamamoto, T. Sumita, T. Yamaki, A. Miyashita, H. Naramoto, *J. Crystal Growth*, **237-239**, 569 (2002).
146. C.C. Hsieh, K.H. Wu, J.Y. Jung, T.M. Uen, J.-Y. Lin, Y.S. Gou, *J. Appl. Phys.*, **92**, 2518 (2002).
147. J.Y. Huang, B.H. Park, D. Jan, X.Q. Pan, Y.T. Zhu, Q.X. Jia, *Phil. Mag. A*, **82**, 735 (2002).
148. R. van de Krol, A. Goossens, *J. Vac. Sci. Technol. A*, **21**, 76 (2003).
149. A.A. Gribb, J.F. Banfield, *Am. Miner.*, **82**, 717 (1997).

150. H. Zhang, J. Banfield, *J. Mater. Chem.*, **8**, 2073 (1998).
151. J.Y. Huang, B.H. Park, D. Jan, X.Q. Pan, Y.T. Zhu, Q.X. Jia, *Phil. Mag. A*, **82**, 735 (2002).
152. J.F. Banfield, D.R. Veblen, *Am. Miner.*, **77**, 545 (1992).
153. T. Ohnishi, K. Shibuya, M. Lippmaa, D. Kobayashi, H. Kumigashira, M. Oshima, H. Koinuma, *Appl. Phys. Lett.*, **85**, 272 (2004).
154. J. Yao, P.B. Merril, S.S. Perry, D. Marton, J.W. Rabalais, *J. Chem. Phys.*, **108**, 1645 (1998).
155. R.J. Francis, S.C. Moss, A.J. Jacobson, *Phys. Rev. B*, **64**, 235425 (2001).
156. R. Hengerer, B. Bolliger, M. Erbudak, M. Grätzel, *Surf. Sci.*, **460**, 162 (2000).
157. N.K. Adam, *Physical Chemistry*, Clarendon Press, Oxford, 1962.
158. M.D. Judd, M.I. Pope, *J. Therm. Anal.*, **4**, 31 (1972).
159. B.V. L'vov, *Thermochim. Acta*, **386**, 1 (2002).
160. S. Gablenz, H.-P. Abicht, E. Pippel, O. Lichtenberger, J. Woltersdorf, *J. Eur. Ceram. Soc.*, **20**, 1053 (2000).
161. V. Ischenko, E. Pippel, R. Köferstein, H.-P. Abicht, J. Woltersdorf, *Solid State Sci.*, **9**, 21 (2007).
162. C.V. Thompson, *Annu. Rev. Mater. Sci.*, **20**, 245 (1990).
163. U.C. Oh, J.H. Je, *J. Appl. Phys.*, **74**, 1692 (1993).
164. U. Diebold, *Surf. Sci. Rep.*, **48**, 53 (2003).
165. H. Zajonz, H.L. Meyerheim, T. Gloege, W. Moritz, D. Wolf, *Surf. Sci.*, **398**, 369 (1998).
166. E. Landree, L.D. Marks, P. Zschack, C.J. Gilmore, *Surf. Sci.*, **408**, 300 (1998).
167. C.A. Muryn, P.J. Hardman, J.J. Crouch, G.N. Raiker, G. Thornton, *Surf. Sci.*, **251-252**, 741 (1991).
168. A. Szabo, T. Engel, *Surf. Sci.*, **329**, 241 (1995).
169. O. Bikonda, C.L. Pang, C.A. Muryn, B.G. Daniels, S. Ferrero, E. Michelangeli, G. Thornton, *J. Phys. Chem. B*, **108**, 16768 (2004).
170. L. Zhao, A.T. Chien, F.F. Lange, J.S. Speck, *J. Mater. Res.*, **11**, 1325 (1996).
171. Y. Suyama, Y. Oda, A. Kato, *Chem. Lett.*, **8**, 987 (1979).
172. R.A. Bennet, S. Poulston, P. Stone, M. Bowker, *Phys. Rev. B*, **59**, 10341 (1999).
173. A. Graff, S. Senz, D. Völtzke, H.-P. Abicht, D. Hesse, *J. Eur. Ceram. Soc.*, **25**, 2201 (2006).
174. A.D. Smigelskas, E.O. Kirkendall, *Trans. AIME*, **171**, 130 (1947).
175. P.G. Shewmon, *Diffusion in Solids*, McGraw-Hill, New York, 1963.

176. Y. Yin, R.M. Rioux, C.K. Erdonmez, S. Hughes, G.A. Somorjai, A.P. Alivisatos, *Science*, **304**, 711 (2004).
177. H.J. Fan, M. Knez, R. Scholz, K. Nielsch, E. Pippel, D. Hesse, M. Zacharias, U. Gösele, *Nature Mater.*, **5**, 627 (2006).
178. K.N. Tu, U. Gösele, *Appl. Phys. Lett.*, **86**, 09311 (2005).
179. L.P. Zhang, M. Li, U. Diebold, *Surf. Sci.*, **412-413**, 242 (1998).
180. H. Nörenberg, H.J. Harding *Surf. Sci.*, **471**, 151 (2001).
181. D. Hesse, *J. Vac. Sci. Technol. A*, **5**, 1696 (1987).

# Appendix

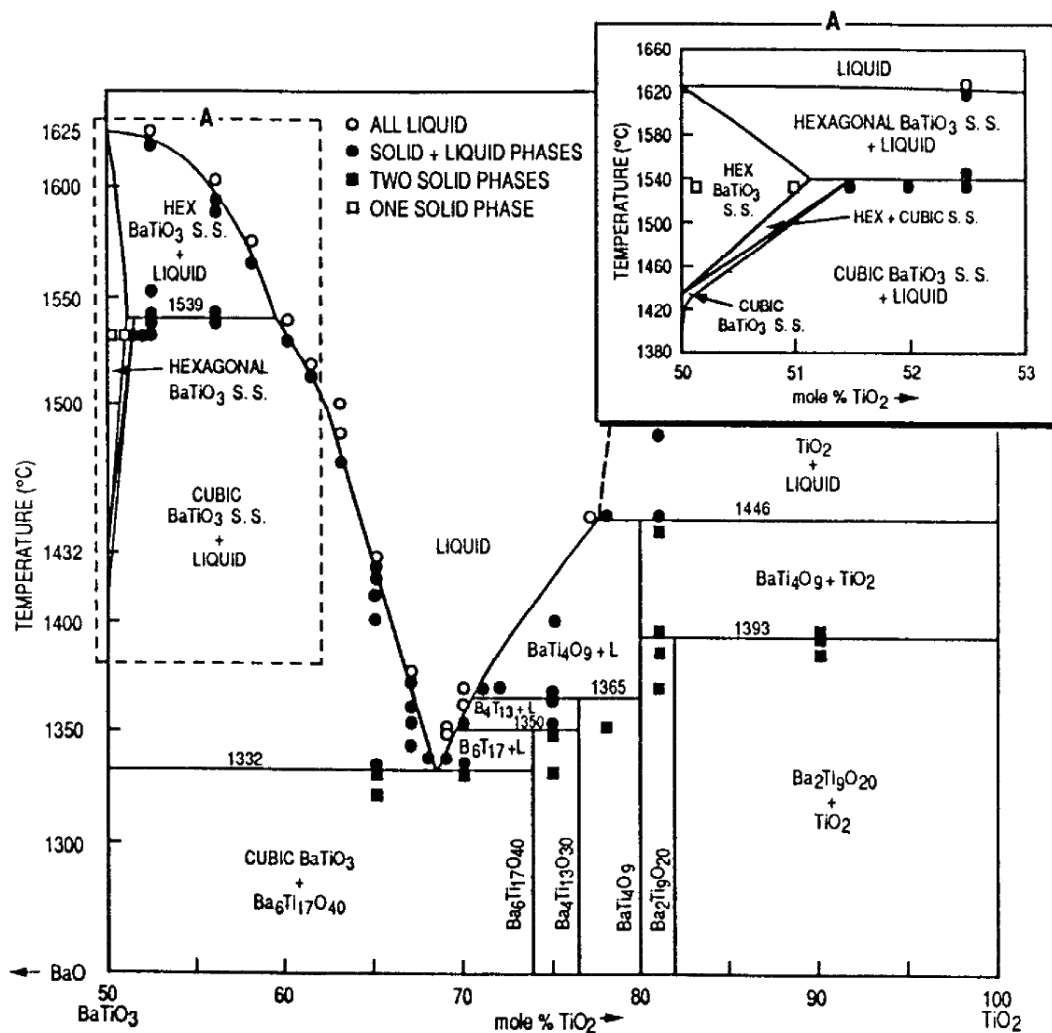


Fig. A.1.  $\text{BaTiO}_3\text{-TiO}_2$  equilibrium phase diagram.<sup>45</sup>

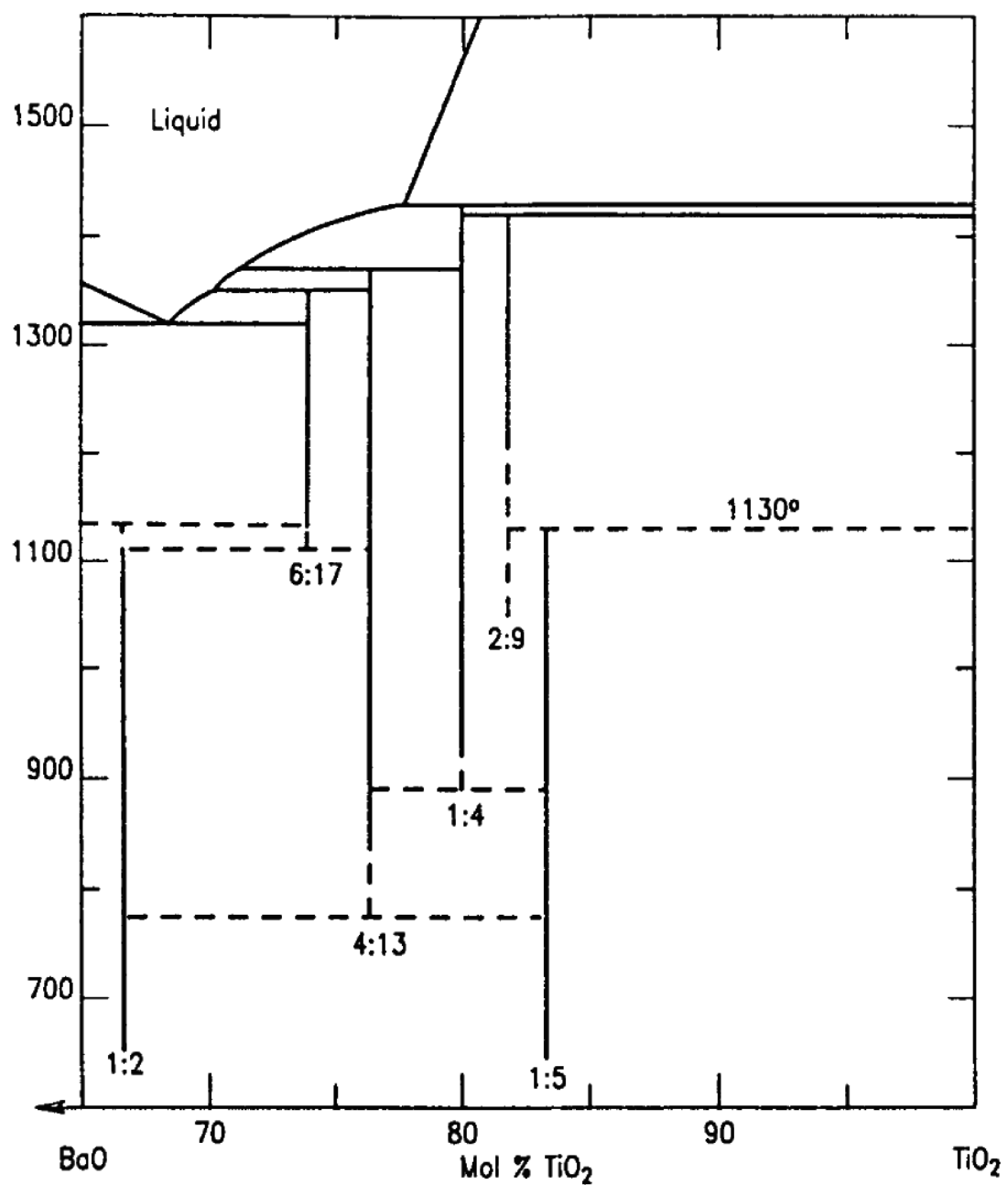


Fig. A.2. Low temperature BaTiO<sub>3</sub>-TiO<sub>2</sub> phase diagram.<sup>78</sup>

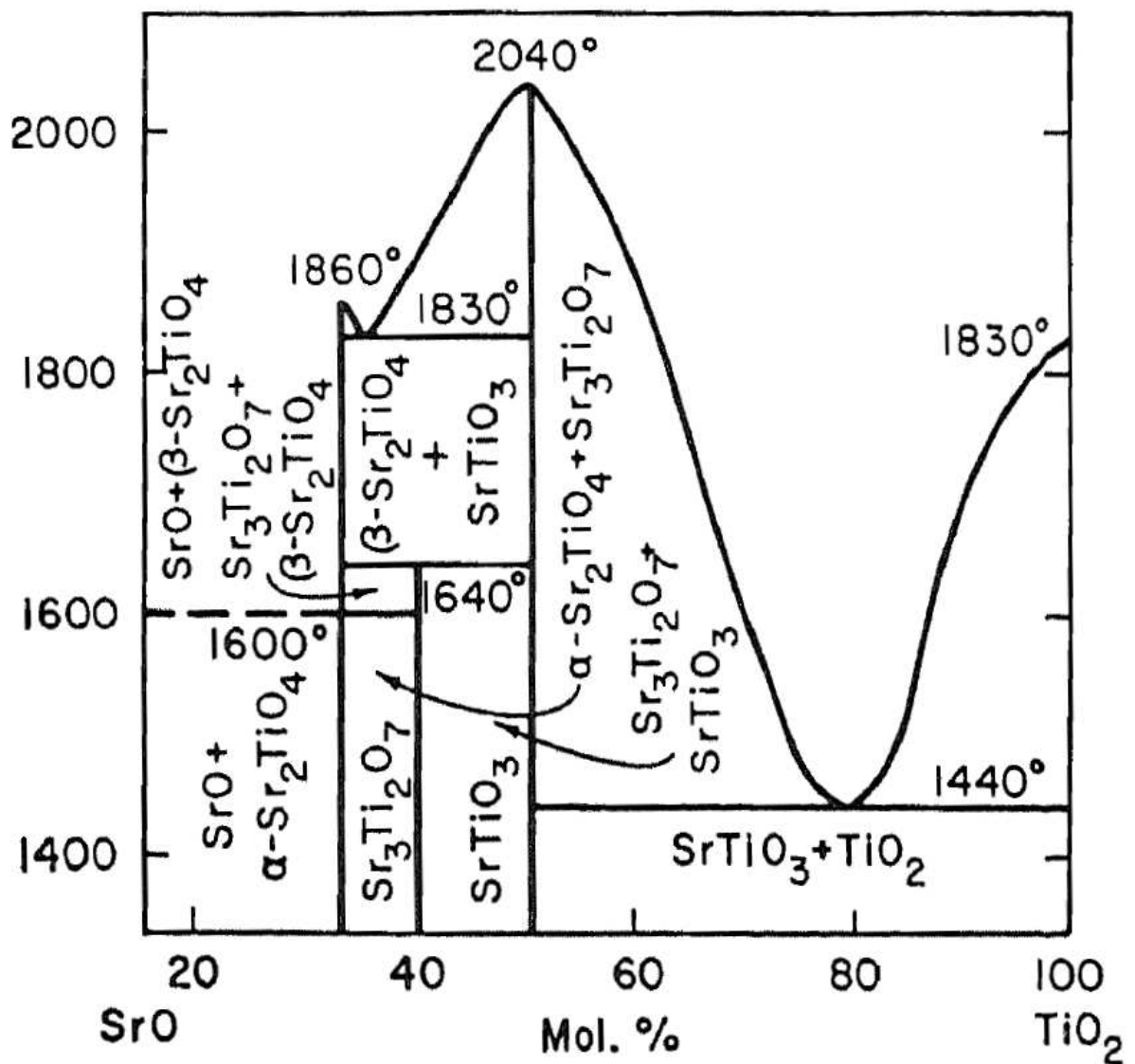
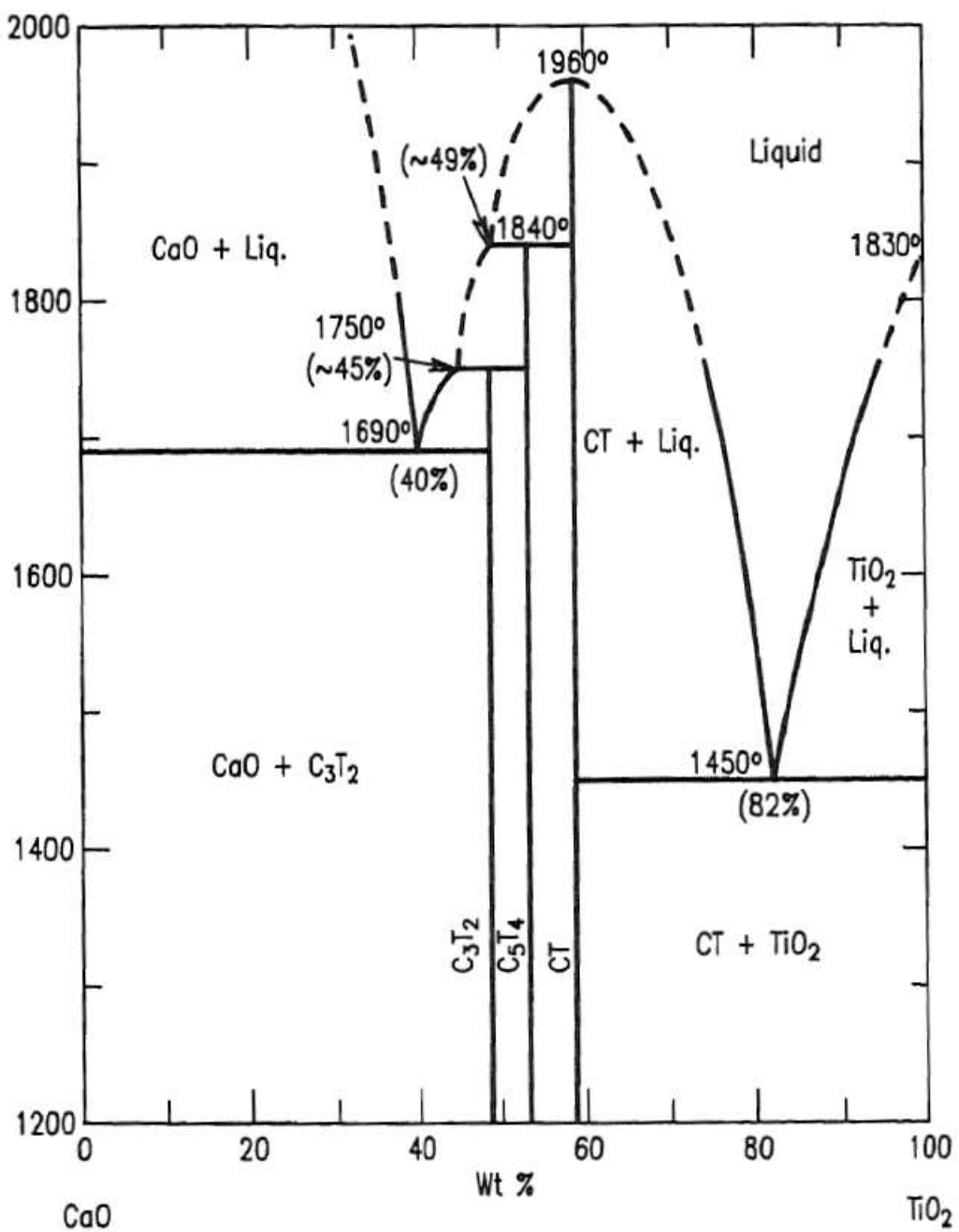


Fig. A.3. Phase diagram of the system SrO-TiO<sub>2</sub> (Fig. 297 in Ref.<sup>101</sup>).



**Fig. A.4.** Phase diagram of the system CaO-TiO<sub>2</sub> (Fig. 6385 in Ref.<sup>101</sup>). C= CaO, T= TiO<sub>2</sub>.

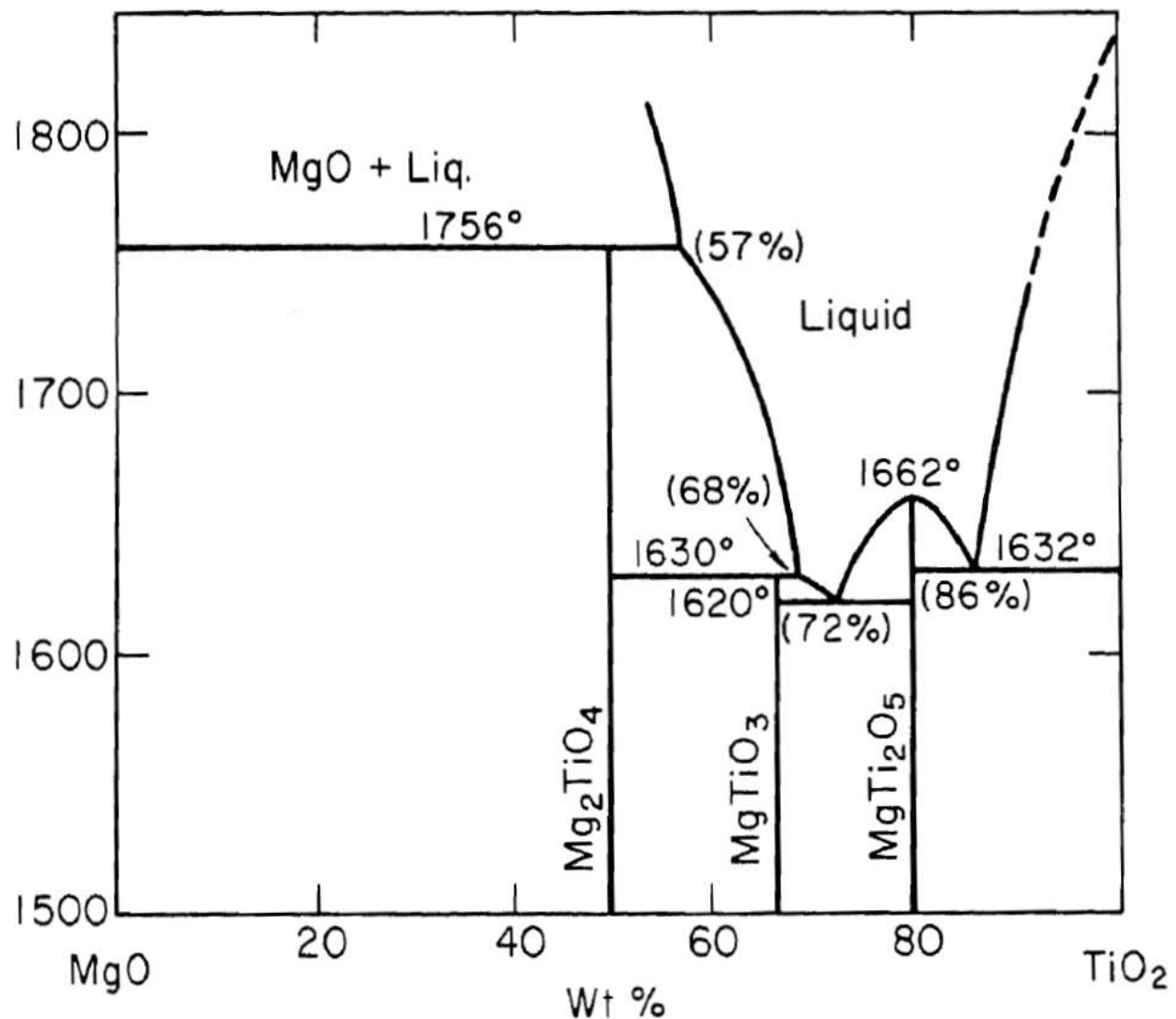
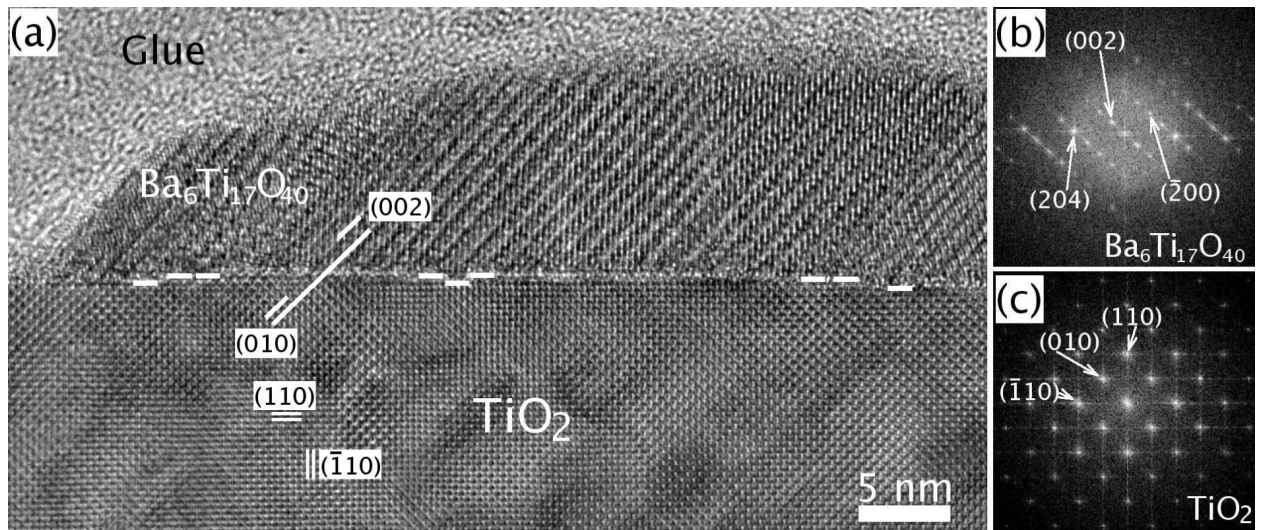
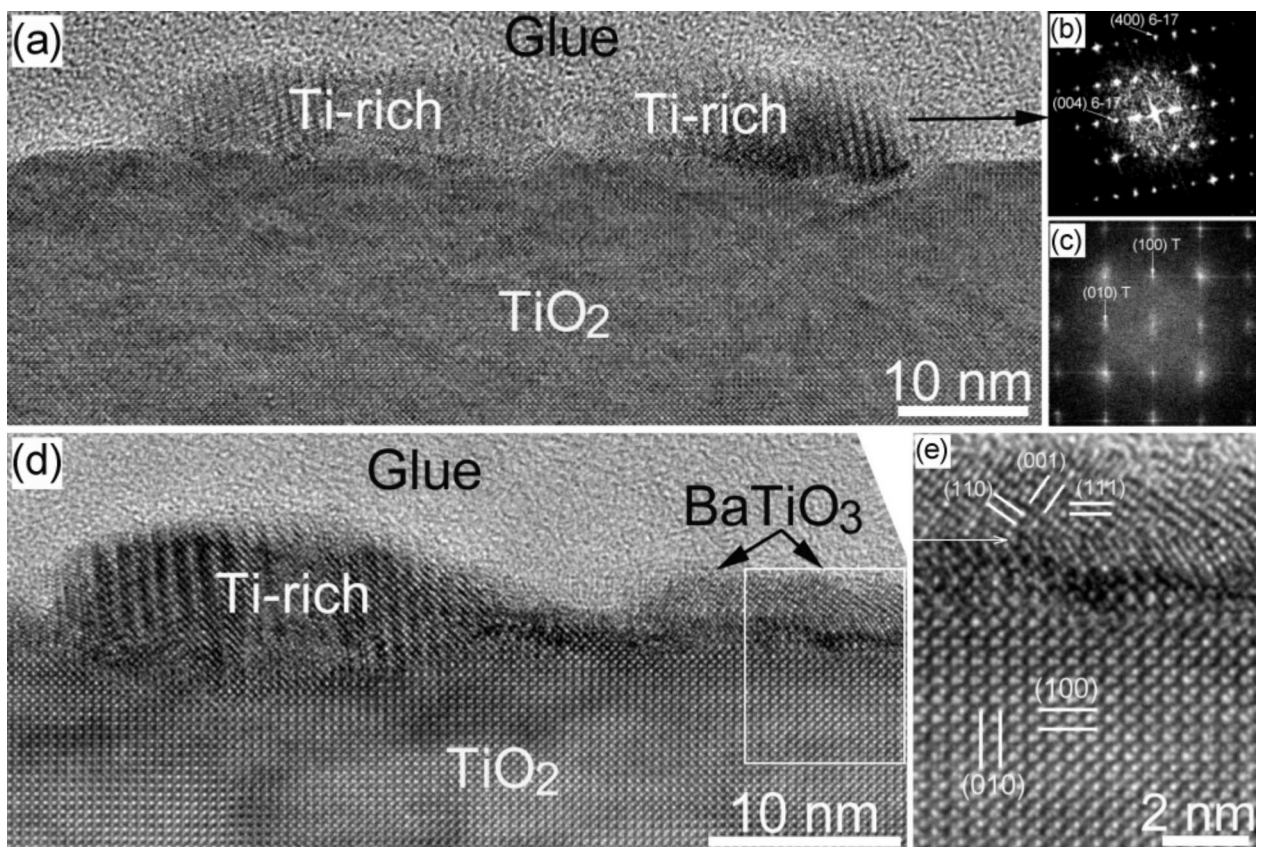


Fig. A.5. Phase diagram of the system MgO-TiO<sub>2</sub> (Fig. 4336 in Ref.<sup>101</sup>).



**Fig. A.6.** HRTEM image of a sample after the reaction of a  $\text{BaO}$  vapour with a  $(110) \text{TiO}_2$  (rutile) substrate at  $900^\circ\text{C}$ . The nominal thickness of  $\text{BaO}$  was  $\approx 1 \text{ nm}$ . (a) Part of a Ti-rich island on the rutile substrate. The long white line in the image indicates  $(002) \text{Ba}_6\text{Ti}_{17}\text{O}_{40} \parallel (010) \text{TiO}_2$ . The dashes show steps on the  $\text{TiO}_2$  surface. (b) FFT image of a  $\text{Ba}_6\text{Ti}_{17}\text{O}_{40}$  Ti-rich grain. (c) FFT image of the rutile substrate. Viewing direction is  $[010] \text{Ba}_6\text{Ti}_{17}\text{O}_{40} \parallel [001] \text{TiO}_2$ .



**Fig. A.7.** HRTEM images of a sample after the reaction of a  $\text{BaO}$  vapour with a  $(100) \text{TiO}_2$  (rutile) substrate at  $900^\circ\text{C}$ . The nominal thickness of  $\text{BaO}$  was  $\approx 1 \text{ nm}$ . (a) Ti-rich islands on the rutile substrate. (b) FFT image of a  $\text{Ba}_6\text{Ti}_{17}\text{O}_{40}$  (6-17) Ti-rich grain. (c) FFT image of the rutile substrate (T). Viewing direction is  $[010] \text{Ba}_6\text{Ti}_{17}\text{O}_{40} \parallel [001] \text{TiO}_2$ . (d) Ti-rich and  $\text{BaTiO}_3$  grains on the rutile substrate. (e) Computer-processed lattice plane images of  $\text{BaTiO}_3$  and the rutile substrate (magnified section of image (d)). The arrow in image (e) marks a  $(111)$  twin boundary in  $\text{BaTiO}_3$ . Viewing direction is  $[1\bar{1}0] \text{BaTiO}_3 \parallel [001] \text{TiO}_2$ .

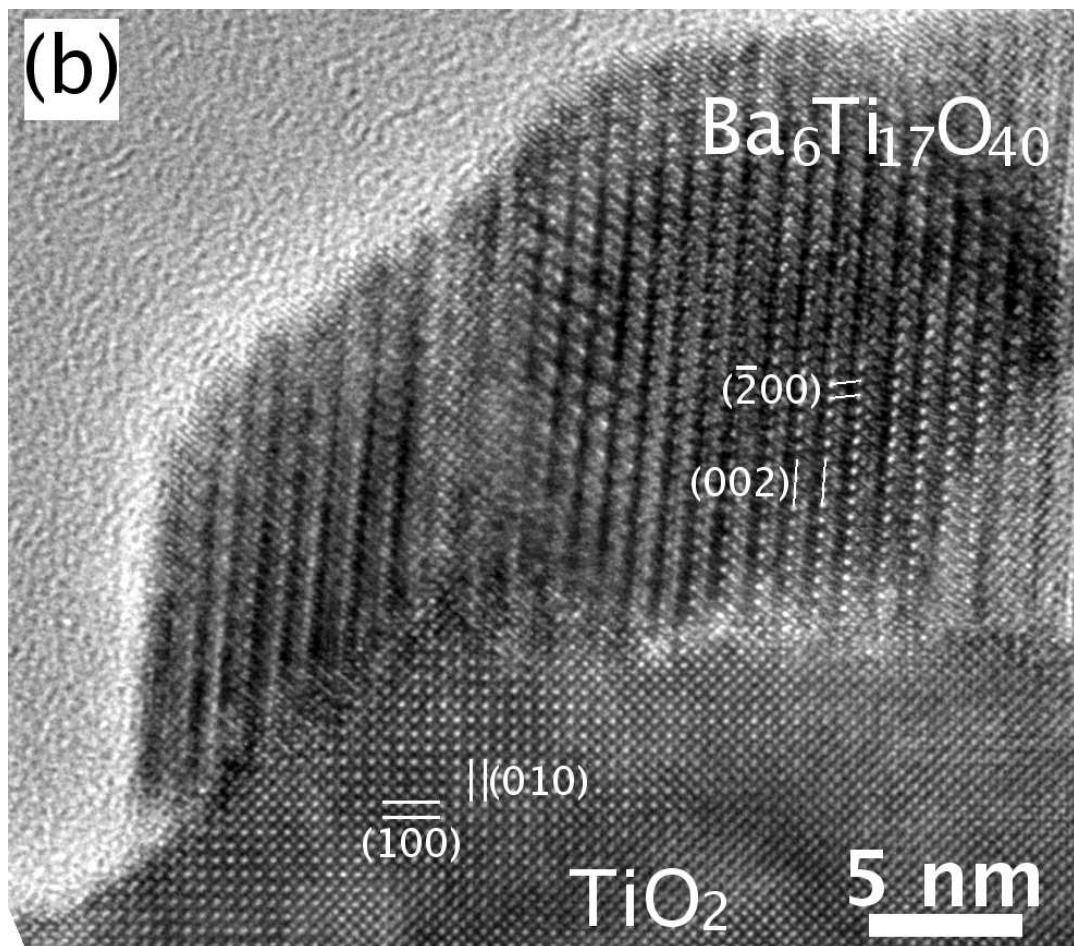


**Fig. A.8.** HRTEM image of a sample made by a vapour-solid reaction on a (100)  $\text{TiO}_2$  (rutile) substrate at 900 °C. The nominal thickness of BaO was  $\approx 5$  nm. b) lattice plane images of  $\text{Ba}_6\text{Ti}_{17}\text{O}_{40}$  and the rutile substrate. Viewing direction is  $[010] \text{Ba}_6\text{Ti}_{17}\text{O}_{40} \parallel [001] \text{TiO}_2$ .

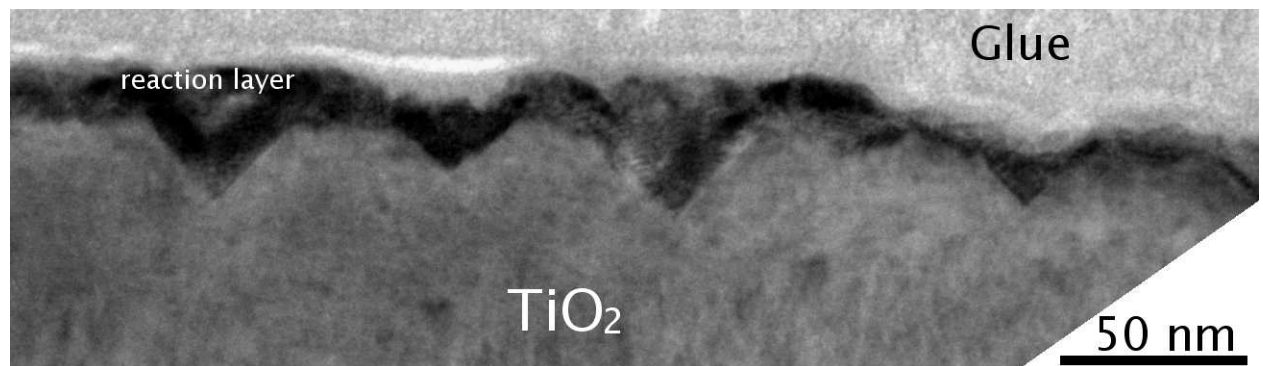


**Fig. A.9.** TEM image of a sample made by vapour-solid reaction of a BaO vapour with (100)  $\text{TiO}_2$  (rutile) surface at 700 °C. Large (110) and  $(1\bar{1}0)$   $\text{TiO}_2$  facets have developed after the reaction.

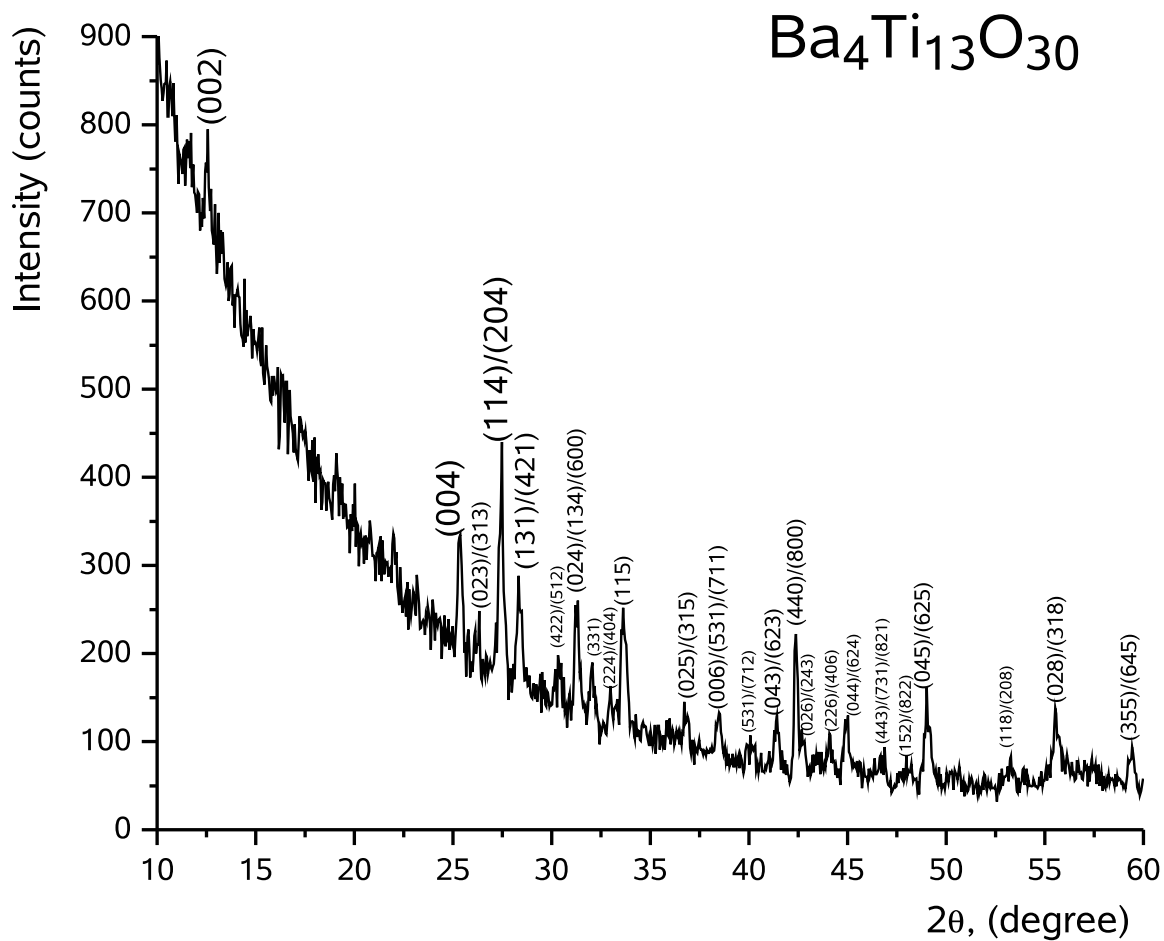


**Fig. A.10.** XRD  $2\theta$  scan of a sample made by a solid-solid reaction in air at  $900\text{ }^\circ\text{C}$  for 30 min between a (100)  $\text{TiO}_2$  (rutile) substrate and a  $\text{BaCO}_3$  thin film grown at  $500\text{ }^\circ\text{C}$ . The pattern was indexed according to JCPDS 84-2213. The scan speed was  $0.001\text{ }^\circ/\text{s}$ .

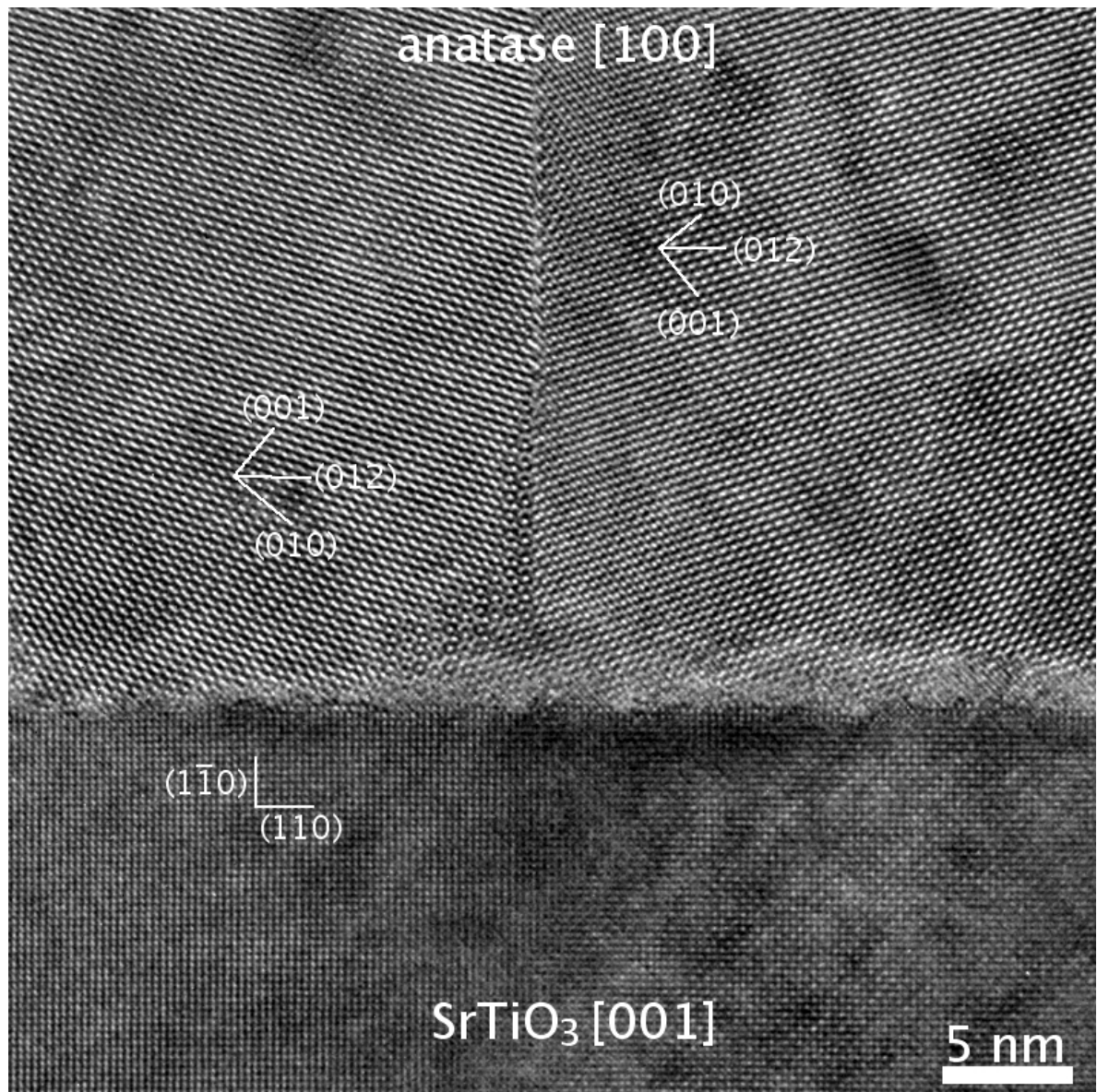


**Fig. A.11.** HRTEM image of an epitaxial  $\text{TiO}_2$  (anatase) thin film grown on a (110)  $\text{SrTiO}_3$  substrate at 700 °C.

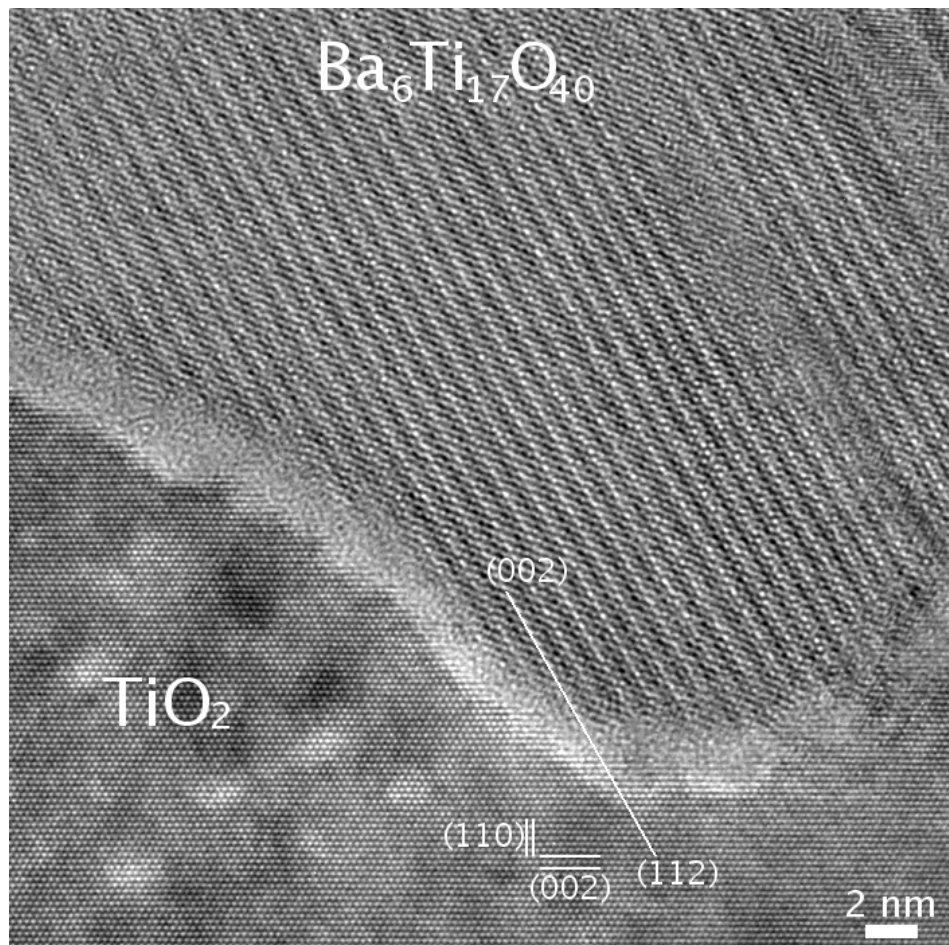


**Fig. A.12.** Lattice plane image of an epitaxial (001)  $\text{TiO}_2$  (anatase) film and a  $\text{Ba}_6\text{Ti}_{17}\text{O}_{40}$  grain. The long white lines mark the  $(001) \text{ Ba}_6\text{Ti}_{17}\text{O}_{40} \parallel (112) \text{ TiO}_2$  (anatase) planes. Viewing direction is  $[010] \text{ Ba}_6\text{Ti}_{17}\text{O}_{40} \parallel [1\bar{1}0] \text{ TiO}_2$  (anatase).

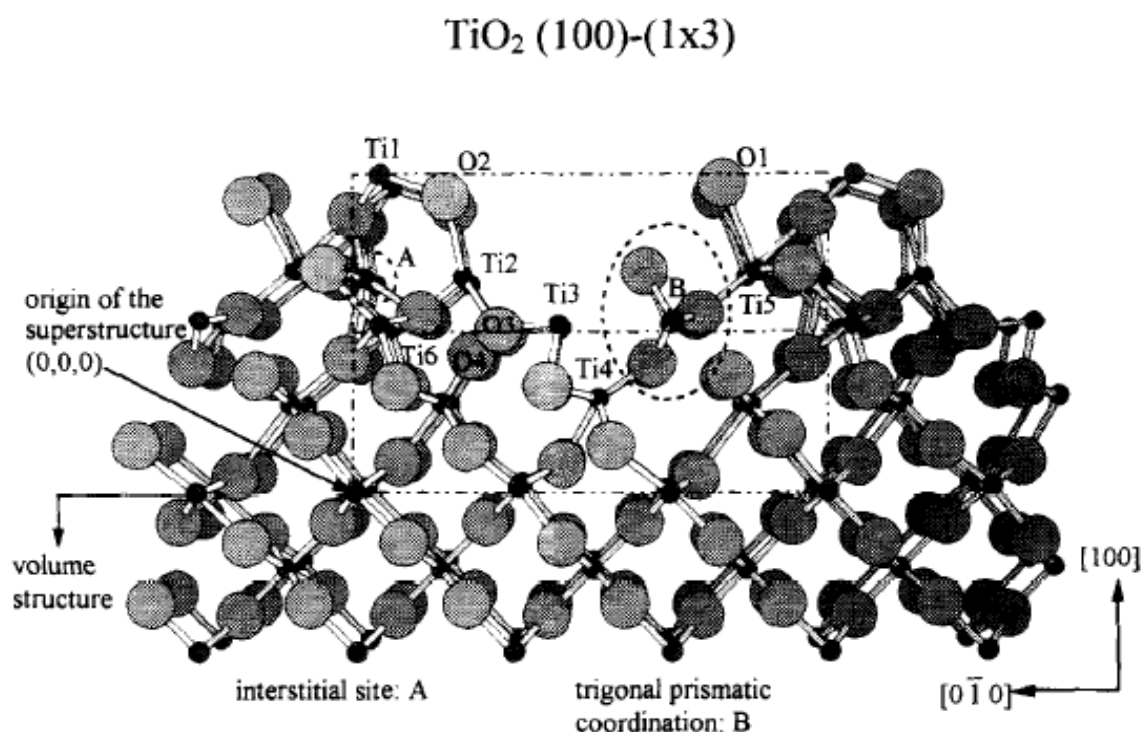


**Fig. A.13.** Structure model of the rutile (100)-(1x3) surface projected along [001]. The origin of the superstructure cell is indicated by an arrow. The titanium atoms labelled Ti1-Ti5 and A, B are coordinated by oxygen as follows: Ti1 three-fold; Ti2 five-fold; Ti3 bridge site; Ti4 six-fold; Ti5 six-fold; A five-fold (interstitial site); B six-fold (trigonal prismatic). This heavily relaxed model was proposed by Zajonz *et al.*<sup>165</sup>

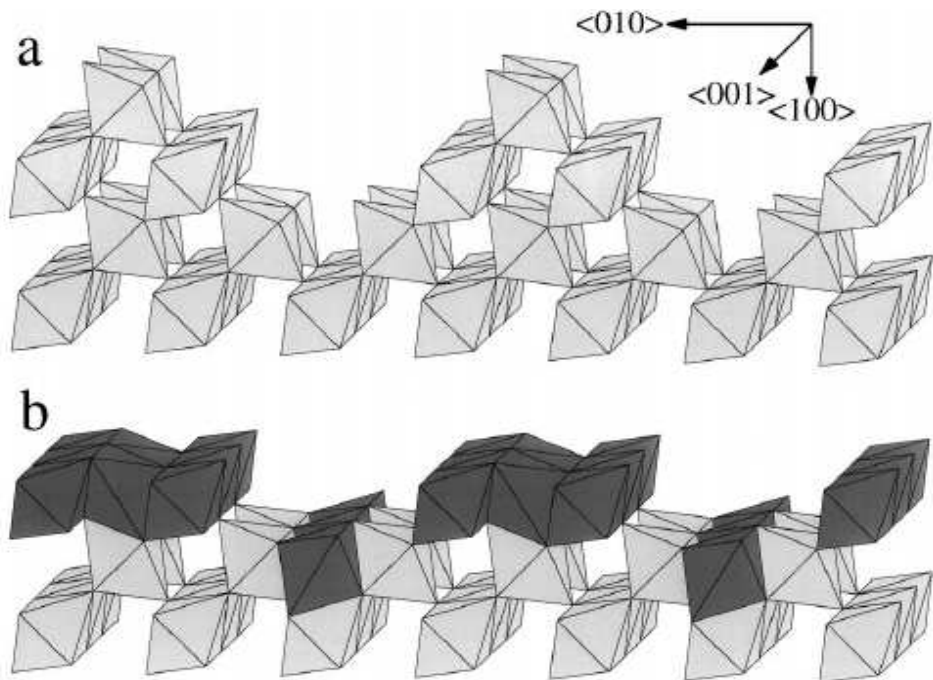


**Fig. A.14.** Octahedra models: schematic representation of (a) the microfacet model and (b) the model proposed by E. Landree *et al.*<sup>166</sup> At the center of each octahedron is a titanium atom and oxygen atoms are positioned at the corners. The darker shade is used to highlight the major differences between (a) and (b).

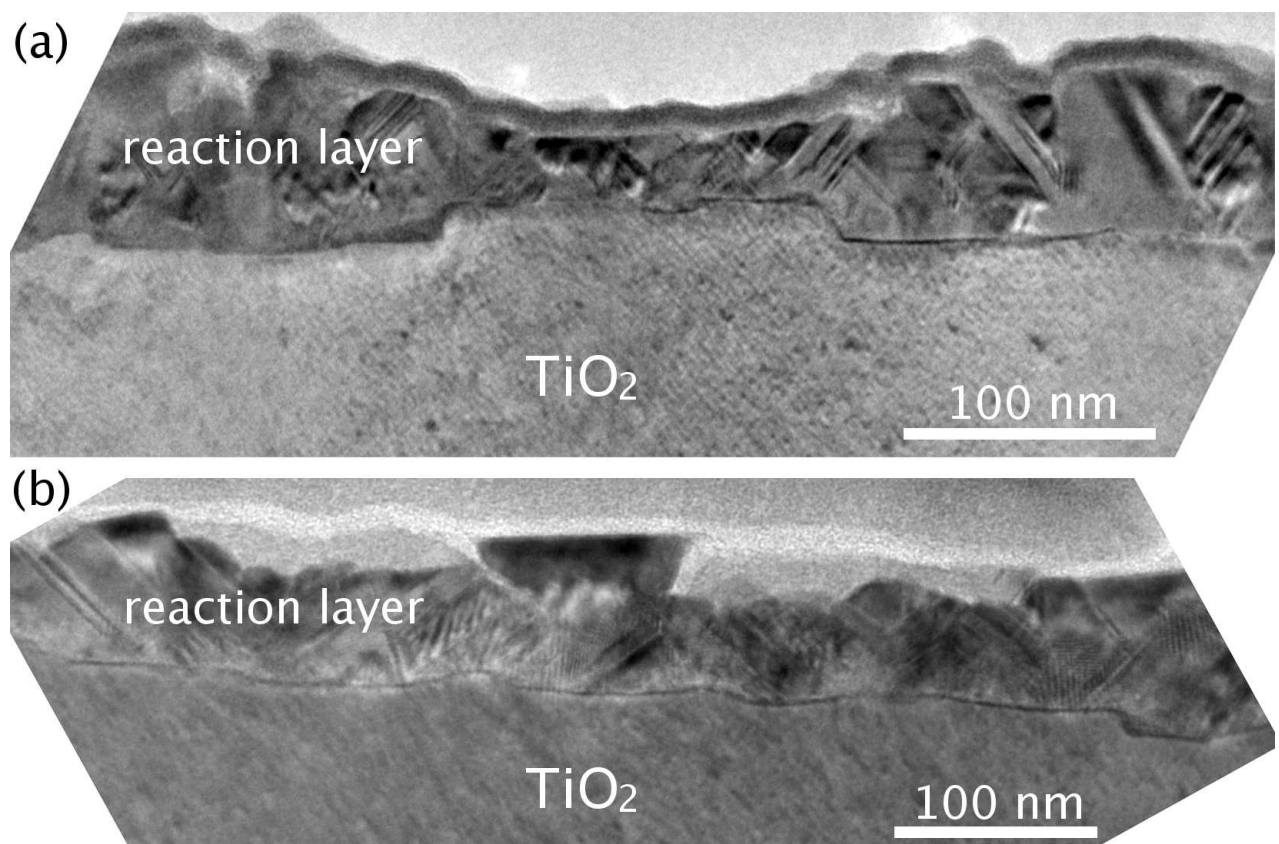


**Fig. A.15.** TEM images of a sample made by a solid-solid reaction between a  $\text{BaCO}_3$  film and a (110)  $\text{TiO}_2$  (rutile) surface at  $800^\circ\text{C}$  for 30 min in vacuum. The  $\text{BaCO}_3$  layer was grown at a substrate temperature of  $500^\circ\text{C}$ .

# **Eidesstattliche Erklärung**

Hiermit erkläre ich, dass ich meine Dissertation selbständig und ohne fremde Hilfe verfasst und keine anderen als die von mir angegebenen Quellen und Hilfsmittel zur Erstellung meiner Dissertation verwendet habe. Den benutzten Werken wörtlich oder inhaltlich entnommene Stellen sind als solche gekennzeichnet.

Andriy Lotnyk,

Halle (Saale), 26 April 2007

# Acknowledgments

Working on a Ph.D. thesis is truly a walk in "mystery forest", and I would not have been able to complete this journey without the aid and support of the people around me over the past three years who helped me to find an adequate way in the forest.

It was a pleasure for me to work at the Max Planck Institute of Microstructure Physics in Halle. I would like to express my gratitude to Prof. Dr. Ulrich Gösele for offering me this opportunity.

I would specially like to express my gratefulness towards my supervisor, Dr. Stephan Senz. I am really happy to have such a great supervisor. It was a great challenge and pleasure for me to work together with him and part of my knowledge is due to his constant support and many long discussions. He spent a lot of time helping me to gain a deep knowledge in transmission electron microscopy. I want to thank him for his "Geduld" to me, for his German course, for his "How to Write a Paper", for his "How to Read a Paper", for his criticism and many others "How to's" relating not only to scientific fields. I learned a lot during this time and I am convinced that this knowledge will help me in the future.

I am very grateful to Prof. Dr. Dietrich Hesse for his constant encouragement and his advise on scientific aspects. It was a pleasure for me to have such a supportive co-supervisor. I enjoyed his interest in my research and fruitful discussions. I thank him for all his effort and his help.

I would like to thank Prof. Dr. H.-P. Abicht and his group from Fachbereich Chemie at Martin-Luther-Universität Halle-Wittenberg for helpful discussions during the seminars attended by me.

I want to thank Mrs. Sina Swatek for preparing the numerous samples for transmission electron microscopy investigations. I also thank Mr. Sven-Holger Stephan who took care of equipment for preparation of the samples for transmission electron microscopy analysis.

My special word of appreciation goes out to my wife and my son, my parents and my mother-in-law for their love, for believing in me, for encouragement and constant support.

I am also indebted to all colleagues and friends as well as all staff members of the Max Planck Institute of Microstructure Physics who helped me in one or another way but are not mentioned here.

The German Research Foundation (DFG) via SFB 418 (Project A1) at Martin-Luther-Universität Halle-Wittenberg is gratefully acknowledged for financial support.

# **Curriculum Vitae**

## **Personal Information**

First Name: Andriy  
Middle Name: Anatoliyovich  
Last Name: Lotnyk  
Date of birth: 16 March 1980  
Place of birth: Kupjansk city, Kharkiv region, Ukraine  
Nationality: Ukraine  
Sex: Male  
Marital status: Married (1 son)

## **Education and Professional experience**

1987-1992 Primary School, Kupjansk city, Kharkiv region, Ukraine  
1992-1997 Grammar School, Kupjansk city, Kharkiv region, Ukraine  
1997 Graduation  
1997-2002 Study of Physics, Department of Solid State Physics, V. N. Karazin Kharkiv National University, Kharkiv, Ukraine  
2002 Graduation with title of Specialist of Physics (with honour). Speciality: Solid State Physics. Diploma title: "Strengthening of calcium phosphate ceramic" under leadership of Prof. Dr. Z. Zyman and Dr. V. Gluschko  
2002-2004 Scientist, Kharkiv National Academy of Municipal Economy, Department of Physics, Kharkiv, Ukraine  
2004-2007 Ph.D. student at Martin Luther University, Halle-Wittenberg, Germany  
2004-2007 Doctorate study at Max Planck Institute of Microstructure Physics under leadership of Prof. Dr. D. Hesse and Dr. S. Senz, Halle, Germany. Topic: "Solid state reactions in electroceramic systems"

## **Achievements and Awards**

Award 2001-2002 DAAD (German Academic Exchange Service) award for strong academic grades and good scientific achievements

Andriy Lotnyk,

Halle (Saale), 26 April 2007

# List of publications

1. A. Lotnyk, S. Senz, D. Hesse "BaTiO<sub>3</sub> formation by solid-state reactions on rutile single crystals", *Diffusion Fundamentals*, **2**, 51.1-51.2 (2005).
2. A. Lotnyk, S. Senz, D. Hesse "Formation of BaTiO<sub>3</sub> thin films from (110) TiO<sub>2</sub> rutile single crystals and BaCO<sub>3</sub> by solid state reactions", *Solid State Ionics*, **177**, 429-436 (2006).
3. A. Lotnyk, S. Senz, D. Hesse "Growth and characterization of (012)- and (001)-oriented epitaxial anatase thin films", *Advances in Science and Technology*, **46**, 146-151 (2006) (<http://www.scientific.net>, Trans Tech Publications).
4. A. Lotnyk, S. Senz, D. Hesse "Epitaxial growth of TiO<sub>2</sub> thin films on SrTiO<sub>3</sub>, LaAlO<sub>3</sub> and yttria-stabilized zirconia substrates by electron beam evaporation", *Thin Solid Films*, **515**, 3439-3447 (2007).
5. A. Lotnyk, S. Senz, D. Hesse "Thin film solid state reactions of solid BaCO<sub>3</sub> and BaO vapor with (100) rutile substrates", *Acta Mater.*, **55**, 2671-2681 (2007).
6. A. Lotnyk, S. Senz, D. Hesse "Orientation relationships of SrTiO<sub>3</sub> and MgTiO<sub>3</sub> thin films grown by vapor-solid reactions on (100) and (110) TiO<sub>2</sub> (rutile) single crystals", *J. Phys. Chem. C*, **111**, 6372-6379 (2007).
7. A. Lotnyk, A. Graff, S. Senz, N. D. Zakharov, D. Hesse "Topotaxial formation of titanium-rich barium titanates during solid-state reactions on (110) TiO<sub>2</sub> (rutile) and (001) BaTiO<sub>3</sub> single crystals", *Solid State Sci.*, in press, doi:10.1016/j.solidstatesciences.2007.08.001, (2007).

# Conference contributions

1. A. Lotnyk, S. Senz, A. Graff, D. Hesse "Phase formation and microstructure in the system BaO-TiO<sub>2</sub> during solid-state reactions on rutile single crystal surfaces", International Workshop on Nanoscale Structure and Dynamics, Leucorea, Lutherstadt, Wittenberg, Germany, 20.-22.09.2004, *Poster*.
2. A. Lotnyk, A. Graff, S. Senz, D. Hesse "Phase formation sequence during thin film solid-state reactions in the BaO-TiO<sub>2</sub> system", Frühjahrstagung des Arbeitskreises Festkörperphysik der Deutschen Physikalischen Gesellschaft, Berlin, Germany, 04.-09.03.2005, *Poster*.
3. A. Lotnyk, S. Senz, D. Hesse "BaTiO<sub>3</sub> formation by solid state reactions on rutile single crystals", Autumn School on Materials Science and Electron Microscopy "Microscopy of Tomorrow's Industrial Materials", Berlin, Germany, 03.-08.10.2005, *Poster*.
4. A. Lotnyk, S. Senz, D. Hesse "Epitaxial anatase (012) and (001) grown on (110) and (100) SrTiO<sub>3</sub>", Frühjahrstagung des Arbeitskreises Festkörperphysik der Deutschen Physikalischen Gesellschaft, Dresden, Germany, 27.-31.03.2006, *Talk*.
5. A. Lotnyk, S. Senz, D. Hesse "Phase and microstructure evolution during BaTiO<sub>3</sub> formation by solid state reactions on TiO<sub>2</sub> surfaces", Frühjahrstagung des Arbeitskreises Festkörperphysik der Deutschen Physikalischen Gesellschaft, Dresden, Germany, 27.-31.03.2006, *Poster*.
6. A. Lotnyk, S. Senz, D. Hesse "Epitaxial growth of anatase thin films on (110) and (100) SrTiO<sub>3</sub>", 11<sup>th</sup> International Ceramic Congress and 4<sup>th</sup> Forum on New Materials (CIMTEC 2006), Acireale, Italy, 04.-09.06.2006, *Talk*.
7. A. Lotnyk, S. Senz, D. Hesse "Role of crystallography in topotaxial first-phase selection", Frühjahrstagung des Arbeitskreises Festkörperphysik der Deutschen Physikalischen Gesellschaft, Regensburg, Germany, 26.-30.03.2007, *Talk*.